

**Reactivity of Strained Bimetallic Systems:
A Case Study of Au-Ni Nanoparticles**

**Thesis Submitted to AcSIR
For the Award of the Degree of
DOCTOR OF PHILOSOPHY
In
Chemical Sciences**



By

Vysakh A B

Registration Number: 10CC11A26007

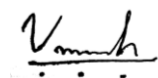
**Under the Guidance of
Dr. Vinod C Prabhakaran**

**CSIR- National Chemical Laboratory
Pune- 411008, India**

December 2016

CERTIFICATE

This is to certify that the work incorporated in this Ph.D. thesis entitled “*Reactivity of strained bimetallic systems: A case study of Au-Ni nanoparticles*” submitted by **Mr. Vysakh A B** to Academy of Scientific and Innovative Research (AcSIR) in fulfilment of the requirements for the award of the Degree of *Doctor of Philosophy in Chemical Sciences*, embodies original research work under my supervision. I further certify that this work has not been submitted to any other University or Institution in part or full for the award of any degree or diploma. Research material obtained from other sources has been duly acknowledged in the thesis. Any text, illustration, table etc., used in the thesis from other sources, have been duly cited and acknowledged.



Mr. Vysakh A B
(Student)



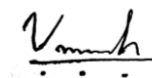
Research Guide
(Name & Signature)
Dr. Vinod. C. Prabhakaran

DECLARATION

I hereby declare that the work described in the thesis entitled “*Reactivity of strained bimetallic systems: A case study of Au-Ni nanoparticles*” submitted for the degree of *Doctor of Philosophy* in *Chemical Sciences* to the Academy of Scientific and Innovative Research (AcSIR), New Delhi, has been carried out by me at the Catalysis and Inorganic Chemistry Division, CSIR-National Chemical Laboratory, Pune-411008, India under the supervision of **Dr. Vinod. C. Prabhakaran**. I further declare that the material obtained from other sources has been duly acknowledged in this thesis. The work is original and has not been submitted in part or full by me for any other degree or diploma to this or any other university.

Date: 29th December 2016

CSIR-NCL, Pune



Vysakh A B

Research Scholar

.....dedicated to

my Beloved Parents

One day during my childhood I went out with my “amma” (mother) to the market nearby my village. She told me by pointing to a big shop, “you can get anything from there.... except your ‘amma and appa’....”. I smiled at her that day when I was only 8 years old, because I understood the simple concept which conveys that they are valuable to me. But after that incident, each and every stage of my life taught me the diversity of that sentence. And today, I have 1000 meanings for her simple words and I am pretty sure that I will go on with that sentence eternally.....

She is the best teacher ever in my life....

ACKNOWLEDGEMENT

My research career at CSIR-National Chemical Laboratory has been one of the most memorable experiences in my life. On this occasion of accomplishment of my Ph.D career at CSIR-NCL, I would like to acknowledge all my teachers, friends, family members and well wishers who included me in their prayers and gave their blessings throughout my life.

First and foremost, I would like to express my heartfelt and sincere gratitude to my research supervisor Dr. Vinod. C. Prabhakaran, who introduced me to an interesting field of research in nanoscience and catalysis. He has been the source of motivation during my Ph.D career; whether scientific or non-scientific and I have been greatly inspired by his way of problem-solving. I am thankful for his inspiration, patience, timely advice and the constant support provided throughout my research tenure. I consider very fortunate for my association with him and it was a great honor working with him.

I am thankful to Prof. Ashwini Kumar Nangia, Director of CSIR-NCL Pune, Dr. Sourav Pal and Dr. V. K. Pillai (former directors) and Head of Catalysis and Inorganic Chemistry Division Dr. D. Srinivas, Dr. A. P. Singh (former H.O.D) for their kind help, encouragement and extending all possible infrastructural facilities to complete my research work. I thank the University Grants Commission (UGC), New Delhi, for award of research fellowship. I extend my sincere gratitude to all my DAC members Dr. C. S. Gopinath, Dr. K. Sreekumar and Dr. S. K. Asha for their timely suggestions and instructions throughout my Ph.D program.

I am grateful to Dr. C. S. Gopinath for his valuable discussions, research expertise, teaching skills and stable support which have always been a source of encouragement to me. I wish to sincerely thank him for giving me the opportunity to be a part of APPES surface science project and helping me to perform the high pressure experiments with XPS instrument. I also express my gratitude to Dr. P. A. Joy for his continuous support and his students (Govind and Jaya) for carrying out the magnetic measurements of the samples. I thank Dr. A. P. Singh for providing me the high pressure liquid phase reactors and G.C facilities to carry out catalyst activity experiments. I would like to acknowledge Dr. T. Raja and his research group for their support and co-operation throughout my doctoral studies. I would like to extend my thanks to Dr. K. Sreekumar, Dr. R. Nandini Devi, Ms. Violet Samuel, and the Electron microscopy group at

NCL for their valuable helps in catalyst characterization. Special thanks to Dr. Dinesh Jagadeesan and Dr. Ekambaram Balaraman and other members of our seminar group for giving me the opportunity to be a part of extended research topics and discussions.

I am thankful to Mr. P. K. Purushothaman, Mr. Madhu (Catalysis Division) and all the other technical staffs of CSIR - NCL for their official support and assistance during these years. I wish to thank all NCL New Hostel mess workers and other members for providing me calm and excellent atmosphere with timely food at the final stages of my research work.

I must say that it is a great privilege for me to work with Dr. Vinod. C. Prabhakaran right from the beginning of our lab. My association with him and his family, Mrs. Nita, Varadh (tiger senior) and Nikith (tiger junior) made my life at NCL a memorable occasion. It gives me great pleasure to thank seniors from Dr. C. S. Gopinath's group especially Dr. Edwin and Dr. Sivaranjani for their advice and valuable help at the earlier stages of our lab commencement. I have high regards for my lab mates Sunil, Sreedhala, Sudheesh (former) and Meera (former) for their helping hand and co-operation particularly at the initial stages. I would like to thank all my lab mates Sharad, Yogita, Preeti, Tanmay, Sumanta, Govind and Betsy for their patience, friendship, arguments, understanding, "brainstorming" discussions and making the lab feel like an enjoyable family. I am highly indebted to my collaborators Ruchi Jain for her immense efforts while carrying out high pressure experiments and Anish for his guidance to conduct the liquid phase reactions. I personally thank my juniors Chinchu, Belvin, Yadukiran, Shebin, Debojit and Mridul who did their undergraduate projects with me and helped me in various projects. It has been a great and challenging experience to mentor them and I truly believe they will be very successful in the future. I would like to extend my thanks to all the project students (past and present) of our lab.

Many thank to all my colleagues especially Ashok, Anju, Laxmi Prasad, Anil nagaraj, Praveen, Suman, Rajendra Prasad and many more for creating a cheerful atmosphere. I am also grateful to all my divisional friends Dr. Rajesh, Dr. Soumya, Dr. Thushara, Dr. Rajambal, Dr. Kanak, Dr. Unnikrishnan, Dr. Atul, Jijil, Leena, Shibin, Devaraj, Kshirodra, Pradnya, Anjani, Manoj, Prabhakar for their suggestions and help at various stages of my research. A very special appreciation to all my Malayali friends Shoy, Kiran, Govind, Sarath, Eldho bhai, Alson, Suresh bhai, Sreekuttan, Venu, Anumon, Jithesh, Sanjush, Jayaprabha, Prajitha, Nishamol, juniors in NCL and outside (specially Ekka's shop at complex) for their encouragement and support throughout my stay at NCL.

I sincerely thank my teachers Divakaran sir and Indira teacher (Prof., Sree Kerala Varma College, Thrissur) for their invaluable help and moral support which gave me strength to enter the research career. My heartfelt thanks to Vinod sir, Ajith sir, Jayaram sir (Sakthan Thampuran College, Thrissur) and Roji sir (CUSAT) for providing me all the facilities and guiding me to the right way during my CSIR-NET examination period.

I want to express my deepest gratitude to my best friend Senju (Asst. Prof., S.H. College, Ernakulam) who motivated me to qualify my competitive examination and directed me to research profession. Many thank to my dear friends Vijesh, Sijo and Jaseena for their kind support during my difficult times and making my journey cheerful.

I am very grateful to have the opportunity of studying here at CSIR-NCL, under the guidance of eminent scientists and meet many reputed scientists from other institutions. Their valuable suggestions and assistance gave me the inspiration throughout my research period. I am grateful to all my former and present teachers, also people who have inspired me and gave their blessings directly or indirectly in my career.

I have no words to thank my parents, deepest gratitude from my heart goes to them and I owe them each and every bit of the good I have in me. My heartfelt gratitude and respect to my father for his support, inspiration and perception to overcome the challenges in life. I also thank my younger brother and sister for their love, support, encouragement and caring our lovable parents. Finally, from my heart I say “Matha Pitha Guru Deivam”. “Mother, Father, Teacher and God”, it is the greatest truth and I believe God is real and all four are just different forms.

Above all, I thank God; the almighty for guiding me in my life.

Though, many have not been mentioned, none is forgotten.

Vysakh A Bharathan

Table of Contents

Abstract.....i-iv

Chapter 1: General Introduction and Literature Survey.....1-43

1.1 Nanomaterials and Heterogeneous Catalysis.....2

1.1.1 Nano: Quantum Confinement Effects and its Unique Properties.....2

1.1.2 Nanoparticles in Catalysis.....4

1.1.3 Recent Progress in Heterogeneous Catalysis.....4

1.2 A Brief History of Bimetallic Systems and Their Development as Catalytic Materials.....7

1.2.1 Bimetallic Synergism: Geometric and Electronic Effects.....8

1.2.2 Inspiration from Surface Science and Theoretical Investigations.....9

1.2.3 Bridging the Material and Pressure Gap: Surface Science Aspects to
Real World Catalysis.....10

1.2.4 Importance of Gold (Au)-Nickel (Ni) Bimetallic Systems and Analysis
of Au-Ni Model Surfaces.....12

1.3 Bimetallic Nanoparticles: Synthesis and Catalytic Applications.....14

1.3.1 General Synthesis Methods for Bimetallic Nanoparticles.....14

1.3.2 Synthesis of Gold (Au)-Nickel (Ni) Bimetallic Nanostructures.....20

1.3.3 Core-shell Bimetallic Nanoparticles for Colloidal Phase Catalysis.....21

1.3.4 Gold (Au)-Nickel (Ni) Bimetallic Nanoparticles in Catalysis.....23

1.3.5 Characterisation of Bimetallic Nanoparticles.....24

1.4 Objectives of this Thesis.....33

1.5 References.....34

**Chapter 2: Organic Phase Synthesis and Catalytic Activity Results
of Au@Ni Core-shell Nanoparticles**.....44-108

2.1 Introduction.....45

Chapter 2A: Synthesis of Magnetically Diverse Au@Ni Core-shell Nanoparticles by Using Thermal Reduction: Oxidation Resistance Analysis and Catalytic Application for Nitro (-NO₂) Group Reductions.....50

| | |
|--|----|
| 2A.1 Experimental Section..... | 50 |
| 2A.2 Results and Discussion..... | 53 |
| 2A.2.1 UV-Vis Spectroscopy Analysis of Au@Ni Core-shell Nanoparticle Formation..... | 53 |
| 2A.2.2 Transmission Electron Microscopy Studies (TEM)..... | 55 |
| 2A.2.3 X-Ray Diffraction Studies (XRD)..... | 63 |
| 2A.2.4 XRD Studies on Au@Ni _{FCC} and Au@Ni _{HCP} Nanoparticles under Ambient Pressure Annealing..... | 66 |
| 2A.2.5 Magnetic Measurements (SQUID-VSM)..... | 68 |
| 2A.2.6 X-ray Photoelectron Spectroscopy Investigation (XPS)..... | 70 |
| 2A.2.7 Catalytic Activity Results of Au@Ni Core-shell Nanoparticles for Nitro (-NO ₂) to Amino (-NH ₂) Group Conversion and Effect of Temperature Pre-treatment..... | 73 |
| 2A.2.8 Effect of Nickel Shell Thickness on the Catalytic Activity of Magnetic Au@Ni Core-shell Nanoparticles for Nitro (-NO ₂) Group Reductions..... | 78 |

Chapter 2B: Synthesis of Magnetic Au@Ni Core-shell Nanoparticles under Mild Conditions and Catalytic Activity Results for Selective Hydrogenation of Phenylacetylene (P.A).....83

| | |
|---|----|
| 2B.1 Experimental Section..... | 83 |
| 2B.2 Results and Discussion..... | 84 |
| 2B.2.1 UV-Vis Spectroscopy Analysis (UV-Vis)..... | 84 |
| 2B.2.2 Transmission Electron Microscopy Studies (TEM)..... | 85 |
| 2B.2.3 X-Ray Diffraction Studies (XRD)..... | 86 |
| 2B.2.4 Magnetic Measurements (VSM)..... | 87 |
| 2B.2.5 X-ray Photoelectron Spectroscopy Investigation (XPS)..... | 88 |
| 2B.2.6 Catalytic Activity Results of Au@Ni Core-shell Nanoparticles for Selective Hydrogenation of Phenylacetylene (P.A) to Styrene and Ethylbenzene (E.B)..... | 89 |

Chapter 2C: Green Route (Soyabean Oil as Solvent) for the Synthesis of Au@Ni Core-shell Nanostructures and Their Catalytic Activity Studies.....93

| | |
|---|-----|
| 2C.1 Experimental Section..... | 93 |
| 2C.2 Results and Discussion..... | 94 |
| 2C.2.1 UV-Vis Spectroscopy Analysis (UV-Vis)..... | 94 |
| 2C.2.2 Transmission Electron Microscopy Studies (TEM)..... | 95 |
| 2C.2.3 X-Ray Diffraction Studies (XRD)..... | 97 |
| 2C.2.4 Magnetic Measurements (VSM)..... | 98 |
| 2C.2.5 X-ray Photoelectron Spectroscopy Investigation (XPS)..... | 99 |
| 2C.2.6 Catalytic Activity Results of Au@Ni Core-shell Nanostructures for Selective Hydrogenation of Phenylacetylene (P.A)..... | 100 |
| 2.2 Conclusions..... | 103 |
| 2.3 References..... | 104 |

Chapter 3: Synthesis of Au@Ni Core-shell Nanoparticle in Aqueous Medium: NAPXPS Studies on Oxidation Resistance and its Application in Selective Hydrogenation...109-133

| | |
|---|-----|
| 3.1 Introduction..... | 110 |
| 3.2 Experimental Section..... | 111 |
| 3.3 Results and Discussion..... | 114 |
| 3.3.1 UV-Vis Spectroscopy Analysis (UV-Vis)..... | 114 |
| 3.3.2 Transmission Electron Microscopy Studies (TEM)..... | 116 |
| 3.3.3 Magnetic Measurements (VSM)..... | 118 |
| 3.3.4 X-Ray Diffraction Studies (XRD)..... | 119 |
| 3.3.5 UHV and In-situ NAP-XPS Analysis of Au@Ni Core-shell Nanoparticles [Au ₈₀ @Ni ₂₀ , Au ₆₅ @Ni ₃₅ and Au ₅₀ @Ni ₅₀] under Various Temperature and Pressure Conditions..... | 121 |
| 3.3.6 Catalytic Activity Results of Au@Ni Core-shell Nanoparticles [Au ₈₀ @Ni ₂₀ , Au ₆₅ @Ni ₃₅ and Au ₅₀ @Ni ₅₀] for Selective Hydrogenation of Phenylacetylene (P.A)..... | 128 |
| 3.4 Conclusions..... | 131 |
| 3.5 References..... | 131 |

| | |
|--|----------------|
| Chapter 4: Surfactant free Synthesis of Au@Ni Core-shell Nanochains in Aqueous Medium as Efficient Transfer Hydrogenation Catalysts..... | 134-155 |
| 4.1 Introduction..... | 135 |
| 4.2 Experimental Section..... | 137 |
| 4.3 Results and Discussion..... | 139 |
| 4.3.1 UV-Vis Spectroscopy Analysis (UV-Vis)..... | 139 |
| 4.3.2 Transmission Electron Microscopy Studies (TEM)..... | 140 |
| 4.3.3 X-Ray Diffraction Studies (XRD)..... | 143 |
| 4.3.4 Magnetic Measurements (VSM)..... | 144 |
| 4.3.5 NAP-XPS Analysis of Au@Ni Core-shell Nanochains under Various Temperature and Pressure Conditions..... | 145 |
| 4.3.6 Catalytic Activity Results of Au@Ni Core-shell Nanochains for Transfer Hydrogenation of Acetophenone by Using Isopropanol as Hydrogen Donor..... | 148 |
| 4.4 Conclusions..... | 152 |
| 4.5 References..... | 152 |
| Chapter 5: Summary and Conclusions..... | 156-160 |

List of Figures

| | | |
|---------------------|---|----|
| Figure 1.1 | <i>I</i> (current)- <i>V</i> (voltage) characteristics obtained for Au clusters | 3 |
| Figure 1.2 | Scheme showing various types of catalysis, advancement in the catalyst..... | 5 |
| Figure 1.3 | A comparative schematic representations of bulk and nano materials | 8 |
| Figure 1.4 | Image showing the complexity of material gap between the surface science aspects and industrial catalysts | 11 |
| Figure 1.5 | Schematic representation of different bimetallic architectures..... | 14 |
| Figure 1.6 | Hydrogen generation from ammoniaborane (AB) aqueous solution..... | 21 |
| Figure 1.7 | Catalytic activity and selectivity results of icosahedral Au@Pd core-shell..... | 22 |
| Figure 1.8 | Rates of formic acid decomposition over M-core Pd shell (1:1) catalysts..... | 23 |
| Figure 1.9 | A digital photograph of the NAPXPS instrument at NCL | 31 |
| Figure 2A.1 | Schematic representation of various stages involved in the formation of Au@Ni _{FCC} and Au@Ni _{HCP} core-shell nanoparticles | 54 |
| Figure 2A.2 | Schematic representation of the formation of magnetic Au@Ni core-shell nanoparticles with different nickel shell thickness | 54 |
| Figure 2A.3 | UV-Vis spectra obtained for the preformed gold nanoparticle seeds and its sequential conversion into Au@Ni core-shell nanoparticles..... | 55 |
| Figure 2A.4 | TEM and HR-TEM images of (a-c) magnetic Au@Ni _{FCC} and (d-f) non-magnetic Au@Ni _{HCP} core-shell nanoparticles..... | 56 |
| Figure 2A.5 | HR-TEM images focussed on a group of Au@Ni _{FCC} nanoparticles..... | 57 |
| Figure 2A.6 | HR-TEM images of Au@Ni _{HCP} core-shell nanoparticles..... | 58 |
| Figure 2A.7 | Histogram analysis of (a) Au@Ni _{FCC} and (b) Au@Ni _{HCP} core-shell | 58 |
| Figure 2A.8 | TEM and HR-TEM images of Au@Ni core-shell nanoparticles..... | 59 |
| Figure 2A.9 | HR-TEM images of (a-b) Au@Ni _{1:0.5} , (c-d) Au@Ni _{1:1} and (e-f) Au@Ni _{1:2} ... | 60 |
| Figure 2A.10 | HR-TEM images (a-c) and histogram analysis (d-f) of Au@Ni _{1:0.5} , Au@Ni _{1:1} and Au@Ni _{1:2} core-shell nanoparticles | 61 |
| Figure 2A.11 | (a) Large area TEM image of Au@Ni _{1:2} core-shell nanoparticles | 61 |
| Figure 2A.12 | The EDX data obtained for the magnetic Au@Ni core-shell nanoparticles ... | 62 |

| | | |
|---------------------|---|----|
| Figure 2A.13 | Large area TEM images obtained for (a) initial stage gold nanoparticle seeds and (b) physical mixture of gold and nickel monometallic | 63 |
| Figure 2A.14 | XRD pattern obtained for (a) magnetic Au@Ni _{FCC} and (b) non-magnetic Au@Ni _{HCP} core-shell nanoparticles..... | 64 |
| Figure 2A.15 | XRD patterns of core-shell (a) Au@Ni _{1:0.5} , (b) Au@Ni _{1:1} and (c) Au@Ni _{1:2} nanoparticles..... | 65 |
| Figure 2A.16 | XRD patterns of monometallic (a) gold and (b) nickel nanoparticles | 66 |
| Figure 2A.17 | Temperature-dependent XRD analysis of (a) Au@Ni _{FCC} and (b) Au@Ni _{HCP} core-shell nanoparticles..... | 68 |
| Figure 2A.18 | Hysteresis loops of magnetic Au@Ni _{FCC} and non-magnetic Au@Ni _{HCP} core-shell nanoparticles at room temperature | 69 |
| Figure 2A.19 | Hysteresis loops obtained for (a) Au@Ni _{1:0.5} (b) Au@Ni _{1:1} and (c) Au@Ni _{1:2} core-shell nanoparticles..... | 69 |
| Figure 2A.20 | Individual XP spectra recorded for (a) Ni 2p and (b) Au 4f region in Au@Ni _{FCC} core-shell nanoparticles..... | 71 |
| Figure 2A.21 | XP spectra of Ni 2p and Au 4f obtained for the as synthesized (a) Au@Ni _{1:0.5} , (b) Au@Ni _{1:1} and (c) Au@Ni _{1:2} core-shell nanoparticles..... | 72 |
| Figure 2A.22 | UV-Vis spectra recorded for PNP reductions by using Au@Ni _{FCC} | 76 |
| Figure 2A.23 | UV-Vis spectra recorded for PNP reductions by using Au@Ni _{HCP} | 76 |
| Figure 2A.24 | Rate of PNP reduction reaction catalyzed by both Au@Ni _{FCC} and Au@Ni _{HCP} core-shell nanoparticles..... | 77 |
| Figure 2A.25 | UV-Vis peak quantification showing the decrease in the absorbance of nitrophenolate ion at 400 nm during PNP reduction..... | 77 |
| Figure 2A.26 | UV-Vis spectra obtained for PNP reduction by using as synthesised (a) Au@Ni _{1:0.5} , (b) Au@Ni _{1:1} and (c) Au@Ni _{1:2} nanoparticles..... | 79 |
| Figure 2A.27 | UV-Vis spectra obtained for PNTp reduction by using as synthesised (a) Au@Ni _{1:0.5} , (b) Au@Ni _{1:1} and (c) Au@Ni _{1:2} nanoparticles..... | 79 |
| Figure 2A.28 | The reactivity trend obtained for (i) Au@Ni _{1:0.5} , (ii) Au@Ni _{1:1} and (iii) Au@Ni _{1:2} nanoparticles towards (a) PNP and (b) PNTp reduction..... | 81 |
| Figure 2A.29 | (a) Rate of reaction obtained for PNP reduction by using Au@Ni _{1:0.5} catalyst (recyclability) (b) XRD pattern of Au@Ni _{1:0.5} after 4 cycles..... | 81 |
| Figure 2B.1 | UV-Vis spectra recorded for (a) colloidal gold seed solution and | |

| | | |
|--------------------|--|-----|
| | (b) Au@Ni core-shell nanoparticles..... | 84 |
| Figure 2B.2 | (a) Large area TEM and (b-d) HR-TEM images of Au@Ni core-shell..... | 85 |
| Figure 2B.3 | XRD patterns of monometallic (a) Ni (b) Au and bimetallic (c) Au@Ni..... | 86 |
| Figure 2B.4 | Hysteresis loops obtained for Au@Ni core-shell nanoparticles..... | 87 |
| Figure 2B.5 | (a) Wide scan XP spectra obtained for Au@Ni core-shell nanoparticles..... | 88 |
| Figure 2B.6 | Phenylacetylene (P.A) conversion (brown) and ethylbenzene (E.B) selectivity (blue) in methanol obtained for Au@Ni..... | 90 |
| Figure 2B.7 | Selectivity results (red and yellow) obtained for complete conversion of P.A in various solvents by using Au@Ni core-shell catalysts..... | 92 |
| Figure 2C.1 | UV-Vis spectra recorded for (a) gold colloid and (b and c) Au@Ni core-shell nanochains and nanoparticles..... | 95 |
| Figure 2C.2 | TEM and HR-TEM images of core-shell (a, b and e) Au@Ni nanochains and (c, d and f) Au@Ni nanoparticles..... | 96 |
| Figure 2C.3 | (I) XRD patterns of (a) Nickel nanoparticles, (b) Au@Ni nanochains and (c) Au@Ni nanoparticles..... | 97 |
| Figure 2C.4 | (a) and (b) are the hysteresis loops obtained for Au@Ni nanochains and Au@Ni nanoparticles obtained in VSM analysis..... | 99 |
| Figure 2C.5 | Individual XP spectra of nickel (Ni 2p) and gold (Au 4f) recorded for core-shell (a-b) Au@Ni nanochains and (c-d) Au@Ni nanoparticles..... | 100 |
| Figure 2C.6 | Conversion (red and yellow bars) and selectivity (blue and green bars) results obtained for Au, Au@Ni nanochains (Au@Ni C), Au@Ni nanoparticles (Au@Ni P) and Ni for P.A hydrogenation..... | 102 |
| Figure 2C.7 | Conversion of P.A to ethylbenzene (E.B) in MeOH by using Au@Ni nanochains (blue bar) and Au@Ni nanoparticles..... | 102 |
| Figure 3.1 | Scheme showing various steps involved in the formation of Au@Ni | 114 |
| Figure 3.2 | UV-Vis spectra recorded at each stage of synthesis of Au@Ni..... | 115 |
| Figure 3.3 | TEM images of Au@Ni core-shell nanoparticles..... | 116 |
| Figure 3.4 | TEM and HR-TEM images of Au@Ni core-shell nanoparticles..... | 117 |
| Figure 3.5 | C 1s and Au 4f spectra of the as synthesized (a) Au ₈₀ @Ni ₂₀ (b) Au ₆₅ @Ni ₃₅ and (c) Au ₅₀ @Ni ₅₀ core-shell nanoparticles..... | 118 |
| Figure 3.6 | Hysteresis loops of (a) Au ₈₀ @Ni ₂₀ (b) Au ₆₅ @Ni ₃₅ and (c) Au ₅₀ @Ni ₅₀ | 119 |
| Figure 3.7 | XRD patterns of core-shell (a) Au ₈₀ @Ni ₂₀ , (b) Au ₆₅ @Ni ₃₅ and | |

| | | |
|--------------------|---|-----|
| | (c) Au ₅₀ @Ni ₅₀ nanoparticles..... | 120 |
| Figure 3.8 | Ni 2p _{3/2} spectra and its deconvolution obtained for Au ₈₀ @Ni ₂₀ , Au ₆₅ @Ni ₃₅ and Au ₅₀ @Ni ₅₀ core-shell nanoparticles under UHV-RT..... | 121 |
| Figure 3.9 | Ni 2p _{3/2} spectra and its deconvolution obtained for Au ₈₀ @Ni ₂₀ , Au ₆₅ @Ni ₃₅ and Au ₅₀ @Ni ₅₀ under O ₂ atmosphere & temperature..... | 123 |
| Figure 3.10 | Changes in percentage composition of various nickel species present in Au ₈₀ @Ni ₂₀ , Au ₆₅ @Ni ₃₅ and Au ₅₀ @Ni ₅₀ | 124 |
| Figure 3.11 | Ni 2p _{3/2} spectra and its deconvolution obtained for Au ₈₀ @Ni ₂₀ , Au ₆₅ @Ni ₃₅ and Au ₅₀ @Ni ₅₀ core-shell nanoparticles..... | 125 |
| Figure 3.12 | Pie chart demonstrating the percentage composition of various surface species of nickel formed from the decomposition of Ni(OOH)..... | 126 |
| Figure 3.13 | Total percentage composition of Au and Ni at the surface in Au ₈₀ @Ni ₂₀ , Au ₆₅ @Ni ₃₅ and Au ₅₀ @Ni ₅₀ core-shell nanoparticles..... | 127 |
| Figure 3.14 | Au 4f spectra obtained for (I) Au ₈₀ @Ni ₂₀ , (II) Au ₆₅ @Ni ₃₅ and (III) Au ₅₀ @Ni ₅₀ under oxygen atmosphere..... | 128 |
| Figure 3.15 | P.A hydrogenation in MeOH by using Au@Ni core-shell nanoparticles with various shell thickness..... | 129 |
| Figure 3.16 | Catalytic activity results obtained for P.A hydrogenation by using Au ₈₀ @Ni ₂₀ nanoparticles in MeOH and DCM..... | 130 |
| Figure 4.1 | Scheme showing various stages of generating surfactant free Au@Ni core-shell nanochains in aqueous medium..... | 139 |
| Figure 4.2 | UV-Vis spectra recorded at various stages of synthesis of Au@Ni core-shell nanochains..... | 140 |
| Figure 4.3 | (a-d) TEM, HR-TEM images and (e-f) SEM images of Au@Ni core-shell nanochains..... | 142 |
| Figure 4.4 | HR-TEM images and lattice fringe analysis from different spots of Au@Ni core-shell nanochains..... | 142 |
| Figure 4.5 | Temperature-dependent XRD of Au@Ni core-shell nanochains. | 143 |
| Figure 4.6 | Hysteresis loop measured at room temperature for Au@Ni magnetic core-shell nanochains..... | 145 |
| Figure 4.7 | In-situ NAPXPS data recorded individually for Ni, O and Au at various O ₂ pressure and temperature conditions..... | 146 |

| | | |
|-------------------|--|-----|
| Figure 4.8 | Graph represents the conversion of acetophenone at various time intervals using Au@Ni catalysts at 80 °C and 120 °C..... | 151 |
| Figure 4.9 | Recyclability tests done for Au@Ni catalysts for acetophenone transfer hydrogenation using IPA..... | 151 |

List of Tables

| | | |
|-------------------|--|-----|
| Table 2B.1 | Hydrogenation results obtained for P.A by using Au@Ni catalysts and Ni nanoparticles in MeOH (50 ml) and DCM (50 ml)..... | 92 |
| Table 4.1 | Optimized reaction conditions for acetophenone transfer hydrogenation with Au@Ni catalysts using IPA (3 ml) as hydrogen donor..... | 149 |

List of abbreviations

| | |
|----------------|--|
| Uv-Vis | Ultraviolet- Visible |
| XRD | X-Ray Diffraction |
| SEM | Scanning Electron Microscopy |
| HR-TEM | High Resolution-Transmission Electron Microscopy |
| EDX | Energy Dispersive X-rays |
| VSM | Vibrating Sample Magnetometer |
| SQUID | Superconducting Quantum Interference Device |
| XPS or PES | X-ray Photoelectron Spectroscopy |
| UPS | Ultra-violet Photoelectron Spectroscopy |
| APXPS or APPEs | Ambient Pressure X-ray Photoelectron Spectroscopy |
| NAPPEs/NAPXPS | Near Ambient Pressure (X-ray) Photoelectron Spectroscopy |
| PNP | Para- nitrophenol |
| PAP | Para- aminophenol |
| PNTP | Para- nitrothiophenol |
| PATP | Para- aminothiophenol |
| P.A | Phenylacetylene |
| E.B | Ethylbenzene |
| CTAB | Cetyltrimethyl ammonium bromide |
| G.C | Gas Chromatography |
| UHV | Ultra High Vacuum |
| RT | Room Temperature |
| B.E | Binding Energy |
| nm | nanometer |
| FWHM | Full Width at Half Maximum |
| SPR | Surface Plasmon Resonance |
| FCC | Face Centered Cubic |
| HCP | Hexagonal Close Packing |

Abstract of the thesis

The electronic/geometric effects arising at the interface of bimetallic structures result in materials with interesting chemical and physical properties. Such materials can be created by choosing metals with large lattice mismatch which creates strained bimetallic overlayers. It is evident from the surface science studies that gold-nickel (Au-Ni) surfaces behave differently when they combine and form nanoscale interfaces. The earlier investigations demonstrated the oxidation and coke formation resistance respectively on these bimetallic Au-Ni model surfaces. In this regard, synthesis of Au@Ni bimetallic core-shell nanoparticles with controlled size is challenging because of their large lattice mismatch of approx. 16 %. To meet the demands of sustainable and efficient catalytic processes new tailor made materials must be synthesized for obtaining optimum activity and selectivity. The main disadvantages of nickel monometallic catalyst is that it undergo severe chemical and surface modifications while synthesis and during catalysis. To validate the synergism in gold-nickel system, Au@Ni core-shell structures are synthesized by energy efficient and eco-friendly routes and operando investigation of the surface states of nickel carried out by using near ambient pressure x-ray photoelectron spectroscopy (NAP-XPS) under reactive environment. The enhanced catalytic behavior of these core-shell bimetallic Au-Ni nanostructures are explored and compared with monometallic systems for various types of hydrogenation reactions. The thesis is presented in five chapters; a brief summary of each chapter is given below.

Chapter 1: This chapter reports the recent developments in the heterogeneous catalysis and advancement in characterization techniques for the analysis of nanoparticles. The quantum size effects in metal nanoparticles are briefly explained along with the colloidal catalysis by using bare nanoparticles. The step-wise growth of nanoengineered bimetallic systems from model surfaces to real world catalysis is explained in detail. The importance of electronically/geometrically modified surfaces when one metal comes in contact with the lattice of different metal is discussed to design new hybrid catalytic materials. The chapter also explains the importance of bridging the “material and pressure gap” existing between the surface science studies and real world catalysis. In the later stage of the chapter, the importance of gold (Au) - nickel (Ni) bimetallic surfaces are explained along with their

previous surface science investigations. The need for such electronically and geometrically modified bimetallic surfaces in the nanoregime for applications in various catalytic reactions are discussed. The chapter also illustrates the synergistic effect of other bimetallic combinations and their colloidal phase synthesis protocols. Apart from this, the working principles of different spectroscopic, microscopic and magnetic techniques used for the investigation of the physiochemical properties of the synthesized materials are explained. The advancement in XPS characterization tool, near ambient pressure photoelectron spectroscopy (NAPXPS) is explained in detail for carrying out operando analysis.

Chapter 2: Chapter 2 is divided in to three sub-divisions namely 2A, 2B and 2C.

Chapter 2A: In this chapter synthesis of Au@Ni core-shell bimetallic nanoparticles, with gold core and thin nickel shell with overall size less than 10 nm are reported. The nickel shell in the core-shell nanoparticles are stabilized in two different forms, cubic (FCC) and hexagonal (HCP) phase. Due to their unique crystal, electronic, and geometric structure, they show interesting magnetic and chemical properties. Au@Ni_{FCC} is magnetic, whereas Au@Ni_{HCP} is non-magnetic. Both the bimetallic nanostructures are stable to surface oxidation until 150 °C and show excellent catalytic activity for p-nitrophenol reduction reaction. The chapter also demonstrates the synthesis of Au@Ni core-shell bimetallic nanoparticles with varying nickel shell thickness and their synergistic effect in catalysis is explored through nitro group reduction in p-nitrophenol and p-nitrothiophenol. In this chapter, a clear evidence for synergism in Au@Ni core-shell nanoparticles having ultrathin Ni shell (1-2 nm) around Au core (6-10 nm) resulting in enhanced catalytic activity is observed. The rates observed from thin nickel shell are higher than the monometallic Au or Ni nanoparticles of similar size or with thicker Ni shell of 6-8 nm.

Chapter 2B: This chapter describes the synthesis of Au@Ni bimetallic core-shell nanoparticles through an energy efficient (lower temperature) route in oleylamine following a sequential reduction strategy. The method is found to be useful for the synthesis of a very thin nickel shell (2 nm) over a gold core (15 nm). Synergistic catalytic activity results are observed for the selective hydrogenation of phenylacetylene to styrene and ethyl benzene under different solvent conditions.

Chapter 2C: In this chapter, synthesis of Au@Ni bimetallic core-shell nanostructures using

commercially available soya bean oil as the solvent through a sequential reduction strategy is reported. The energy efficiency and economic viability comes from the much milder temperatures and replacement of expensive and environmentally hazardous solvents like long chain organic amines and acids previously reported for synthesis. Thus, core-shell nanoparticles having size regime of 10-15 nm with an excellent control over the nickel shell thickness (2 nm) over the gold core (8-10 nm) and Au@Ni nanochains is achieved. The synthesized materials are demonstrated to catalyze hydrogenation of C-C multiple bonds with much better activity and selectivity as compared to individual nanoparticle counterparts.

Chapter 3: This chapter deals with the synthesis of Au@Ni nanoparticles with core-shell morphology in aqueous medium by using a seed mediated low temperature sequential reduction method. The nickel shell thickness on the gold core in the nanostructures can be tuned from 2 nm up to about 10 nm. Near Ambient Pressure XPS (NAPXPS) studies under oxygen shows that Au₈₀@Ni₂₀ with extremely thin nickel shell (~2 nm) shows a distinctly different decomposition pathway of metastable Ni(OOH) species compared to larger shell thickness which behave more like individual nickel surface. Thus, Ni(OOH) on Au₈₀@Ni₂₀ decomposes to metallic Ni at 100 °C and is found to resist oxidation at 0.1 mbar oxygen at these temperatures. Those with larger nickel shell thickness behave more like monometallic Ni in their decomposition and oxidation properties. The Au@Ni system with an ultra thin nickel over layer (2 nm) shows high catalytic activity and selectivity in phenylacetylene hydrogenations under mild conditions which outweigh its monometallic counterparts and with the ones with higher nickel shell thickness.

Chapter 4: A surfactant free aqueous phase synthesis method is reported in this chapter for the generation of highly lattice mismatched Au@Ni core-shell nanochains without using any expensive and hazardous organic ligands. As synthesised Au@Ni nanochain structures show high thermal stability and bulk oxidation resistance up to 300 °C. In-situ NAPXPS analysis done on bare Au@Ni nanochain surfaces under oxygen atmosphere and at different temperatures show evidence for the surface oxidations resistance of naked Au@Ni nanochains up to 200 °C. Ligand/capping agent free Au@Ni nanochain surfaces are also shown to be highly active for transfer hydrogenation of acetophenone under various temperature and base conditions. The bimetallic Au@Ni nanochains catalyze transfer hydrogenation of acetophenone under mild conditions and with minimum amount of catalyst.

Chapter 5: The major findings of the work illustrated in the thesis are summarized in Chapter 5. The chapter gives the summary and conclusions of the various synthesis strategies, structural features, and synergistic catalytic results of the core-shell nanoparticle systems.

Chapter 1

General Introduction and Literature Survey

➤ Outline of the chapter

- ✓ **Nanomaterials and Heterogeneous Catalysis**
- ✓ **Bimetallic Synergism: Geometric and Electronic Effects**
- ✓ **Bridging the Material and Pressure Gap in Heterogeneous Catalysis**
- ✓ **Synthesis and Characterization of Core-shell Bimetallic Nanoparticles**
- ✓ **Importance of Gold (Au)-Nickel (Ni) Bimetallic Systems**
- ✓ **Bimetallic Nanoparticles in Catalysis**

Chapter 1: General Introduction and Literature Survey

1.1 Nanomaterials and Heterogeneous Catalysis

The last decade has seen the need for stable and sustainable catalytic materials with tunable activity and selectivity and has led to innovative designing of nanomaterials in heterogeneous catalysis¹⁻⁴. The fascinating properties of these materials motivated the researchers across the world to engineer the physiochemical properties of nanomaterials for diverse applications like biomedical, electronic devices, magnetic storage, electrochemical, solar energy harvesting, optics, photonics and catalysis⁵⁻¹⁴. Nanomaterial engineering has special place in catalysis as size, shape and composition primarily controls the activity and selectivity of a process¹⁵⁻¹⁷. Both, monometallic and bimetallic catalysts have received considerable attention over the years due to unprecedented trend in activity that it demonstrates with respect to the effects mentioned before¹⁸⁻²⁰. It is well known that any change in size, shape and composition of mono and bimetallic nanostructures cause the local electronic and geometric effects to get perturbed^{4, 21}. As heterogeneous catalysis is surface phenomena it is necessary to understand the complexity in the geometric and electronic effects arising at the surface especially in the case of multi metallic nanostructures in the nano scale⁴. To realize the concept of “Designed Architectures for novel catalysis” needs fundamental insights from studies carried out on such surfaces. The advancement in synthesis methods provided major breakthrough in the recent past for engineering various nanostructures which are perfectly suited for studying structure vs. activity correlations.

1.1.1 Nano: Quantum Confinement Effects and its Unique Properties

The unique properties of the materials in nano size regime which are entirely different from those of their bulk analogues represent quantum size properties²². Nanoparticles are generally known for their unpredictable properties and stand for a quasi metastable phase that exists between atoms and bulk of the materials. For material in solid state, the band theory is successful in explaining the properties of materials in bulk which fails to give satisfactory explanation for the properties of nanomaterials. When the size of the material is reduced below certain critical limits (less than 5 nm) it is observed that the nanoparticles/clusters thus formed have a tendency to show atomistic properties such as discrete energy levels instead of

band concept of solids. For instance, in the case of metals there is a transition from metallic to non-metallic character (Figure 1.1) when the size of the materials is reduced all the way to nanoclusters indicating the appearance of discrete energy levels (atomic orbitals)²³⁻²⁴. Semiconductor quantum dots also fall in to the similar observations when compared with their bulk²⁵⁻²⁶. Apart from these there are a lot of changes happening to the physical properties of the materials depending on the size, shape and composition²⁷. The yellow metal gold (Au) and its other group members such as silver (Ag), and copper (Cu) show surface plasmon resonance (SPR) which is a clear evidence for the quantum size effect and it operates when the particle size reaches nano regime where surface electrons resonates with the suitable wavelength of electromagnetic radiations²⁸⁻²⁹. SPR is described as the collective oscillation of the electron gas at the metal surface up on interaction with the electromagnetic radiation resulting in the absorption of a suitable wavelength³⁰⁻³¹. The absorption falls in the visible region for gold, silver and copper metal nanoparticles which imparts colour to their respective colloidal phase and it strongly dependent on the size and shape of the nanoparticles³². Thus the quantum confinement effects offer unique properties for the nanomaterials which can be utilized for various areas like drug delivery, solar energy, sensors, electronics, catalysis etc³³⁻

37

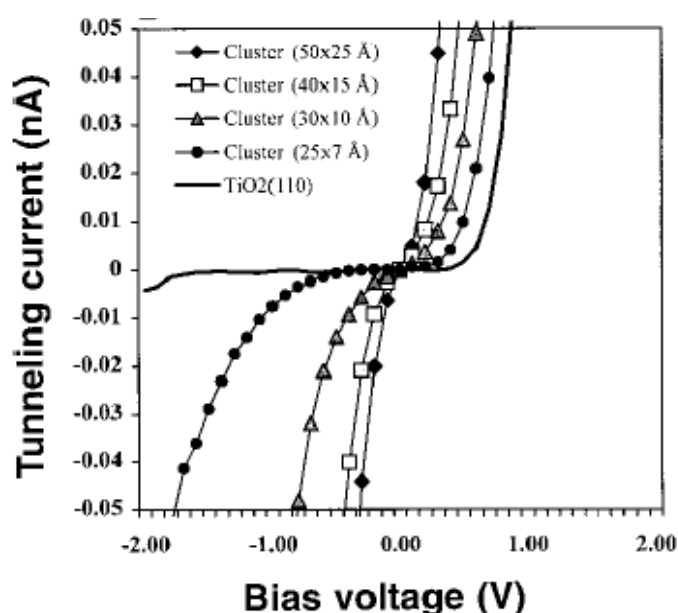


Figure 1.1 I (current)- V (voltage) characteristics obtained for Au clusters of varying sizes supported on TiO_2 (110)-(1x1) surface for different Au coverages from 0.2 to 4.0 ML using scanning tunneling spectroscopy (STS). A metal-to-non metal transition occurs as the cluster size is decreased below $3.5 \times 1.0 \text{ nm}^2$ (3.5 nm in diameter and 1.0 nm in height)²⁴.

1.1.2 Nanoparticles in Catalysis

Nanocatalysis is a rapidly growing field in heterogeneous catalysis and generally uses metal/metal oxide nanoparticles or in their combined form for tuning the catalytic activity and selectivity to get maximum efficiency³⁸⁻⁴⁰. Apart from quantum size effects other advantages of nanostructures are the high surface to volume ratio, excess surface free energy and high degree of under coordinated atoms⁴¹⁻⁴². Reducing the particle size for a given volume of the material drastically increases the surface area in nano size regimes⁴³. From the catalysis point of view, only the surface atoms are exposed to the reactants and adsorption is the basic phenomena of catalysis. Hence catalysis highly depends on the surface area and chemical nature of the surface including the bonding structure, electronic states and geometrical arrangement of atoms⁴⁴. As a whole the “active site” of a catalyst where catalysis happens is determined by the physiochemical nature of the surface of the catalyst⁴⁵⁻⁴⁶. For example gold is known for its highly inert character and in bulk is a poor material for any catalytic application. But pioneering works done by Haruta and Hutchings illustrated the high catalytic activity of gold by controlling the size below certain “nano” regimes⁴⁷⁻⁴⁸. It is more interesting to note that at an optimum size regime of 3 nm gold nanoparticles supported catalysts showed high catalytic activity for various oxidation and reduction reactions⁴⁸⁻⁴⁹. Particularly interesting is the CO (Carbon monoxide) oxidation reactions even at sub ambient temperatures⁵⁰. Moreover, the catalysis by finely divided nanoclusters with definite number of atoms makes the catalysis more economically viable and reduces the expense and wastage of catalyst materials especially in case of costly noble metals like Pt, Ru, Au, etc⁵¹. One can then imagine the possibilities of engineering various properties of nanoparticles as mere tuning of size alone demonstrated a highly inert material to a very active material for catalysis. Following section will reveal the current status of the designing of heterogeneous catalyst materials in their nano form, single atom site and hybrid systems.

1.1.3 Recent Progress in Heterogeneous Catalysis

The industrial application of heterogeneous catalysis is paramount and it always looks for upgrading the catalyst materials for better activity, selectivity and sustainability of the applied materials⁵². There are intense investigations going on for the discovery of new breed of catalysts to realize the concept of an efficient and sustainable catalytic process. This can be realized either by surface modifications or by designing well defined nanoarchitectures⁵³⁻⁵⁴.

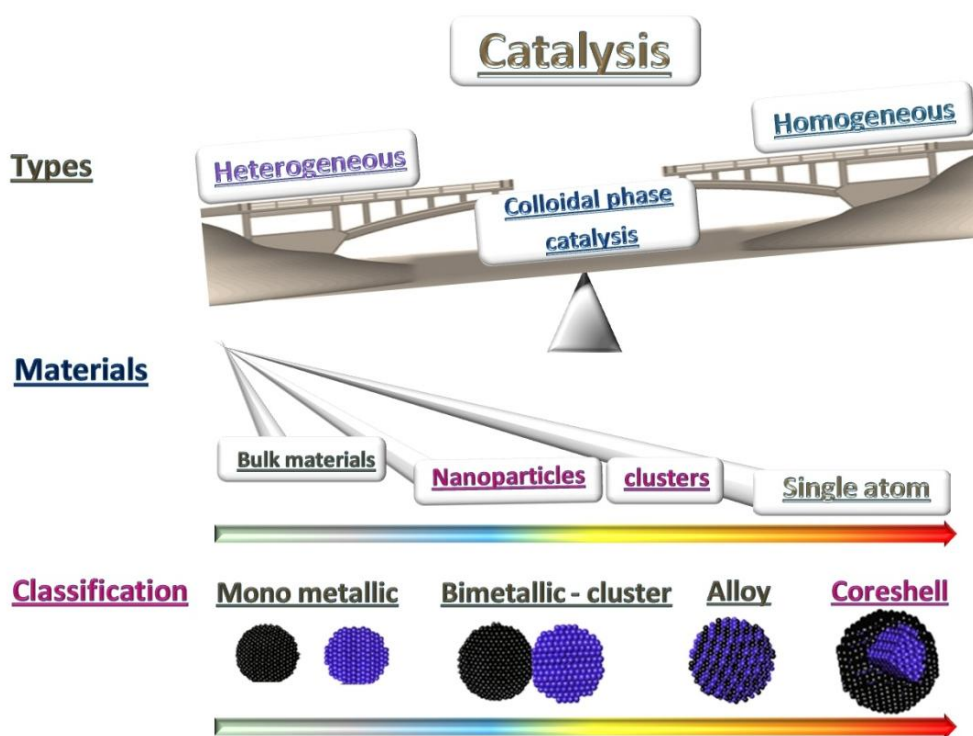


Figure 1.2 Scheme showing various types of catalysis, advancement in the catalyst materials used in heterogeneous catalysis and different types of nanoparticle catalysts (monometallic and bimetallic).

Nanoparticles/clusters promise a bright future in the heterogeneous catalysis to meet the industrial demands of a catalyst material⁵⁵. Nanoparticles without any supports (metal oxides preferably) are widely used in colloidal phase catalysis which can bridge the drawbacks of heterogeneous and homogeneous catalysis (Figure 1.2)⁵⁶. Colloidal catalysis by the bare nanoparticles has been considered as a new area in heterogeneous catalysis which can provide excellent turn over frequencies for catalytic transformations. The enhanced activity of metal nanoparticles for the catalytic conversions mainly depends on the under coordinated atoms which are present at the corners, edges and various facets of the exposed nanoparticle surfaces⁵⁷. Obviously a fine tuning can be done for increasing the density of under coordinated atoms to observe a steady increase in the catalytic activity⁵⁸. Similarly, recent reports showed that the activity and selectivity of a catalyst depend up on certain planes (or facet) exposed on the surface^{18, 59-60}. Controlling the geometry of the arrangement of atoms on the nanoparticle surface is a great challenge as the nanoparticle formation itself is thermodynamically not favourable process. Recent developments of nanoparticle synthesis have shown that well defined nanoparticles with specific planes can be achieved using wet

chemical reduction routes with help of proper stabilising agents⁶¹⁻⁶³. The challenge in the shape control or facet engineering is achieved by carefully designing the synthesis strategies allowing thermodynamically unstable facets trapped in a kinetically favoured growth mechanism. The utilization of such shape controlled nanoparticle catalysts for enhancing the selectivity and to control the reactivity trends are demonstrated by various research groups^{16, 64}.

Another recent highlight in heterogeneous catalysis is the ‘Single Atom Catalysis’ (SAC)⁶⁵. Reducing the catalytically active material to single (few) atoms promises an atom economical catalysis for the future. SAC offers more economic advantage especially for noble metal catalysis with nominal amounts of metal loading⁶⁶ on to the supports resulting in high T.O.F values⁶⁷. One of the main advantages of SAC is the uniformity in the well dispersed active site. The identical nature of active sites are capable of avoiding unwanted reaction pathways thereby increasing the selectivity⁶⁸. Along with the size and shape influence in heterogeneous catalysis, the effect of combinations and compositions of different elements are really worth mentioning and they offer endless possibilities for various multi metallic architectures. Among these hybrid materials bimetallic systems are well studied and explored for various catalytic applications ranging from normal oxidation reduction reactions to high temperature industrial catalysis.

Bimetallic nanoparticles constituting two different metals in specific atomic arrangements (Figure 1.2) are found to show entirely different catalytic properties as compared to their monometallic counterparts. Quantum size effects are considered as the dominant factor in nanoscale phenomena of monometallic systems, where as in addition to that geometric and electronic modifications are found to strongly influence the trends in catalytic activity of various bimetallic structures. In the following part of the thesis, the background of bimetallic concepts including surface science aspects, theoretical predictions and their advancement in understanding the real world catalysis discussed in literature is presented.

1.2 A Brief History of Bimetallic Systems and Their Development as Catalytic Materials

The designing of hybrid materials having two or more components with modified properties is challenging and one must have a precise understanding about the physiochemical properties of the combining elements. The composition plays a crucial role for changing the characteristics of the resultant hybrid materials for a particular combination. Bimetallic structures are generally formed when two dissimilar metals combine irrespective of their dissimilarities in physiochemical properties (lattice spacing, melting point etc)⁶⁹. Usually these hybrid materials exhibit altered physical and chemical properties which mainly depend on degree of interaction between the metals. In the bulk, thermodynamic phase diagram clearly indicates the feasibility and stability of different bimetallic compositions as a function of temperature⁷⁰. In contrast, the bimetallic combinations in nanoregime offer lot of surprise. Even if the bulk alloy phase diagram rules out alloy formation, nano alloy formation has been reported at much lower temperature⁷¹. Furthermore the bonding interaction of dissimilar atoms in bimetallic system results in heteroleptic bonding and causes a large strain especially at the surfaces⁷². All these parameters along with the quantum confinement effects provide unique properties for the bimetallic nanoparticles and make it highly interesting system for catalytic applications. Attempt for understanding the synergism of bimetallic combinations started with the works done by Sinfelt and co-workers in 1970's where they tried to bring out the possibilities of various bimetallic combinations by using Pt, Ru, Ir etc⁷³⁻⁷⁵. Later, in early 90's Goodman and co-workers made pioneering works using surface science tools for characterising bimetallic compositions⁷⁶⁻⁷⁷. They showed the existence of synergistic effects in bimetallic combinations showing different chemical state thereby to exhibit altered properties than that of monometallic counterparts⁷⁸⁻⁷⁹. In the late 90's Nørskov and Stensgaard reported the ensemble effect and electronic perturbations of Au-Ni bimetallic surfaces leading to sustainable catalytic activity⁸⁰. They predicted the possibility of geometric and electronic modifications by the changes in the chemical environment of atoms located in a dissimilar matrix (For schematic representation of bimetallic model surfaces and nanoparticles see Figure 1.3). The surface science studies on model surfaces shows that bimetallic nanostructures are important in catalysis and is a rapidly growing field with enormous potential to deal with the future perspectives of catalyst materials.

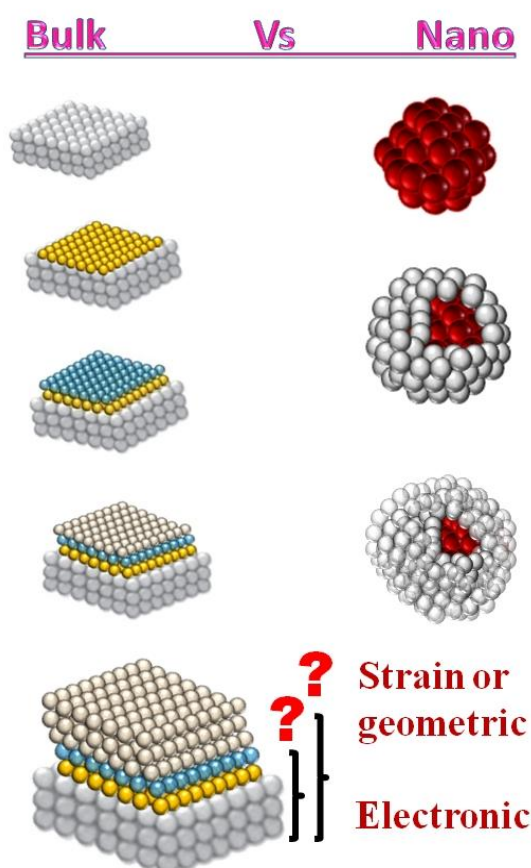


Figure 1.3 A comparative schematic representations of bulk and corresponding nano materials in monometallic and bimetallic structures. Bimetallic model surfaces constitute different overlayers of foreign metal on the surface of a dissimilar metal and the colour change of overlayers indicates the difference in electronic and geometric effects operating at different atomic layers (left). Corresponding core-shell morphology of bimetallic nanoparticles with different shell thickness (right).

1.2.1 Bimetallic Synergism: Geometric and Electronic Effects

When two dissimilar metals combine together to form bimetallic nanoparticle following major factors comes to play. They are lattice parameter, surface geometry of atoms, surface strain, and creation of under coordinated sites. These surface effects that originate in bimetallic nanostructures have been classified as “ensemble, ligand and geometric effects”. Ensemble effect operates when the surface atoms exist in a matrix of dissimilar atoms, individually or in small groups (ensembles) thereby altering the mechanistic features, as demonstrated in case of nickel-gold for steam reforming catalytic reaction⁸⁰. Ligand effects are caused by the atomic interactions of two different surface metal atoms having different

electronic properties that induces electronic charge redistribution between the atoms, and thus affects their electronic band structure. In modern terminology the ligand effect stands for the electronic effect in bimetallic combinations. Finally, in geometric effects the differences in reactivity arise due to the mixing of metals with different lattice parameters resulting in an altered atomic arrangement of surface atoms and may include compressed or expanded lattice strain. Electronic and geometric effects operate individually or in some cases simultaneously and influence the catalytic activity and selectivity trends⁸¹⁻⁸². As a net result bimetallic nanomaterials with a metastable phase and thermodynamically unstable structures can be realised with enhanced reactivity for catalysis. In bimetallic surfaces, the over layer structure may have altered bonding geometry and cause strain resulting from the distorted atomic arrangements at the interfaces⁸³. Such a surface with high degree of lattice strain and altered electronic density of states leads to unique optical, electronic, mechanical and catalytic properties. Tuning the nature of such active sites is highly important in catalysis, since it is the major cause of catalytic reactivity enhancement⁸⁴. The selective poisoning of the highly active catalytic sites by integrating with a foreign moiety (preferably different kind of atom) has also received much attention as it enhances the stability and promises a sustainable catalytic action⁸⁰. Likewise the potential uses of such combinations are diverse in action and it requires grass route analysis to understand the basic phenomena of bimetallic synergism.

1.2.2 Inspiration from Surface Science and Theoretical Investigations

The use of bimetallic surfaces for catalytic applications were explored by surface science investigations done by Goodman^{78, 83, 85}, Ertl⁸⁶⁻⁸⁷ and Somorjai⁸⁸⁻⁸⁹ on various bimetallic surfaces. These early studies by using surface sensitive tools provided valuable insight into the catalytic nature of modified surfaces. The adsorption of small gas molecules on the modified metal surfaces were used to probe the altered reactivity and chemical properties of bimetallic surfaces. Their findings proved that surface hetero metallic bonding nature have crucial effects and it alters the electron density around the metal atoms thereby altering the chemical properties of the metal. The XPS and UPS analysis of metal overlayers on different metal substrates showed a shift in binding properties which was in accordance with the desorption studies of mono and bimetallic surfaces by using CO as probe molecule^{78, 83}. They found that the extent of hetero nuclear metal-metal bond induces electronic and geometric effects and account for the modified bimetallic surface with different chemical properties.

Nørskov and co-workers were successful in explaining the properties of mono and bimetallic surfaces using the concept of d-band model⁹⁰⁻⁹². By considering the highly strained bonding nature at the surface of bimetallic structures with large under coordinated atoms, they calculated the changes in the d-band electronic levels resulting in the shift of d-band center from the Fermi level⁹¹. They predicted the positive or negative shift in the d-band center will depend on the nature of guest metal (second metal) which comes in contact with the host metal. They also claimed that there must be a flow of electron charge density from the metal with high electron density in the d-band level to the metal with highly vacant orbitals. The phenomenon is thoroughly investigated by Nørskov and Hammer with the help of DFT calculations and considering the strain induced lattice expansion or contraction in metal overlayers^{91, 93}. According to them the perturbations happens mainly because of the lattice mismatch of the adjoining atomic layers of different elements having different structural arrangements and also due to the changes in the electronic distribution in d-band energy levels. The shift in valence band electronic levels of modified metal surfaces directly influences the adsorption nature of the materials⁹⁴. Hence such surfaces with modified electronic and geometric properties offer new pathways for the adsorption and stabilization of reactants and intermediates during a catalytic cycle. In turn, with a better understanding of the d-band shift one can design new class of bimetallic surfaces with suitable energy profiles that matches with the adsorption energies of reactants to initiate the catalytic cycle.

1.2.3 Bridging the Material and Pressure Gap: Surface Science Aspects to Real World Catalysts

Molecular level understanding of how a real catalyst works has been a real challenge for the surface science community. To break the complexity of the real catalyst, surface scientist created model surfaces and utilized a variety of spectroscopic and microscopic techniques to study their behaviour towards reactive gas molecules. The origin of synergism has been proved beyond doubts in bimetallic model surfaces and later studies consist of nanoparticles deposited on different kinds of support surfaces (metal or oxide) which mimic the real world catalysts⁹⁵. This can be done by growing metal nanoparticles on the thin oxide films, as well as single crystal surfaces. These model systems are a step ahead of the traditional metal over layer structures in bridging the “material gap” to the real world catalyst materials⁹⁶. Still the main disadvantage remains the same since these structures were also

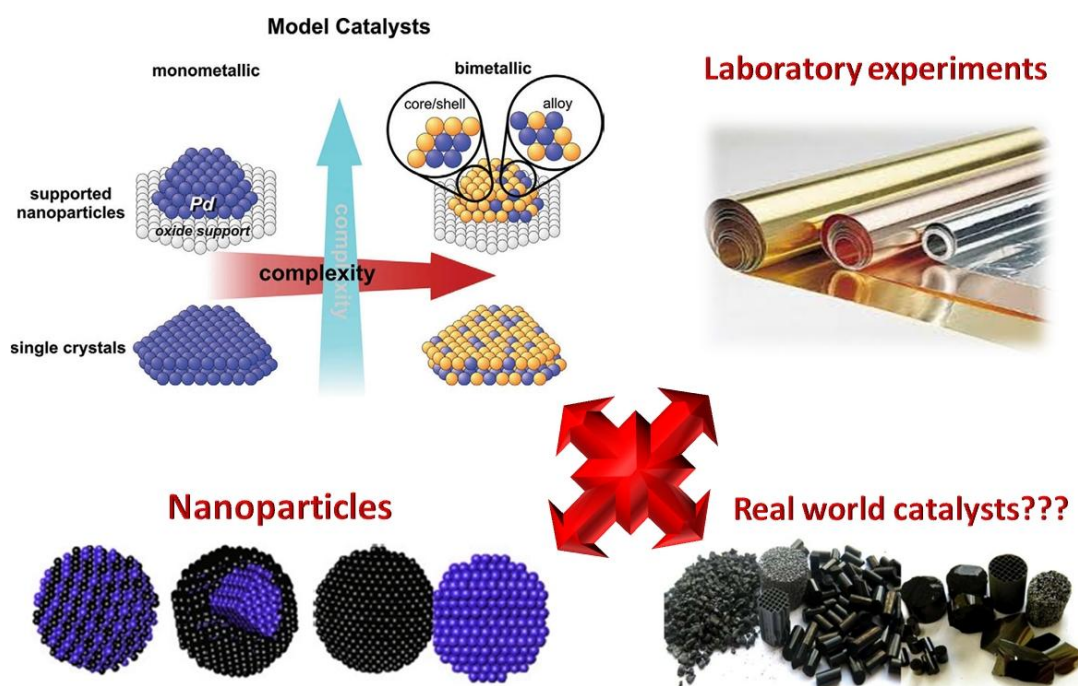


Figure 1.4 Image showing the complexity of material gap between the surface science aspects (laboratory experiments-bulk metal crystals/nanoparticles supported on model surfaces) and industrial catalysts (real world catalysts-nanoparticles deposited on supports)

prepared under ultra clean conditions which are utilized for surface science measurements. Figure 1.4 demonstrates the complexity in the material gap existing between the ultra clean surface science analysis and complex real world catalysts. It can be seen from the Figure 1.4 that irrespective of monometallic or bimetallic systems the model surface analysis constitute bulk single crystal surface investigations and mono/bi metallic nanoparticle deposition on oxide supports prepared under highly controlled clean conditions to mimic the real catalyst materials. Besides that the surface studies of these model surfaces are also carried out in ultra clean and high vacuum conditions. The results obtained from such investigations cannot be translated into understanding real catalysis as reactions happens at harsh atmospheres of pressure, temperature and other impurities. Meanwhile the advancement in characterisation tools offered investigation of catalyst materials even under high pressure and temperature conditions close to operation conditions⁹⁷⁻⁹⁸. The catalyst investigations under operational conditions generally termed as “operando” analysis⁹⁹. The approach made led to realization of bridging the “pressure gap” between the surface science analysis and catalyst under action¹⁰⁰. Also it is worth mentioning that while making the assumptions about the reaction mechanism

on a modified surface, the possibilities of short-lived species or intermediates also should be considered which are crucial in a catalytic cycle. Such species can only be present under reaction conditions, and must be examined under in-situ methods (under reaction environments such as high pressure and temperature conditions)¹⁰¹. The discussions instigate the importance of synthesising and investigating the catalysts under realistic conditions¹⁰². The recent advancement in characterisation tools and synthetic strategies allows the bridging of “material gap and pressure gap” of catalysts and reactions respectively¹⁰³⁻¹⁰⁵.

The behaviour of a catalyst under the reaction conditions is highly dynamic in nature and it is important to study them under those conditions¹⁰⁶. Recent advancement in instrumental techniques like ambient pressure XPS¹⁰⁷⁻¹⁰⁸, environmental TEM^{104, 109}, high pressure STM¹¹⁰, in-situ XRD¹¹¹, in-situ EXAFS⁶⁸ etc allows the possibility of characterisation under operational conditions of a catalyst. Tao and group has contributed to a large extent to this field by using various in-situ surface science instruments¹⁰⁰. Recently they developed a high pressure STM (Scanning Tunneling Microscopy) reactor which can operate under wide range of pressure ranging from UHV to a pressure higher than 1 atm and temperature (300-700K)¹¹⁰. They also built a custom-made in-house APPEP (or APXPS) reactor cell that can work under near ambient pressures which can go up to 500 °C with simultaneous analysis of catalyst surface¹⁰⁷. The instrument is used for revealing the dynamic nature of various catalyst surfaces under different reaction conditions. By using APPEP, surface composition changes and switching of Rh-Pd and Pt-Pd bimetallic core-shell nanoparticles under reactive environments have been reported¹¹². In a similar study, Yang et al showed the thermal stability and core-shell structure reconstruction of Ni@Co core-shell nanoparticles using in-situ TEM and XPS analysis¹¹³. Their results are in agreement with the alloying behaviour of metals at higher temperatures and in case of Ni@Co, they found the core-shell morphology is stable only up to 440 °C.

1.2.4 Importance of Gold (Au)-Nickel (Ni) Bimetallic Systems and Analysis of Au-Ni Model Surfaces

Synthesis of bimetallic nanoparticles with matching properties like lattice parameter, ease of alloying, similarity in atomic size, etc is straightforward, whereas the metals with large lattice mismatch are challenging¹¹⁴⁻¹¹⁵. Gold-Nickel (Au-Ni) system falls under this class having a lattice mismatch of approximately 16 % and less investigated in surface science and

catalysis perspective compared to the other bimetallic combinations. The thermodynamic phase diagram of Au and Ni also shows that bulk alloy formation is never possible even under extreme conditions with a large and positive heat of solution of Au in Ni¹¹⁶. One of the early surface science studies showed drastic difference in the reactivity trend of gold-nickel bimetallic combination as compared to monometallic gold and nickel¹¹⁷. Thus, sub monolayer coverages of Ni on Au surface were found to resist oxidation and were showing chemical properties atypical of nickel in bulk or nano regime. For Au-Ni, where an interface created by depositing Ni over Au surface is less sticky towards oxygen due to the geometric and electronic effects discussed previously. Ceyer et al also observed a similar trend in the oxygen adsorption nature on Au-Ni surface alloys and they proved by using high resolution electron energy loss spectroscopy (HREELS). Here, the dissociation of molecular oxygen was hindered on Au-Ni (111) surface in contrary where it is facile on a nickel metal¹¹⁸. In an effort to identify the various active sites generated during bimetallic mixing of metals, Holgado et al synthesized Au-Ni supported on ceria and analysed by using IR spectroscopy⁸¹. They showed the appearance of a new CO stretching frequency at 2190 cm⁻¹ in Au-Ni system which is atypical of monometallic Au and Ni. The new band is assigned to binding of CO to the electronically modified Au-Ni centres which in turn alters the reactivity trends of the bimetallic system.

An early scanning tunneling microscopy (STM) work has demonstrated that in spite of all the physical constraints, Au at sub monolayer coverages can form surface alloy on Ni with interesting surface structures and chemical properties⁸⁰. They observed unexpected alloying nature of Au atoms in to the nickel lattice at the surface resulted in the formation of ensembles that are completely promoted by electronic and geometric modifications. The STM being extremely local can successfully probe the electron density of the nickel atoms in the close vicinity of gold. The under coordinated Ni atoms that exist in the close vicinity of Au atoms on the surface layer experience a higher electron density or higher effective coordination atmosphere resulting in the lowering of Ni surface energy. Such Au-Ni surface was predicted to be coke resistant during steam reforming reactions. Meanwhile Rao et al also proved the synergism operating in bimetallic Au-Ni surfaces using spectroscopy techniques (XPS) which originated due to the alloying effect under sub monolayer coverages¹¹⁹. They successfully probed the shift in core level binding energy of nickel deposited on gold with simultaneous variations in valence band features. The enhancement in catalytic activity of Au-Ni surfaces for CO oxidation at low temperatures inspected by Ceyer et al and Besenbacher et al also

corroborated well with the concept of electronically/geometrically modified active sites on the surfaces as observed from the IR studies by using CO as probe molecule¹²⁰⁻¹²¹.

1.3 Bimetallic Nanoparticles: Synthesis and Catalytic Applications

From the previous discussions about the surface science studies on bimetallic over layers, it is clear that their chemical properties are distinctly different from monometallic systems. Following section discusses the synthesis and catalytic application of important bimetallic systems reported in literature.

1.3.1 General Synthesis Methods for Bimetallic Nanoparticles

Bimetallic nanostructures are composed of two dissimilar metals irrespective of their size, shape, composition and morphology. But for the sake of simplicity and understanding the influence of structural arrangement of atoms on the physiochemical properties and catalytic activity in nano size regime, bimetallic nanoparticles can be classified in to three basic systems¹²². The widely accepted three combinations of bimetallic nanoparticles are given below.

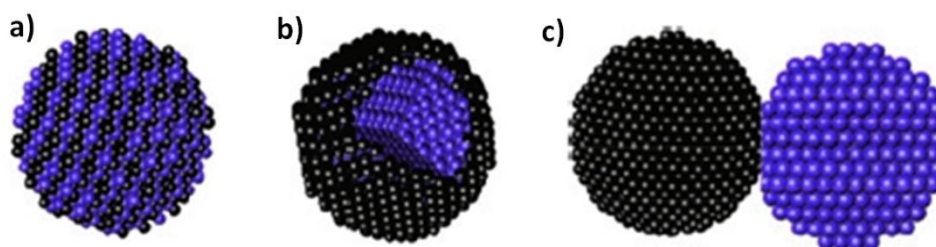


Figure 1.5 Schematic representation of different bimetallic architectures based on the chemical ordering of atoms (a) ordered alloy, (b) core-shell and (c) heteroaggregate nanoparticles.

- 1) Bimetallic alloy nanoparticles
- 2) Bimetallic core-shell nanoparticles and
- 3) Bimetallic heteroaggregate nanoparticles

Schematic representations of various bimetallic nanoparticle systems are depicted in Figure 1.5. Despite the fact that, there are endless possibilities of arranging two kinds of metal atoms in a nanoparticle on an atomic scale, these are the most studied bimetallic systems, also reported extensively in literature. The classification is purely based on the geometrical distribution of the two kinds of metal atoms in a single unit of bimetallic nanoparticle. Due to

the difference in the distribution of atoms these structures shows drastically different physiochemical properties even though they comprises of same type of elements with same composition. The major reasons for this versatility in the nature of these nanoparticles are due to the difference in interaction between the two metal atoms. In fact, degree of heteroleptic bonds is quite different in these structures from one another and it decides the inherent properties of these hybrid structures.

As seen from the Figure 1.5a, it is clear that an ordered alloy nanoparticle allows the complete mixing of both the metal atoms throughout the system homogeneously. It is considered as a solid solution with uniformity everywhere and also imparts different properties from those of monometallic counterparts. Since it allows ordered phase alloying in atomic scale one can imagine that it completely lacks the characteristic features and structural identity of the parent metals. In the alloy form itself sometimes there is non-homogeneity in the atomic arrangements. This leads to the further classification of alloys and can be specifically termed as a) Ordered alloy b) Disordered alloy or Random alloy. Coming to the next classification, the core-shell bimetallic nanoparticles (Figure 1.5b) is the second most investigated bimetallic combination especially in nano size. Core-shell systems can be considered as a special form of alloy materials but with intra particle segregation and possess variable properties from that of monometallic systems of the same kind. A core-shell system consist of a core area which is made up of a single kind of metal (M_1) atoms and it is totally surrounded by a shell composed of second metal atoms (M_2). In other words the core metal nanoparticle is completely coated and masked by the shell material. In core-shell system the size of core metal, extent of shell thickness and overall size of the nanoparticle plays crucial role in deciding the nature of the material especially at the surface. Lastly, the heteroaggregate bimetallic nanoparticles (Figure 1.5c) are different from those of alloy and core-shell type. They are also known as cluster-in-cluster bimetallic nanoparticles. As the name indicates these nanoparticles are formed by the attachment of two individual monometallic units (linked monometallic units) and exist as a single entity with modified properties. Here also the bimetallic synergism happens because of the same basic effects that originate only at the interface of both the clusters. These structures bear the minimum degree of heteroleptic bonding and they provide more complexity for the catalysis studies because the exposed surfaces contain both the monometallic types in addition to that the bimetallic interface. From catalysis point of view, core-shell system has its own importance in many aspects. Since the

core-shell nanoparticles exposes a homogeneous surface consisting of only one metal, the basic understanding of catalytic mechanisms and surface modifications can be elucidated more easily. The core-shell system provides a unique nature for all the active sites avoiding active sites with different geometrical arrangement of both the metal atoms. The identical nature of active sites obviously leads to higher selectivity in a catalytic reaction, meanwhile the active site take the complete advantage of geometrical and electronic effects as it relaxes on a completely different core metal atomic lattices. The versatility of a core-shell surface arises from these facts and bimetallic synergism can be explored fully with complete activity enhancement due to electronic/geometric modifications and selectivity due to the homogeneity. But it must be emphasized that in a core-shell system the possibility of heteroleptic bonding which is the prime cause of bimetallic synergism operates only at the interfaces of particle segregation. The parameters like geometric effects, electronic effects, lattice mismatch, and atomic interactions will operate extensively at the interface of both the metal atoms. So before carefully designing core-shell architecture for catalytic application it should be borne in mind that the size of the core, thickness of the shell, the total particle size and the nature of the metals involved.

Catalysis by nanoparticles is known from many decades back but the lack of adequate synthesis procedures and effective characterisation tools for these finely divided materials remained as a hurdle for the development of new heterogeneous catalysts. In recent years the development of controlled synthetic protocols for nanomaterials and advancement in the instrumentation changed the face of nano science and its applications¹²³⁻¹²⁴. In general nanoparticle synthesis can be done either by physical methods or by chemical methods. But for achieving good yield and homogeneity in size and shape of the nanoparticles, chemical methods are predominantly used. Chemical methods also offer a broad spectrum of synthesis protocol including simple reduction methods to electrochemical dispersion techniques. This “bottom-up” approach of nanoparticle generation starting from the metal precursors received much attention especially for precise control over the size and shape⁶⁹. Typical nanoparticle synthesis through a wet chemical reduction route requires a metal precursor, reducing agent and a stabilizer ligand. Metal precursor serves up on reduction with the reducing agent, produces metal atoms subsequently combine to form stable nuclei and they get stabilized by the ligands (or capping agents or surfactants or stabilizer)¹²⁵. The uses of ligands are very common in these solution phase reduction strategy in order to stabilise the nanoparticle.

Ligands are multi functional in nature they prevent inter particle agglomeration, they prevent uncontrolled growth, they stabilises the thermodynamically high energy surfaces and they also acts for the selective formation of facets¹²⁶⁻¹²⁸. The complexity of nanoparticle formation further increased by the involvement of other parameters like time scale, temperature, reduction potential of metal and reducing agent. Out of these, time scale and temperature affect the nucleation and growth stages directly and other two parameters acts indirectly. The choice of metal precursor and suitable reducing agent depends on the reduction potential and strength of the reducing agent. Reducing agent strength enhances the nucleation and growth of nanoparticles. For instance a strong reducing agent favours fast nucleation resulting in large number of nuclei with smaller size where as a weak reducing agent favours slow growth and eventually ends up with bigger size nanoparticles with more uniformity in size¹²⁹. Most widely accepted strong reducing agents are sodium borohydride (NaBH_4) and hydrazine hydrate ($\text{N}_2\text{H}_4\cdot\text{H}_2\text{O}$)¹³⁰⁻¹³¹. Other compounds like trisodiumcitrate and ascorbic acid can be used as weak reducing agents¹³²⁻¹³³. Apart from these factors the solvent also helps in nanoparticle formation. Some typical organic solvents provide precise control over the nanoparticle size and they themselves can act as reducing agent at elevated temperatures preferably above $150\text{ }^\circ\text{C}$ ¹³⁴. Oleylamine is highly explored in this regard and extensively used for nanoparticle synthesis¹³⁵.

The bimetallic nanoparticle synthesis can also be carried out through the same nucleation and growth kinetics in wet chemical reduction path from their respective metal precursor salts. This can be carried out either in a one-pot synthesis strategy or in a two-step reduction strategy. The thermodynamic phase diagrams of the mixing metals are important to know the stability of the bimetallic combinations. Otherwise either in the nucleation stage due to the immiscibility it can form monometallic nanoparticles or after the formation stage, segregation can lead to phase separation of the atoms¹³⁶. Lattice matching and energetic correlation are also important for the formation and stabilization of the bimetallic nanoparticles¹³⁷. The major factors in bimetallic nanoparticle formation are the size of interacting atoms, crystallization (close packing) and lattice parameters. If these parameters are at extreme ends then the thermodynamic possibility of forming nanoparticles either in any of the bimetallic forms will be extremely difficult. In the case of alloys these thermodynamic barriers are real hurdles and it allows the system to retain their stability by phase segregation under elevated conditions especially temperature^{136, 138}. But in the case of core-shell

nanoparticles or hetero aggregate the bimetallic system rearrange themselves in order to decrease the surface free energy and surface strain by lattice relaxation or distortion at the interfaces¹³⁹. The surface strain causes a lattice expansion or compression in the lattice structure of adjacent atomic layers and it allows the growth of hetero atomic layers on top of it¹⁴⁰. Depending up on the possibility of lattice relaxation these adjoining atomic layers at the interface can go through various pattern of growth mechanism at the hetero atomic junctions. Mainly the lattice relaxation can occur through epitaxial growth of the atomic layers or pseudo-morphic growth which can stabilize the architecture¹⁴¹. The epitaxial and pseudo-morphic growth, governed by high lattice mismatch is studied by various groups and lattice strain relaxation shown on different bimetallic systems^{84, 93, 140}. The following section briefly explains the possible bimetallic architectures that can be synthesised through a solution phase reduction method. The general reduction methods employed in bimetallic nanoparticle synthesis can be divided in to three. They are 1) Co-reduction or simultaneous reduction of metal precursors 2) Sequential (successive) reduction or Step-wise reduction 3) Galvanic replacement¹⁴².

Co-reduction generally involves a single step (one-pot) synthesis strategy which allows the reduction of both the metal precursors in a suitable solvent simultaneously. Depending up on the reduction potential values and other reaction parameters this method can generate alloy nanostructures or core-shell morphology as a result of co-nucleation and delayed nucleation. But in general, co-reduction favours the rapid nucleation and leads to the formation of alloys. Using a strong reducing agent in a solvent medium containing both the metal precursor salts preferably leads to the formation of an alloy type bimetallic nanoparticle where as a weak reducing agent favour the core-shell morphology. A general approach for carrying out Ag based bimetallic alloy nanoparticle synthesis has been reported by Xie and group, and they successfully employed the method for Ag-Au, Ag-Pd and Ag-Pt alloy systems¹⁴³. Sequential (Successive) reduction is a well known protocol for the synthesis of core-shell morphology. It can be done either as a one-pot or in a two-step reduction method. Sequential reduction technique follows first with the reduction of a single metal precursor in solution forming monometallic nanoparticles (seed), followed by the subsequent reduction of second metal precursor on the surface of the preformed seeds. Successive reduction can be carried out by using two different reducing agents in the same medium and the metal precursors undergo reduction at different time intervals. It must be noted that in a one-pot

synthesis method first metal precursor is reduced to generate in-situ seeds followed by the reduction of second metal precursor in the same reaction medium, and it can be done either by using different chemical reducing agents or by applying thermal, photochemical, sonochemical, microwave irradiation reduction¹⁴⁴⁻¹⁴⁸. Compared to other reduction techniques thermal reduction is most widely accepted, and it is highly effective in producing homogeneous and size-controlled nanoparticles especially in organic medium. Thermal reduction does not require additional reducing agents and hence it over come the disadvantage of high temperature requirements ranging from 150-250 °C. Oleyl amine is a high boiling organic solvent and it widely explored for the monometallic and bimetallic nanoparticle synthesis via thermal reduction of the metal-oleylamine complexes^{135, 149}. Yang et al has reported a general synthesis protocol for making a series of core-shell nanoparticles by using thermal reduction method¹⁴⁵. In the case of two-pot reduction method, the monometallic nanoparticles are synthesised and stabilised in one medium and transferred to other solution containing second metal precursor with necessary surfactants followed by the second stage reduction¹⁵⁰.

Epitaxial growth of metals with comparatively lesser lattice mismatch has been reported by Tian and co-workers for the transformation of gold nano-octahedra seed to Au@Ag and Au@Pd nanocubes by following a two-step reduction route¹⁵⁰. A careful analysis of the core-shell materials by using HR-TEM analysis proved the core-shell formation with epitaxial growth confirmed by the presence of Moire' patterns in Au@Ag and Au@Pd nanocubes. An aqueous phase approach by controlling the morphology of Au and Pd for core-shell structures like tetrahedral, concaveoctahedral, and octahedral shapes have also been reported¹⁵¹. They extended the aqueous phase synthesis concept to form Au@Ag core-shell nanoparticles with morphologies like cubic, truncated cubic, cuboctahedral, truncatedoctahedral and octahedral structures once again by tuning the reaction parameters especially in the second phase of kinetically controlled reduction by using ascorbic acid as a weak reducing agent¹⁵². Galvanic replacement method is entirely based on the redox potential values of the metals and here also the synthesis proceeds through stepwise manner in which one kind of metal nanoparticles are generated initially followed by the addition of second metal ions. Depending on the reduction potential values of metals the second metal ion can get reduced on the preformed metal nanoparticle surface at the expense of oxidation of the surface metal atoms. Depending on the metal concentrations and rate of galvanic replacement, it is possible to control the size of core and shell thickness. Galvanic replacement method can

be used for the tuning of geometry to core-shell and further extended to multi metallic hollow nanostructures with unique properties. Wang et al has demonstrated the formation of highly complex Ag-Pd bimetallic nanostructures by altering the synthesis parameters during galvanic replacement¹⁵³. They have achieved fine control over the compositions, interior architectures, and surface morphologies of Ag-Pd bimetallic hollow nanoparticles with increased structural complexity.

1.3.2 Synthesis of Gold (Au)-Nickel (Ni) Bimetallic Nanostructures

Synthesis of core-shell Au-Ni bimetallic nanostructures because of the large lattice mismatch of individual components is a big challenge in achieving the desired morphology and composition. The successful generation of core-shell morphology with control over the size is really a hurdle especially in case of Au-Ni. She et al successfully synthesized Au@Ni and Ni@Au core-shell nanoparticles for exploring optical and magnetic properties¹⁵⁴. They reported a non-aqueous approach for the synthesis and Au@Ni core-shell nanoparticle with size varied from 40-70 nm with a thick nickel shell over the gold core. Even though the sizes of Au@Ni core-shell nanoparticles are quite higher for catalytic applications they successfully synthesised such designed architectures through wet chemical reduction route. Synthesis challenges kept apart, nickel shows fascinating magnetic properties in the bulk as well as in nanoregime and there are several reports dealing with the diverse magnetic and non-magnetic behaviour of nickel. It is well known that bulk Ni has an inherent ferromagnetic property and crystallizes in FCC structure, where as the HCP crystallization form of nickel is not ferromagnetic even down to the liquid helium temperature¹⁵⁵. Thus creating bimetallic Ni nanostructures that are less than 10 nm in size which are robust at ambient pressures and elevated temperatures will provide interesting physiochemical properties to nickel along with catalytic enhancement. Tsuji et al demonstrated a two-step reductive method to epitaxially grow Au@Ni core-shell nanocrystals despite of their large lattice mismatch¹¹⁴. Even though the Au core size was several tens of nanometers, epitaxial growth was observed for the Ni shell up to 10 nm thickness. A comparatively lesser nickel shell thickness on icosahedral Au core has been reported by Wang and co-workers where the epitaxial relationship and Moire' patterns were clearly visible in the TEM analysis¹⁵⁶. In a two step successive reduction strategy Zhang et al reported the synthesis of Au cores of size ranging from 5-10 nm with fairly large nickel shells resulting in Au@Ni nanoparticles with an overall size around 20-30 nm¹⁵⁷. The surface analysis of these Au@Ni core-shell nanoparticles by XPS showed the

presence of 20 % metallic nickel in the as prepared Au@Ni nanoparticles where as a 15 nm monometallic nickel was completely surface oxidized. Apart from the synthesis challenge, the stability of these core-shell systems is also a major concern. Even though wet chemical methods allow the synthesis of kinetically stable materials, annealing at high temperatures will transform these materials into their thermodynamically stable structures as reported in case of Ni-Co and Pt-Ni bimetallic combinations which possess large lattice mismatch^{113, 158}.

1.3.3 Core-shell Bimetallic Nanoparticles for Colloidal Phase Catalysis

Colloidal phase catalysis by using nanoparticles has emerged as an interesting area in catalysis as it bridges homogeneous and heterogeneous catalysis area as it bridges the advantages of homogeneous and heterogeneous catalysis. In the as synthesized form the finely divided materials are stabilized by suitable ligands and generally suspended in solvents which are termed as colloids¹⁵⁹. They have been used as catalyst materials for simple oxidation-reduction reactions to major transformations like cross coupling, hydrogen generation, steam reforming, hydrogenation reactions, etc^{4, 160-162}. Xu and co workers demonstrated hydrogen production from hydrogen rich compounds like ammonia borane by using various bimetallic combinations¹⁶³⁻¹⁶⁴. Au@Co nanoparticles showed excellent conversion at room temperature as compared to their monometallic counter parts and Au-Co alloy nanoparticles (Figure 1.6). The work received much attention in the area of hydrogen production, since hydrogen is considered as the future energy and its production at ambient conditions is necessary for various applications.

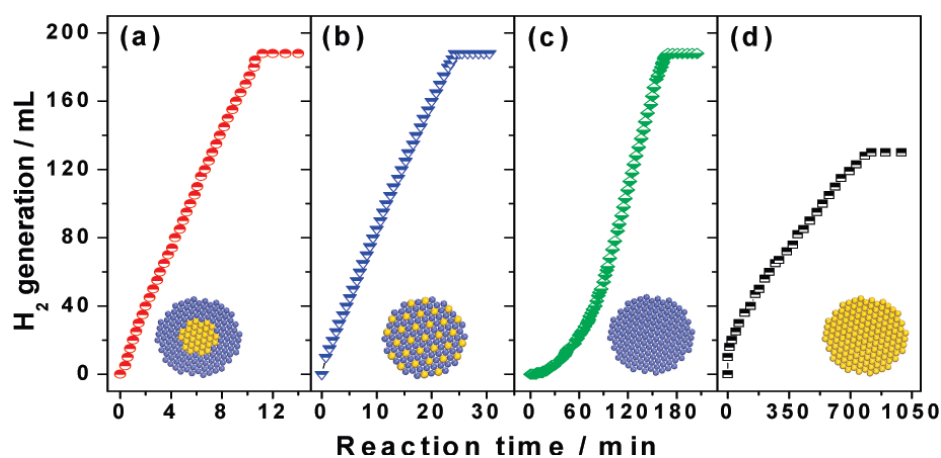


Figure 1.6 Hydrogen generation from ammoniabborane (AB) aqueous solution catalyzed by (a) Au@Co, (b) Au-Co, (c) Co, and (d) Au nanoparticles under ambient atmosphere at room temperature¹⁶⁴.

Henning et al has shown the utilization of Au@Pd nanoparticles for the solvent free oxidation of benzyl alcohol to benzaldehyde¹⁶⁵. They successfully synthesised Au@Pd core-shell nanoparticles with precise control over Pd shell thickness ranging up to 3.2 nm on the gold core with same size. The Au@Pd core-shell system with varying shell thickness provided an effective way for understanding the synergistic catalytic behaviour of the materials as a function of shell thickness. Their results showed drastic difference in the T.O.F of core-shell nanoparticles with various shell thickness and an optimum shell thickness of 2.2 nm is identified for the maximum conversion of benzyl alcohol (Figure 1.7a). In fact the optimum Pd shell thickness catalyst gave a noticeable change in selectivity for benzaldehyde (Figure 1.7b) product as compared to other bimetallic core-shell catalysts.

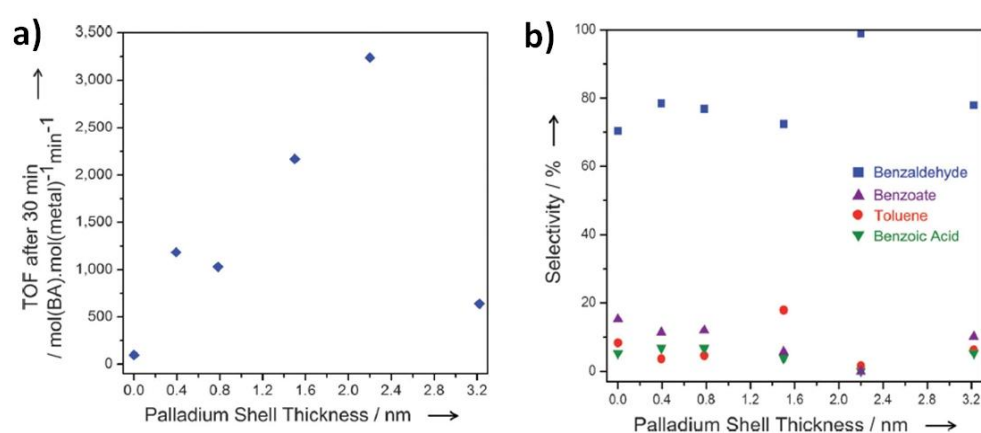


Figure 1.7 Catalytic activity and selectivity results of icosahedral Au@Pd core-shell nanocrystals with varying Pd shell thicknesses for the solvent-free oxidation of benzyl alcohol. a) Turnover frequency (TOF) and b) Selectivity vs Pd shell thickness in the benzyl alcohol oxidation¹⁶⁵.

Tedsree et al also reported the hydrogen generation from formic acid using core-shell nanoparticles which is more difficult task at ambient temperatures¹⁶⁶. They managed to synthesise palladium shell on various core metals such as Ag, Rh, Au, Ru and Pt. The core-shell nanoparticle colloids were tested for formic acid decomposition and they found that synergism operates maximum in the case of Ag@Pd core-shell system and they successfully related the catalytic enhancement with the work function of the core metal (Figure 1.8a). Their studies concluded that Ag with largest difference in work function showed maximum electronic promotion to the Pd shell for efficient hydrogen production. They also probed the effect of Pd shell thickness which is necessary for tuning the optimum activity, and it showed maximum rate of formic acid decomposition for Ag:Pd at 1:1 mole ratio (Figure 1.8b).

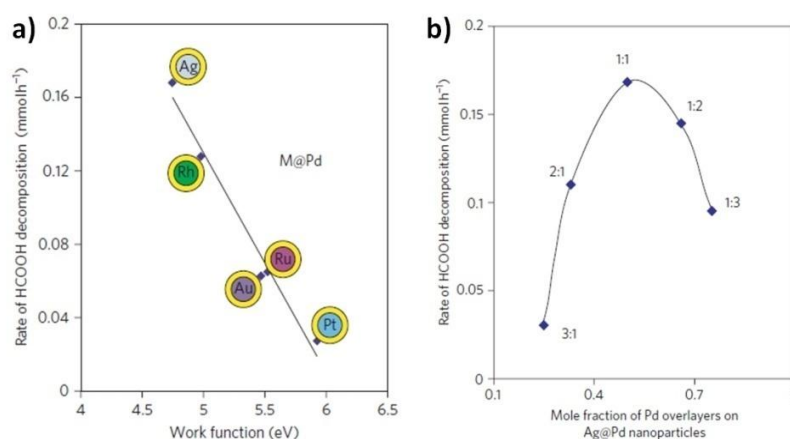


Figure 1.8 Rates of formic acid decomposition over M-core Pd shell (1:1) catalysts. a) Correlation with the work function of the M core, where M=Ag, Rh, Au, Ru, Pt or Ru. b) Rates of formic acid decomposition over Ag@Pd at different mole ratios of Ag and Pd; the 1:1 ratio shows an optimum composition¹⁶⁶.

1.3.4 Gold (Au)-Nickel (Ni) Bimetallic Nanoparticles in Catalysis

Monometallic gold nanoparticles are known for oxidation reactions, whereas nickel is widely accepted as hydrogenation catalysts¹⁶⁷⁻¹⁶⁸. In the bimetallic form, the catalytic investigation of Au-Ni system is less as explored to other common bimetallic systems. Many groups made useful findings about the synergistic behaviour of Au-Ni bimetallic system as efficient catalysts especially in their supported forms on suitable metal oxides¹⁶⁹⁻¹⁷⁰. There are very scarce reports for the utilization of Au-Ni bimetallic nanoparticles in colloidal phase catalysis (without support)¹⁷¹. The catalytic efficiency of the materials is generally governed by the Sabatier principle, whereby the interactions of adsorbate molecules are largely controlled by the electronic structure of the catalyst surface¹⁷². Hence in case of these electronically/geometrically modified bimetallic Au-Ni surfaces, the catalytic enhancement and sustainability of the materials will provide a better way to overcome the drawbacks of their monometallic counterparts. Pal et al reported the application of Ni-Au bimetallic hierarchical nanostructures for nitro phenol reduction and found that bimetallic interfaces promotes the catalytic rate and outweighed activity by Ni or Au alone surfaces¹⁷¹. Au-Ni bimetallic structures in the supported form are used for versatile catalytic applications like CO oxidation⁸¹, steam reforming¹⁷³, hydrogen generation¹⁶⁹, nitro reduction¹⁷⁴, hydrodechlorination¹⁷⁵, synthesis of 1-D carbon nanostructures¹⁷⁶, dehydrogenation¹⁷⁰, etc. Most of the catalytic activity results in the case of supported Au-Ni catalysts emphasize the importance of Au-Ni interface in enhancing the catalytic activity.

1.3.5 Characterisation of Bimetallic Nanoparticles

Characterization tools play a pivotal role in nano science and especially nanocatalysis. Structure-property-activity correlations can only be accomplished with good set of characterization tools. Especially in the case of bimetallic nanoparticles an in-depth investigation is necessary to get precise understanding about the synergistic behaviour. Metal-metal interaction in the bimetallic nanostructures may alter the geometry of metal-metal bonds at the surface, composition of metals in the bulk-interface-surface, oxidation state of metals and electronic nature particularly at the interface. X-ray based techniques are most popular and widely used for determining the structural features and chemical nature of the nanoparticles. They are mainly X-ray Photoelectron Spectroscopy (XPS or PES) and X-Ray Diffraction (XRD). Due to the Surface Plasmon Resonance (SPR) properties of the SPR active metal nanoparticles UV-Vis spectroscopy is also used for the preliminary analysis of colloidal dispersions of Au, Ag and Cu. Under the microscopic techniques the inevitable tools for imaging the nanomaterials are Transmission Electron Microscopy (TEM) and Scanning Electron Microscopy (SEM). The spectroscopic techniques are highly efficient to get informations about the structural and chemical compositions of the nanoparticles where as microscopic tools are successful in probing the morphological characteristics like size and shape. And in the case of magnetic nanoparticles their magnetic behaviour can be analyzed by using SQUID-VSM analysis. The following part of the thesis will give a brief description about the potential uses of these advanced characterisation tools that are used for the bimetallic nanoparticle analysis in this thesis.

Electron microscopy is a powerful tool for characterizing the nanomaterials with atomic resolutions. It is very popular and used for the imaging of bulk or nano materials. With the recent developments in electron microscopy, it is possible to visualize the morphologies of the materials and structural arrangements in the atomic level. The most common electron microscopic techniques are Transmission Electron Microscopy (TEM) and Scanning Electron Microscopy (SEM). Both the techniques are different in their basic features and acquiring data but in both cases high energy electron beams are used as the source to analyze the specimen. The major difference in the instrumentation between TEM and SEM is that TEM uses transmitted electrons for imaging the specimen while SEM uses the back scattered electrons from the specimen for imaging. TEM and SEM techniques have their own importance and applications especially in nanomaterials characterization. In the case of TEM,

a parallel high energy primary electron beam from the source is used to analyse the sample and it is allowed to impinge on an ultra thin specimen. Usually thermionic gun (tungsten filament or LaB₆ crystal) or field emission gun (FEG) are used as an electron source to illuminate the sample. The electrons produced from the source are accelerated to very high voltages and passed through a condenser lens system which finally focuses on to the specimen. The resolution of the electron microscope can be altered by tuning the wavelength of the primary electron beam accelerated at very high voltages typically in the range of 100-300 kV. A standard TEM operates at very low pressures and microscope column is always maintained at high vacuum levels (10^{-6} mbar) to prevent scattering of electrons by the gas atmosphere inside the microscope and thereby increasing the mean free path of the electrons. When the high energy electron beam interacts with matter (sample) various phenomena can occur, out of that TEM is based on the investigation of transmitted electron beam generated from the sample. As the attenuation of the electron beam coming out of the specimen depends on the density and thickness, the transmitted electrons forms a two-dimensional projection of the sample mass, which is subsequently magnified by electromagnetic lenses to produce a bright field image. Whereas, the dark field image is obtained from the diffracted electron beams, which are slightly off angle from the transmitted beam. The scattering efficiency will be different for various elements; scattering of the electrons will increase with the increase in atomic number. Hence, heavy metals with high atomic number can form images with good contrast. HR-TEM is an imaging mode of the transmission electron microscope which works at higher acceleration voltage preferably 300 kV to produce high resolution images. At present, the highest point resolution realised in phase contrast TEM is around 0.5 Å at magnifications above 50 million times.

TEM provide the informations like size, shape and atomic structure of the nanoparticles. It can reach up to angstrom (Å) level resolutions and gives atomic resolution images. From low resolution TEM images particle size distribution and 2-D structural features of the materials can be obtained. Under High Resolution TEM (HR-TEM) imaging mode elemental characterization through lattice fringe analysis (or d-spacing value) is possible. It helps in the identification of exposed facets (particular planes) in a nanoparticle surface which is useful for correlating with the catalytic activity of the nanomaterials. It also used to obtain the electron diffraction of the materials for analysis of crystallographic planes in SAED (Selected Area Electron Diffraction) mode. From the SAED analysis it is also possible to

conclude the crystalline or amorphous nature of the materials. Advanced features of TEM include the HAADF (High Angle Annular Dark Field) and STEM (Scanning Transmission Electron Microscopy) imaging modes equipped with EDS (Energy Dispersive Spectroscopy) analysis to confirm the elemental compositions and atomic distribution in nanoparticles. Normal TEM imaging works under bright field imaging mode whereas HAADF-STEM mode works in dark field. In any case, these modes are highly dependent on the atomic mass of the elements which in turn produces contrast difference in the final images. In the thesis, the TEM images were obtained by using TF-30 and TF-20 FEI Tecnai instruments. FEI Tecnai TF-30 electron microscope, operating at 300 keV, was used for High Resolution Transmission Electron Microscopy (HR-TEM) sample observations and lower magnification images are collected by using TF-20.

In SEM, instead of transmission (unlike to that of TEM), the specimen will be scanned with a focussed beam of electrons (5-50 kV) and detects the yield of either secondary or back-scattered electrons as a function of the position of the primary beam to produce the surface images. The focussed beam of electrons interacts with atoms in the specimen, which results into various signals and SEM deals with the investigation of mainly signals such as secondary electrons (SE), reflected or back-scattered electrons (BSE), photons of characteristic X-rays and light (cathodoluminescence). In the most common or standard detection mode in SEM, secondary electrons are used for imaging (SEI). And it can produce very high-resolution images of a sample surface, revealing details less than 1 nm in size since the secondary electrons are emitted from very close to the sample surface. The elastic scattering of the electron beam from the specimen results in back-scattered electrons (BSE). They emerge from deeper locations within the sample and apparently the resolution of images obtained from analysing the BSE is generally poorer than SE images. However, BSE are commonly used for analytical SEM along with the spectra made from the characteristic X-rays to identify the composition and measure the abundance of elements in the sample and it is termed as energy dispersive X-rays analysis (EDAX). More importantly the sample requirement for SEM imaging is that specimens must be electrically conductive, at least at the surface. Hence, before imaging of the non-conductive specimens, surface could be made conducting by a thin coating of electrically conducting material. Advanced SEM instruments are useful to obtain the surface characteristics or textural features along with crystalline structure and orientation of the materials. SEM in combination with EDS (Energy Dispersive Spectroscopy) used for

the analysis of chemical composition variation in the materials. In the present work, SEM imaging were performed on a FEI, Model Quanta 200 3D instrument equipped with energy dispersive spectral analysis setup at an operating potential of 30 kV.

UV-Vis absorption spectroscopy is relatively quick and straightforward technique and it is ideally used for gaining a first impression of the optical response of SPR active colloidal metal nanoparticles. UV-Vis measures the collective response of nanoparticle samples to a broad spectrum of electromagnetic radiation, ranging from UV to near IR through visible wavelengths. The resulting extinction spectrum (absorbance or reflectance) includes the combined effect of both scattering and absorption of electromagnetic radiation by all of the particles in the sample. Spectra are acquired for the sample in solution and with the reference solvent. It is highly useful for the analysis of nanostructures consists of Au, Ag and Cu since their absorption bands falls in the visible region. It is successful in providing preliminary informations about the size, shape and composition of the SPR active metal nanoparticles. UV-Vis analysis reported in the thesis was carried out by using a Varian Cary 50 Conc UV-Vis spectrophotometer with a dual beam source.

The magnetic properties of the nanoparticles can be measured through VSM analysis. The most common measurement method employed for hysteresis loop determinations of magnetic materials at ambient temperature is the Vibrating Sample Magnetometer (VSM). An advanced version is SQUID (superconducting quantum interference device) which is a very sensitive magnetometer capable of measuring extremely subtle magnetic features. The basic theory of magnetic measurements using VSM is that when a material is placed within a uniform magnetic field H , a magnetic moment m will be induced in the sample. And in VSM, the sample is mechanically vibrated and the resulting magnetic flux changes are probed by using a sensing coil that is proportional to the magnetic moment of the sample. The external magnetic field may be generated by an electromagnet, or a superconducting magnet. In the case of a typical recording medium the hysteresis loop gives the relation between the magnetization M and the applied field H . The parameters extracted from the hysteresis loop measurements that are commonly used to characterize the magnetic properties of the materials include mainly the saturation magnetization M_s , the remanence M_r , and the coercivity H_c . Magnetic measurements are found to be highly useful for the detection of variation in magnetic features of materials in their nanoregime from that of bulk. Magnetic measurements of the materials reported in thesis were done on a Quantum Design MPMS 7T SQUID-VSM.

Powder X-ray diffraction (PXRD or XRD) technique is the most common X-ray based technique and employed for routine analysis for the nanoparticles. It follows the basic principles of X-ray diffraction as in the case of bulk materials. The informations about the crystallographic structure (planes), phase purity, chemical compositions and crystallite size are obtained from XRD analysis. It is based on the diffraction of X-rays from an ordered lattice planes. Hence it gives the information about the continuity in the lattice structure of a solid crystalline material. The diffraction peaks obtained in the XRD spectra corresponds to the lattice spacing of various planes present in the material. Constructively scattered monochromatic X-rays from different crystal planes are responsible for a diffraction pattern. And the scattered X-rays will become constructive only at a particular angle when the path difference between the two rays, differ by an integral number of wavelength. Bragg's relationship explains the lattice spacing (or inter planar spacing) of the samples which is characteristic of the materials.

$$n\lambda = 2d \sin\theta ; \quad n = 1,2,3,\dots$$

where λ is the wavelength of X-rays, d is the distance between two lattice planes, θ is the angle between incoming X-rays and the normal to the reflecting lattice plane and n is an integer known as the order of reflection. Each plane is characterized by miller indices values given by (hkl). It is generally found that the nanoparticles shows the diffraction peak at same position as that of the bulk material but with drastic increase in the FWHM values (or peak broadening). The full width at half maximum (FWHM) values of the diffractions peaks are used for the calculation of crystallite size of the nanoparticles. Hence the broadening of the XRD peaks indirectly relates to the smaller size of the nanoparticles. Crystallite sizes of materials are calculated with the help of Scherrer formula which relates crystal size to peak width (FWHM) as,

$$\tau = \frac{K\lambda}{\beta \cos\theta}$$

where τ is the mean crystallite size, λ is the X-ray wavelength, β is the full width at half maximum (FWHM) of the peak, θ is the angle between the beam and the normal to the

reflecting plane and K is a constant often taken as 0.9. Commonly, nanoparticles are polycrystalline in nature and show various diffraction peaks at different positions. The intensity of the XRD peaks also gives information about the stability and most exposed planes in the material. In case of metals with FCC arrangement the stable plane is [111] and in turn it shows the maximum intense peak in XRD analysis. Since the lattice spacing values are characteristic for particular elements the diffraction peak positions help in the elemental analysis and also chemical structure of the system. Powder X-ray diffraction (XRD) of all the samples mentioned in the thesis was measured on a PANalytical X'pert Pro dual goniometer diffractometer working under 40 kV and 30 mA. The Cu $K\alpha$ (1.5418 Å) radiation was used with a Ni filter. The data collection was carried out using a flat holder in Bragg–Brentano geometry. An X'celerator solid-state detector with a scan speed of 0.0120min^{-1} was employed in measuring wide angle X-ray diffractions.

Another X-ray based characterization technique is X-ray Photoelectron Spectroscopy (XPS). It is also known as Electron Spectroscopy for Chemical Analysis (ESCA) or Photoelectron Spectroscopy (PES). The major difference between XRD and XPS is that the former one is used for the bulk analysis of the material whereas the later one is highly surface sensitive. The surface sensitivity of XPS in the chemical state analysis and elemental detection makes it a highly relevant tool in catalysis. The principle of X-ray photoelectron spectroscopy (XPS) is the photoelectric effect discovered by Heinrich Hertz and explained later by Albert Einstein. Einstein's photoelectric equation explains the energy conservation during the photoelectric effect as

$$h\nu = B.E + K.E + \phi$$

The total photon energy ($h\nu$) is used up in the form of binding energy (B.E) required to excite an electron from any occupied level to the Fermi level (E_F), the additional energy required to remove an electron from the Fermi level into vacuum is the work function (ϕ) of the solid, and the remaining energy is associated with the photoelectron in the form of kinetic energy (K.E). PES is based on the detection of core level photoelectrons ejected from a material surface upon shining with monochromatic X-rays. Due to the extremely small mean free path (maximum 10 nm) of the inelastically scattered photoelectrons, only those electrons from the outermost atomic layer of the materials will be analysed. XPS gives information about the surface composition and chemical state/oxidation state of the elements. XPS is highly relevant

in structure-activity correlation in catalysis because it is important to compare the catalytic activity with the surface chemical states of a material rather than bulk. Despite the oxidation state analysis XPS can also be employed for the identification and synergism of bimetallic combinations. The existence of synergism in bimetallic surfaces is mainly probed through XPS analysis by various groups and they found shifts in the core level binding energies of elements when it forms bimetallic combination.

Recent developments in XPS instrumentation has led to the next generation of XPS spectrometer called ambient pressure XPS (APXPS or APPEs)¹⁷⁷. APPEs instruments are designed with the focus of understanding the surface dynamics of materials under reactive environments especially during catalysis. Different custom-made APPEs instruments are available at various research laboratories around the world¹⁰⁷. The following section will be discussing about the aspects of a custom-built ambient pressure photoelectron spectrometer (Lab-APPEs, Figure 1.9) unit which was commissioned at CSIR-National Chemical Laboratory (NCL), Pune¹⁰⁸. The Lab-APPEs at CSIR-NCL is built and supplied by Prevac, Poland with an Al K α monochromator MX 650 and R3000HP model analyzer from VG Scienta, Sweden. By using Lab-APPEs, XPS/UPS measurements can be carried out up to 1 mbar pressure and up to 873 K by conventional heating methods and at least up to 1273 K by a laser heating method on the solid surfaces. Much advancement has been done over the instrumental techniques of normal UHV-XPS in the past decade, in order to realize the sample analysis particularly at higher pressures (under operando conditions). One of the major constraints in the development of UHV surface science tools to work at high pressures is the capture and detection of “raw electrons with characteristic signature of the material” without any inelastic collision during its travel to reach the detector. The inelastic collision of the free electrons with gas molecules or other contaminants results in the reduced life time and mean free path of the free electrons and also loses its characteristic behaviour by losing their energy partially/completely. The only way to get around the problem with mean free path of photoelectrons is to avoid the inelastic collisions as much as possible and to help the photoelectrons to find a UHV atmosphere as soon as it ejected out from the surface of the material. However it is rather impossible to avoid the inelastic collision of photo electrons completely since the sample surface is kept at high pressure conditions and the ejected photoelectrons have to cross the gas environment to reach the analyzer cone and thereafter to the detector.

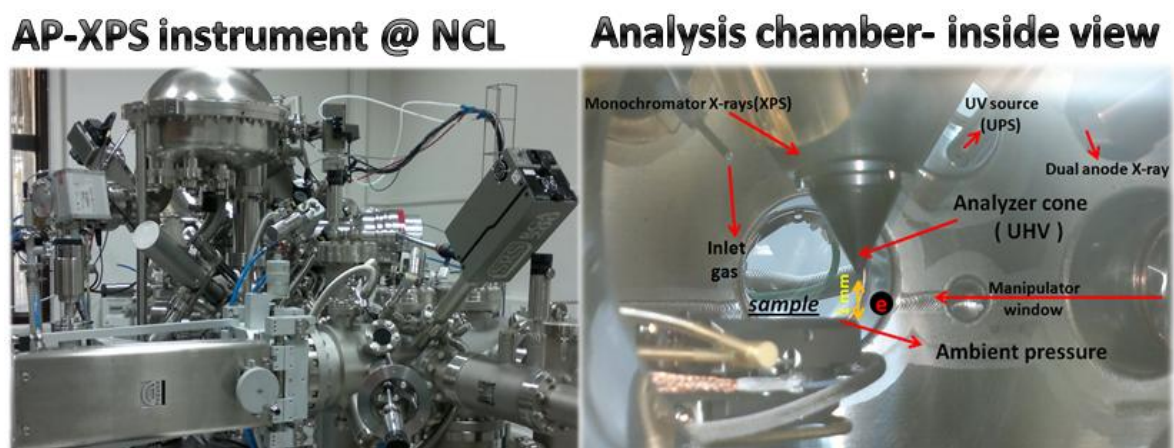


Figure 1.9 A digital photograph of the near ambient pressure XPS (NAPXPS) instrument at NCL and its analysis chamber view (A specially designed analyzer cone is marked in the image).

Even though to make sure an effective data acquisition maximum number of photoelectrons must be collected especially from a close proximity of the sample surface without losing their kinetic energy. In this regard, the most important achievement was the development of an advanced electrostatic lens regime (ELR) with effective electrostatic focusing of the electrons inside the analyzer cone. In APPES where the inelastic collision rates are higher and the number of electrons collected into the ELR at high pressure is significantly lower. Hence, to improve the electron count reaching the detector, various modifications are made in the analyzer (VG Scienta R3000HP) of the Lab-APPES at NCL, Pune. Firstly a specially designed analyzer cone (Figure 1.9) with different apertures ranging from 0.3-5 mm is attached to the ELR. And the sample surface is kept very close to the tip of the cone typically 0.5-1 mm to minimize the loss of electrons due to inelastic collisions under high pressure conditions. The design of the cone with its extremely low aperture width which is different from the normal UHV-XPS helps the photoelectrons to easily pass through to the analyzer whereas gas molecules are prevented and thereby creating a better vacuum inside the analyzer. To make sure that the successful utilization of photoelectrons those enter in to the analyzer segment for data acquisition, effective differential pumping and the converging of electrons in the ELR have been employed. In the Lab-APPES at NCL, to maintain a UHV atmosphere near to the electron energy analyzer (EEA), three effective differential pumping stages are designed. The first differential pumping starts from the analyzer cone connected to ELR itself, thereby providing a better vacuum for the photoelectrons that enter immediately to the analyzer from the sample surface. And as the photoelectrons progress to the next

differential pumping stages it finds better vacuum as compared to the former and hence a pressure gradient has been built from the cone to EEA which is kept at completely ultra high vacuum (10^{-7} - 10^{-8} mbar). With these modifications in the instrument, in-situ XPS measurements can be carried out up to 1 mbar gas environment on the sample surface. All the UHV and NAPXPS measurements reported in the thesis were carried out by using ambient pressure X-ray photoelectron spectrometer [APXPS] from Prevac, Poland. The X-rays work with an acceleration voltage of a maximum of 15 kV and the X-ray monochromator is isolated from the analysis chamber by a thin aluminum foil window (5 μ m). The aluminum window efficiently seals the monochromator region to keep the high vacuum atmosphere during the ambient pressure experiments. The analysis chamber also carries a UV source for the production of stable He I and He II ultraviolet radiation which enables a clean valence band photoelectron spectroscopy (UV-PES) analysis under UHV as well as high pressure conditions up to 1 mbar.

1.4 Objectives of this Thesis

The importance of nickel in heterogeneous catalysis is already well appreciated especially for hydrogenation, methanation and reforming reactions. Metallic nickel is the active phase for these chemical transformations and any changes in the chemical state can be detrimental in catalytic ability. The major challenges for nickel catalyst especially for steam reforming reactions in the industry are the coke deposition, sulphur poisoning, agglomeration and stable activity¹⁷⁸. The steam reforming which takes place at high temperature and steam conditions in presence of hydrocarbons creates extremely harsh atmosphere for the nickel surface. During the decomposition of hydrocarbons on the nickel surface the active sites of nickels shows high affinity for carbon deposition¹⁷⁹⁻¹⁸⁰. This will block the active sites thereby killing the catalyst. As the reaction progress this carbon deposition slowly grows in to other catalytically active sites and finally forms stable and irreversible nickel carbide. Due to this the recyclability and stability of the catalyst which is the major attractions of the heterogeneous catalyst also becomes a hurdle in case of nickel. It requires major chemical modification in the catalyst surface to prevent deactivation and to provide sustainable catalytic activity. Another route for deactivation is the reactive nature of nickel with oxygen. Even under ambient atmosphere nickel is highly prone to oxidation and it ultimately leads to the formation of various nickel oxidic species on the catalyst surface. These metastable oxidic species on the surface eventually converts to stable nickel oxide and deactivates the catalyst. In the case of nanoparticles, the situation changes from bad to worse as nickel nanoparticles undergoes rapid oxidation under ambient conditions. Hence it is highly desirable to create a nickel catalyst, which has active metallic nickel surface for catalysis and retain its stability for higher number of catalytic cycles. From the previous surface science studies it is understood that Ni in combination with Au can create surfaces which can prevent coke formation as well as resistant to oxidation. To realize these surface science concepts, Au@Ni bimetallic nanoparticles were synthesized by wet chemical route employing surfactants which are cheap and environment friendly. An aqueous route for the synthesis of Au@Ni nanoparticles is also established in this thesis. All these materials were thoroughly characterised by different microscopy and spectroscopy techniques. The synthesized materials are also demonstrated for synergistic catalysis for various hydrogenation reactions. The nature of the Ni surface is also probed using NAPXPS to understand the oxidation and decomposition landscapes of different metastable oxides.

1.5 References

1. Luc, W.; Jiao, F., Synthesis of Nanoporous Metals, Oxides, Carbides, and Sulfides: Beyond Nanocasting. *Acc. Chem. Res.* **2016**, *49* (7), 1351-1358.
2. Munnik, P.; de Jongh, P. E.; de Jong, K. P., Recent Developments in the Synthesis of Supported Catalysts. *Chem. Rev.* **2015**, *115* (14), 6687-6718.
3. Johnson, B. F., Nanoparticles in catalysis. *Top. Catal.* **2003**, *24* (1-4), 147-159.
4. Jiang, H.-L.; Xu, Q., Recent progress in synergistic catalysis over heterometallic nanoparticles. *J. Mater. Chem.* **2011**, *21* (36), 13705-13725.
5. Gao, J.; Gu, H.; Xu, B., Multifunctional Magnetic Nanoparticles: Design, Synthesis, and Biomedical Applications. *Acc. Chem. Res.* **2009**, *42* (8), 1097-1107.
6. Kruis, F. E.; Fissan, H.; Peled, A., Synthesis of nanoparticles in the gas phase for electronic, optical and magnetic applications—a review. *J. Aerosol Sci.* **1998**, *29* (5–6), 511-535.
7. Talapin, D. V.; Lee, J.-S.; Kovalenko, M. V.; Shevchenko, E. V., Prospects of Colloidal Nanocrystals for Electronic and Optoelectronic Applications. *Chem. Rev.* **2010**, *110* (1), 389-458.
8. Kamat, P. V., Meeting the Clean Energy Demand: Nanostructure Architectures for Solar Energy Conversion. *J. Phys. Chem. C* **2007**, *111* (7), 2834-2860.
9. Barnes, W. L.; Dereux, A.; Ebbesen, T. W., Surface plasmon subwavelength optics. *Nature* **2003**, *424* (6950), 824-830.
10. West, J. L.; Halas, N. J., Engineered Nanomaterials for Biophotonics Applications: Improving Sensing, Imaging, and Therapeutics. *Annu. Rev. Biomed. Eng.* **2003**, *5* (1), 285-292.
11. Clavero, C., Plasmon-induced hot-electron generation at nanoparticle/metal-oxide interfaces for photovoltaic and photocatalytic devices. *Nat. Photon* **2014**, *8* (2), 95-103.
12. Frey, N. A.; Peng, S.; Cheng, K.; Sun, S., Magnetic nanoparticles: synthesis, functionalization, and applications in bioimaging and magnetic energy storage. *Chem. Soc. Rev.* **2009**, *38* (9), 2532-2542.
13. Xia, Y.; Yang, H.; Campbell, C. T., Nanoparticles for Catalysis. *Acc. Chem. Res.* **2013**, *46* (8), 1671-1672.
14. Zhu, C.; Du, D.; Eychmüller, A.; Lin, Y., Engineering Ordered and Nonordered Porous Noble Metal Nanostructures: Synthesis, Assembly, and Their Applications in Electrochemistry. *Chem. Rev.* **2015**, *115* (16), 8896-8943.
15. Cao, S.; Tao, F.; Tang, Y.; Li, Y.; Yu, J., Size- and shape-dependent catalytic performances of oxidation and reduction reactions on nanocatalysts. *Chem. Soc. Rev.* **2016**, *45* (17), 4747-4765.
16. Narayanan, R.; El-Sayed, M. A., Catalysis with Transition Metal Nanoparticles in Colloidal Solution: Nanoparticle Shape Dependence and Stability. *J. Phys. Chem. B* **2005**, *109* (26), 12663-12676.
17. Crespo-Quesada, M.; Yarulin, A.; Jin, M.; Xia, Y.; Kiwi-Minsker, L., Structure Sensitivity of Alkynol Hydrogenation on Shape- and Size-Controlled Palladium Nanocrystals: Which Sites Are Most Active and Selective? *J. Am. Chem. Soc.* **2011**, *133* (32), 12787-12794.
18. Bratlie, K. M.; Lee, H.; Komvopoulos, K.; Yang, P.; Somorjai, G. A., Platinum Nanoparticle Shape Effects on Benzene Hydrogenation Selectivity. *Nano Lett.* **2007**, *7* (10), 3097-3101.
19. Wu, Y.; Cai, S.; Wang, D.; He, W.; Li, Y., Syntheses of Water-Soluble Octahedral, Truncated Octahedral, and Cubic Pt–Ni Nanocrystals and Their Structure–Activity Study in Model Hydrogenation Reactions. *J. Am. Chem. Soc.* **2012**, *134* (21), 8975-8981.

20. Huang, X.; Li, Y.; Li, Y.; Zhou, H.; Duan, X.; Huang, Y., Synthesis of PtPd Bimetal Nanocrystals with Controllable Shape, Composition, and Their Tunable Catalytic Properties. *Nano Lett.* **2012**, *12* (8), 4265-4270.
21. Zhang, P.; Sham, T. K., X-Ray Studies of the Structure and Electronic Behavior of Alkanethiolate-Capped Gold Nanoparticles: The Interplay of Size and Surface Effects. *Phys. Rev. Lett.* **2003**, *90* (24), 245502.
22. Halperin, W. P., Quantum size effects in metal particles. *Rev. Mod. Phys.* **1986**, *58* (3), 533-606.
23. Xu, C.; Lai, X.; Zajac, G. W.; Goodman, D. W., Scanning tunneling microscopy studies of the TiO₂ (110) surface: Structure and the nucleation growth of Pd. *Phys. Rev. B* **1997**, *56* (20), 13464-13482.
24. Valden, M.; Lai, X.; Goodman, D. W., Onset of Catalytic Activity of Gold Clusters on Titania with the Appearance of Nonmetallic Properties. *Science* **1998**, *281* (5383), 1647-1650.
25. Alivisatos, A. P., Semiconductor Clusters, Nanocrystals, and Quantum Dots. *Science* **1996**, *271* (5251), 933-937.
26. Weller, H., Colloidal Semiconductor Q-Particles: Chemistry in the Transition Region Between Solid State and Molecules. *Angew. Chem., Int. Ed. Engl.* **1993**, *32* (1), 41-53.
27. El-Sayed, M. A., Small Is Different: Shape-, Size-, and Composition-Dependent Properties of Some Colloidal Semiconductor Nanocrystals. *Acc. Chem. Res.* **2004**, *37* (5), 326-333.
28. Eustis, S.; El-Sayed, M. A., Why gold nanoparticles are more precious than pretty gold: Noble metal surface plasmon resonance and its enhancement of the radiative and nonradiative properties of nanocrystals of different shapes. *Chem. Soc. Rev.* **2006**, *35* (3), 209-217.
29. Chan, G. H.; Zhao, J.; Hicks, E. M.; Schatz, G. C.; Van Duyne, R. P., Plasmonic Properties of Copper Nanoparticles Fabricated by Nanosphere Lithography. *Nano Lett.* **2007**, *7* (7), 1947-1952.
30. Crowell, J.; Ritchie, R. H., Surface-Plasmon Effect in the Reflectance of a Metal. *J. Opt. Soc. Am.* **1970**, *60* (6), 794-799.
31. Pitarke, J. M.; Silkin, V. M.; Chulkov, E. V.; Echenique, P. M., Theory of surface plasmons and surface-plasmon polaritons. *Rep. Prog. Phys.* **2007**, *70* (1), 1.
32. Halas, N. J.; Lal, S.; Chang, W.-S.; Link, S.; Nordlander, P., Plasmons in Strongly Coupled Metallic Nanostructures. *Chem. Rev.* **2011**, *111* (6), 3913-3961.
33. Pissuwan, D.; Niidome, T.; Cortie, M. B., The forthcoming applications of gold nanoparticles in drug and gene delivery systems. *J. Controlled Release* **2011**, *149* (1), 65-71.
34. Zhou, X.; Liu, G.; Yu, J.; Fan, W., Surface plasmon resonance-mediated photocatalysis by noble metal-based composites under visible light. *J. Mater. Chem.* **2012**, *22* (40), 21337-21354.
35. Saha, K.; Agasti, S. S.; Kim, C.; Li, X.; Rotello, V. M., Gold Nanoparticles in Chemical and Biological Sensing. *Chem. Rev.* **2012**, *112* (5), 2739-2779.
36. Stewart, M. E.; Anderton, C. R.; Thompson, L. B.; Maria, J.; Gray, S. K.; Rogers, J. A.; Nuzzo, R. G., Nanostructured Plasmonic Sensors. *Chem. Rev.* **2008**, *108* (2), 494-521.
37. Ozbay, E., Plasmonics: Merging Photonics and Electronics at Nanoscale Dimensions. *Science* **2006**, *311* (5758), 189-193.
38. Jia, C.-J.; Schuth, F., Colloidal metal nanoparticles as a component of designed catalyst. *Phys. Chem. Chem. Phys.* **2011**, *13* (7), 2457-2487.
39. Jin, R.; Zeng, C.; Zhou, M.; Chen, Y., Atomically Precise Colloidal Metal Nanoclusters and Nanoparticles: Fundamentals and Opportunities. *Chem. Rev.* **2016**, *116* (18), 10346-10413.

40. Schauermaun, S.; Nilius, N.; Shaikhutdinov, S.; Freund, H.-J., Nanoparticles for Heterogeneous Catalysis: New Mechanistic Insights. *Acc. Chem. Res.* **2013**, *46* (8), 1673-1681.
41. Aiken Iii, J. D.; Finke, R. G., A review of modern transition-metal nanoclusters: their synthesis, characterization, and applications in catalysis. *J. Mol. Catal. A: Chem.* **1999**, *145* (1–2), 1-44.
42. Fujita, T.; Guan, P.; McKenna, K.; Lang, X.; Hirata, A.; Zhang, L.; Tokunaga, T.; Arai, S.; Yamamoto, Y.; Tanaka, N.; Ishikawa, Y.; Asao, N.; Yamamoto, Y.; Erlebacher, J.; Chen, M., Atomic origins of the high catalytic activity of nanoporous gold. *Nat. Mater.* **2012**, *11* (9), 775-780.
43. Sonstrom, P.; Baumer, M., Supported colloidal nanoparticles in heterogeneous gas phase catalysis: on the way to tailored catalysts. *Phys. Chem. Chem. Phys.* **2011**, *13* (43), 19270-19284.
44. Norskov, J. K.; Bligaard, T.; Hvolbaek, B.; Abild-Pedersen, F.; Chorkendorff, I.; Christensen, C. H., The nature of the active site in heterogeneous metal catalysis. *Chem. Soc. Rev.* **2008**, *37* (10), 2163-2171.
45. Somorjai, G. A., Active Sites in Heterogeneous Catalysis. In *Advances in Catalysis*, D.D. Eley, H. P.; Paul, B. W., Eds. Academic Press: 1977; Vol. Volume 26, pp 1-68.
46. Zaera, F., The surface chemistry of heterogeneous catalysis: Mechanisms, selectivity, and active sites. *The Chemical Record* **2005**, *5* (3), 133-144.
47. Haruta, M., Chance and Necessity: My Encounter with Gold Catalysts. *Angew. Chem. Int. Ed.* **2014**, *53* (1), 52-56.
48. Hashmi, A. S. K.; Hutchings, G. J., Gold Catalysis. *Angew. Chem. Int. Ed.* **2006**, *45* (47), 7896-7936.
49. Hutchings, G. J., Catalysis by gold. *Catal. Today* **2005**, *100* (1–2), 55-61.
50. Masatake, H.; Tetsuhiko, K.; Hiroshi, S.; Nobumasa, Y., Novel Gold Catalysts for the Oxidation of Carbon Monoxide at a Temperature far Below 0 °C. *Chem. Lett.* **1987**, *16* (2), 405-408.
51. Hunt, S. T.; Milina, M.; Alba-Rubio, A. C.; Hendon, C. H.; Dumesic, J. A.; Román-Leshkov, Y., Self-assembly of noble metal monolayers on transition metal carbide nanoparticle catalysts. *Science* **2016**, *352* (6288), 974-978.
52. Heveling, J., Heterogeneous Catalytic Chemistry by Example of Industrial Applications. *J. Chem. Educ.* **2012**, *89* (12), 1530-1536.
53. Sankar, M.; Dimitratos, N.; Miedziak, P. J.; Wells, P. P.; Kiely, C. J.; Hutchings, G. J., Designing bimetallic catalysts for a green and sustainable future. *Chem. Soc. Rev.* **2012**, *41* (24), 8099-8139.
54. Zhang, Q.; Lee, I.; Joo, J. B.; Zaera, F.; Yin, Y., Core–Shell Nanostructured Catalysts. *Acc. Chem. Res.* **2013**, *46* (8), 1816-1824.
55. Bell, A. T., The Impact of Nanoscience on Heterogeneous Catalysis. *Science* **2003**, *299* (5613), 1688-1691.
56. Prati, L.; Villa, A., Gold Colloids: From Quasi-Homogeneous to Heterogeneous Catalytic Systems. *Acc. Chem. Res.* **2014**, *47* (3), 855-863.
57. Roldan Cuenya, B., Metal Nanoparticle Catalysts Beginning to Shape-up. *Acc. Chem. Res.* **2013**, *46* (8), 1682-1691.
58. Sneed, B. T.; Young, A. P.; Tsung, C.-K., Building up strain in colloidal metal nanoparticle catalysts. *Nanoscale* **2015**, *7* (29), 12248-12265.
59. Chiu, C.-Y.; Chung, P.-J.; Lao, K.-U.; Liao, C.-W.; Huang, M. H., Facet-Dependent Catalytic Activity of Gold Nanocubes, Octahedra, and Rhombic Dodecahedra toward 4-Nitroaniline Reduction. *J. Phys. Chem. C* **2012**, *116* (44), 23757-23763.

60. An, K.; Somorjai, G. A., Size and Shape Control of Metal Nanoparticles for Reaction Selectivity in Catalysis. *ChemCatChem* **2012**, *4* (10), 1512-1524.
61. Grzelczak, M.; Perez-Juste, J.; Mulvaney, P.; Liz-Marzan, L. M., Shape control in gold nanoparticle synthesis. *Chem. Soc. Rev.* **2008**, *37* (9), 1783-1791.
62. Zhang, L.; Niu, W.; Xu, G., Synthesis and applications of noble metal nanocrystals with high-energy facets. *Nano Today* **2012**, *7* (6), 586-605.
63. Xia, Y.; Xiong, Y.; Lim, B.; Skrabalak, S. E., Shape-Controlled Synthesis of Metal Nanocrystals: Simple Chemistry Meets Complex Physics? *Angew. Chem. Int. Ed.* **2009**, *48* (1), 60-103.
64. Zhou, K.; Li, Y., Catalysis Based on Nanocrystals with Well-Defined Facets. *Angew. Chem. Int. Ed.* **2012**, *51* (3), 602-613.
65. Yang, X.-F.; Wang, A.; Qiao, B.; Li, J.; Liu, J.; Zhang, T., Single-Atom Catalysts: A New Frontier in Heterogeneous Catalysis. *Acc. Chem. Res.* **2013**, *46* (8), 1740-1748.
66. Lucci, F. R.; Liu, J.; Marcinkowski, M. D.; Yang, M.; Allard, L. F.; Flytzani-Stephanopoulos, M.; Sykes, E. C. H., Selective hydrogenation of 1,3-butadiene on platinum-copper alloys at the single-atom limit. *Nat. Commun.* **2015**, *6*, 8550.
67. Qiao, B.; Liang, J.-X.; Wang, A.; Xu, C.-Q.; Li, J.; Zhang, T.; Liu, J. J., Ultrastable single-atom gold catalysts with strong covalent metal-support interaction (CMSI). *Nano Res.* **2015**, *8* (9), 2913-2924.
68. Zhang, S.; Nguyen, L.; Liang, J.-X.; Shan, J.; Liu, J.; Frenkel, A. I.; Patlolla, A.; Huang, W.; Li, J.; Tao, F., Catalysis on singly dispersed bimetallic sites. *Nat. Commun.* **2015**, *6*, 7938.
69. Toshima, N.; Yonezawa, T., Bimetallic nanoparticles-novel materials for chemical and physical applications. *New J. Chem.* **1998**, *22* (11), 1179-1201.
70. T.B. Massalski, J. L. M., L.H. Bennett and H. Baker, Binary Alloy Phase Diagrams, Vol 1. *American Society for Metals, Metals Park, OH* **1986**.
71. Zhou, S.; Jackson, G. S.; Eichhorn, B., AuPt Alloy Nanoparticles for CO-Tolerant Hydrogen Activation: Architectural Effects in Au-Pt Bimetallic Nanocatalysts. *Adv. Funct. Mater.* **2007**, *17* (16), 3099-3104.
72. Hwang, B.-J.; Sarma, L. S.; Chen, J.-M.; Chen, C.-H.; Shih, S.-C.; Wang, G.-R.; Liu, D.-G.; Lee, J.-F.; Tang, M.-T., Structural Models and Atomic Distribution of Bimetallic Nanoparticles as Investigated by X-ray Absorption Spectroscopy. *J. Am. Chem. Soc.* **2005**, *127* (31), 11140-11145.
73. Sinfelt, J. H., Supported "bimetallic cluster" catalysts. *J. Catal.* **1973**, *29* (2), 308-315.
74. Sinfelt, J. H., Catalysis by alloys and bimetallic clusters. *Acc. Chem. Res.* **1977**, *10* (1), 15-20.
75. Schwank, J., Bimetallic catalysts: Discoveries, concepts, and applications. By John H. Sinfelt, John Wiley & Sons, 1983. XI + 164 pp. *AIChE J.* **1985**, *31* (8), 1405-1405.
76. Rodriguez, J.; Wayne Goodman, D., High-pressure catalytic reactions over single-crystal metal surfaces. *Surf. Sci. Rep.* **1991**, *14* (1), 1-107.
77. Campbell, R. A.; Rodriguez, J. A.; Goodman, D. W., Chemical and electronic properties of ultrathin metal films: The Pd/Re(0001) and Pd/Ru(0001) systems. *Phys. Rev. B* **1992**, *46* (11), 7077-7087.
78. Rodriguez, J. A.; Goodman, D. W., The Nature of the Metal-Metal Bond in Bimetallic Surfaces. *Science* **1992**, *257* (5072), 897-903.
79. Campbell, R. A.; Rodriguez, J. A.; Goodman, D. W., Nature of Metal-Metal Bonding in Mixed Metal Catalysts. In *Stud. Surf. Sci. Catal.*, L. Guzzi, F. S.; P, T., Eds. Elsevier: 1993; Vol. Volume 75, pp 333-344.
80. Besenbacher, F.; Chorkendorff, I.; Clausen, B. S.; Hammer, B.; Molenbroek, A. M.;

- Nørskov, J. K.; Stensgaard, I., Design of a Surface Alloy Catalyst for Steam Reforming. *Science* **1998**, 279 (5358), 1913-1915.
81. Holgado, J. P.; Ternero, F.; Gonzalez-delaCruz, V. M.; Caballero, A., Promotional Effect of the Base Metal on Bimetallic Au–Ni/CeO₂ Catalysts Prepared from Core–Shell Nanoparticles. *ACS Catal.* **2013**, 3 (9), 2169-2180.
82. Chandler, B. D.; Long, C. G.; Gilbertson, J. D.; Pursell, C. J.; Vijayaraghavan, G.; Stevenson, K. J., Enhanced Oxygen Activation over Supported Bimetallic Au–Ni Catalysts. *J. Phys. Chem. C* **2010**, 114 (26), 11498-11508.
83. Rodriguez, J. A.; Goodman, D. W., Surface science studies of the electronic and chemical properties of bimetallic systems. *J. Phys. Chem.* **1991**, 95 (11), 4196-4206.
84. Strasser, P.; Koh, S.; Anniyev, T.; Greeley, J.; More, K.; Yu, C.; Liu, Z.; Kaya, S.; Nordlund, D.; Ogasawara, H.; Toney, M. F.; Nilsson, A., Lattice-strain control of the activity in dealloyed core–shell fuel cell catalysts. *Nat. Chem.* **2010**, 2 (6), 454-460.
85. Rodriguez, J. A.; Campbell, R. A.; Goodman, D. W., Electronic interactions in bimetallic systems: an x-ray photoelectron spectroscopic study. *J. Phys. Chem.* **1990**, 94 (18), 6936-6939.
86. Christmann, K.; Ertl, G.; Shimizu, H., Model studies on bimetallic Cu/Ru catalysts. *J. Catal.* **1980**, 61 (2), 397-411.
87. Christmann, K.; Ertl, G., Surface studies with bimetallic model catalyst systems. *J. Mol. Catal.* **1984**, 25 (1), 31-49.
88. Godbey, D. J.; Somorjai, G. A., The adsorption and desorption of hydrogen and carbon monoxide on bimetallic Re–Pt(111) surfaces. *Surf. Sci.* **1988**, 204 (3), 301-318.
89. Sachtler, J. W. A.; Somorjai, G. A., Influence of ensemble size on CO chemisorption and catalytic n-hexane conversion by Au–Pt(111) bimetallic single-crystal surfaces. *J. Catal.* **1983**, 81 (1), 77-94.
90. Nørskov, J. K.; Abild-Pedersen, F.; Studt, F.; Bligaard, T., Density functional theory in surface chemistry and catalysis. *Proc. Natl. Acad. Sci.* **2011**, 108 (3), 937-943.
91. Ruban, A.; Hammer, B.; Stoltze, P.; Skriver, H. L.; Nørskov, J. K., Surface electronic structure and reactivity of transition and noble metals. *J. Mol. Catal. A: Chem.* **1997**, 115 (3), 421-429.
92. Xin, H.; Vojvodic, A.; Voss, J.; Nørskov, J. K.; Abild-Pedersen, F., Effects of d-band shape on the surface reactivity of transition-metal alloys. *Phys. Rev. B* **2014**, 89 (11), 115114.
93. Kitchin, J. R.; Nørskov, J. K.; Barteau, M. A.; Chen, J. G., Role of Strain and Ligand Effects in the Modification of the Electronic and Chemical Properties of Bimetallic Surfaces. *Phys. Rev. Lett.* **2004**, 93 (15), 156801.
94. Hammer, B.; Morikawa, Y.; Nørskov, J. K., CO Chemisorption at Metal Surfaces and Overlayers. *Phys. Rev. Lett.* **1996**, 76 (12), 2141-2144.
95. Freund, H.-J.; Kuhlenbeck, H.; Libuda, J.; Rupprechter, G.; Bäumer, M.; Hamann, H., Bridging the pressure and materials gaps between catalysis and surface science: clean and modified oxide surfaces. *Top. Catal.* **2001**, 15 (2), 201-209.
96. Yu, W.; Porosoff, M. D.; Chen, J. G., Review of Pt-Based Bimetallic Catalysis: From Model Surfaces to Supported Catalysts. *Chem. Rev.* **2012**, 112 (11), 5780-5817.
97. Park, J. Y.; Somorjai, G. A., Bridging Materials and Pressure Gaps in Surface Science and Heterogeneous Catalysis. In *Current Trends of Surface Science and Catalysis*, Park, J. Y., Ed. Springer New York: New York, NY, 2014; pp 3-17.
98. Oosterbeek, H., Bridging the pressure and material gap in heterogeneous catalysis: cobalt Fischer-Tropsch catalysts from surface science to industrial application. *Phys. Chem. Chem. Phys.* **2007**, 9 (27), 3570-3576.

99. Topsøe, H., Developments in operando studies and in-situ characterization of heterogeneous catalysts. *J. Catal.* **2003**, *216* (1–2), 155-164.
100. Tao, F.; Crozier, P. A., Atomic-Scale Observations of Catalyst Structures under Reaction Conditions and during Catalysis. *Chem. Rev.* **2016**, *116* (6), 3487-3539.
101. Baumer, M.; Libuda, J.; Neyman, K. M.; Rosch, N.; Rupprechter, G.; Freund, H.-J., Adsorption and reaction of methanol on supported palladium catalysts: microscopic-level studies from ultrahigh vacuum to ambient pressure conditions. *Phys. Chem. Chem. Phys.* **2007**, *9* (27), 3541-3558.
102. Weckhuysen, B. M., Determining the active site in a catalytic process: Operando spectroscopy is more than a buzzword. *Phys. Chem. Chem. Phys.* **2003**, *5* (20), 4351-4360.
103. Frenkel, A. I.; Rodriguez, J. A.; Chen, J. G., Synchrotron Techniques for In-situ Catalytic Studies: Capabilities, Challenges, and Opportunities. *ACS Catal.* **2012**, *2* (11), 2269-2280.
104. Yang, J. C.; Small, M. W.; Grieshaber, R. V.; Nuzzo, R. G., Recent developments and applications of electron microscopy to heterogeneous catalysis. *Chem. Soc. Rev.* **2012**, *41* (24), 8179-8194.
105. Alayoglu, S.; Krier, J. M.; Michalak, W. D.; Zhu, Z.; Gross, E.; Somorjai, G. A., In-situ Surface and Reaction Probe Studies with Model Nanoparticle Catalysts. *ACS Catal.* **2012**, *2* (11), 2250-2258.
106. Tao, F., Synthesis, catalysis, surface chemistry and structure of bimetallic nanocatalysts. *Chem. Soc. Rev.* **2012**, *41* (24), 7977-7979.
107. Tao, F., Design of an in-house ambient pressure AP-XPS using a bench-top X-ray source and the surface chemistry of ceria under reaction conditions. *Chem. Commun.* **2012**, *48* (32), 3812-3814.
108. Roy, K.; Vinod, C. P.; Gopinath, C. S., Design and Performance Aspects of a Custom-Built Ambient Pressure Photoelectron Spectrometer toward Bridging the Pressure Gap: Oxidation of Cu, Ag, and Au Surfaces at 1 mbar O₂ Pressure. *J. Phys. Chem. C* **2013**, *117* (9), 4717-4726.
109. Su, D. S.; Zhang, B.; Schlögl, R., Electron Microscopy of Solid Catalysts—Transforming from a Challenge to a Toolbox. *Chem. Rev.* **2015**, *115* (8), 2818-2882.
110. Tao, F.; Tang, D.; Salmeron, M.; Somorjai, G. A., A new scanning tunneling microscope reactor used for high-pressure and high-temperature catalysis studies. *Rev. Sci. Instrum.* **2008**, *79* (8), 084101.
111. Oezaslan, M.; Hasché, F.; Strasser, P., In-situ Observation of Bimetallic Alloy Nanoparticle Formation and Growth Using High-Temperature XRD. *Chem. Mater.* **2011**, *23* (8), 2159-2165.
112. Tao, F.; Grass, M. E.; Zhang, Y.; Butcher, D. R.; Renzas, J. R.; Liu, Z.; Chung, J. Y.; Mun, B. S.; Salmeron, M.; Somorjai, G. A., Reaction-Driven Restructuring of Rh-Pd and Pt-Pd Core-Shell Nanoparticles. *Science* **2008**, *322* (5903), 932-934.
113. Bonifacio, C. S.; Carenco, S.; Wu, C. H.; House, S. D.; Bluhm, H.; Yang, J. C., Thermal Stability of Core-Shell Nanoparticles: A Combined in-situ Study by XPS and TEM. *Chem. Mater.* **2015**, *27* (20), 6960-6968.
114. Tsuji, M.; Yamaguchi, D.; Matsunaga, M.; Ikeda, K., Epitaxial Growth of Au@Ni Core-Shell Nanocrystals Prepared Using a Two-Step Reduction Method. *Cryst. Growth & Des.* **2011**, *11* (5), 1995-2005.
115. Jin, M.; Zhang, H.; Wang, J.; Zhong, X.; Lu, N.; Li, Z.; Xie, Z.; Kim, M. J.; Xia, Y., Copper Can Still Be Epitaxially Deposited on Palladium Nanocrystals To Generate Core-Shell Nanocubes Despite Their Large Lattice Mismatch. *ACS Nano* **2012**, *6* (3), 2566-2573.
116. Hultgren, R. R.; Metals, A. S. f., *Selected Values of the Thermodynamic Properties of*

Binary Alloys. American Society for Metals: 1973.

117. Kulkarni, G. U.; Vinod, C. P., Diverse reactivity patterns observed in the interaction of oxygen with nickel deposited on gold and tungsten surfaces. *Appl. Surf. Sci.* **1997**, *115* (4), 336-341.
118. Leon, C. C.; Lee, J.-G.; Ceyer, S. T., Oxygen Adsorption on Au–Ni(111) Surface Alloys. *J. Phys. Chem. C* **2014**.
119. Santra, A. K.; Rao, C. N. R., Surface alloy formation in Pd/Ag, Cu/Au and Ni/Au bimetallic overlayers. *Appl. Surf. Sci.* **1995**, *84* (4), 347-350.
120. Lahr, D. L.; Ceyer, S. T., Catalyzed CO Oxidation at 70 K on an Extended Au/Ni Surface Alloy. *J. Am. Chem. Soc.* **2006**, *128* (6), 1800-1801.
121. Knudsen, J.; Merte, L. R.; Peng, G.; Vang, R. T.; Resta, A.; Lægsgaard, E.; Andersen, J. N.; Mavrikakis, M.; Besenbacher, F., Low-Temperature CO Oxidation on Ni(111) and on a Au/Ni(111) Surface Alloy. *ACS Nano* **2010**, *4* (8), 4380-4387.
122. Alayoglu, S.; Nilekar, A. U.; Mavrikakis, M.; Eichhorn, B., Ru-Pt core-shell nanoparticles for preferential oxidation of carbon monoxide in hydrogen. *Nat. Mater.* **2008**, *7* (4), 333-338.
123. Daniel, M.-C.; Astruc, D., Gold Nanoparticles: Assembly, Supramolecular Chemistry, Quantum-Size-Related Properties, and Applications toward Biology, Catalysis, and Nanotechnology. *Chem. Rev.* **2004**, *104* (1), 293-346.
124. Yeh, Y.-C.; Czeran, B.; Rotello, V. M., Gold nanoparticles: preparation, properties, and applications in bionanotechnology. *Nanoscale* **2012**, *4* (6), 1871-1880.
125. Zhao, P.; Li, N.; Astruc, D., State of the art in gold nanoparticle synthesis. *Coord. Chem. Rev.* **2013**, *257* (3–4), 638-665.
126. Brust, M.; Fink, J.; Bethell, D.; Schiffrin, D. J.; Kiely, C., Synthesis and reactions of functionalised gold nanoparticles. *J. Chem. Soc., Chem. Commun.* **1995**, (16), 1655-1656.
127. Tao, A. R.; Habas, S.; Yang, P., Shape control of colloidal metal nanocrystals. *small* **2008**, *4* (3), 310-325.
128. Wang, W.; Banerjee, S.; Jia, S.; Steigerwald, M. L.; Herman, I. P., Ligand Control of Growth, Morphology, and Capping Structure of Colloidal CdSe Nanorods. *Chem. Mater.* **2007**, *19* (10), 2573-2580.
129. Watzky, M. A.; Finke, R. G., Transition Metal Nanocluster Formation Kinetic and Mechanistic Studies. A New Mechanism When Hydrogen Is the Reductant: Slow, Continuous Nucleation and Fast Autocatalytic Surface Growth. *J. Am. Chem. Soc.* **1997**, *119* (43), 10382-10400.
130. Jana, N. R.; Gearheart, L.; Murphy, C. J., Seed-mediated growth approach for shape-controlled synthesis of spheroidal and rod-like gold nanoparticles using a surfactant template. *Adv. Mater.* **2001**, *13* (18), 1389.
131. Wu, S.-H.; Chen, D.-H., Synthesis and characterization of nickel nanoparticles by hydrazine reduction in ethylene glycol. *J. Colloid Interface Sci.* **2003**, *259* (2), 282-286.
132. Jana, N. R.; Gearheart, L.; Murphy, C. J., Seed-Mediated Growth Approach for Shape-Controlled Synthesis of Spheroidal and Rod-like Gold Nanoparticles Using a Surfactant Template. *Adv. Mater.* **2001**, *13* (18), 1389-1393.
133. Ji, X.; Song, X.; Li, J.; Bai, Y.; Yang, W.; Peng, X., Size Control of Gold Nanocrystals in Citrate Reduction: The Third Role of Citrate. *J. Am. Chem. Soc.* **2007**, *129* (45), 13939-13948.
134. Herricks, T.; Chen, J.; Xia, Y., Polyol Synthesis of Platinum Nanoparticles: Control of Morphology with Sodium Nitrate. *Nano Lett.* **2004**, *4* (12), 2367-2371.
135. Mourdikoudis, S.; Liz-Marzán, L. M., Oleylamine in Nanoparticle Synthesis. *Chem. Mater.* **2013**, *25* (9), 1465-1476.

136. Peng, L.; Ringe, E.; Van Duyne, R. P.; Marks, L. D., Segregation in bimetallic nanoparticles. *Phys. Chem. Chem. Phys.* **2015**, *17* (42), 27940-27951.
137. Liao, H.; Fisher, A.; Xu, Z. J., Surface Segregation in Bimetallic Nanoparticles: A Critical Issue in Electrocatalyst Engineering. *Small* **2015**, *11* (27), 3221-3246.
138. Calvo, F., Thermodynamics of nanoalloys. *Phys. Chem Chem. Phys.* **2015**, *17* (42), 27922-27939.
139. Bhattarai, N.; Casillas, G.; Ponce, A.; Jose-Yacaman, M., Strain-release mechanisms in bimetallic core-shell nanoparticles as revealed by Cs-corrected STEM. *Surf. Sci.* **2013**, *609* (0), 161-166.
140. Wu, J.; Li, P.; Pan, Y.-T.; Warren, S.; Yin, X.; Yang, H., Surface lattice-engineered bimetallic nanoparticles and their catalytic properties. *Chem. Soc. Rev.* **2012**, *41* (24), 8066-8074.
141. Brune, H.; Kern, K., Chapter 5 Heteroepitaxial metal growth: the effects of strain. In *The Chemical Physics of Solid Surfaces*, King, D. A.; Woodruff, D. P., Eds. Elsevier: 1997; Vol. Volume 8, pp 149-206.
142. Wang, D.; Li, Y., Bimetallic Nanocrystals: Liquid-Phase Synthesis and Catalytic Applications. *Adv. Mater.* **2011**, *23* (9), 1044-1060.
143. He, W.; Wu, X.; Liu, J.; Hu, X.; Zhang, K.; Hou, S.; Zhou, W.; Xie, S., Design of AgM Bimetallic Alloy Nanostructures (M = Au, Pd, Pt) with Tunable Morphology and Peroxidase-Like Activity. *Chem. Mater.* **2010**, *22* (9), 2988-2994.
144. Serpell, C. J.; Cookson, J.; Ozkaya, D.; Beer, P. D., Core@shell bimetallic nanoparticle synthesis via anion coordination. *Nat. Chem.* **2011**, *3* (6), 478-483.
145. Hou, P.; Liu, H.; Li, J.; Yang, J., One-pot synthesis of noble metal nanoparticles with a core-shell construction. *CrystEngComm* **2015**, *17* (8), 1826-1832.
146. Yamauchi, T.; Tsukahara, Y.; Yamada, K.; Sakata, T.; Wada, Y., Nucleation and Growth of Magnetic Ni-Co (Core-Shell) Nanoparticles in a One-Pot Reaction under Microwave Irradiation. *Chem. Mater.* **2011**, *23* (1), 75-84.
147. Mizukoshi, Y.; Fujimoto, T.; Nagata, Y.; Oshima, R.; Maeda, Y., Characterization and Catalytic Activity of Core-Shell Structured Gold/Palladium Bimetallic Nanoparticles Synthesized by the Sonochemical Method. *J. Phys. Chem. B* **2000**, *104* (25), 6028-6032.
148. Mallik, K.; Mandal, M.; Pradhan, N.; Pal, T., Seed Mediated Formation of Bimetallic Nanoparticles by UV Irradiation: A Photochemical Approach for the Preparation of "Core-Shell" Type Structures. *Nano Lett.* **2001**, *1* (6), 319-322.
149. Huizhang, G.; Yuanzhi, C.; Xiaozhen, C.; Ruitao, W.; Guang-Hui, Y.; Dong-Liang, P., Facile synthesis of near-monodisperse Ag@Ni core-shell nanoparticles and their application for catalytic generation of hydrogen. *Nanotechnology* **2011**, *22* (19), 195604.
150. Fan, F.-R.; Liu, D.-Y.; Wu, Y.-F.; Duan, S.; Xie, Z.-X.; Jiang, Z.-Y.; Tian, Z.-Q., Epitaxial Growth of Heterogeneous Metal Nanocrystals: From Gold Nano-octahedra to Palladium and Silver Nanocubes. *J. Am. Chem. Soc.* **2008**, *130* (22), 6949-6951.
151. Lu, C.-L.; Prasad, K. S.; Wu, H.-L.; Ho, J.-a. A.; Huang, M. H., Au Nanocube-Directed Fabrication of Au-Pd Core-Shell Nanocrystals with Tetrahedral, Concave Octahedral, and Octahedral Structures and Their Electrocatalytic Activity. *J. Am. Chem. Soc.* **2010**, *132* (41), 14546-14553.
152. Tsao, Y.-C.; Rej, S.; Chiu, C.-Y.; Huang, M. H., Aqueous Phase Synthesis of Au-Ag Core-Shell Nanocrystals with Tunable Shapes and Their Optical and Catalytic Properties. *J. Am. Chem. Soc.* **2014**, *136* (1), 396-404.
153. Jing, H.; Wang, H., Structural Evolution of Ag-Pd Bimetallic Nanoparticles through Controlled Galvanic Replacement: Effects of Mild Reducing Agents. *Chem. Mater.* **2015**, *27* (6), 2172-2180.

154. She, H.; Chen, Y.; Chen, X.; Zhang, K.; Wang, Z.; Peng, D.-L., Structure, optical and magnetic properties of Ni@Au and Au@Ni nanoparticles synthesized via non-aqueous approaches. *J. Mater. Chem.* **2012**, *22* (6), 2757-2765.
155. Chen, Y.; Peng, D.-L.; Lin, D.; Luo, X., Preparation and magnetic properties of nickel nanoparticles via the thermal decomposition of nickel organometallic precursor in alkylamines. *Nanotechnology* **2007**, *18* (50), 505703.
156. Huang, L.; Shan, A.; Li, Z.; Chen, C.; Wang, R., Phase formation, magnetic and optical properties of epitaxially grown icosahedral Au@Ni nanoparticles with ultrathin shells. *CrystEngComm* **2013**, *15* (13), 2527-2531.
157. Zhang, H.; Ding, J.; Chow, G.; Ran, M.; Yi, J., Engineering Magnetic Properties of Ni Nanoparticles by Non-Magnetic Cores. *Chem. Mater.* **2009**, *21* (21), 5222-5228.
158. Ahmadi, M.; Behafarid, F.; Cui, C.; Strasser, P.; Cuenya, B. R., Long-Range Segregation Phenomena in Shape-Selected Bimetallic Nanoparticles: Chemical State Effects. *ACS Nano* **2013**, *7* (10), 9195-9204.
159. Wu, Y.; Wang, D.; Li, Y., Nanocrystals from solutions: catalysts. *Chem. Soc. Rev.* **2014**, *43* (7), 2112-2124.
160. Singh, A. K.; Xu, Q., Synergistic Catalysis over Bimetallic Alloy Nanoparticles. *ChemCatChem* **2013**, *5* (3), 652-676.
161. Peng, X.; Pan, Q.; Rempel, G. L., Bimetallic dendrimer-encapsulated nanoparticles as catalysts: a review of the research advances. *Chem. Soc. Rev.* **2008**, *37* (8), 1619-1628.
162. Wei, Z.; Sun, J.; Li, Y.; Datye, A. K.; Wang, Y., Bimetallic catalysts for hydrogen generation. *Chem. Soc. Rev.* **2012**, *41* (24), 7994-8008.
163. Jiang, H.-L.; Akita, T.; Xu, Q., A one-pot protocol for synthesis of non-noble metal-based core-shell nanoparticles under ambient conditions: toward highly active and cost-effective catalysts for hydrolytic dehydrogenation of NH_3BH_3 . *Chem. Commun.* **2011**, *47* (39), 10999-11001.
164. Yan, J.-M.; Zhang, X.-B.; Akita, T.; Haruta, M.; Xu, Q., One-Step Seeding Growth of Magnetically Recyclable Au@Co Core-Shell Nanoparticles: Highly Efficient Catalyst for Hydrolytic Dehydrogenation of Ammonia Borane. *J. Am. Chem. Soc.* **2010**, *132* (15), 5326-5327.
165. Henning, A. M.; Watt, J.; Miedziak, P. J.; Cheong, S.; Santonastaso, M.; Song, M.; Takeda, Y.; Kirkland, A. I.; Taylor, S. H.; Tilley, R. D., Gold-Palladium Core-Shell Nanocrystals with Size and Shape Control Optimized for Catalytic Performance. *Angew. Chem. Int. Ed.* **2013**, *52* (5), 1477-1480.
166. Tedsree, K.; Li, T.; Jones, S.; Chan, C. W. A.; Yu, K. M. K.; Bagot, P. A. J.; Marquis, E. A.; Smith, G. D. W.; Tsang, S. C. E., Hydrogen production from formic acid decomposition at room temperature using a Ag-Pd core-shell nanocatalyst. *Nat. Nano* **2011**, *6* (5), 302-307.
167. Min, B. K.; Friend, C. M., Heterogeneous gold-based catalysis for green chemistry: low-temperature CO oxidation and propene oxidation. *Chem. Rev.* **2007**, *107* (6), 2709-2724.
168. Alonso, F.; Riente, P.; Yus, M., Nickel Nanoparticles in Hydrogen Transfer Reactions. *Acc. Chem. Res.* **2011**, *44* (5), 379-391.
169. Jiang, H.-L.; Umegaki, T.; Akita, T.; Zhang, X.-B.; Haruta, M.; Xu, Q., Bimetallic Au-Ni Nanoparticles Embedded in SiO_2 Nanospheres: Synergetic Catalysis in Hydrolytic Dehydrogenation of Ammonia Borane. *Chem. - Eur. J.* **2010**, *16* (10), 3132-3137.
170. Yan, Z.; Goodman, D. W., Silica-Supported Au-Ni Catalysts for the Dehydrogenation of Propane. *Catal. Lett.* **2012**, *142* (5), 517-520.
171. Sarkar, S.; Sinha, A. K.; Pradhan, M.; Basu, M.; Negishi, Y.; Pal, T., Redox Transmetalation of Prickly Nickel Nanowires for Morphology Controlled Hierarchical Synthesis of Nickel/Gold Nanostructures for Enhanced Catalytic Activity and SERS

- Responsive Functional Material. *J. Phys. Chem. C* **2010**, *115* (5), 1659-1673.
172. Norskov, J. K.; Bligaard, T.; Rossmeisl, J.; Christensen, C. H., Towards the computational design of solid catalysts. *Nat. Chem.* **2009**, *1* (1), 37-46.
173. Chin, Y.-H.; King, D. L.; Roh, H.-S.; Wang, Y.; Heald, S. M., Structure and reactivity investigations on supported bimetallic AuNi catalysts used for hydrocarbon steam reforming. *J. Catal.* **2006**, *244* (2), 153-162.
174. Cárdenas-Lizana, F.; Gómez-Quero, S.; Jacobs, G.; Ji, Y.; Davis, B. H.; Kiwi-Minsker, L.; Keane, M. A., Alumina Supported Au–Ni: Surface Synergism in the Gas Phase Hydrogenation of Nitro-Compounds. *J. Phys. Chem. C* **2012**, *116* (20), 11166-11180.
175. Yuan, G.; Louis, C.; Delannoy, L.; Keane, M. A., Silica- and titania-supported Ni–Au: Application in catalytic hydrodechlorination. *J. Catal.* **2007**, *247* (2), 256-268.
176. Sharma, R.; Chee, S.-W.; Herzing, A.; Miranda, R.; Rez, P., Evaluation of the Role of Au in Improving Catalytic Activity of Ni Nanoparticles for the Formation of One-Dimensional Carbon Nanostructures. *Nano Lett.* **2011**, *11* (6), 2464-2471.
177. Salmeron, M.; Schlögl, R., Ambient pressure photoelectron spectroscopy: A new tool for surface science and nanotechnology. *Surf. Sci. Rep.* **2008**, *63* (4), 169-199.
178. Sehested, J., Four challenges for nickel steam-reforming catalysts. *Catal. Today* **2006**, *111* (1–2), 103-110.
179. Bengaard, H. S.; Nørskov, J. K.; Sehested, J.; Clausen, B. S.; Nielsen, L. P.; Molenbroek, A. M.; Rostrup-Nielsen, J. R., Steam Reforming and Graphite Formation on Ni Catalysts. *J. Catal.* **2002**, *209* (2), 365-384.
180. Trimm, D. L., Coke formation and minimisation during steam reforming reactions. *Catal. Today* **1997**, *37* (3), 233-238.

Chapter 2 (2A, 2B & 2C)

Organic Phase Synthesis and Catalytic Activity Results of Au@Ni Core-shell Nanoparticles

➤ Outline of the chapter

- ✓ Synthesis of Au@Ni core-shell nanostructures in non-aqueous medium
- ✓ Magnetically diverse Au@Ni nanoparticles (Au@Ni_{FCC} & Au@Ni_{HCP})
- ✓ Oxidation resistance of core-shell nanoparticles
- ✓ Synergistic effect - tuning of nickel shell thickness for optimum activity
- ✓ Enhanced catalytic activity for nitro group reduction of PNP & PNTP
- ✓ Selective hydrogenation of phenyl acetylene to styrene and ethylbenzene

This chapter is adapted from the following publications:

1. Vysakh, A. B.; Raj, G. K.; Joy, P. A.; Vinod, C. P., Synthesis and reactivity of magnetically diverse Au@Ni core-shell nanostructures. *Particle & Particle Systems Characterization* 2014, 31 (2), 236-244.
2. Vysakh, A. B.; Babu, C. L.; Vinod, C. P., Demonstration of synergistic catalysis in Au@Ni bimetallic core-shell nanostructures. *The Journal of Physical Chemistry C* 2015, 119 (15), 8138-8146.
3. Vysakh, A. B.; Lazar, A.; Yadukiran, V.; Singh, A. P.; Vinod, C. P., Phenylacetylene hydrogenation on Au@Ni bimetallic core-shell nanoparticles synthesized under mild conditions. *Catalysis Science & Technology* 2016, 6 (3), 708-712.
4. Vysakh, A. B.; Yadukiran, V.; Lazar, A.; Singh, A. P.; Vinod, C. P., Synthesis of Au@Ni bimetallic core-shell nanoparticle and nanochains in soyabean oil and their catalytic hydrogenation reactions. *ChemistrySelect* 2016, 1 (2), 140-146.

Chapter 2: Organic Phase Synthesis and Catalytic Activity Results of Au@Ni Core-shell Nanoparticles

2.1 Introduction

Core-shell bimetallic nanoparticles can be synthesized through wet chemical reduction method following a sequential or simultaneous reduction strategy¹⁻³. In the case of gold (Au) and nickel (Ni), they show large difference in their reduction potential values in which gold possess higher reduction potential (positive) than nickel (negative). Hence it was found that gold undergoes reduction easily as compared to metals with less reduction potential in suitable solvents with controlled reduction kinetics (slow reducing agents)³⁻⁴. Organic phase synthesis protocol allows the synthesis of metal nanoparticles with high mono dispersity and precise size control as compared to aqueous phase methods⁵⁻⁶. Nanoparticle syntheses in organic medium using unsaturated amines and acids as solvent have been widely reported in the literature^{5, 7-8}. Since these compounds can act both as solvent and capping agent (sometimes even as reducing agent) for the nanoparticles in solution, the methods adopted till now are widely accepted for their size controlled synthesis^{6-7, 9}. For instance, solvents like long chain amines, acids or phosphines are extensively used for the shape and size selective synthesis of magnetic nanoparticles like Ni, Fe, Co and plasmonic nanostructures like gold and silver^{6, 10-12}. Oleylamine is widely accepted as a suitable organic solvent for the synthesis of metal nanoparticles¹³. It has found great application in the nanoparticle synthesis especially for highly stable colloids of magnetic nanoparticles like Ni, Co and Fe^{9, 13-14}. There are many literature reports for the effective utilization of oleylamine in nanoparticle synthesis including noble metals and non-noble metals¹³. The thermal decomposition of nickel metal salts at higher temperatures (usually above 200 °C) in oleyl amine results in Ni nanoparticles with good control over size and crystallinity⁹. She et al and Zhang et al reported the synthesis of Au@Ni core-shell nanoparticles following the thermal decomposition routes with less control over the size which goes above 10 nm¹⁵⁻¹⁶. But the precise control over the size of the core-shell nanoparticles is necessary especially for catalytic applications. To fully explore the quantum confinement effects also it is always beneficial to limit the size below 10 nm or less. From the surface science analysis of model systems, the surface modifications in bimetallic systems are effective with minimum atomic overlayers¹⁷ and hence careful designing of the

bimetallic structures is necessary with ultimate control over the shell thickness for catalytic applications¹⁸. By keeping these factors in mind for efficient catalytic application one should design a core-shell system with precise control over the overall size and shell thickness. Also the tuning of shell thickness is necessary to optimize the composition ratio and to understand the length scales of synergistic operating from the gold core¹⁸.

In the present chapter of the thesis, a one-pot reduction strategy in organic phase for the synthesis of Au@Ni bimetallic core-shell nanoparticles through various methods and their synergistic catalysis is reported. The chapter consists of three sub-divisions namely 2A, 2B and 2C, where all three sections emphasize the synthesis of Au@Ni core-shell structures employing different synthesis protocol that offers energy efficient and environmentally benign routes. All the synthesis methods adopt a non-aqueous synthesis (organic phase) approaches for achieving the Au@Ni core-shell morphology. A one-pot reduction strategy with sequential reduction method results in the core-shell morphology. Au@Ni core-shell nanoparticles synthesized through various methods are thoroughly characterised by using UV-Vis spectroscopy, XRD, XPS, TEM and SQUID-VSM to establish the physical and chemical nature of the synthesized material. The synergistic catalytic properties of tailor made core-shell nanoparticles are also verified for different types of hydrogenation/reduction reactions under various temperature and pressure conditions. In the section 2A, the synthesis of Au@Ni core-shell nanoparticles are reported in an organic phase with size less than 10 nm by using oleylamine as solvent following a thermal reduction strategy. Synthesis of monometallic gold and nickel nanoparticles using oleylamine has been reported by many groups^{5, 9, 19}. Oleylamine plays several roles, as a solvent, capping agent and reducing agent in nanoparticle synthesis. Under normal conditions it can act as a very good capping agent for the nanoparticles to prevent the particle growth and to protect the inter particle agglomeration, whereas at higher temperatures it functions as both reducing agent and capping agent. The chemistry behind the oleylamine reduction of metal nanoparticles basically lies in the decomposition of metal-oleate complex formed in oleylamine¹³. Such metal complexes undergo reduction preferably at higher temperatures, depending on the reduction potential values of the metal salts; they get reduced at different temperature ranges. For nickel, the temperature range required is 200-250 °C to bring the complete reduction⁹ where as gold undergoes reduction at relatively lower temperatures but with higher sizes¹⁵. Nickel can crystallize both in FCC and HCP crystal lattices under varying reduction temperatures leading

to changes in its magnetic behaviour. The thermodynamically stable form of nickel is magnetic FCC phase which preferably forms over the metastable phase HCP which is non-magnetic. Literature reports shows the possibility of tuning the crystallization of nickel in to pure FCC, HCP and mixed forms by changing the reduction kinetics and it highly depend on the reduction temperature^{7, 9}. Hence the synthesis of magnetically diverse Au@Ni core-shell nanoparticles are reported here namely Au@Ni_{FCC} (magnetic) and Au@Ni_{HCP} (non-magnetic) with control over the size and shell thickness. Apart from demonstrating the synthetic control over the Au@Ni core-shell system, a major goal of this work is to understand the catalytic activity variation as a function of shell thickness. A major discussion part is on Au@Ni_{FCC} core-shell nanoparticles to explore and understand the extent of synergistic behaviour, because they are more stable and preferable structures of nickel for catalytic applications compared to HCP nickel. To understand the role of shell thickness and promotional effect by the core material to the surface, three different series of Au-Ni bimetallic core-shell nanoparticles were synthesized with variable shell thickness namely Au@Ni_{1:0.5}, Au@Ni_{1:1} and Au@Ni_{1:2}. To probe the role of electronic and geometric modifications on nickel by gold and its implication to real world applications, catalytic activity analysis is carried out for nitro group reduction to amino group. There is a growing interest in the discovery of a clean and green heterogeneous catalyst for the conversion of nitro group²⁰ especially in compounds like PNP, which is a refractory pollutant to the produce PAP an important intermediate in analgesic and antipyretic drugs²¹⁻²². Hence the synergistic effects is investigated by carrying out model reactions viz p-nitrophenol (PNP) and p-nitrothiophenol (PNTP) reduction reactions²³⁻²⁴. These reactions proceed without any side products and have the advantage of deriving accurate kinetic rate constant data from surface-modified catalysts for arriving at structure versus activity correlations. Meanwhile, the synthesis of aromatic amines with high selectivity towards amino group is always challenging²⁵⁻²⁶. Even though nickel is known for its exceptionally high hydrogenation activity, first row transition metals including nickel are prone to ambient oxidation which adversely affects their use in sustainable catalytic applications. In hydrogenation reactions mediated by metal catalysts in colloidal phase, the sluggish initial rate of the reaction is caused by the induction period of the catalyst²⁷. This period is used to regenerate the metallic phase of the surface that is active for the reduction reactions. The presence of surface oxide layer is unavoidable in the case of first row transition metals since they are highly reactive towards molecular oxygen even at ambient conditions and inhibit the adsorption of reactant molecules which in turn lowers the catalytic activity.

The reduction of nitro group on the metal catalyst surface follows pseudo first order kinetics in the presence of excess of the reducing agent (sodium borohydride)^{23, 28}. This helps in a straightforward demonstration of the rate kinetics and hence the activity comparison of the different catalysts. In the later stage of catalytic activity tests, nitro group reduction to amino group is carried out in the presence of thiol (-SH) moieties such as paranitrothiophenol (PNTTP) which is more challenging as the activity is poor because of the poisoning nature of S group²⁹. Recent reports indicate that such poisoning effect (strong thiol interaction) can be overcome by creating well defined structures or by making bimetallic combinations^{24, 30}. In the second part 2B of this chapter, the synthesis of Au@Ni core-shell nanoparticles at a relatively milder temperature than the ones reported in the literature is discussed¹⁶. The previous literature analysis on the synthesis of Au-Ni or Ni nanoparticles using oleylamine as the solvent shows that the reduction of nickel ions take place above 200 °C resulting in the formation of nickel nanoparticles^{9, 15}. The synthesis method adopted in the chapter 2A, is modified to synthesis the core-shell nanoparticles at much lower temperature to make it more energy efficient way. Chapter 2B deals with a one-pot two-step sequential reduction strategy, but avoiding the thermal reduction of nickel precursor. Instead of thermal reduction, an external reducing agent hydrazine hydrate (N₂H₄.H₂O) has been employed to reduce the nickel ions. Reduction of nickel ions using hydrazine is well known especially in aqueous and polyol medium due to the compatibility with the solvent medium³¹⁻³³. Also hydrazine requires an alkaline medium to boost the reduction of metal ions which is generally provided by the sodium/potassium hydroxide combination. With this method, Au@Ni core-shell nanoparticles ranging from 15-20 nm with control over the nickel shell thickness (approximately 2 nm) have been achieved at milder temperatures so far reported in oleyl amine based solvents. They are demonstrated for high activity for the phenylacetylene (P.A) hydrogenation reactions. Styrene is an industrially important monomer for the polymerisation reactions to form many valuable compounds³⁴. The formation of ethylbenzene from P.A demonstrates the activity of the catalysts for the complete hydrogenation of unsaturated compounds. The synergistic effect once again plays the key role in activity and selectivity enhancement of the Au@Ni core-shell catalyst which is having an optimum nickel shell thickness over the gold core.

Even though the commonly used compounds like oleylamine¹⁴, oleic acid³⁵, octadecyl amine³⁶, etc are efficient, their cost, availability and hazardous effects, which was excellently reviewed recently³⁷, has prompted the search for alternative green surfactants and solvents.

The criteria for choosing a solvent medium in nanoparticle synthesis are also important and depend on many parameters. It should protect the nanoparticles from agglomeration by acting as capping agent apart from providing a facile medium for a controlled growth of nanoparticles with specific size and shape. Soyabean oil which is rich in long chain unsaturated fatty acid content could potentially be a suitable eco friendly candidate for replacing harmful organic solvents³⁷. The edible nature of the soyabean oil also adds to the advantage of safety and handling issues encountered by other hazardous solvents used in nanoparticle synthesis. In the sections 2A and 2B, Au@Ni bimetallic nanoparticles synthesis by using oleylamine with a good control over nickel shell thickness and showing synergistic catalysis is demonstrated. And section 2C demonstrates soyabean oil for the synthesis of Au@Ni core-shell nanostructures with the aid of a reducing agent thereby avoiding high temperature reduction methods previously reported¹⁵⁻¹⁶. With the help of an external reducing agent the reduction temperature is drastically reduced (from 210 °C to 70 °C) resulting in the successful synthesis of Au@Ni core-shell structures. This section also shows that using the surfactant CTAB in the medium one can obtain inter connected core-shell Au@Ni nanochains. The synthesis strategy demonstrated for Au@Ni core-shell morphology is in eco-friendly soyabean oil solvent and in addition to that by slightly changing the reaction parameters Au@Ni nanochains are generated at mild temperature conditions. Both these nanostructures are further demonstrated to synergistically catalyse the selective hydrogenation of phenylacetylene (P.A).

Chapter 2A: Synthesis of Magnetically Diverse Au@Ni Core-shell Nanoparticles by Using Thermal Reduction: Oxidation Resistance Analysis and Catalytic Application for Nitro (-NO₂) Group Reductions

2A.1 Experimental Section

Metal precursors, hydrogen tetrachloroaurate trihydrate [HAuCl₄.3H₂O] and nickel acetylacetonate [Ni(acac)₂] along with other reagents oleylamine, sodium borohydride [NaBH₄] and 1-octadecene were purchased from Sigma Aldrich [Germany] and used as received. Triphenylphosphine [TPP], ethanol, hexane, p-nitrophenol [PNP] and p-nitrothiophenol [PNTP] were purchased from Merck.

Synthesis of Magnetic Au@Ni Core-shell (Au@Ni_{FCC}) Nanoparticles

In a typical synthesis, Ni(acac)₂ [0.2 mmol] is added to oleylamine [6 ml] which is preheated to 45 °C. The gold precursor, HAuCl₄.3H₂O [0.1 mmol] was dissolved in a mixture of oleylamine [2 ml] and 1-octadecene [1 ml] and transferred into the nickel-oleylamine solution with vigorous stirring. To the resultant solution NaBH₄ [0.5 mmol] is added with a slow stirring rate of 200 rpm and stirring continued for 5 minutes. The solution turned to wine red colour quickly which implies the reduction of gold (III) ions to gold nanoparticles immediately after the addition of sodiumborohydride. In the later stage, gold seeds act as the nucleation sites and the nickel ions undergo thermal reduction on the gold surface by the decomposition of nickel-oleylamine complex at high temperatures. Now the entire reaction medium is heated to 210 °C with a ramping rate of 5 °C/minute to assure the crystallization of reduced nickel nanoparticles in to FCC crystal structure. At 210 °C, TPP [0.2 mmol] is added to the heated solution which immediately brings about the reduction of nickel ions resulting in a black colloidal solution. The temperature retained at 210 °C for 20 minutes for complete reduction of nickel ions to get magnetic core-shell Au@Ni_{FCC} nanoparticles. The reaction setup is cooled down to room temperature. The thickness of the nickel shell can be increased by changing the nickel precursor concentration keeping rest of the conditions same. The magnetic core-shell nanoparticles are recovered with the help of a magnet, washed with ethanol-hexane mixture thoroughly to remove excess of capping agents and redispersed in hexane for further characterizations.

Synthesis of Non-magnetic Au@Ni Core-shell (Au@Ni_{HCP}) Nanoparticles

The synthesis of non-magnetic Au@Ni core-shell nanoparticles (Au@Ni_{HCP}) carried out in a similar procedure as described in the previous section for Au@Ni_{FCC} core-shell nanoparticles with minor modifications. Here in the case of Au@Ni_{HCP} nanoparticles 1-octadecene [2 ml] was added to the mixture of Ni(acac)₂ [0.2 mmol] and oleylamine [6 ml] in the initial stage itself. Then the reduction of HAuCl₄.3H₂O was carried out like before. After the formation of gold nanoparticles, the entire reaction medium is heated to 240 °C with a ramping rate of 15 °C/minute (instead of 210 °C applied in the case of Au@Ni_{FCC}) to assure the crystallization of reduced nickel nanoparticles in to HCP crystal structure. At 240 °C, TPP [0.2 mmol] was added to the solution as reported in the previous section to form a black colloidal solution. The temperature retained at 240 °C for 20 minutes for the complete reduction of nickel ions in to the desired Au@Ni core-shell system. Magnetic separations of bimetallic nanoparticles are not possible since they show nonmagnetic behaviour. The colloidal solution is centrifuged at 8000 rpm and washed thoroughly with a mixture of ethanol and hexane, then redispersed in hexane.

Synthesis of Magnetic Au@Ni Core-shell Nanoparticles with Varying Shell Thickness

The synthesis procedure for obtaining magnetic Au@Ni core-shell (Au@Ni_{FCC}) nanoparticles mentioned in the preceding experimental sections was modified to obtain Au@Ni core-shell nanoparticles with varying nickel shell thickness around the gold core of approximately 6-8 nm. The synthesis strategy was optimized by changing the metal precursor ratios (nickel to gold) in order to get core-shell nanoparticles with various nickel shell thickness starting from the same gold seed. The size of gold core was kept same in all the series of magnetic Au@Ni catalysts for a better understanding of promotional effect of core to the shell material. In a typical synthesis, both the metal precursors were weighed accurately with desired mole ratio and transferred to a round bottom flask containing a mixture of oleylamine [8 ml] and 1-octadecene [2 ml] which is preheated to 45 °C. The resulting solution was stirred well for 10 minutes for good dispersion, followed by the addition of NaBH₄ [0.5 mmol]. An immediate colour change from yellowish brown to wine red colour was occurred which indicate the formation of small gold seeds. The resultant colloidal solution was then heated to 210 °C with a ramping rate of 5 °C/minute and at this temperature TPP [0.2 mmol] was added to the solution to facilitate the thermal reduction of nickel on the surface of preformed gold seeds. At this stage the colour of colloidal solution changed from wine red to

black which indicated the successful generation of core-shell nanoparticles. The temperature was kept at 210 °C for 20 minutes for complete reduction of nickel ions. The whole setup was then cooled down to room temperature and final core-shell catalysts were easily separated by using an external magnet. These core-shell nanoparticles were thoroughly washed with hexane and ethanol and then analyzed for the catalyst activity tests. Three series of core-shell catalysts were prepared namely Au@Ni_{1:0.5}, Au@Ni_{1:1} and Au@Ni_{1:2}. The metal precursor ratio used for gold to nickel were 0.1 mmol:0.2 mmol, 0.1 mmol:0.4 mmol and 0.1 mmol:0.8 mmol [HAuCl₄.3H₂O: Ni(acac)₂] respectively for the above mentioned catalysts.

Reduction of p-nitrophenol Catalyzed by Magnetic and Non-magnetic Au@Ni Core-shell (Au@Ni_{FCC} and Au@Ni_{HCP}) Nanoparticles

In the first stage of catalytic activity analysis, Au@Ni_{FCC} and Au@Ni_{HCP} core-shell nanoparticles were checked for the nitro group reduction in PNP to form PAP (paraaminophenol). Reduction of 4-NP (PNP) was carried out by using both magnetic and non-magnetic core-shell catalysts (Au@Ni_{FCC} and Au@Ni_{HCP}) in a well-stoppered quartz cuvette under ambient conditions. 3 mL aqueous solution of 10⁻⁴M 4-NP was added to the cuvette followed by the addition of 0.5 mL of 0.1M aqueous solution of NaBH₄. The immediate colour change of the solution from a pale yellow to deep yellow colour indicates the formation of nitrophenolate ion in the presence of NaBH₄. Then the catalyst (1 mg) was introduced to the resultant solution, and the reaction was spectrophotometrically monitored with the help of a UV-Visible spectrophotometer. The entire reaction conditions were repeated with other series of catalysts which were preheated at various high temperatures and reactions monitored under ambient conditions. The magnetically recoverable catalysts are easily separated after the completion of the reaction and checked for recyclability.

Reduction of p-nitrophenol (PNP) and p-nitrothiophenol (PNTTP) by Magnetic Au@Ni Nanoparticles with Varying Nickel Shell Thickness

Reduction of both nitrophenol and nitrothiophenol were carried out by using the three series of magnetic Au@Ni core-shell catalysts with varying nickel shell thickness (Au@Ni_{1:0.5}, Au@Ni_{1:1} and Au@Ni_{1:2}) and their rate curves are compared with the activity of bare gold and nickel nanoparticles. All the nitro group reduction reactions were done in a well-stoppered quartz cuvette under ambient conditions as described in the previous section. In the case of PNTTP reduction, the reactions were carried out in a similar way as that of PNP

by using the same concentration PNTTP solution. The fixed amounts of catalysts (1 mg) were introduced to the cuvette which contained 3 mL aqueous solution of 10^{-4} M 4-NTP and 0.5 mL of 0.1M aqueous solution of NaBH_4 . The entire reaction was repeated for the three catalysts having different shell thickness along with that of gold and nickel nanoparticles. All the magnetic Au@Ni core-shell catalysts were easily recovered from the reaction medium with the help of an external magnet and could be reused.

2A.2 Results and Discussion

2A.2.1 UV-Vis Spectroscopy Analysis of Au@Ni Core-shell Nanoparticle Formation

The schematic showing the formation of both magnetic and non-magnetic Au@Ni ($\text{Au@Ni}_{\text{FCC}}$ and $\text{Au@Ni}_{\text{HCP}}$) bimetallic nanoparticles is depicted in Figure 2A.1. The in-situ generation of gold nanoparticle seeds in a single pot containing nickel precursor is the key to the synthesis sub 10 nm Au-Ni core-shell bimetallic nanostructures. The gold seeds formed in the first stage act as the nucleation sites for the adsorption of nickel precursor, which subsequently undergoes reduction at higher temperatures to form the bimetallic core-shell nanoparticles. The reduction of gold precursor with reducing agent NaBH_4 in oleylamine solvent, results in the formation of a wine red colour gold colloid solution. The different stages of the synthesis were monitored using UV-Vis spectroscopy by following the SPR property of gold nanoparticles. The formation of gold seeds with size below 10 nm was indicated by the UV-Vis analysis which gave a strong absorption with a peak maximum at 515 nm (Figure 2A.3a)³⁸. The thermal reduction of nickel ions on the surface of gold nanoparticles performed at higher temperatures above 200 °C and it is favoured by the addition of TPP. By slightly changing the final reduction temperature and the heating rate, a black colloidal suspension is formed, which was behaving distinctly different with an external magnet. It has been reported in the literature that kinetic and thermodynamic factors play a crucial role in the formation of stable FCC and metastable HCP crystalline phases of nickel nanoparticles^{7, 9}, one resulting in separation and sticking of the particles towards a magnet and other fairly dispersed in the solution. The progressive damping of the gold plasmon band on formation of nickel shell on the gold core is an indication of the successful generation of core-shell morphology¹⁸ in both the cases of magnetic (FCC) and non-magnetic Au@Ni nanoparticles (HCP) (Figure 2A.3a). The solvent oleylamine and 1-octadecene acts as capping agents for the Au@Ni core-shell nanoparticles.

formation of three series of magnetically active Au@Ni core-shell nanoparticles stabilized in FCC phase with different nickel shell thickness starting from the same gold core. The UV-Vis spectroscopy analysis at different stages showed the same pattern as obtained for the general synthesis of Au@Ni core-shell nanoparticles mentioned in the preceding section. During the intermediate stages of Ni encapsulation the intensity of the gold plasmon band decreased. The complete damping of the gold plasmon band, in the UV-Vis spectrum, after the reduction of nickel over the gold surface confirms the successful generation of core-shell morphology in all the three cases (Figure 2A.3b).

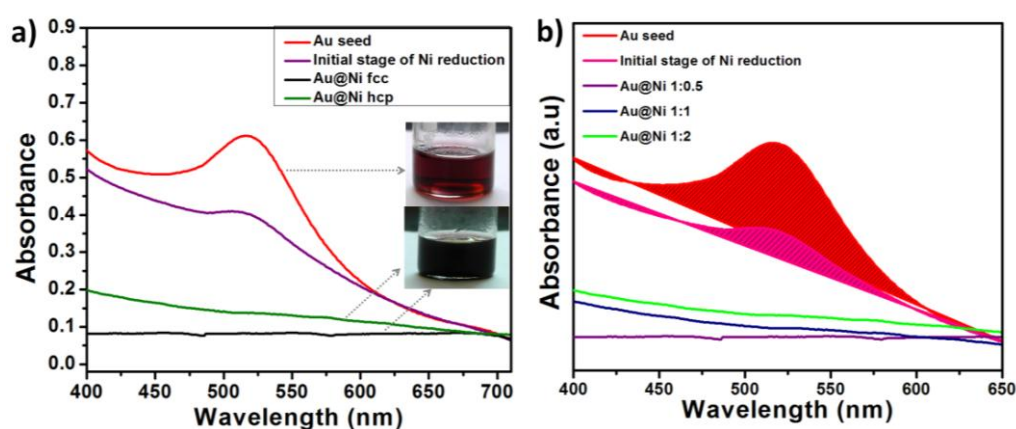


Figure 2A.3 UV-Vis spectra obtained for the preformed gold nanoparticle seeds and its sequential conversion into Au@Ni core-shell nanoparticles. (a) UV-Vis spectra during the formation of Au@Ni_{FCC} and Au@Ni_{HCP}, the inset photographs show the colour of corresponding colloidal solutions at various stages. (b) UV-Vis spectra recorded at various stages of Au@Ni core-shell nanoparticles with different nickel shell thickness.

2A.2.2 Transmission Electron Microscopy Studies (TEM)

Microscopic investigation confirmed the core-shell morphology of the bimetallic nanoparticles mainly through the lattice fringe analysis and colour contrast difference of the metals. Since the gold is a 5d transition metal and nickel exists in the 3d transition series, there is a large difference in the atomic size and d-spacing value of gold and nickel. Apart from this the heavier noble metal gold shows high contrast as compared with lighter nickel metal while imaging under transmission electron microscopy in the bright field mode. Figure 2A.4 shows the TEM and HR-TEM images of the as synthesized magnetic Au@Ni (a-c) and non-magnetic Au@Ni (d-f) nanostructures drop cast on the Cu grid. The large-area

transmission electron microscopy (TEM) image (Figure 2A.4a and d) indicates that most of the bimetallic nanoparticles are having size below 10 nm in both Au@Ni_{FCC} and Au@Ni_{HCP} core-shell nanoparticles. The HR-TEM image from one of the Au@Ni_{FCC} core-shell nanoparticle is shown in Figure 2A.4b, which shows a clear contrast difference at the center and outer surface of the nanoparticle indicating the formation of core-shell morphology. The lattice spacing measured from the core and the shell gave the standard values of Au (111) - 2.38 Å in the core and Ni (111) - 2.04 Å in the shell confirming that nickel is present as the shell and gold at the core¹⁵. The gold core size in this case was approximately 6-8 nm with a nickel shell thickness of approximately 2 nm. Similar observations are obtained in the case of Au@Ni_{HCP} core-shell nanoparticles (Figure 2A.4e) in which the core is comprised of gold whereas nickel is present at the shell with characteristic lattice fringe values and colour contrast difference. The electron diffraction pattern (FFT) in the inset of Figure 2A.4c and f shows spots corresponding to gold and nickel lattice in the bimetallic nanoparticle. Figure 2A.5 and 2A.6 corresponds to HR-TEM images of a group of nanoparticles collected from Au@Ni_{FCC} and Au@Ni_{HCP} samples respectively.

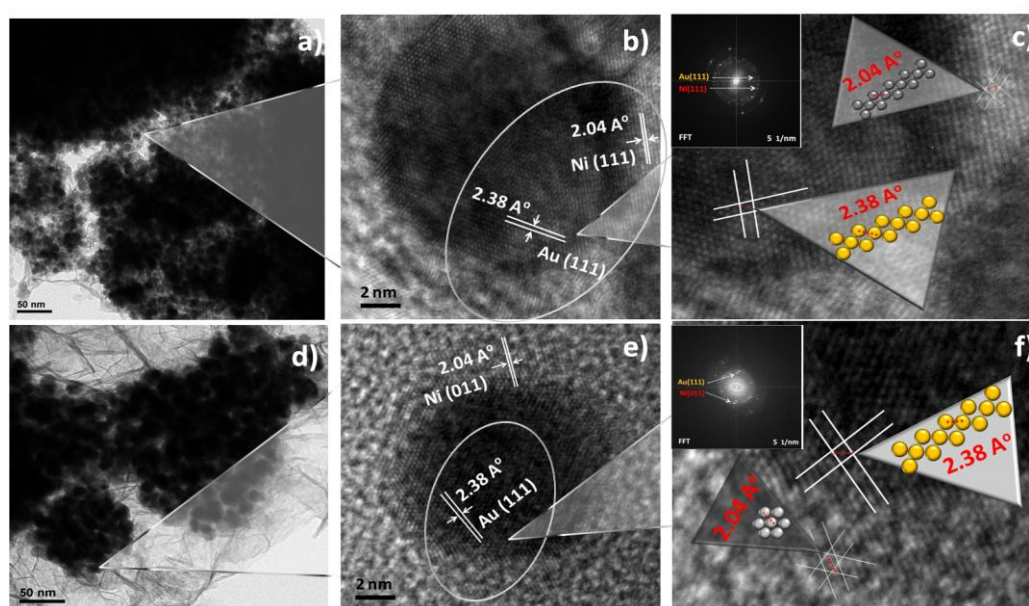


Figure 2A.4 TEM and HR-TEM images of (a-c) magnetic Au@Ni_{FCC} and (d-f) non-magnetic Au@Ni_{HCP} core-shell nanoparticles. (a,d) Large-area TEM images of Au@Ni_{FCC} and Au@Ni_{HCP} nanoparticles respectively. (b,e) HR-TEM images of a single core-shell nanoparticle of Au@Ni_{FCC} and Au@Ni_{HCP} with different lattice spacing in core and shell. High-resolution image with a schematic representation of atomic arrangement of gold and nickel lattices is shown in (c,f). Inset show the FFT pattern corresponding to Au and Ni.

In both the images, well resolved lattice fringe analysis is shown for the individual nanoparticles which are appeared in the large area TEM image to identify the core-shell structure in all the cases. It is also worth mentioning that the detailed analysis from HR-TEM images did not show evidence for NiO lattice values in both the cases³⁹. Thus, the synthesis procedure adopted here was able to create both magnetic and non-magnetic bimetallic core-shell nanostructures of sub 10 nm size with fairly good mono dispersity as revealed by the histogram analysis (Figure 2A.7).

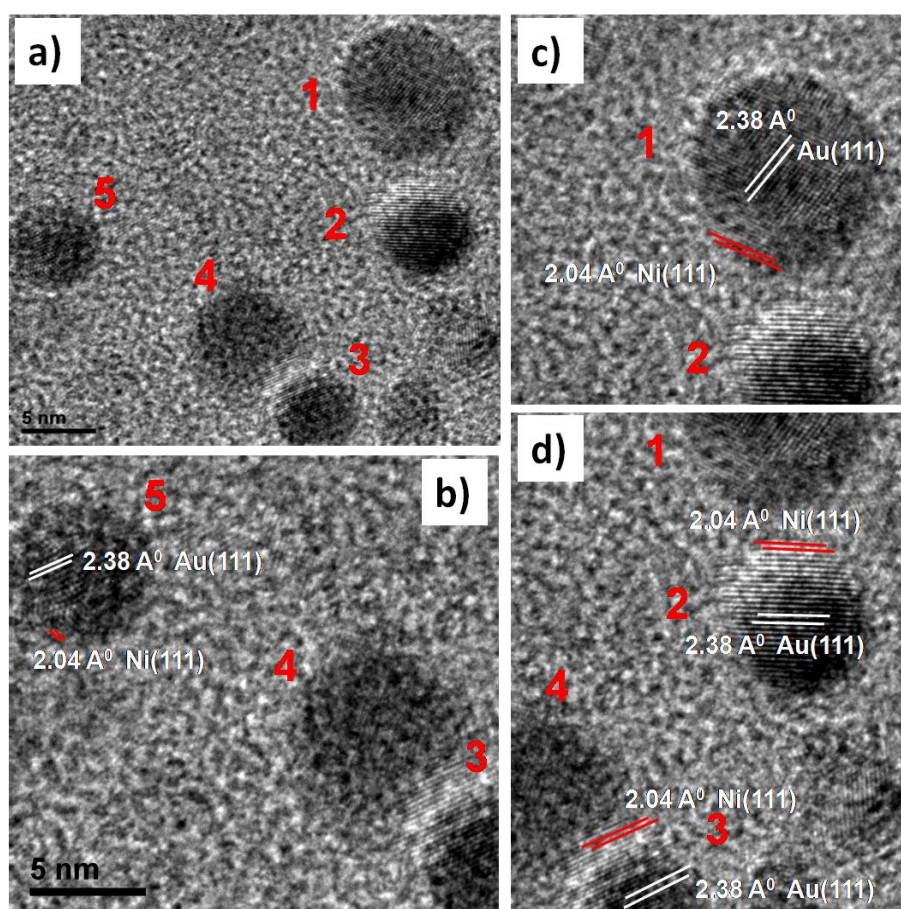


Figure 2A.5 HR-TEM images focussed on a group of Au@Ni_{FCC} nanoparticles. The images (b, c and d) in the figure shows lattice fringe details of the nanoparticles numbered in the main figure (a).

The large area TEM images of the as synthesized magnetic Au@Ni (FCC) core-shell nanoparticles with various nickel shell thickness are shown in Figure 2A.8 a-c and their corresponding high resolution images in Figure 2A.8 d-f.

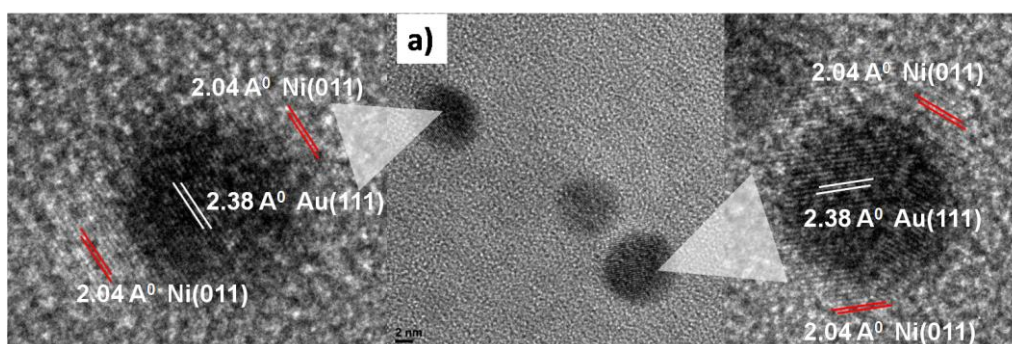


Figure 2A.6 HR-TEM images of Au@Ni_{HCP} core-shell nanoparticles. The images to the left and right of (a) shows the lattice details of gold and nickel in individual nanoparticles and confirms core-shell structure.

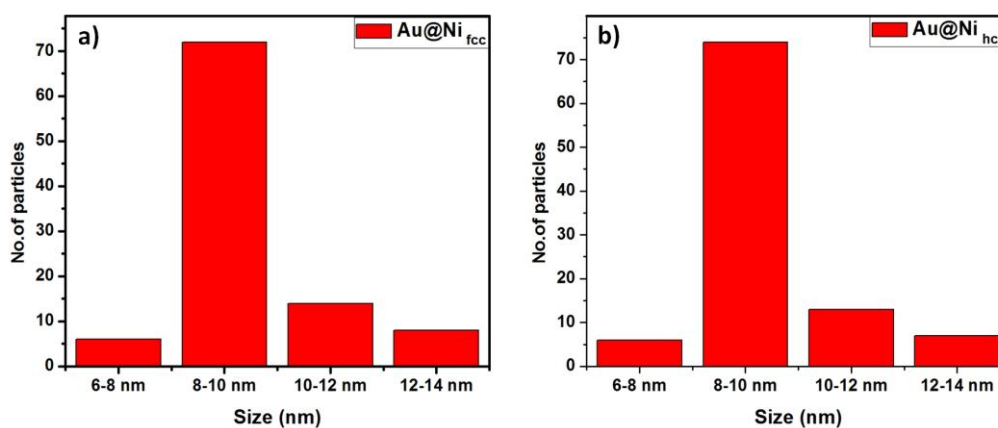


Figure 2A.7 Histogram analysis of (a) Au@Ni_{FCC} and (b) Au@Ni_{HCP} core-shell nanoparticle size distribution.

A careful HR-TEM analysis proved that the characteristic features of Au@Ni core-shell nanoparticles in the FCC phase remains intact even after depositing more nickel on the gold surface. From the large area TEM images it is evident that as the nickel ratio increases the particles were found to be more attracted to each other due to the increased magnetic character as expected in case of larger shell thickness which is well corroborated with XRD and magnetic measurements. It is also visible from the TEM images that most of the bimetallic nanoparticles have size below 10 nm for Au@Ni_{1:0.5} which has the same composition as that of Au@Ni_{FCC} (reported in the previous section) and size gradually increases with the shell thickness which is clear from the histogram analysis (Figure 2A.10d-f). The histogram analysis shows that the overall size of the as synthesized Au@Ni_{1:0.5} catalysts have size around 10 nm which increases up to 20 nm in case of a larger nickel shell.

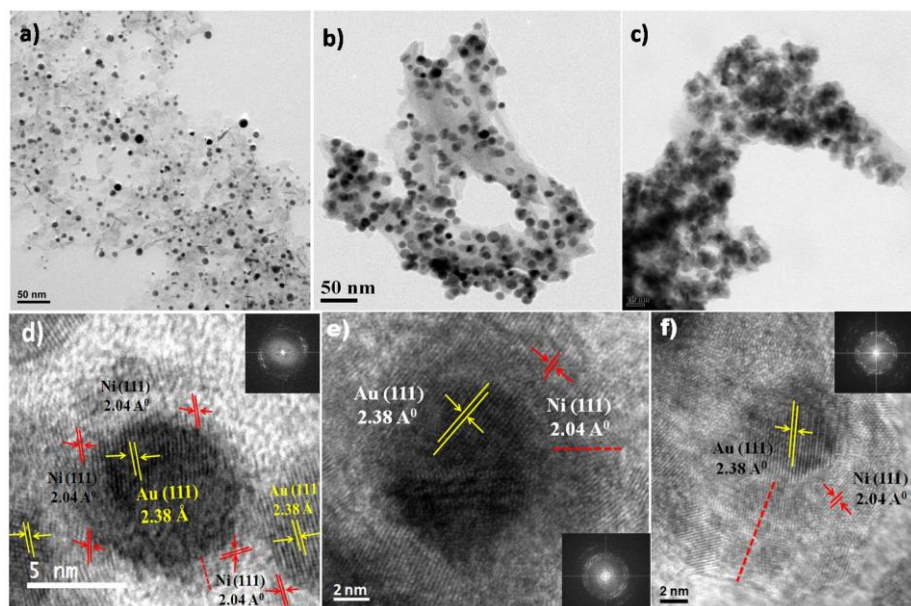


Figure 2A.8 TEM and HR-TEM images of Au@Ni core-shell nanoparticles with different nickel shell thickness. (a-c) are the large area TEM images of Au@Ni_{1:0.5}, Au@Ni_{1:1} and Au@Ni_{1:2} and (d-f) are the corresponding HR-TEM images of single nanoparticles. Inset shows FFT pattern of respective core-shell nanoparticles.

The darker gold core with a lighter nickel shell is visible in the high resolution images from individual bimetallic nanoparticles and it also demonstrates gold and nickel lattice features for all the three compositions. For thicker nickel shell, even the large area TEM image also shows dark gold core and a lighter Ni shell (Figure 2A.11) confirming core-shell morphology. The inter planar distances between the lattice fringes are clearly visible and precisely measured from the HR-TEM images (Figure 2A.8d-f) and it corresponds to 2.04 Å in the lighter contrast region (shell) which is composed of nickel as compared to the dark contrast of heavier metal gold in the core with a spacing of 2.38 Å. The d-spacing values of 2.38 Å matches well with Au (111) and 2.04 Å with Ni (111) planes in the core-shell nanoparticles¹⁵. Figure 2A.9a-f shows more lattice resolved HR-TEM images of Au@Ni core-shell nanoparticles. The larger shell in the Figure 2A.9f indicates a high amount of nickel deposition on the gold core when the nickel ratio increased to 1:2 (Au:Ni). Thus Au@Ni_{1:0.5} has a shell thickness of 1-2 nm, Au@Ni_{1:1} 3-4 nm and Au@Ni_{1:2} 6-8 nm. It is also evident from the TEM images that the size of resultant Au@Ni core-shell nanoparticles can be tuned by changing the metal precursor ratios. Even with a large lattice mismatch of Au-Ni system, there were recent reports demonstrating the possibility to epitaxially grow Ni on Au^{15, 40-41}.

Au@Ni nanoparticles presented here also showed the evidence for Moiré pattern with spacing approximately 1.50 nm indicating possible epitaxial relationship during bimetallic growth similar to previous literature reports (discussed in the following section). This also confirms the growth of nickel on a dissimilar gold lattice and indicates the core-shell geometry. In all three series of core-shell system, the nanoparticles with suitable orientation to the electron beam in the TEM revealed the Moiré fringes which confirmed the epitaxial growth (Figure 2A.10a-c). It must be emphasized; such a bimetallic system with large lattice mismatch allows the growth of a heavy nickel shell up to 8 nm on the sub 10 nm gold seeds (Figure 2A.11). It is highly difficult to synthesize such core-shell systems which can destabilize and collapse at any stage of core-shell formation even after generating the morphology. The present work demonstrates the ease of synthesis and stabilization of a core-shell system with large lattice mismatch even at very high metal overlayers.

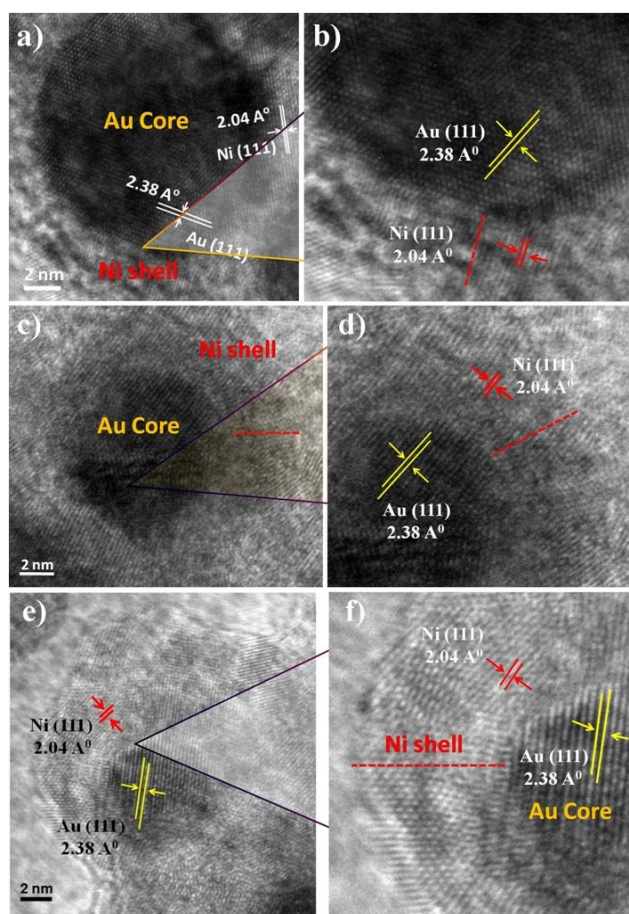


Figure 2A.9 HR-TEM images of (a-b) Au@Ni_{1:0.5}, (c-d) Au@Ni_{1:1} and (e-f) Au@Ni_{1:2} with lattice spacing corresponding to gold at core and nickel at shell. Red dotted lines indicate the nickel shell thickness around the gold core.

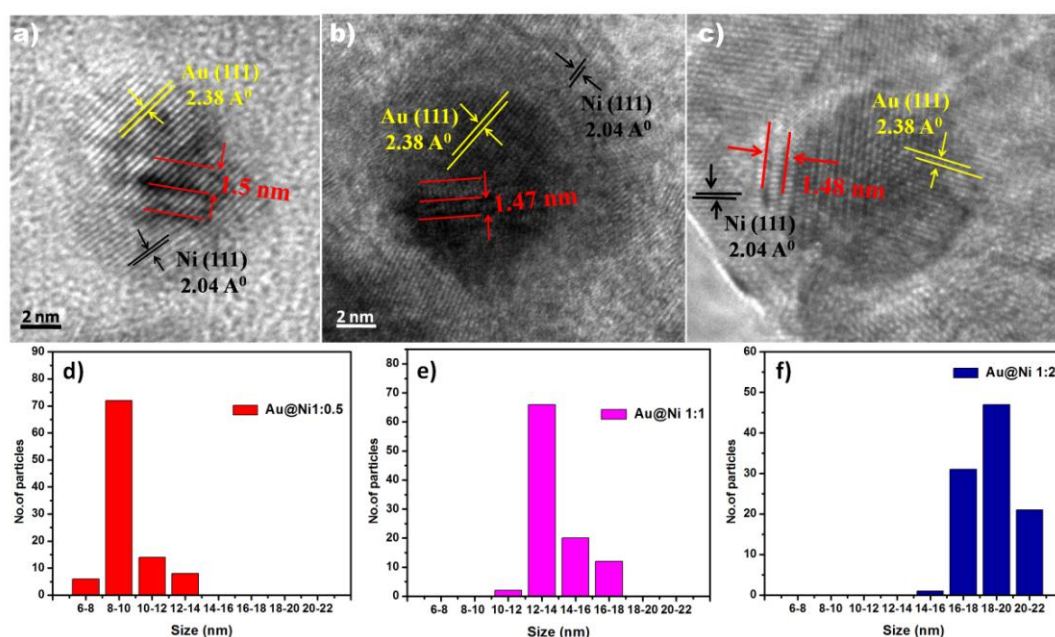


Figure 2A.10 HR-TEM images (a-c) and histogram analysis (d-f) of Au@Ni_{1:0.5}, Au@Ni_{1:1} and Au@Ni_{1:2} core-shell nanoparticles respectively. Presence of Moiré fringes (~1.5 nm) in HR-TEM images shows the possible epitaxial relationship between gold core and nickel shell lattices.

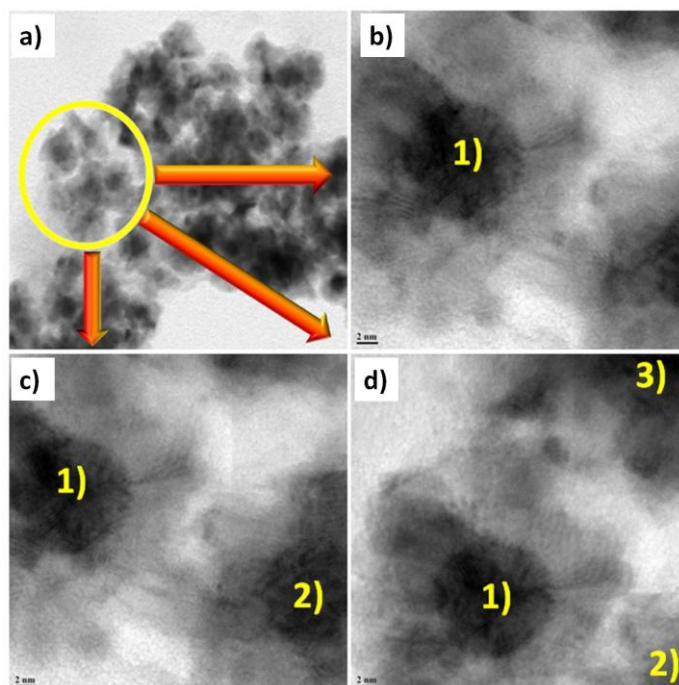


Figure 2A.11 (a) Large area TEM image of Au@Ni_{1:2} core-shell nanoparticles with a thick nickel shell and images (b-d) are the HR-TEM images of nanoparticles marked in yellow circle of image (a) exhibiting clear contrast difference between gold core and nickel shell.

Apart from the above informations, EDX analysis of Au@Ni core-shell nanoparticles have been carried out and the results are shown in Figure 2A.12a-c. The data showed the presence of gold (Au) and nickel (Ni) along with Cu, C (both from the C coated Cu TEM grid) and O (atmospheric oxygen contamination/oxygenated species on the sample and grid). The results from EDX analysis showed a successive increase in the quantified amount of nickel as compared to gold in the case of core-shell nanoparticles with higher shell thickness. The change in gold-nickel ratio was obvious and it showed in accordance with the metal precursor ratio used for each composition to obtain different nickel shell thickness. Thus the TEM results are indicative of successful synthesis of gold core of approximately 6-8 nm in all the three cases while nickel shell thickness was variable from 1-2 nm to 6-8 nm.

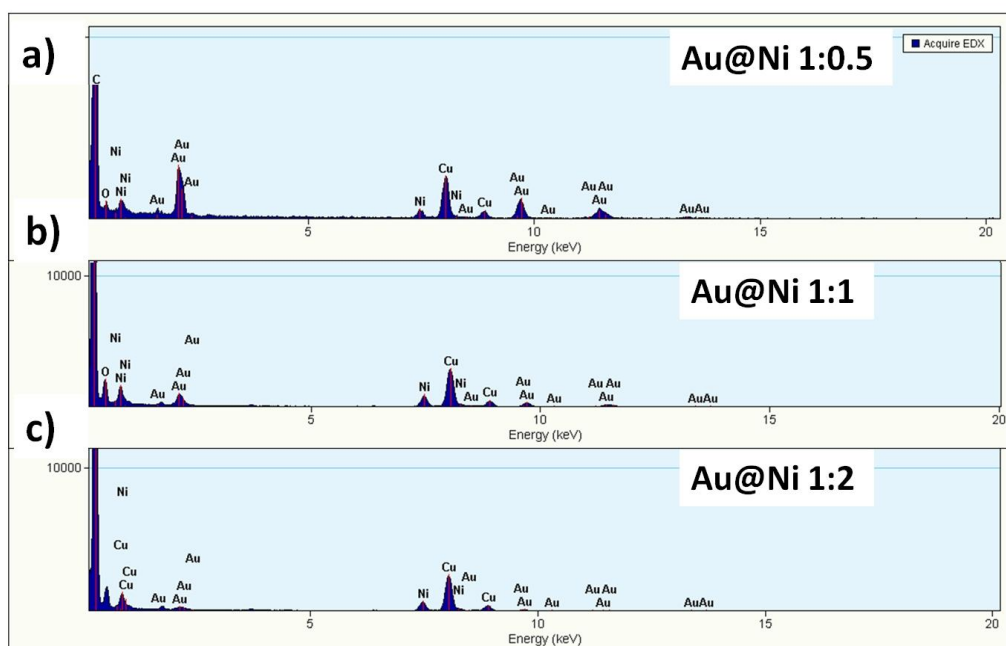


Figure 2A.12 (a-c) The EDX data obtained for the magnetic Au@Ni core-shell nanoparticles with different shell thickness synthesised by varying gold to nickel metal ratios.

For validating the core-shell synthesis strategy and the TEM observations/analysis, control experiments are carried out and the samples were analyzed under microscopy. The metal nanoparticles were synthesized through the same synthesis method but in the absence of counter metal precursor. The monometallic gold nanoparticles thus obtained are shown in Figure 2A.13a which confirmed that the size regime of gold nanoparticles are in between 6-8 nm which serves as gold seeds in bimetallic synthesis strategy and it shows good agreement

with the bimetallic nanoparticle TEM analysis. The dense gold nanoparticles are also visible from the large area TEM image. Similarly, nickel monometallic nanoparticles were also synthesized following thermal reduction in the absence of gold seeds. In an approach to distinguish between the dense gold and lighter nickel nanoparticles, both the monometallic gold and nickel nanoparticles were mixed physically and the resultant solution has been analyzed under TEM. The image obtained for the physical mixture of gold and nickel nanoparticles are depicted in Figure 2A.13b. From the large area images it is highly evident that the distinction between gold and nickel based on the contrast difference is very much valid, since the mixture shows the existence of gold nanoparticles with heavy dark contrast as compared to lighter nickel nanoparticles. The control experiments showed the formation of both the nanoparticles and authorized their characteristic features which confirmed the successful generation of core-shell morphology in Au-Ni bimetallic nanostructures demonstrated here.

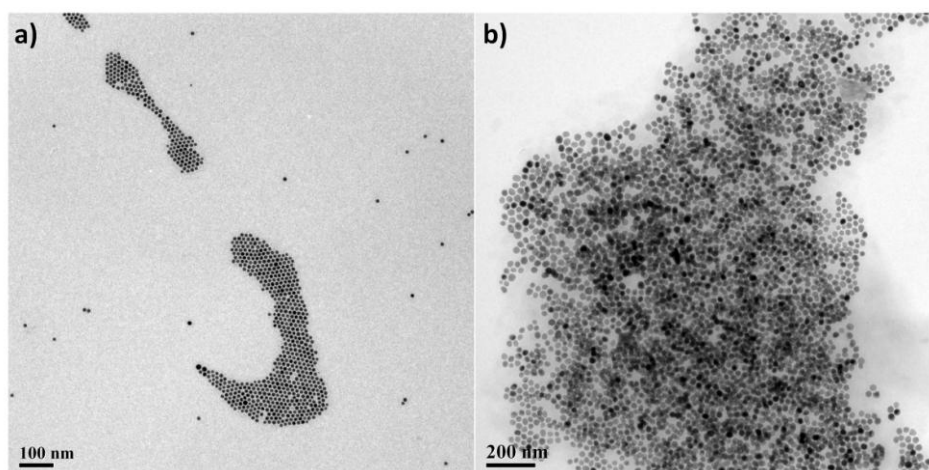


Figure 2A.13 Large area TEM images obtained for (a) initial stage gold nanoparticle seeds and (b) physical mixture of gold and nickel monometallic nanoparticles which shows the contrast difference between the Au and Ni nanoparticles.

2A.2.3 X-Ray Diffraction Studies (XRD)

The structural characterization by powder X-ray diffraction (XRD) demonstrated the formation of two different crystalline phases of nickel which were magnetically diverse in nature, namely Au@Ni_{FCC} and Au@Ni_{HCP} bimetallic nanoparticles. The curve a in Figure 2A.14, which is the powder XRD pattern obtained from the nanoparticle synthesis where reduction of nickel was carried out at 210 °C and yielded magnetic nanostructures

(Au@Ni_{FCC}). The reflections at 2θ values at 44.5 correspond to both Au (200) and Ni (111) and 51.8 for Ni (200). This along with strong reflections from gold core at 38.2 for Au (111), 64.6 for Au (220) and 77.8 for Au (311) matches with the literature values for an FCC structure of gold¹⁵⁻¹⁶. Since there is strong overlap of lower order reflections from gold and nickel, the most discernible peak for the presence of FCC nickel is at 2θ value 51.8. The magnetic core-shell nanoparticles (denoted as Au@Ni_{FCC} in the following text) therefore is stabilized with nickel in pure FCC structure. In contrast, the non-magnetic form of the Au@Ni bimetallic nanoparticles (curve b in Figure 2A.14) showed characteristic reflections of the HCP nickel at 39.1, 41.5, and 58.6 for the (010), (002), and (012) planes respectively⁴². Moreover the absence of nickel FCC (200) phase at 51.8 and the presence of (012) phase at 58.6 indicate that the synthesis has yielded bimetallic Au@Ni system with nickel in pure HCP phase (denoted as Au@Ni_{HCP} in the rest of the text) and not a mixed phase^{9, 43}. This is also evident from the magnetic measurements done on the core-shell nanostructures which will be discussed in the following sections. The fairly large full width at half-maximum (FWHM) of the XRD peak especially those obtained from nickel in both the core-shell structures are also indicative of the small size and shell thickness of the particles. Indeed, the crystallite size calculated using Debye-Scherrer equation by considering Au (111) reflection gave values of approximately 10 nm for both Au@Ni_{FCC} and Au@Ni_{HCP} core-shell nanoparticles.

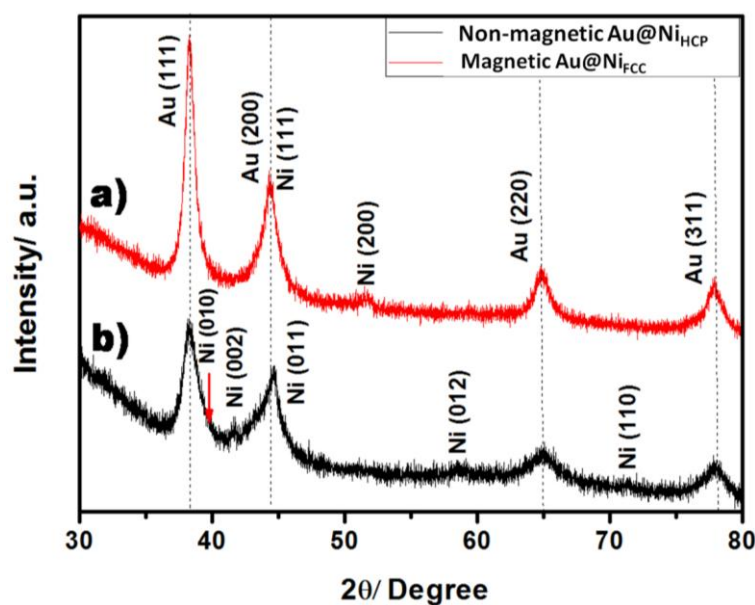


Figure 2A.14 XRD pattern obtained for (a) magnetic Au@Ni_{FCC} and (b) non-magnetic Au@Ni_{HCP} core-shell nanoparticles. Dotted lines represent the standard reflections of Au.

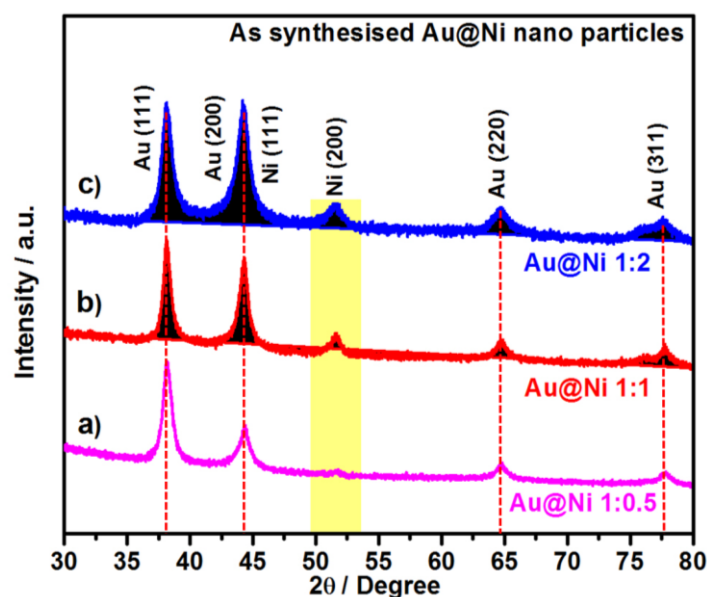


Figure 2A.15 XRD patterns of core-shell (a) Au@Ni_{1:0.5}, (b) Au@Ni_{1:1} and (c) Au@Ni_{1:2} nanoparticles with different nickel shell thickness. Reflection highlighted in yellow bar is specific to nickel and the red dotted lines correspond to the standard reflections of gold.

Meanwhile, the powder XRD patterns obtained from the as synthesized catalysts with various nickel shell thickness stabilised in the magnetic FCC phase namely (a) Au@Ni_{1:0.5}, (b) Au@Ni_{1:1} and (c) Au@Ni_{1:2} are given in Figure 2A.15. The curve a in the Figure 2A.15 corresponds to Au@Ni_{1:0.5} and b and c represents Au@Ni_{1:1} and Au@Ni_{1:2} respectively. Here also, the fairly large FWHM values obtained for all the three series of nanoparticles indicating the smaller size of core-shell structures. It is evident from the XRD pattern that as the nickel concentration increase there is a simultaneous increase in the intensity of major diffraction for nickel planes at 2θ values 44.5 and 51.8. As in the case of Au@Ni_{FCC} nanoparticles, due to the merging of the major reflection of Ni (111) with the Au (200) plane, it is more appropriate to follow Ni (200) reflections at 51.8 2θ value. In the case of Au@Ni_{1:0.5} very broad peak at 51.8 (reflection highlighted in shaded box in Figure 2A.15) indicates the formation of a thin shell which relaxes on the gold core. The intensity of the above mentioned peak increases with the nickel loading confirming the further growth of nickel lattice formation leading to a thicker shell. Also a decrease in the FWHM of the major reflections of nickel in XRD peaks while moving from a to c in Figure 2A.15 is an indication of gradual increase of the nickel lattice. The polycrystallinity of the core-shell particles are confirmed by the reflections at 2θ values 38.2, 44.3, 64.6 and 77.8 which correspond to different planes of Au (111), Au (200), Au

(220) and Au (311) respectively¹⁶. Also, the reflections at 44.5 and 51.8 confirmed the presence of polycrystalline nickel shell in FCC lattice⁹. Despite of the literature reports for the crystalline phases of the metal nanoparticles, monometallic gold and nickel nanoparticles were synthesized under the same experimental procedures and analyzed for the X-ray diffraction pattern and the results are showed in Figure 2A.16. The core-shell nanoparticles showed the respective diffraction patterns corresponding to gold and nickel and confirmed the pure crystalline phases in bimetallic structures. All these results for both the metals in combination with microscopic lattice fringe analysis in TEM substantiate the formation of FCC-Au and FCC-Ni. The comparative increase in the intensity of Au-Ni overlapping reflections at 44.5 as compared to pure Au (111) is a major indication of the growth of nickel FCC lattice over gold. The crystallite size of bimetallic nanoparticles are also calculated using Debye-Scherrer equation and found to be in good agreement with the size distribution obtained from TEM histogram analysis in all the bimetallic nanoparticles.

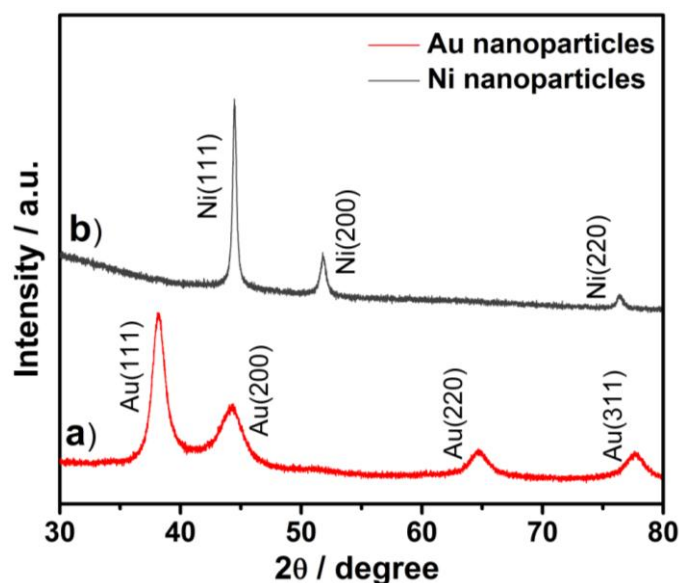


Figure 2A.16 XRD patterns of monometallic (a) gold and (b) nickel nanoparticles confirm the FCC crystal lattice for both the metals.

2A.2.4 XRD Studies on Au@Ni_{FCC} and Au@Ni_{HCP} Nanoparticles under Ambient Pressure Annealing

One of the primary motivations for synthesizing the Au@Ni core-shell nanostructures is to understand the effect of gold core in inducing electronic or geometric modifications on the nickel surface and in turn their properties. It is evident from the previous studies that the

Au-Ni bimetallic system not necessarily with core-shell morphology is able to synergistically catalyze a variety of reactions with better activity and selectivity⁴⁴⁻⁴⁸. To understand the influence of the gold core on the physiochemical properties of nickel, the Au@Ni_{FCC} and Au@Ni_{HCP} bimetallic nanoparticles were subjected to heating experiments in ambient atmosphere and the changes were followed by XRD. Figure 2A.17 shows the XRD pattern obtained for Au@Ni_{FCC} and Au@Ni_{HCP} during this heating experiment. It is remarkable to note that the bimetallic nickel surface did not show any evidence for NiO formation until 250 °C which is unlikely for monometallic nickel. The oxidic phase of the Ni coincides with the build up of (111) and (200) reflections at 37.2 and 43.2 2θ values⁴⁹ which are clearly visible after heating the samples to 500 °C. A careful look at both the XRD peaks leads to the assumption that Au@Ni_{FCC} nanoparticle (Figure 2A.17a) is marginally more resistant to oxidation compared with the Au@Ni_{HCP} (Figure 2A.17b). This conclusion is mainly due to the observation of a fully developed NiO feature at 43.2 in the Au@Ni_{HCP} where as it appears as a small shoulder in the case of Au@Ni_{FCC} at 500 °C. It is well known that HCP nickel is metastable, which is more pronounced to oxidation and transform to a stable oxide phase quickly. Here, the metastable phase was found to be fairly stable up to 150 °C against oxidation and broader (111) and (200) reflections were observed beyond this temperature. In either case, it is proven beyond doubt that both these nanostructures are robust towards ambient oxidation up to 150 °C or above. Such a remarkable oxidation resistance is solely possible because of the geometric or/and electronic modification induced by the gold core. The decrease in FWHM of the Au (111) reflection above 300 °C with a marginal increase in intensity (maximum at 500 °C) is possibly due to the agglomeration of the particles at higher temperatures. It is worth pointing out that the nature of metastable HCP nickel has a close structural and magnetic resemblance with nickel carbide (Ni₂C)⁵⁰⁻⁵¹. XRD heating experiments shows that the oxide transformation of metastable Au@Ni_{HCP} takes place at a much lower temperature compared with Au@Ni_{FCC}, which is unlikely if nickel is present as nickel carbide on the surface. Moreover, the remarkable similarity in the rates of p-nitrophenol (PNP) reduction reactions (will be discussed in catalytic activity section) on both these surfaces obviously demonstrates the presence of metallic nickel on the as prepared Au@Ni_{FCC} and Au@Ni_{HCP} core-shell bimetallic nanoparticles.

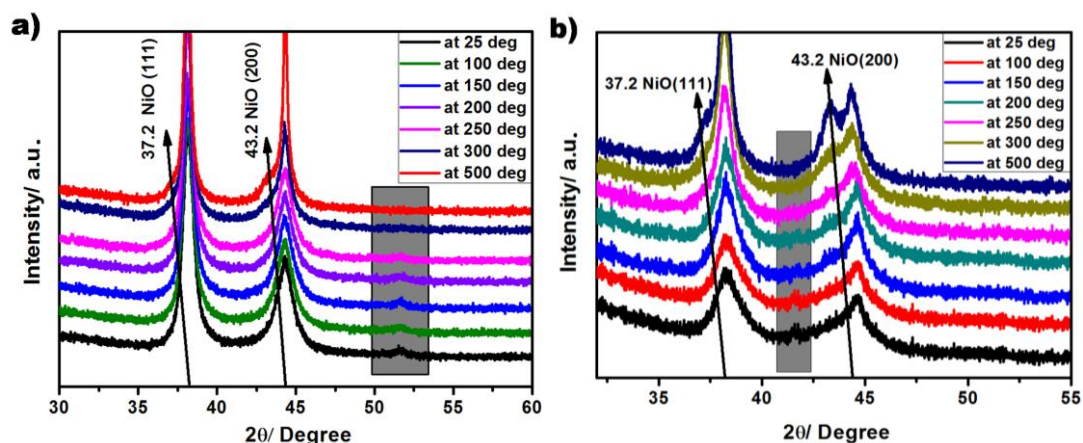


Figure 2A.17 Temperature-dependent XRD analysis of (a) Au@Ni_{FCC} and (b) Au@Ni_{HCP} core-shell nanoparticles. Black arrows indicate the emergence of NiO peak and transformation from the metallic nickel peak (44.5) position. Shaded areas in (a,b) representing the damping of metallic nickel FCC phase (51.8) and HCP phase (41.5) with increase in temperature.

2A.2.5 Magnetic Measurements (SQUID-VSM)

The magnetic properties of the as synthesized bimetallic core-shell nanoparticles with different crystalline phases and various metal ratios stabilized in FCC phase are subsequently probed using superconducting quantum interference device (SQUID) measurements. Ferromagnetism is considered as an intrinsic property of nickel metal with FCC structure and the saturation magnetization changes depending on the nickel concentration^{7, 9}. Initially the hysteresis loops measured at 300 K for different crystalline core-shell nanoparticles Au@Ni_{FCC} and Au@Ni_{HCP}. Core-shell nanoparticles with FCC nickel lattice showed typical hysteric behaviour of a ferromagnetic nickel where a drastic increase in magnetization is observed¹⁵⁻¹⁶, which recorded saturation in the field of 5 kOe. The coercivity of the bimetallic Au@Ni_{FCC} nanoparticles obtained was 25 Oe at 300 K with a saturation magnetization of approximately 2 emu gm⁻¹ (Figure 2A.18a). The relatively low saturation magnetization and coercivity values obtained for Au@Ni_{FCC} core-shell nanoparticles can be due to the thin nickel layer having a shell thickness of approximately 2 nm⁴¹. In contrast, the Au@Ni_{HCP} bimetallic system, magnetization increases slowly and does not achieve saturation magnetization even at 30 kOe which is the characteristic behaviour of HCP nickel (Figure 2A.18b)^{7, 9}. Thus, the magnetic measurements of Au@Ni_{FCC} and Au@Ni_{HCP} corroborate well with the XRD structural characterization confirming the existence of FCC and HCP nickel phases in different core-shell nanoparticles.

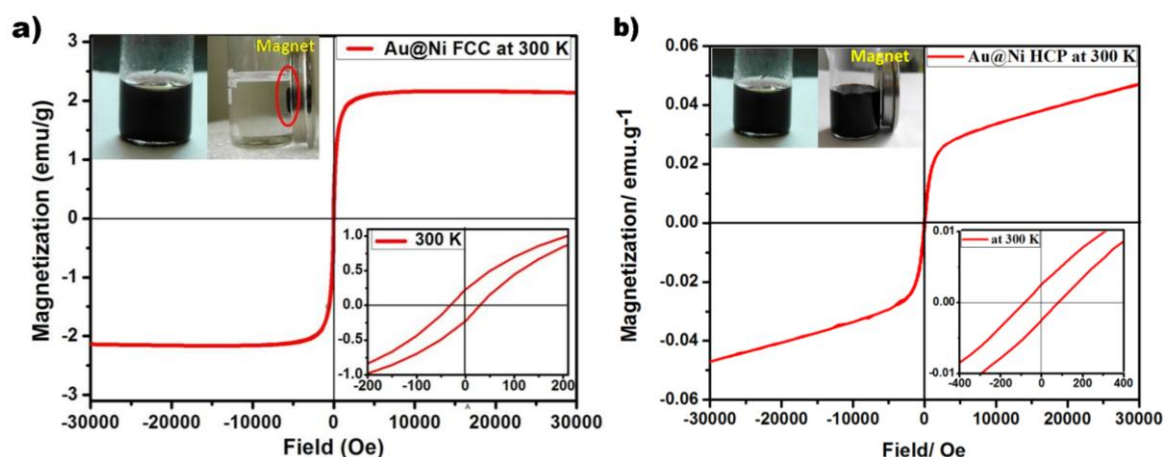


Figure 2A.18 Hysteresis loops of magnetic Au@Ni_{FCC} and non-magnetic Au@Ni_{HCP} core-shell nanoparticles at room temperature measured using SQUID. Inset (upper in a and b) shows the behaviour of core-shell nanoparticles towards a magnet and lower inset (a and b) depicts the coercivity near the zero field.

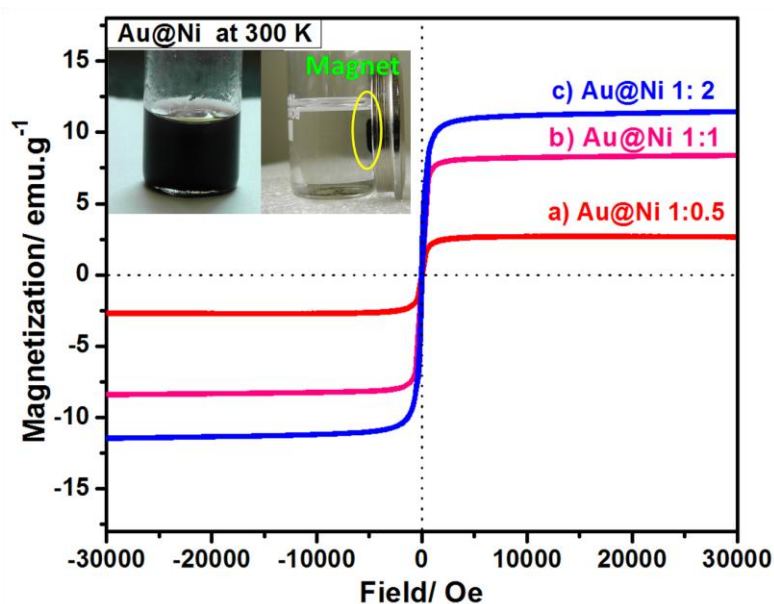


Figure 2A.19 Hysteresis loops obtained for (a) Au@Ni_{1:0.5} (b) Au@Ni_{1:1} and (c) Au@Ni_{1:2} core-shell nanoparticles with different nickel shell thickness obtained at room temperature. Inset shows the digital photograph of the ferromagnetic character in Au@Ni core-shell system.

Au@Ni core-shell nanoparticles with FCC structure and different metal ratio continued to show ferromagnetic behaviour at room temperature which makes them bifunctional nanomaterials for catalytic activity and their magnetic recovery after the reaction

sequences. Figure 2A.19 shows the hysteresis loop measured at room temperature for each of the core-shell samples using SQUID. A typical hysteric behaviour is obtained for all the samples where a sudden increase in magnetization is observed with external field in the beginning which reaches saturation below 5 kOe with different saturation magnetization values around 2.5, 8 and 11 emu/gm for Au@Ni_{1:0.5}, Au@Ni_{1:1} and Au@Ni_{1:2} respectively. The rapid increase in saturation magnetization of the samples Au@Ni with the ratio 1:1 and 1:2 is the result of a fully matured nickel lattice and ferromagnetism is highly pronounced in such cases.

2A.2.6 X-ray Photoelectron Spectroscopy Investigation (XPS)

The XRD being a bulk technique any observable changes during heating commences with bulk oxidation or bulk structural transformations, a preliminary XPS study was carried out to understand the surface characteristics and chemical state of the bimetallic structures with exceptionally high thermal stability, Au@Ni_{FCC} core-shell nanoparticles (as synthesized). The XP spectra obtained for both the metals in all the cases of bimetallic nanoparticles mentioned hereafter are referenced to standard C1s binding energy of 284.6 eV for adventitious carbon. Figure 2A.20a shows the Ni 2p_{3/2} from the Au@Ni_{FCC} core-shell nanoparticles, and the spectrum is dominated by two major peaks at binding energy values 852.6 eV and 855.6 eV. These are reported values for metallic nickel (0) and nickel hydroxide respectively and provide evidence for metallic (852.6 eV) nature of nickel at the surface of the nanoparticles⁵². The absence of NiO (peak at 854 eV) species supports the evidence obtained from XRD and detailed TEM analysis. The presence of Ni(OH)₂ feature at 855.6 eV which was not evident in XRD analysis depicts the importance of surface science analysis since catalysis is a surface phenomena based on adsorption and surface chemical state. The hydroxide feature is expected and has been previously reported for nickel nanoparticles synthesized through wet chemical reduction routes¹⁶. Thus Au@Ni_{FCC} core-shell nanoparticles with a thinnest nickel shell (up to 10 atomic layers) gave approximately 50 % metallic nickel (judging by the peak intensities) with rest being hydroxide. It should be noted that the surface of the nickel nanoparticles synthesized by colloidal route are always dominated by nickel hydroxide species^{16, 53}. Thus retaining almost 50 % of metallic nickel in Au@Ni core-shell system is remarkable which is never possible in the case of a monometallic nickel which always composed of hydroxide and oxide species at the surface⁵³. In fact in most of the cases monometallic nickel lacks any characteristic metallic feature at the surface¹⁶

which shows the significant relevance of Au@Ni core-shell system with high quantity of metallic nickel at the surface even after exposure to atmosphere. Also, all synthesis procedure was carried out without using any inert atmosphere thus making this synthesis and material more versatile. The XPS of gold showed a binding energy value of 84 eV and 87.6 eV (Au 4f_{7/2} and 4f_{5/2}), which is typical of metallic Au (0) (Figure 2A.20b). Any significant shift in the characteristic peak positions of both the metals as reported for their model surface science studies was not observed in the case of core-shell materials¹⁷. The new findings pertaining to temperature-programmed XRD and XPS are noteworthy as previous results showed air oxidation of nickel nanoparticles at ambient conditions and clearly observed using XRD technique⁵⁴⁻⁵⁵.

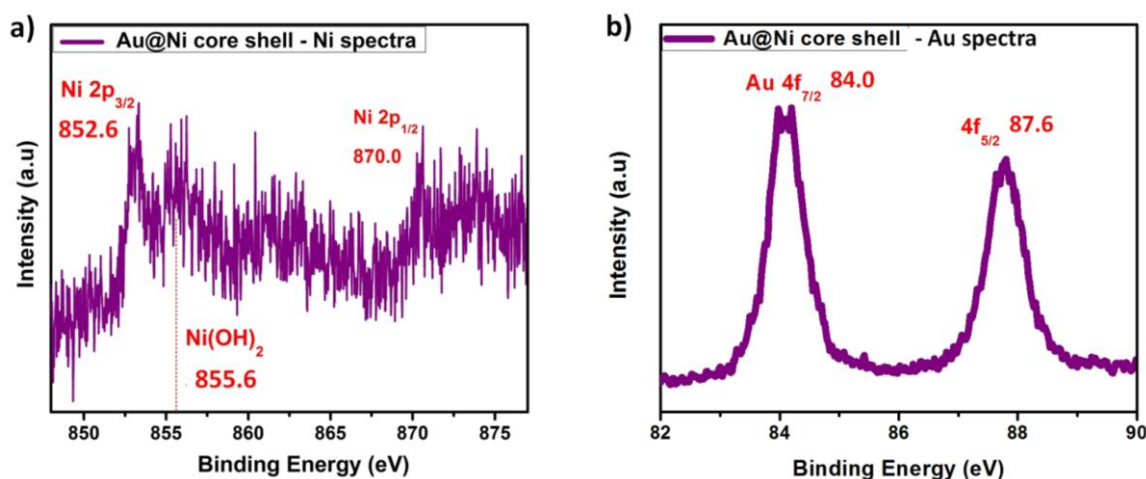


Figure 2A.20 Individual XP spectra recorded for (a) Ni 2p and (b) Au 4f region in Au@Ni_{FCC} core-shell nanoparticles.

Figure 2A.21 shows the Ni 2p_{3/2} and Au 4f_{7/2} spectra obtained from the three bimetallic compositions with varying nickel shell thickness. The bottom spectrum in the Figure 2A.21 corresponds to Au@Ni_{1:0.5} having nickel shell with a thickness of approximately 2 nm. And it showed the same metallic nickel feature at 852.6 eV, similar to that of Au@Ni_{FCC}, since both are equivalent composition. Retaining such a large degree of metallic nickel (around 50 %) is truly developed from the synergistic effect of the gold core which induces inertness to the nickel surface and resists the oxidation behaviour. The results are in accordance with a recent report from Ceyer et al where high resolution electron energy loss spectroscopy (HREELS) study demonstrated that the dissociation of molecular oxygen was inhibited on Au-Ni (111) surface in contrary where it dissociates readily on mono metallic nickel metal surface⁵⁶.

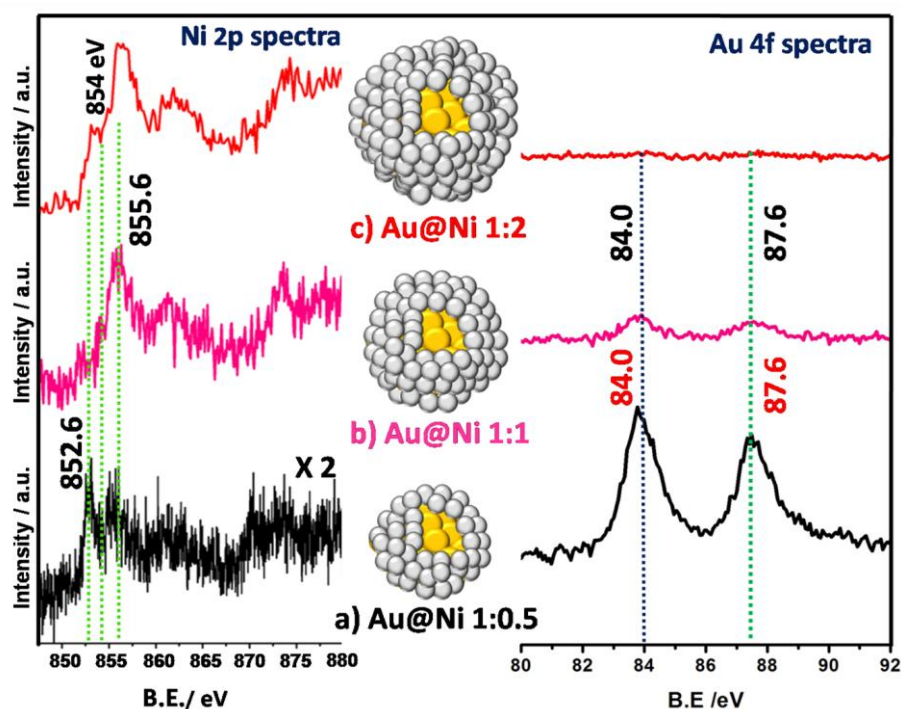


Figure 2A.21 XP spectra of Ni 2p and Au 4f obtained for the as synthesized (a) Au@Ni_{1:0.5}, (b) Au@Ni_{1:1} and (c) Au@Ni_{1:2} core-shell nanoparticles with different shell thickness.

From the Ni 2p_{3/2} spectrum it can also be inferred that the concentration of metallic nickel is barely seen in the case of Au@Ni_{1:1}. A clear shift in the Ni 2p peak centroid towards lower binding energy is observed in the case of Au@Ni_{1:2} with development of a shoulder at binding energy value of approximately 854 eV which according to the literature report corresponds to nickel oxide⁵². Thus for a 1:2 composition of Au:Ni, the main peak is dominated by contributions from Ni(OH)₂ and nickel oxide which is the characteristic property of monometallic nickel⁵³. As expected the intensity of the Ni 2p_{3/2} increases with the nickel precursor concentration resulting in a better signal to noise spectrum in the case of higher nickel concentrations. The presence of core-shell architecture is also evident from the intensity of Au 4f peak shown in Figure 2A.21. The peak position at 84 eV is consistent with the metallic gold in all three series of samples and the intensity progressively decreasing with the increase in nickel precursor concentration indicating that gold nanoparticles are being buried under thicker nickel shell. Thus XPS results clearly demonstrates that nickel surface is more passive towards oxidation at approximately 2 nm thick shell over gold core exposing more than half of the surface in metallic phase. The electronic or geometric modifications in bimetallic system have revealed several interesting reactivity patterns atypical of

monometallic counterparts^{4, 57-59}. Now the extent to which each of these effects influences the chemical and physical properties are difficult to differentiate and have to be discussed with respect to specific reactions under consideration.

2A.2.7 Catalytic Activity Results of Au@Ni Core-shell Nanoparticles for Nitro (-NO₂) to Amino (-NH₂) Group Conversion and Effect of Temperature Pre-treatment

It is beyond doubt that the remarkable oxidation resistance of nickel shell modified with gold core revealed by XRD and XPS techniques has far reaching implication in catalysis. The catalytic activity tests were carried out in the first stage by using Au@Ni_{FCC} and Au@Ni_{HCP} core-shell nanoparticles for the nitro group reduction in PNP to form the product PAP. The UV-Vis spectra were collected while carrying out the reaction employing the two different core-shell catalysts and also with the catalyst treated at various temperatures to understand the effect of heat treatment on the catalytic activity of the core-shell system. Figure 2A.22 and Figure 2A.23 illustrates the raw UV-Vis spectrum and the corresponding rate curves obtained for Au@Ni_{FCC} and Au@Ni_{HCP} core-shell nanoparticles during PNP reduction. The presence of isosbestic point and absence of any other features in the UV-Vis spectra in all the experiments is a clear indication that the reaction follows without any side products and proceeded to maximum conversion²³. It is well known that the parent molecule PNP shows a characteristic sign of UV-Vis absorption peak at 317 nm which immediately transform to nitrophenolate ions up on treatment with sodium borohydride in aqueous solution⁶⁰. The nitrophenolate ions show a strong absorption at 400 nm immediately after addition of sodium borohydride to PNP solution. The rate of reduction reaction over bimetallic nanoparticles can be easily monitored by carefully following the damping of absorption peak at 400 nm which is the characteristic feature of nitro group. A new absorption peak at 300 nm confirms the formation of amino group in PAP⁶⁰. There was no observable reduction reaction in the absence of catalysts. The UV-Vis data for the as-synthesized catalyst for both FCC and HCP showed excellent activity wherein the reactions were completed within 90 seconds after the commencement of the reaction. A comparison with the previous literature reports on Ni-based systems suggests that these time scales observed for the complete reduction of PNP are exemplary²⁸. The synthesis strategy developed here realized the formation of an extremely active nickel catalyst due to the electronic and geometric

modifications induced by the gold core with diverse magnetic properties. It is important to note that the FCC and HCP catalysts gave similar activities to begin with which also proves the homogeneity of the nickel surface layer in both the bimetallic formulations. The heating pre-treatment of the bimetallic nanoparticles, resulted in the decrease of rate of reaction, which is directly evident from the UV-Vis data in time taken for the complete reduction of the PNP. The UV-Vis data were further processed for finding out the apparent rate constant values. The plot $\ln(A_t/A_0)$, where A_t is the concentration of PNP at time t and A_0 is the value at time zero gave a linear correlation. Figure 2A.24 demonstrates the rate of the reduction reaction versus temperature of heat treatment of both the Au@Ni core-shell catalysts. Both the catalysts showed almost the same activity for PNP reduction until 100 °C after which the rate starts to slow down. It is quite evident that the slope of the linear fits obtained for FCC and HCP Au@Ni shows marked shift for the samples treated at higher temperatures with the HCP showing a dramatic shift in the slope above 100 °C. The rate of the reaction obtained from the linear fits plotted against the temperature at which the bimetallic nanoparticles were heated in air clearly establishes this fact. Even though XRD results suggested the bimetallic nanostructures to be stable for bulk oxidation until 250 °C, it is understandable that surface oxidation starts at a much lower temperature, which is reflected in the catalytic study where the rate tends to fall off after 150 °C. The rate drops down drastically for the HCP nickel phase compared with the FCC for the samples heated above 150 °C. The sluggish rate for the reduction can obviously be correlated to much faster oxide phase formation on the Au@Ni_{HCP}, which is confirmed by XRD study. It is well established from the PNP reduction on various metal nanoparticles that the presence of surface oxide can lead to a considerably large induction period for the reaction⁶⁰. This arises because the first step in the reduction reaction is the adsorption of the nitrophenolate ion on the metal surface and a surface oxide layer is found to inhibit this process. So the reduction of surface oxide by sodium borohydride to generate metal oxide is speculated to be the reason for the induction periods observed for the PNP reduction reactions involving metal surfaces^{27, 61}. This is also observed in the UV-Vis spectra where the samples heated to 150 °C or higher is expected to have significant oxide layer, which has several competing surface processes happening viz: reduction of surface oxide and generating nascent metal surface, adsorption of nitrophenolate ions on this surface followed by its reduction to aminophenol. For instance, the induction period for a selected reaction has been analyzed from a plot of the concentration of 400 nm species with time for the as synthesized as well as for the Au@Ni_{HCP} catalyst calcined at 200 °C (Figure 2A.25).

The reaction being facile on the metallic nickel surface in the case of as synthesized catalyst, where as the induction period of several minutes was observed for Au@Ni_{HCP} catalyst calcined at 200 °C. To prove that the interplay of geometric and electronic effects is responsible for this trend in reactivity, Au@Ni core-shell nanoparticles with varying thickness of nickel shell over the gold core are synthesized and it will be discussed in the following section. Thus, the results obtained here unequivocally proved that surface engineering of nickel by a gold core can generate a nickel surface, which can withstand oxidation even up to 150 °C. The magnetic Au@Ni has tremendous applications in reactions envisaged by nickel metal, which is one of the most promising catalysts for energy-related heterogeneous processes like steam reforming or reduction reactions^{59, 62-64}. On the other hand, a stable non-magnetic Au@Ni (Au@Ni_{HCP}) nanoparticle can readily find use in battery applications, which goes into the magnetic resonance imaging (MRI) room, or for making uniform paint formulations without aggregation.

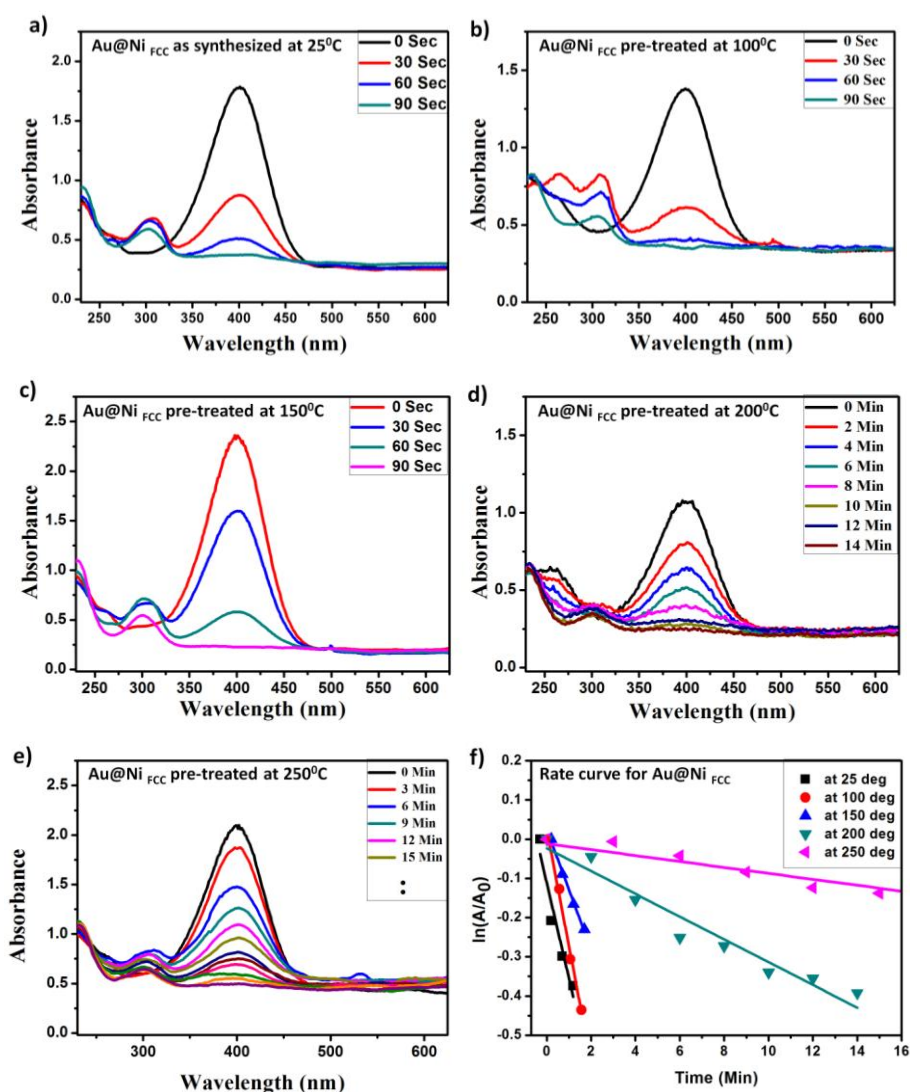


Figure 2A.22 UV-Vis spectra recorded for PNP reductions by using Au@Ni_{FCC} core-shell catalysts in the as synthesised form (Room temperature) and heated at various temperatures (a) RT (b) 100 °C (c) 150 °C (d) 200 °C (e) 250 °C and their corresponding rate curves plotted in (f).

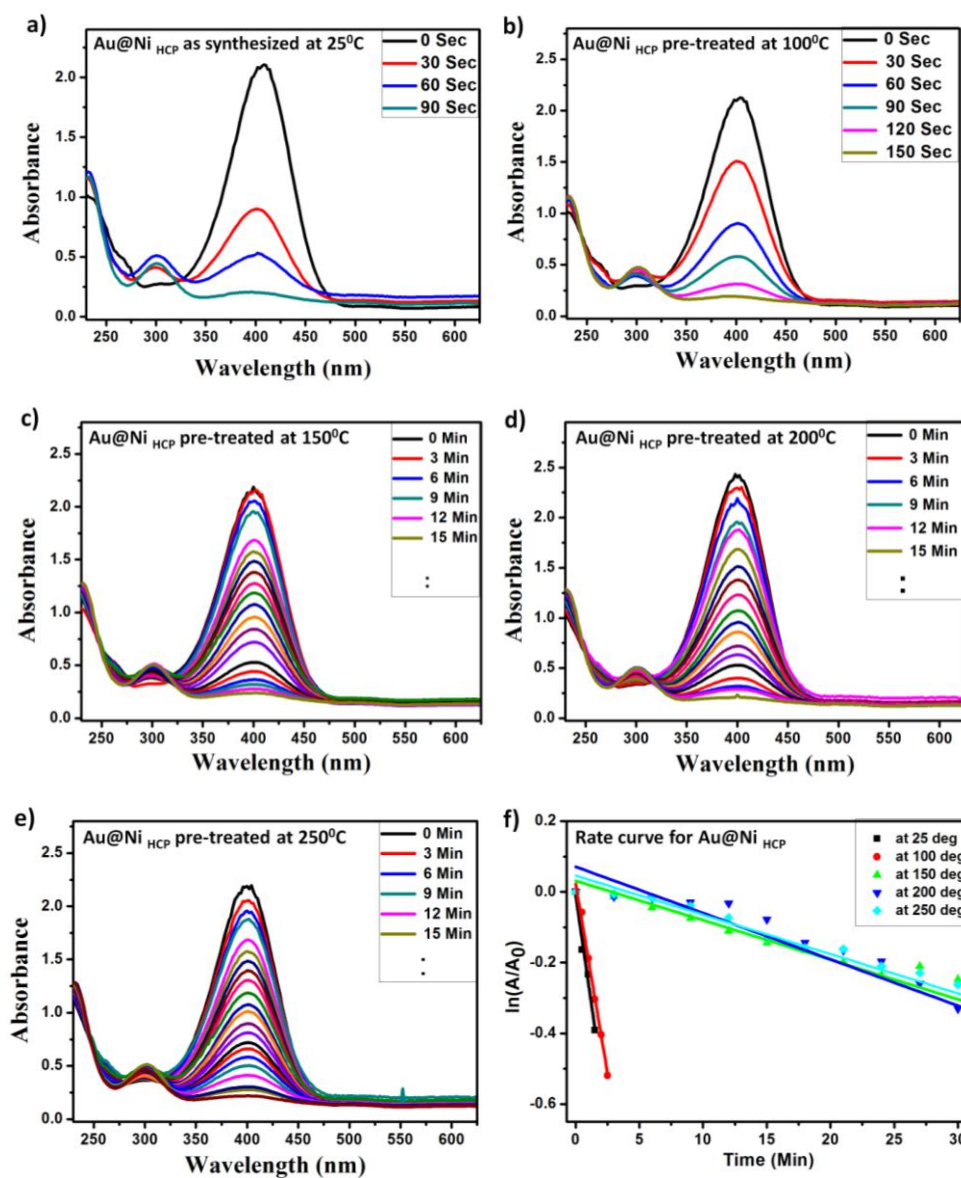


Figure 2A.23 UV-Vis spectra recorded for PNP reductions by using Au@Ni_{HCP} core-shell catalysts in the as synthesised form (Room temperature) and heated at various temperatures (a) RT (b) 100 °C (c) 150 °C (d) 200 °C (e) 250 °C and their corresponding rate curves plotted in (f).

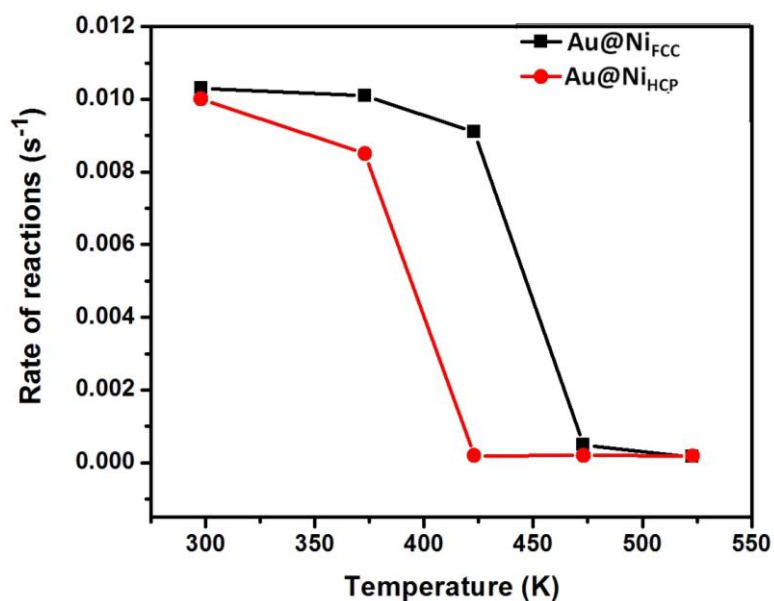


Figure 2A.24 Rate of PNP reduction reaction catalyzed by both Au@Ni_{FCC} and Au@Ni_{HCP} core-shell nanoparticles as a function of annealing temperature of the catalyst pre-treatment.

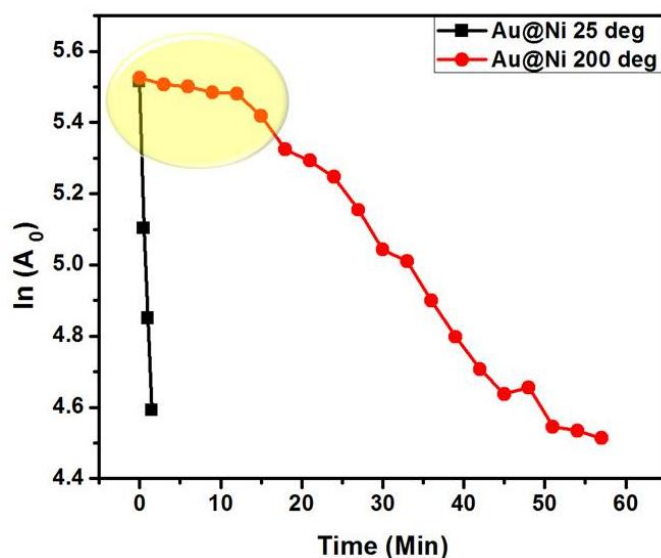
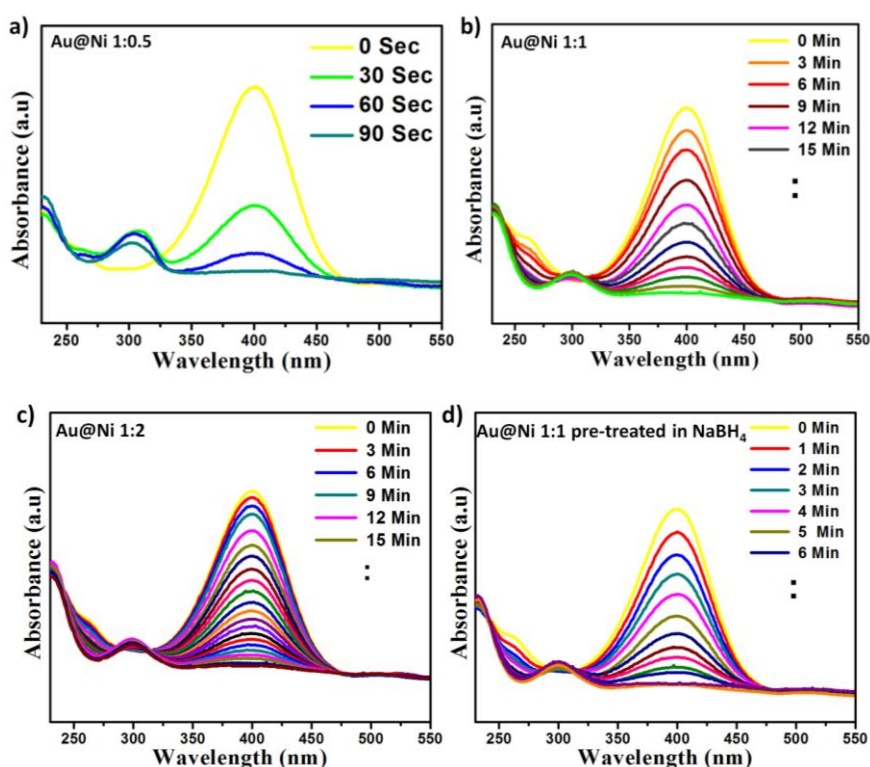


Figure 2A.25 UV-Vis peak quantification showing the decrease in the absorbance of nitrophenolate ion at 400 nm (reactant) during PNP reduction reaction catalyzed by as synthesized (RT) and pre heated (200 °C) Au@Ni_{HCP} core-shell nanoparticles. The yellow shaded region shows the difference in the induction period for initiating the reaction.

2A.2.8 Effect of Nickel Shell Thickness on the Catalytic Activity of Magnetic Au@Ni Core-shell Nanoparticles for Nitro (-NO₂) Group Reductions

Even though, the XPS analysis revealed considerable oxidation resistance to nickel layers over the gold core when the shell thickness was very less, the extent of these modifications that can influence the reactivity of the core-shell bimetallic nanostructures was still unknown. Hence the core-shell nanoparticles with various shell thickness ranging from 2 nm to 8 nm were employed for catalytic nitro group reduction to understand the extent of synergism. Core-shell catalysts Au@Ni_{1:0.5}, Au@Ni_{1:1} and Au@Ni_{1:2} were analyzed for the catalytic activity in nitrophenol reduction and nitrothiophenol reduction. In a similar case as demonstrated in the previous section, nitrophenol reduction started with a peak at 400 nm denoting the nitrophenolate ion, which decreased continuously with time and the emergence of aminophenol peak at 300 nm is noted. Similarly in the case of PNTTP reduction reaction the major absorption peak at 410 nm after addition of sodium borohydride to the parent PNTTP solution indicates the presence of nitrothiophenolate ions which in turn disappears leading to the emergence of new peak at 260 nm for paraaminothiophenol (PATP).



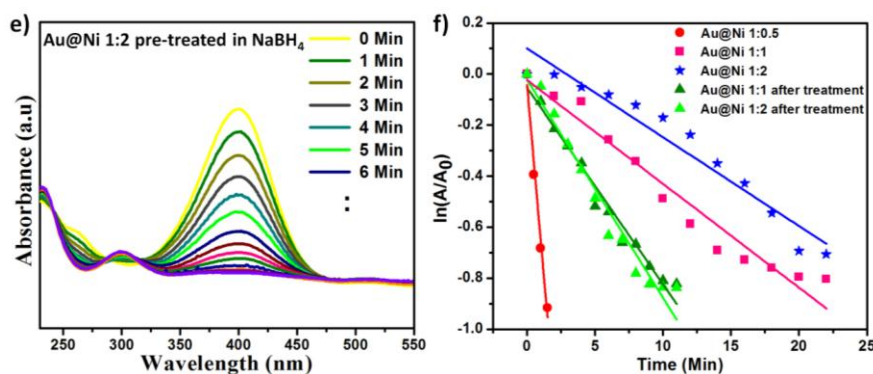


Figure 2A.26 UV-Vis spectra obtained for PNP reduction by using as synthesised (a) Au@Ni_{1:0.5}, (b) Au@Ni_{1:1} and (c) Au@Ni_{1:2} nanoparticles and catalysts (d) Au@Ni_{1:1} and (e) Au@Ni_{1:2} used after NaBH₄ pre-treatment. Their corresponding rate curves are plotted in (f).

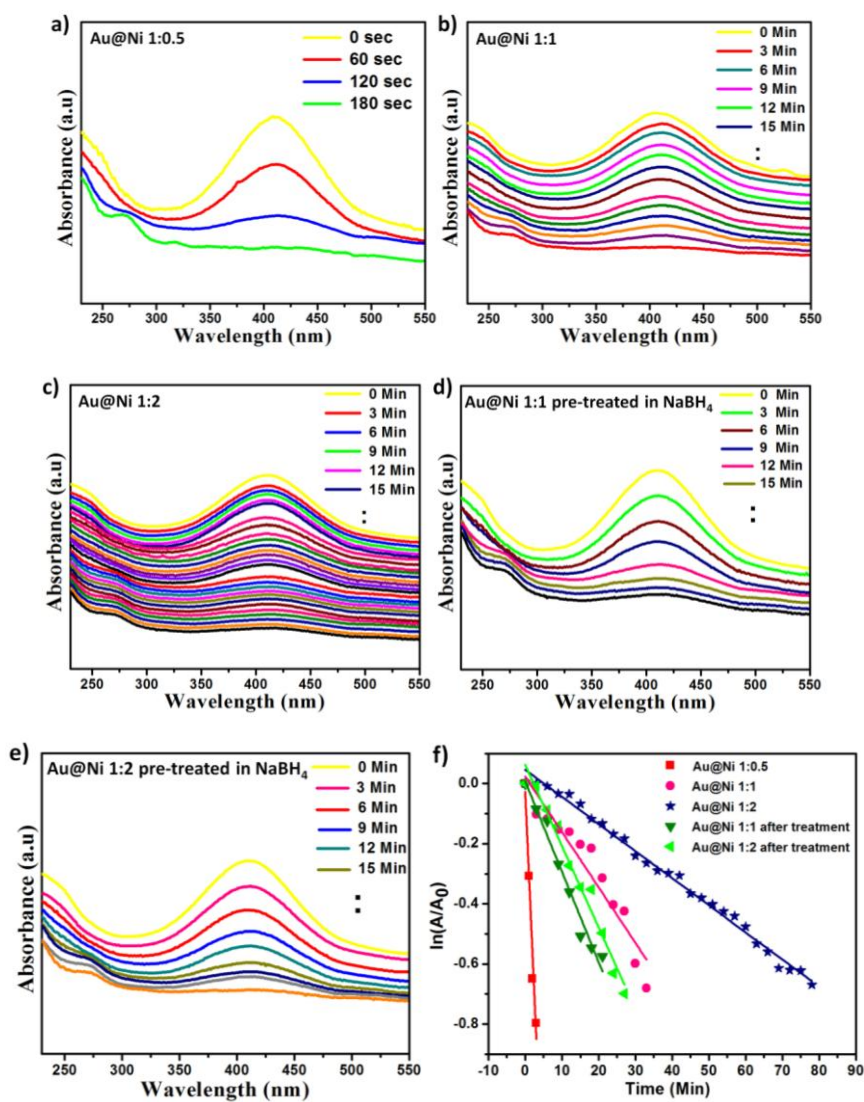


Figure 2A.27 UV-Vis spectra obtained for PNTp reduction by using as synthesised (a) Au@Ni_{1:0.5}, (b) Au@Ni_{1:1} and (c) Au@Ni_{1:2} nanoparticles and catalysts (d) Au@Ni_{1:1} and (e) Au@Ni_{1:2} used after NaBH₄ pre-treatment. Their corresponding rate curves are plotted in (f).

The results of the reduction reaction for catalysts with different Ni shell thickness are shown in Figure 2A.28a and b, where the rates of the reaction for the three catalysts are plotted. (For raw UV-Vis spectra of reduction reactions and their rate curves see Figure 2A.26 and 27). The rate of PNP and PNTP reduction reaction from monometallic gold nanoparticles of approximately 10 nm is also shown in Figure 2A.28a and b for comparison with bimetallic nanoparticles. It should be noted that bare gold nanoparticles are active for the reduction reaction and shows no induction period. This is because the as synthesized gold particles are already in metallic regime unlikely to nickel. From the rate plot it can be clearly seen that a thin nickel shell of approximately 2 nm above the gold core ($\text{Au@Ni}_{1:0.5}$ equivalent to $\text{Au@Ni}_{\text{FCC}}$ in previous discussion) makes a much more active catalyst than bare gold nanoparticles. This is evident from the much better reaction rates and hence time taken for the complete reduction of PNP (plotted in the second Y-axis). It is quite evident that the rate of the reaction becomes extremely sluggish on further increasing the nickel shell thickness. Thus reduction rates were an order lower with several tens of minutes to complete the reduction. The rate pattern was highly reproducible with $\text{Au@Ni}_{1:0.5}$ catalyst showing better activity compared to monometallic gold nanoparticle, nickel nanoparticle or the ones with thicker nickel shell. It is well known that geometric or electronic modification operates only up to few atomic layers. The results from the present study clearly demonstrate that upon growing nickel by more than 2 nm (approximately 10 atomic layers) the synergistic effects are completely lost due to the decoupling of electronic/geometric effects from the gold core thereby behaving the nickel surface more like monometallic nickel. What is more interesting is that when the shell thickness is approximately 2 nm the catalyst is considerably more active than bare gold nanoparticles. Thus, the rate of $\text{Au@Ni}_{1:0.5}$ catalyst is approximately 28 % and 62 % more than bare gold nanoparticle for PNP and PNTP reduction reaction respectively. Similarly, the same catalyst showed 13 and 35 times more enhancement in activity for PNP and PNTP reduction compared to monometallic nickel nanoparticles. The Figure 2A.28a and b also shows the induction period for $\text{Au@Ni}_{1:1}$ and $\text{Au@Ni}_{1:2}$ catalysts plotted in second X-axis. From the figure it is evident that $\text{Au@Ni}_{1:1}$ and $\text{Au@Ni}_{1:2}$ catalysts took approximately 4 and 8 minutes to commence the PNP reduction reaction whereas $\text{Au@Ni}_{1:0.5}$ proceeded without any induction period. The observed large induction period in the case of catalysts with higher nickel shell thickness is considered to be the time required by NaBH_4 to reduce the surface oxide to the active metallic Ni phase²³. A similar trend is observed for the Au@Ni core-shell catalysts in the case of induction period analysis for PNTP reduction results.

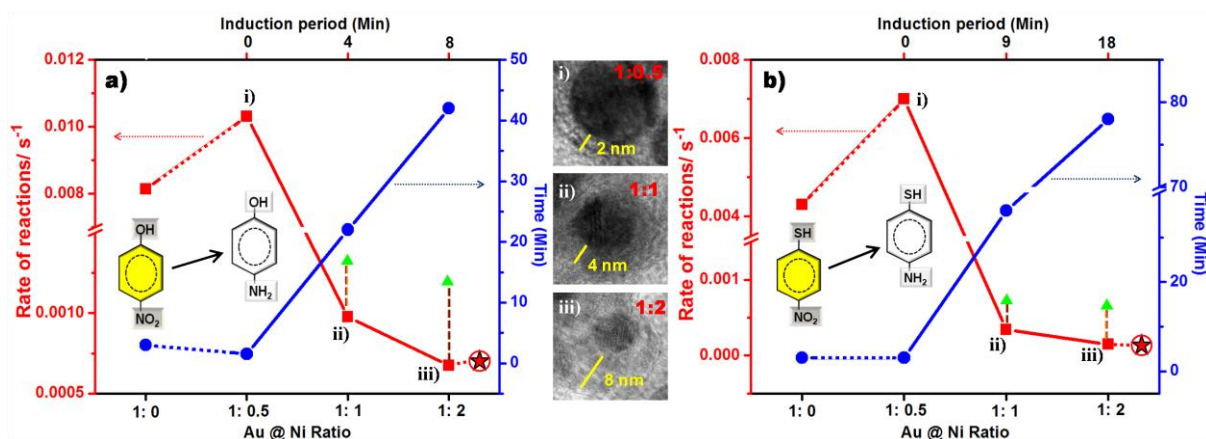


Figure 2A.28 The reactivity trend obtained for (i) Au@Ni_{1:0.5}, (ii) Au@Ni_{1:1} and (iii) Au@Ni_{1:2} nanoparticles towards (a) PNP reduction and (b) PNTTP reduction in comparison with monometallic Au and Ni (Red circled star) nanoparticles and their corresponding HR-TEM images showing the thickness of nickel shell. Green symbols indicate a marginal increase in the rate of nitro reductions by the catalysts Au@Ni_{1:1} and Au@Ni_{1:2} after pre-treatment with NaBH₄. (Red curve indicates the rate of reaction whereas blue curve indicates the time taken for the reaction and is joined by lines to show the trend; note that bare Au and Ni nanoparticles do not have the upper X-axis which stands for induction period).

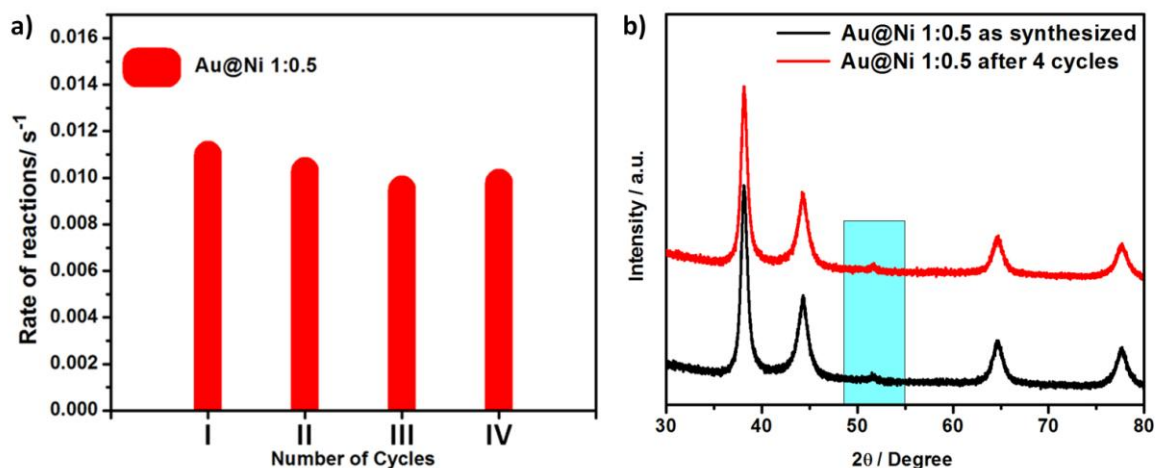


Figure 2A.29 (a) Rate of reaction obtained for PNP reduction by using Au@Ni_{1:0.5} catalyst after recovering the catalyst with an external magnet and tested the recyclability up to four cycles. (b) XRD pattern of Au@Ni_{1:0.5} after 4 cycles of catalyst activity test. The shaded area shows the stability of metallic nickel feature even after various cycles of catalyst recyclability test.

At this stage, it was relevant to check the catalytic activity of a pre-treated catalyst in NaBH_4 which can reduce the surface oxide and expose nickel metal surface. Whether such a surface can show reduction rates for the reaction better or comparable than $\text{Au@Ni}_{1:0.5}$ catalyst? The two catalysts with higher nickel shell thicknesses existing in the core-shell morphology were pre-treated with aqueous NaBH_4 solution and analysed for the catalytic activity. The results of the NaBH_4 pre-treated core-shell catalysts are also depicted in Figure 2A.28a and b. There is a clear indication that even though there is a marginal improvement in reactivity in both the reduction reaction, the rates were nowhere comparable to $\text{Au@Ni}_{1:0.5}$. The results obtained confirmed that $\text{Au@Ni}_{1:0.5}$ catalyst with a thin nickel shell is electronically/geometrically perturbed thereby showing activity drastically different from the monometallic counterparts and with the ones with higher shell thickness. The synergistic effect and the reduction rates corroborate well with the XPS analysis which gave almost 50 % of metallic nickel for $\text{Au@Ni}_{1:0.5}$ whereas $\text{Au@Ni}_{1:1}$ and $\text{Au@Ni}_{1:2}$ showed no signs of metallic features. The sustainability of synergistic catalytic activity of $\text{Au@Ni}_{1:0.5}$ persists even after four cycles as demonstrated by catalyst recyclability test (Figure 2A.29a) done by recovering the catalyst with the aid of an external magnet from the reaction medium. The spent catalyst characterizations using XRD also confirmed that there was no structural change in the $\text{Au@Ni}_{\text{FCC}}$ core-shell nanoparticle catalysts since it retained its metallic signature at 2θ value 51.8 (Figure 2A.29b). The results obtained in the current study shows that the combination of gold with a non-noble metal like nickel can be highly effective for enhancing the rate of reduction of $-\text{NO}_2$ group even in presence of a poisoning group, since the activity trend follows the same order in the presence of both $-\text{OH}$ and $-\text{SH}$ functional groups on the ring.

Chapter 2B: Synthesis of Magnetic Au@Ni Core-shell Nanoparticles under Mild Conditions and Catalytic Activity Results for Selective Hydrogenation of Phenylacetylene (P.A)

2B.1 Experimental Section

Hydrogen tetrachloroaurate trihydrate [HAuCl₄.3H₂O] and Nickelacetylacetonate [Ni(acac)₂] serves as metal precursors whereas NaBH₄, NH₂-NH₂.H₂O/NaOH were used as the reducing agents and they were purchased from Sigma Aldrich [Germany] including solvent Oleyl amine. Remaining compounds like Phenyl acetylene, TPP along with other solvents Methanol, DCM, THF, Ethanol and Hexane were purchased from Merck.

Synthesis of Magnetic Au@Ni Core-shell Nanoparticles at Low Temperature

Au@Ni core-shell nanoparticles were synthesised through an energy efficient way without going for high temperature thermal reduction methods. In the first stage, gold nanoparticles were synthesised by the reduction of 0.025 mmol gold precursor solution dissolved in 6 ml oleylamine using 30µL of 0.1M aqueous NaBH₄ solution. The solution stirred well for 15 minutes for the complete reduction of gold ions in to gold nanoparticles which was evident by the formation of wine red colour colloidal solution. In the second stage, the gold seed solution was heated to 45 °C, followed by the addition of 0.02 mmol of nickel precursor [Ni(acac)₂], the entire solution mixture was heated to 80 °C with simultaneous addition of 0.015 mmol TPP. After reaching the desired temperature 500µL N₂H₄.H₂O/NaOH mixture was added drop wise very slowly [the mixture was prepared by dissolving 50 mg NaOH in 5 ml hydrazine hydrate solution (80 %)]. The solution further stirred well for 20 minutes to get a brownish black colloidal solution which in turn sticks to the magnetic bead inside the solution. The disappearance of wine red colour indicated the reduction of nickel ions on the surface of preformed gold nanoparticles and resulted in a black colloidal solution. Finally magnetic core-shell nanoparticles were recovered with the help of an external magnet, washed with hexane-ethanol mixture thoroughly to remove excess of capping agents and redispersed in hexane for further characterizations. For catalytic applications the Au@Ni core-shell nanoparticles were washed thoroughly with the respective solvents before the hydrogenations reactions were conducted.

Liquid Phase Hydrogenation of Phenylacetylene (P.A)

Hydrogenation of phenylacetylene under different reaction parameters were carried out in a Parr stirred tank reactor having a volume of 100 ml capacity. In a typical hydrogenation reaction the stirred tank is charged with 5 mg of the Au@Ni catalyst dispersed in 50 ml solvent. After that 5 mmol of the substrate was added to the reaction vessel. The reaction vessel was closed and flushed with hydrogen 3 times to remove the air and other impurities from the vessel then pressurised to the desired condition. The reactions were done at desired temperatures with continuous stirring. The samples were collected at specific time intervals and analysed with the help of a Gas chromatograph (GC) having a HP-1 capillary column and equipped with a flame ionization detector. The reactants and products were identified and analysed with the help of calibration using standard samples of the respective compounds.

2B.2 Results and Discussion

2B.2.1 UV-Vis Spectroscopy Analysis (UV-Vis)

The synthesis of gold core nanoparticles and the growth of nickel as a shell over the core can be monitored by the UV-Vis spectroscopy technique as demonstrated in the previous section 2A. The UV-Vis spectra obtained at different stages of the synthesis are shown in Figure 2B.1.

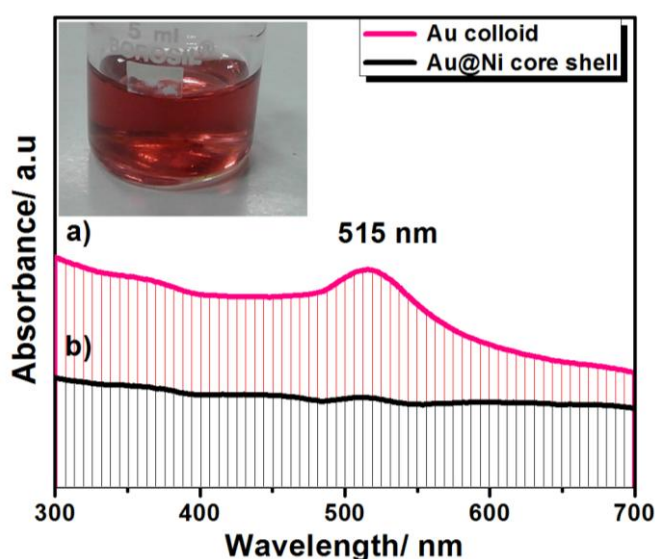


Figure 2B.1 UV-Vis spectra recorded for (a) colloidal gold seed solution and (b) Au@Ni core-shell nanoparticles. (Inset shows the photograph of wine red colour gold colloid).

The wine red colour of the colloidal solution due to the surface plasmon resonance (SPR) after the reduction of gold ions, indicated the formation of gold (Au) nanoparticles which gave an absorption maximum at 515 nm in the UV-Vis analysis³⁸. The preformed gold seeds act as nucleation sites for the adsorption of the nickel ions in the second stage which subsequently undergo reduction upon addition of hydrazine/NaOH mixture at 80 °C to form the bimetallic core-shell nanoparticles. The complete damping of the gold plasmon band resulting in blank absorption spectra in the UV-Vis analysis happened in the final stage of nickel reduction showed the successful coating of nickel shell over the gold core¹⁸.

2B.2.2 Transmission Electron Microscopy Studies (TEM)

Figure 2B.2 shows the TEM image of the as synthesized bimetallic Au@Ni nanoparticles drop cast on the Cu grid after sonication for 5 minutes in hexane. The large area TEM analysis (Figure 2B.2a) showed the size distribution of nanoparticles ranging from 15 to 20 nm. From the Figure 2B.2b and c, it is evident that the gold core size around 12-15 nm and nickel shell thickness of approximately 2 nm. The HR-TEM image of a single particle in Figure 2B.2b shows a clear contrast difference between the heavier noble metal Au and a lighter non-noble metal Ni indicating the formation of a core-shell morphology³⁶. The lattice fringe analysis at the core and shell (Figure 2B.2c) gave the standard values of 2.38 Å and 2.04 Å for gold and nickel respectively, confirming that nickel is present as the shell and gold at the core¹⁵.

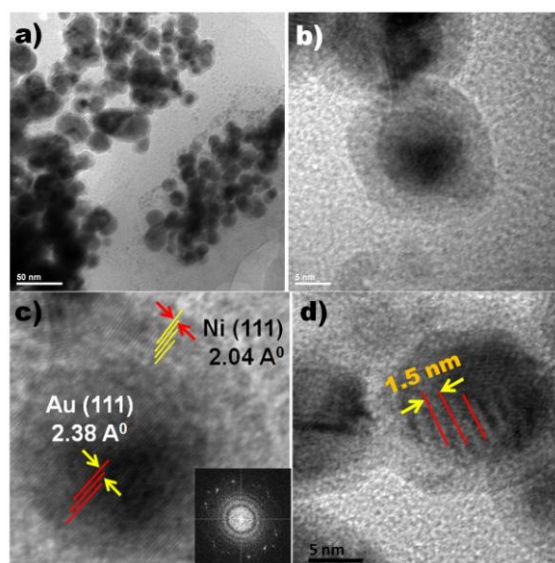


Figure 2B.2 (a) Large area TEM and (b-d) HR-TEM images of Au@Ni core-shell nanoparticles. The inset of (c) shows the FFT pattern of an individual Au@Ni core-shell nanoparticle.

The FFT (Fast Fourier transform) pattern (inset of Figure 2B.2c) also indicated the presence of gold and nickel d-spacing values. Figure 2B.2d shows evidence of Moiré fringes with 1.5 nm distances as observed in the previous case of gold and nickel lattice combinations^{41, 65}. Thus, the microscopy observations provided here confirmed the formation of Au@Ni core-shell system under milder conditions reported so far with oleylamine as the solvent.

2B.2.3 X-Ray Diffraction Studies (XRD)

Powder XRD analysis of Au@Ni bimetallic nanoparticles are shown in Figure 2B.3. The diffraction from the gold and nickel planes indicates that both the metals exist in FCC crystal structure without any alloying effects irrespective of the modified synthesis strategy. The fairly large FWHM (full width at half maximum) values of the XRD peaks indicate the small size of the nanoparticles. The diffraction pattern observed in Figure 2B.3 correspond to monometallic gold (curve b), nickel (curve a) and bimetallic Au@Ni (curve c) core-shell nanoparticles. The diffractions at 2θ values of 38.2, 44.3 and 64.6 correspond to Au (111), Au (200) and Au (220), respectively. Similarly, Ni (111), Ni (200) and Ni (220) are diffracted at 2θ values of 44.5, 51.8 and 76.4, respectively¹⁶. Since there is strong overlap of diffractions from Au (200) and Ni (111) in the case of bimetallic Au-Ni systems, the most discernable peak for the identification of nickel is at 2θ value of 51.8. The less intense and very broad peak at 51.8 in the enlarged Figure 2B.3 (shaded region) of the Au@Ni core-shell nanoparticle gives confirmation of the thin nickel lattice on the gold core⁴¹.

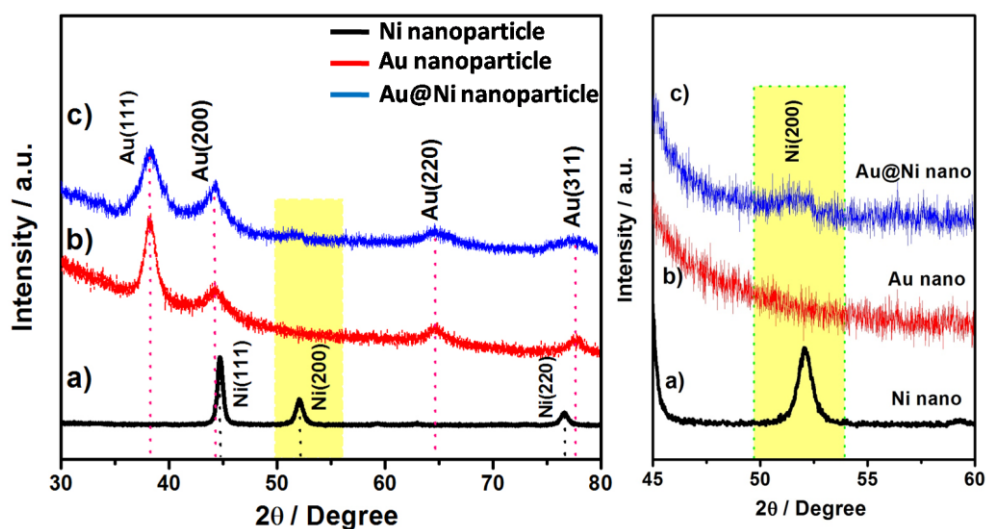


Figure 2B.3 XRD patterns of monometallic (a) Ni nanoparticles, (b) Au nanoparticles and

bimetallic (c) Au@Ni core-shell nanoparticles. Pink and black dotted lines indicate the standard gold and nickel reflections respectively. The enlarged area of the XRD shows the Ni (200) reflection at 51.8 (shaded region) confirming the FCC lattice of metallic nickel.

It is understandable that the diffractions from the nickel lattice in the case of Au@Ni are not clearly visible because of the extremely thin nickel shell on the gold core. However, in the case of monometallic nickel nanoparticles, the reflections are predominant and they confirm the formation of a pure FCC phase⁹ of the nickel metal obtained through the same synthesis protocol.

2B.2.4 Magnetic Measurements (VSM)

Nickel in FCC crystal structure is well known for its ferromagnetic behaviour⁷. The magnetic properties of Au@Ni core-shell nanoparticles are demonstrated by measuring the hysteresis loop using VSM. Figure 2B.4 shows the magnetic behaviour of Au@Ni core-shell nanoparticles with a typical hysteric behaviour of ferromagnetic nickel. A very low saturation magnetization of 2 emu/gm is observed in an applied field of 6 kOe. The inset of the image (below) shows the remanent magnetisation of the material along with very low coercivity values.

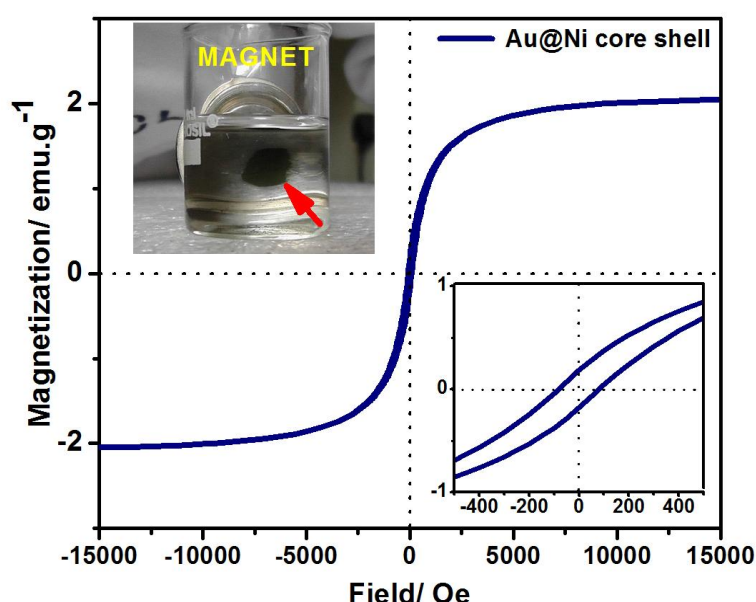


Figure 2B.4 Hysteresis loops obtained for Au@Ni core-shell nanoparticles measured at room temperature in VSM analysis. [Inset (down) shows the hysteresis width near to the origin and photograph (above) of bimetallic nanoparticles attracted towards a magnet].

2B.2.5 X-ray Photoelectron Spectroscopy Investigation (XPS)

To understand the surface electronic state of the core-shell nanoparticles synthesized using low temperature method, XPS analysis was performed. Figure 2B.5a demonstrates the wide area scan of the as synthesized samples. It shows the presence of characteristic signature peaks from gold, nickel, oxygen and carbon [Carbon can be from the atmospheric contamination or from any residual capping agent, similarly oxygen also can be an impurity or from the hydroxide feature]. The peak positions were calibrated by considering a carbon standard value at 284.6 eV. Figure 2B.5b and c are the individual scans performed for gold and nickel core levels, respectively.

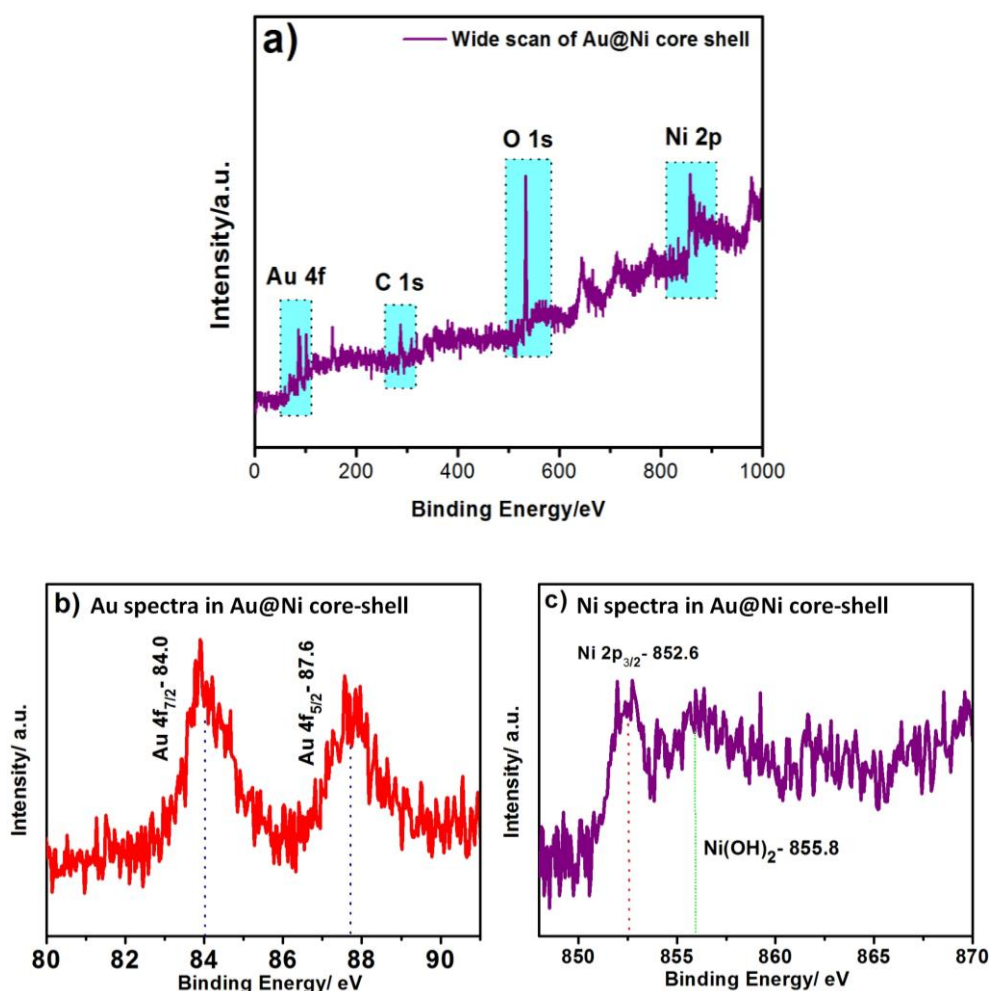


Figure 2B.5 (a) Wide scan XPS spectra obtained for Au@Ni core-shell nanoparticles. The shaded areas indicate the presence of typical binding energy values of Au, Ni, C and O elements. Individual XPS spectra of (b) Au 4f and (c) Ni 2p obtained for Au@Ni core-shell nanoparticles. The red dotted line in (c) indicates the nickel metallic feature, whereas green corresponds to the hydroxide feature.

The Ni 2p_{3/2} spectra (Figure 2B.5c) from the bimetallic Au@Ni core-shell provide evidence for the metallic feature (852.6 eV) along with broad hydroxide feature centered around 855.8 eV⁵². The solution phase synthesis of nickel nanoparticles always produces some amount of hydroxides on the surface which is unavoidable under such wet chemical reduction methods¹⁶. The absence of NiO peak at 854 eV in the nickel spectra and the presence of more than 50 % of metallic nickel species even after exposure to the atmosphere proved the strong surface modification in the Au-Ni bimetallic combination. This observation is a direct demonstration of the gold core-induced surface modification of the ultrathin nickel shell which shows resistance towards surface oxidation. The individual gold scan in XPS (Figure 2B.5b) showed binding energy values of 84 eV (4f_{7/2}) and 87.6 eV (4f_{5/2}) which are typical of metallic gold⁶⁶. These two peaks arise due to the spin orbit splitting of 4f energy levels and the ejection of 4f core level photoelectrons.

2B.2.6 Catalytic Activity Results of Au@Ni Core-shell Nanoparticles for Selective Hydrogenation of Phenylacetylene (P.A) to Styrene and E.B

Our previous results in the chapter 2A demonstrated the need for an extremely thin nickel shell for the optimum synergistic effects in catalysis. The core-shell nanoparticles synthesized through an energy efficient way with a thin nickel shell thickness of approximately 2 nm were tested for potential applications in catalysis by carrying out hydrogenation reactions. Monometallic Ni surface is prone to oxidation even under ambient conditions and it is known to form surface oxides^{16, 53} which poison the catalytic activity of the materials. The formation of oxide layers is found to limit the hydrogenation pathway; hence, the need of retaining of the metallic feature is necessary for efficient catalytic activity⁶⁰. To test the efficiency of the synthesized Au@Ni bimetallic system, the catalytic tests of core-shell particles were carried out for phenylacetylene (P.A) hydrogenation reaction. The reaction is a testing ground for activity and selectivity correlations where ethylbenzene and styrene can be formed as the hydrogenation products. The reaction was carried out using a stirred type Parr reactor which can go up to 300 °C in temperature and up to 50 bar pressure. The reaction conditions were optimized by carrying out a range of experiments by varying the pressure and temperature conditions (conditions shown in the respective Figure captions). The reaction mixture was analyzed with the help of an offline GC. Initially, catalytic tests of the core-shell systems with their monometallic counterparts are carried out for understanding the enhancement in catalytic activity.

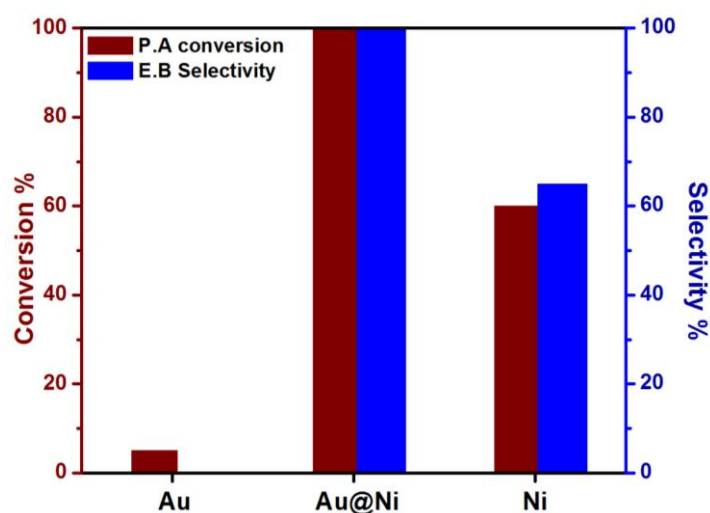


Figure 2B.6 Phenylacetylene (P.A) conversion (brown) and ethylbenzene (E.B) selectivity (blue) in methanol solvent obtained for Au@Ni core-shell catalysts and their monometallic counterparts (Au and Ni). The reaction conditions are given as follows: Temp.- 50 °C and 50 psi H₂ pressure [catalyst weight - 5 mg, substrate - 5 mmol and reaction time - 4 hours].

To exclude the influence of quantum size effects in catalytic activity, the activity of bare gold and nickel nanoparticles having a similar size (around 15 and 20 nm, respectively) are also compared with Au@Ni core-shell nanoparticles. Figure 2B.6 shows the phenylacetylene (P.A) hydrogenation results for monometallic gold nanoparticles, nickel nanoparticles and Au@Ni core-shell nanoparticles in methanol (MeOH) solvent carried out at 50 °C and 50 psi pressure. From the reactivity analysis in Figure 2B.6, it can be seen that Au@Ni core-shell nanoparticles showed excellent reactivity and selectivity for ethylbenzene (E.B). Under similar conditions, nickel nanoparticles achieved only 60 % conversion and 65 % selectivity to E.B with gold nanoparticles being negligibly active. The poor activity on gold can be attributed to the large size of gold nanoparticles in this case (~15 nm), while a recent report has suggested the particle size of ~5 nm for gold nanoparticles to be optimum for selective conversion towards styrene⁶⁷. In the case of nickel nanoparticles, most of the phenylacetylene hydrogenation has been carried out using intermetallics of nickel to tune the selectivity towards industrially important product styrene⁶⁸⁻⁶⁹. The activity of Au@Ni nanoparticles reported here shows that the catalyst is extremely active where the triple bond in P.A can be totally saturated at near ambient conditions. The effect of solvent and temperature on the catalytic activity of Au@Ni core-shell nanoparticles for P.A hydrogenation is shown in Figure 2B.7 and Table 2B.1, respectively. The reaction results show that there is a strong

dependence of solvent and temperature on the conversion rates. The reactions were carried out in different solvents like methanol (MeOH), tetrahydrofuran (THF) and dichloromethane (DCM). These solvents were chosen as it was previously reported that the selectivity towards the desired product (styrene) crucially depends on the solvent⁶⁴. In the presence of methanol and THF as solvents, the optimum conditions for hydrogenation of carbon-carbon triple bonds are 50 °C and 50 psi pressure, produced 100 % conversion and selectivity towards ethylbenzene. The reaction rate was lower in THF which took almost 7 hours for complete conversion compared to 4 hours in methanol. In DCM as solvent, similar conversion results were obtained, whereas the selectivity switched towards styrene with 80 % (Figure 2B.7), which has a high commercial value in the polymer industry, and the remaining product was ethylbenzene. The effect of solvent plays a crucial role in deciding the selectivity which is known for some other bimetallic combination like Fe-Ni reported by Vivek et al⁶⁴, whereas Au@Ni core-shell catalyst is highly active to produce styrene under these mild reaction conditions of temperature and pressure. In DCM solvent, the rate was much slower as compared to MeOH solvent because of the lower optimum temperature (40 °C) used for the hydrogenation reaction. For complete conversion in DCM solvent, it took 10 hours but with good selectivity towards styrene. Under similar conditions, nickel nanoparticles showed only 55 % conversion demonstrating the synergistic effects in Au@Ni core-shell nanoparticles. From the conversion and selectivity analysis, it was noted that methanol is more suitable for ethylbenzene production via the complete hydrogenation and DCM is suitable for the partial hydrogenation to styrene. To explore further on the temperature and solvent effects, a series of hydrogenation reactions were carried out and the results are tabulated in Table 2B.1. A decrease in temperature of the reaction conditions close to room temperature (30 °C) marked a decrease of ~40 % in the conversion rates of both the solvents (MeOH and DCM). Interestingly, the selectivity towards styrene is found higher while lowering the temperature which shows that the complete hydrogenation pathway goes through styrene. From these results, it can be observed that the selectivity towards a desired product can be controlled by temperature and solvent where as the conversion rates of the reaction can be modified by the bimetallic nanoparticles as compared to their parent components.

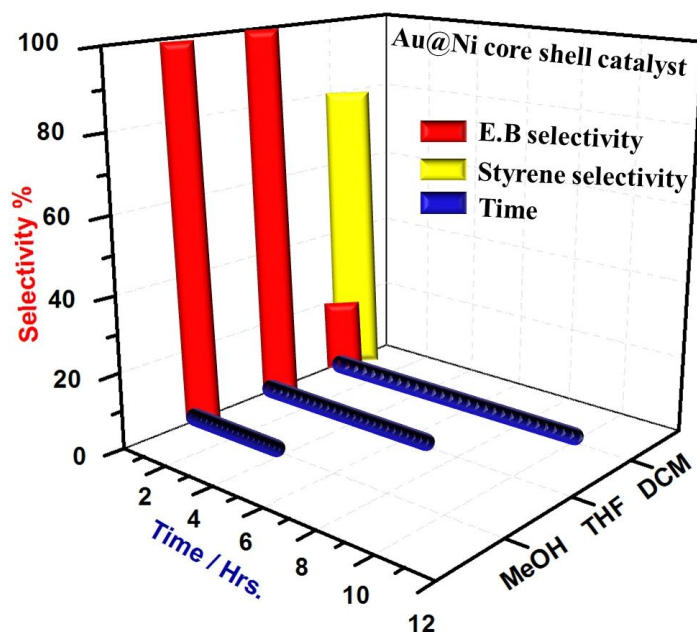


Figure 2B.7 Selectivity results (red and yellow) obtained for complete conversion of P.A in various solvents by using Au@Ni core-shell catalysts. The blue bar represents the time taken for complete conversion [Reaction conditions: for MeOH and THF: Temp.- 50 °C and 50 psi H₂ pressure; catalyst - 5 mg; substrate - 5 mmol. For DCM: Temp.- 40 °C and 50 psi H₂ pressure; catalyst - 10 mg; substrate - 1 mmol].

| Serial No. | Catalyst | Amount (mg) | Time (Hrs) | Solvent | Temp. (deg C) | Press. (psi) | Conversion | Selectivity (%) E.B/Styrene |
|------------|--------------|-------------|------------|-------------|---------------|--------------|-------------|-----------------------------|
| 1 | Ni alone | 5 | 4 | MeOH | 50 | 50 | 60% | 65 / 35 |
| 2 | Au@Ni | 5 | 4 | MeOH | 50 | 50 | 100% | 100 / 0 |
| 3 | Ni alone | 5 | 4 | MeOH | 30 | 50 | 35% | 50 / 50 |
| 4 | Au@Ni | 5 | 4 | MeOH | 30 | 50 | 60% | 60 / 40 |
| 5 | Ni alone | 10 | 10 | DCM | 40 | 50 | 55% | 25 / 75 |
| 6 | Au@Ni | 10 | 10 | DCM | 40 | 50 | 100% | 20 / 80 |
| 7 | Ni alone | 10 | 10 | DCM | 30 | 50 | 30% | 20 / 80 |
| 8 | Au@Ni | 10 | 10 | DCM | 30 | 50 | 65% | 15 / 85 |

Table 2B.1 Hydrogenation results obtained for P.A by using Au@Ni catalysts and Ni nanoparticles in MeOH (50 ml) and DCM (50 ml) under various temperatures [in MeOH and DCM, the substrate is 5 and 1 mmol, respectively]

Chapter 2C: Green Route (Soyabean Oil as Solvent) for the Synthesis of Au@Ni Core-shell Nanostructures and Their Catalytic Activity Studies

2C.1 Experimental Section

Hydrogen tetrachloroaurate tri hydrate [$\text{HAuCl}_4 \cdot 3\text{H}_2\text{O}$] and Nickel acetylacetonate [$\text{Ni}(\text{acac})_2$] were used as metal precursors whereas NaBH_4 and $\text{NH}_2\text{-NH}_2 \cdot \text{H}_2\text{O}$ (80 %)/ NaOH were used as the reducing agents. They were purchased from Sigma Aldrich [Germany]. Phenylacetylene was used for catalyst activity tests and purchased from Merck along with other chemicals NaOH , Methanol, DCM, Ethanol and Hexane. Soya bean oil was purchased from Indian brand Fortune, a product of Adani Wilmar group.

Synthesis of Au@Ni Core-shell Nanoparticles and Nanochains in Soyabean Oil

In a successive reduction method, 2.5×10^{-4} M gold precursor solution was prepared in 50 ml soyabean oil. The solution was stirred well for 15 minutes to get a bright yellow solution. At this stage, 500 μL of freshly prepared ice cold 0.1 M NaBH_4 solution prepared in Millipore water was added to the gold precursor solution with vigorous stirring. An immediate colour change occurs and the solution turned to wine red colour indicating the formation of gold nanoparticles. Immediately after the gold nanoparticle formation 0.01 mmol of nickel precursor was added and the resultant solution further stirred well followed by the addition of 500 μL acetone. The resultant solution was heated to 70°C , at this temperature and 750 μL of $\text{N}_2\text{H}_4 \cdot \text{H}_2\text{O}/\text{NaOH}$ mixture [25 mg NaOH dissolved in 5 ml Hydrazinehydrate (80 %)] was added to the solution drop wise with vigorous stirring. The solution stirred at the same temperature for further 20 minutes, resulting in the formation of black Au@Ni core-shell nanoparticles sticking to the magnetic bead inside the reaction mixture. In the final stage, the magnetically active colloidal Au@Ni core-shell nanochains were removed from the oil by using an external magnet. The absence of wine red colour in the supernatant solution indicates the effective coating of nickel on the gold nanoparticle surface which resulted in the complete damping of gold plasmon. The as synthesised Au@Ni magnetic core-shell nanostructures were thoroughly washed with a mixture of ethanol-hexane solution and redispersed in ethanol for further characterization and analysis. To get Au@Ni magnetic individual core-shell nanoparticles, the synthesis step was modified slightly with the addition of capping agent CTAB. 250 mg CTAB is added to the reaction mixture to protect the magnetic core-shell

nanoparticles after the addition of nickel precursor in the above mentioned synthesis protocol. In the final stage, a black colloidal suspension was obtained in which Au@Ni core-shell nanoparticles were stabilised by the capping agent which in turn sticks to the magnetic bead. For catalytic studies the Au@Ni core-shell nanoparticles/chains were washed repeatedly with the respective solvents before the reactions were conducted.

Liquid Phase Hydrogenation of Phenylacetylene (P.A)

Hydrogenation of phenylacetylene under different reaction parameters were carried out in a Parr stirred tank reactor having a volume of 100 ml capacity. In a typical hydrogenation reaction the stirred tank was charged with 5 mg of the Au@Ni catalyst dispersed in 50 ml solvent. After that 5 mmol of the substrate was added to the reaction vessel. The reaction vessel was closed and flushed with hydrogen 3 times to remove the air and other impurities from the vessel then it is pressurised to the desired condition. The reactions were done at desired temperatures with continuous stirring. The samples were collected at specific time intervals and analysed with the help of a Gas chromatograph having a HP-1 capillary column and equipped with a flame ionization detector. The reactants and products were identified and analysed with the help of calibration using standard samples of the respective compounds.

2C.2 Results and Discussion

2C.2.1 UV-Vis Spectroscopy Analysis (UV-Vis)

In the first stage, gold precursor (tetrachloroauric acid) was dissolved in soyabean oil followed by the addition of the reducing agent, sodium borohydride. The reduction of gold ions results in the formation of gold nanoparticle seeds and it is indicated by the formation of a wine red colour colloidal solution. The formation of gold nanoparticles having size around 10 nm can be monitored with the help of a UV-Vis spectrophotometer due to the surface plasmon resonance (SPR) property of gold nanoparticles³⁸. UV-Vis experimental observations gave the spectroscopic evidence for the formation of gold nanoparticles with an absorbance peak centered at 520 nm after the first stage of reduction¹⁸ (Figure 2C.1). In both the synthesis method, the same gold seed was used in the initial stage, which gave the same SPR pattern in UV-Vis spectra. It is really worth to follow these SPR properties, especially in the case of bimetallic nanoparticle synthesis. In the second stage, nickel precursor was added and

dissolved completely followed by the addition of CTAB (also carried out the synthesis where CTAB was not added to growth medium). Here the role of CTAB is to protect the nickel shell after reduction on gold core. The complete damping of the surface plasmon resonance in the final stage of core-shell nanoparticle synthesis implies the successful generation of core-shell morphology¹⁸ or in other words the complete masking of gold surfaces from the interaction with light. The role of CTAB is clearly visible in TEM images that shows isolated gold-nickel core-shell bimetallic nanoparticles (discussed later). Figure 2C.1 also shows the complete disappearance of this SPR absorbance of gold after the reduction of nickel ions, which showed no absorbance in the UV-Vis region. This is understandable, as nickel is not SPR active and not expected to show absorbance in this spectral region. The supernatant solution after the complete reduction of Ni^{2+} ions and the isolation of Au@Ni nanoparticles with an external magnetic field is also demonstrated in Figure 2C.1.

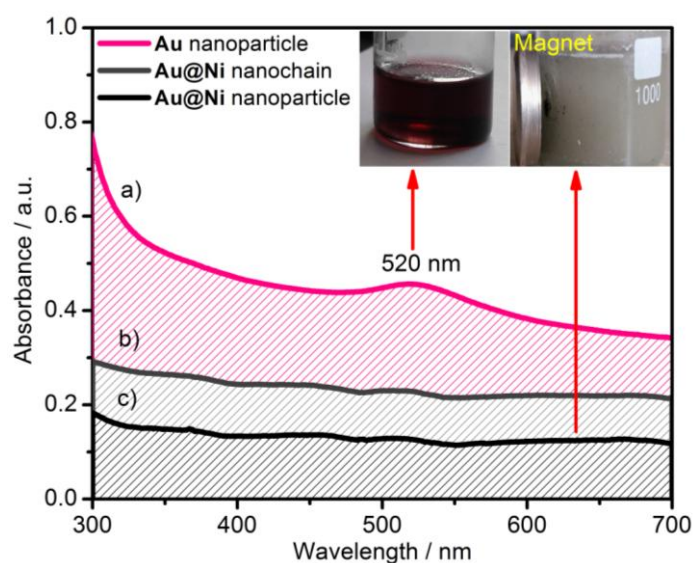


Figure 2C.1 UV-Vis spectra recorded for (a) gold colloid and (b and c) Au@Ni core-shell nanochains and nanoparticles respectively (Inset shows the photograph of gold colloid and magnetic Au@Ni).

2C.2.2 Transmission Electron Microscopy Studies (TEM)

To characterise the nanostructures in detail, electronic microscopy analysis was carried out for the as synthesised samples. Figure 2C.2 shows the TEM and HR-TEM images of both the nanostructures drop cast on Cu grid after sonication for 5 minutes. The microscopic images and their analysis clearly showed the distinct effect of capping agents on the final

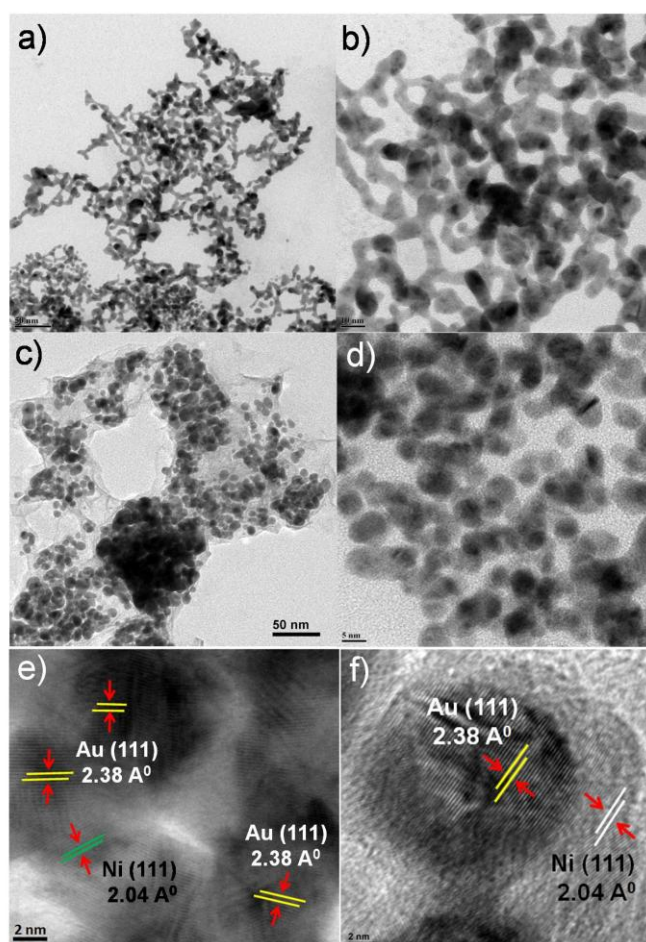


Figure 2C.2 TEM and HR-TEM images of core-shell (a, b and e) Au@Ni nanochains and (c, d and f) Au@Ni nanoparticles. (e) and (f) are the HR-TEM images of Au@Ni nanochains and Au@Ni nanoparticles respectively showing the lattice fringe analysis.

morphology of the nanostructures. The low resolution images (Figure 2C.2a-d) showed the size distribution of both nanostructures to be around 10-15 nm. Fairly good mono dispersity was observed in the case of Au@Ni core-shell nanoparticles. What is remarkable to note here is that when the surfactant CTAB was not used in the synthesis, the nanoparticles randomly aligned to form nanochains like structures, which is evident from the microscopy images. Even though, the core and shell structures are not well isolated as in the case of Au@Ni nanoparticles, the nickel covered gold particles were observed in several regions of the nanochain. There is a growing interest in making metal nanoarchitectures with nanoporous or nanochain like morphology for catalytic applications as they offer better stability with specifically exposed active sites⁷⁰⁻⁷¹. Thus the synthesis route offers a convenient protocol for making Au-Ni nanochains with a cheap and environmentally benign solvent and without

using any other surfactants. The high resolution images shows the contrast difference between gold and nickel which in turn helps to arrive at the core and shell morphology and also to make a fair measurement of core size and shell thickness. The HR-TEM images of both the nanostructures are also shown in Figure 2C.2e and f. Figure 2C.2f illustrate an individual core-shell nanoparticle with a nickel covering over the gold core. The lattice fringe analysis at the core and the shell area gave the d-spacing values of 2.38 Å and 2.04 Å respectively confirming that the Au (2.38 Å) is present as inner core and the Ni (2.04 Å) in the outer shell^{15, 36}. In the case of nanochains (Figure 2C.2e), interpenetrated Ni lattice over Au core was observed extending over several tens of nanometers. It is found that the overall size of the core-shell nanoparticle is around 15 nm with a core size around 10-12 nm and shell thickness of approximately 2 nm.

2C.2.3 X-Ray Diffraction Studies (XRD)

Powder XRD pattern obtained from Au@Ni core-shell nanoparticles and nanochains are shown in Figure 2C.3 along with monometallic nickel nanoparticles (size ~ 25 nm). The diffraction pattern observed from the core-shell nanostructures confirmed the polycrystallinity of the particles with the reflections from different planes of gold without any shift in peak positions. A fairly large FWHM value indicates that crystallite sizes of the particle are small. The diffraction experiments failed to probe the nickel shell over the gold core; possibly due to the extremely thin nickel shell. Since Au (200) and the most intense Ni (111) reflection fall in the same 2θ value, it is difficult to characterise the thin nickel shell with the XRD technique.

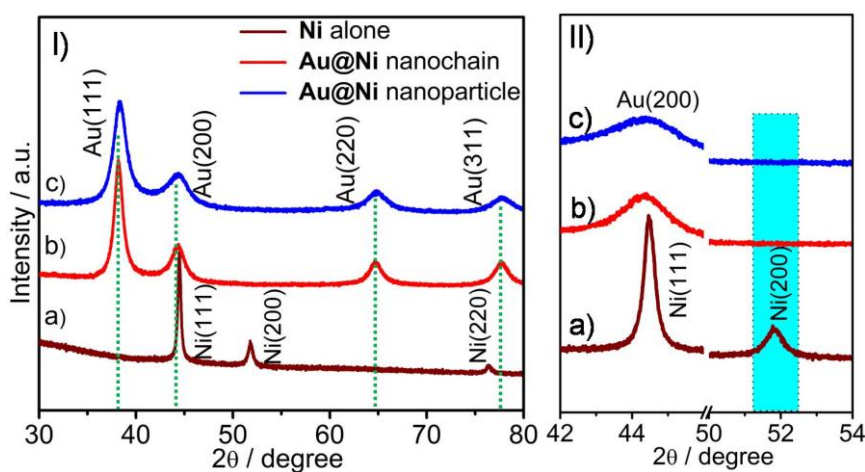


Figure 2C.3 (I) XRD patterns of (a) Nickel nanoparticles, (b) Au@Ni nanochains and (c) Au@Ni nanoparticles. Green dotted lines indicate the standard gold reflections. (II) is the enlarged area of (I) and the shaded region corresponds to the reflection specific to nickel.

To confirm the behaviour of nickel lattice, bare nickel nanoparticles were synthesised with the same amount of nickel precursor and found that the material gave all the reflections of standard nickel along with the lower order reflections. The thin nickel shell showed pure FCC phase which was confirmed by its ferromagnetic properties from the magnetic measurements (will be discussed in the next section). The diffraction peaks at 2θ values 38.2, 44.3 and 64.6 correspond to Au (111), Au (200) and Au (220) respectively. Similarly Ni (111), Ni (200) and Ni (220) are marked at 2θ values 44.5, 51.8 and 76.4 respectively¹⁶. The zoomed area of the XRD peak (Figure 2C.3II) shows the overlapping of Au (200) with Ni (111) with the absence of lower order reflection at 51.8 [Ni (200) - shaded area] which is contrary to the diffraction pattern obtained in the case of core-shell materials reported in the previous sections of this thesis and it can be because of the slightly higher amount of hydroxide species as evident from XPS analysis (will be addressed in XPS discussion).

2C.2.4 Magnetic Measurements (VSM)

Since XRD failed to probe the signature features of nickel metal, it is indispensable to prove the identity of nickel in bimetallic Au@Ni core-shell structures and hence magnetic measurements were carried out. Apart from identifying the FCC crystal structure of nickel, the ferromagnetic property also exposed through the VSM analysis, where the material aligns in the direction of an external magnetic field. The literature reports clearly claims ferromagnetic behaviour for the FCC nickel and diamagnetic response for HCP nickel^{7,9}. The magnetic properties of the two Au@Ni core-shell nanostructures were explored by measuring the hysteresis loop using VSM. The magnetic behaviour of core-shell nanostructures are shown in Figure 2C.4a and b. Hysteresis loops were measured at room temperature (300 K) for both the nanostructures and they showed typical hysteric behaviour of a ferromagnetic nickel with saturation magnetization 2 emu/gm in presence of applied magnetic field. The inset of the image (Figure 2C.4a and b) shows the coercivity of the hysteresis loop which were found to be almost same for both individual and chain like bimetallic nanostructures. Thus the synthesis strategy provided a more efficient route for the formation of diverse structures of Au@Ni core-shell system in an eco friendly solvent and at comparatively low temperatures.

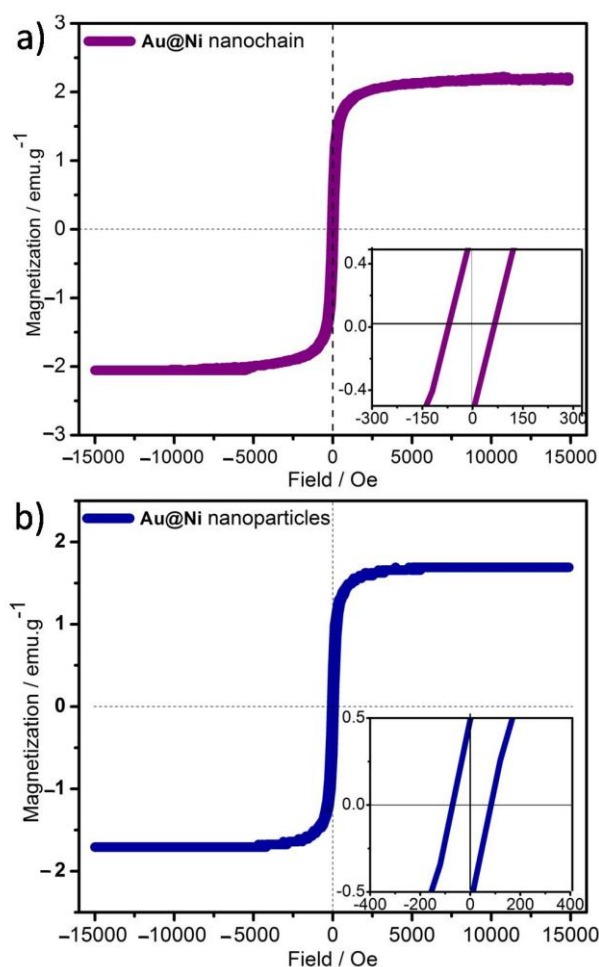


Figure 2C.4 (a) and (b) are the hysteresis loops obtained for Au@Ni nanochains and Au@Ni nanoparticles obtained in VSM analysis. (Inset of a and b shows the width of the hysteresis loop near the zero field).

2C.2.5 X-ray Photoelectron Spectroscopy Investigation (XPS)

Figure 2C.5 shows the individual XP Spectra obtained for the two metals (Au and Ni) in both the nanostructures. XPS analysis proved that despite the morphology being different; they showed same binding energy features for gold and nickel in both the species. Ever since the discovery of nickel for catalytic applications, it was always a hurdle to maintain the metallic feature, which is active phase for several catalytic applications. This is mainly due to the high heats of adsorption of oxygen on nickel; it undergoes aerial oxidation very easily⁷². A careful analysis of Ni 2p_{3/2} XP spectra (Figure 2C.5a and c) revealed that metallic feature of nickel (852.6 eV) was present along with the major feature at 855.8 eV corresponding to nickel hydroxide⁵².

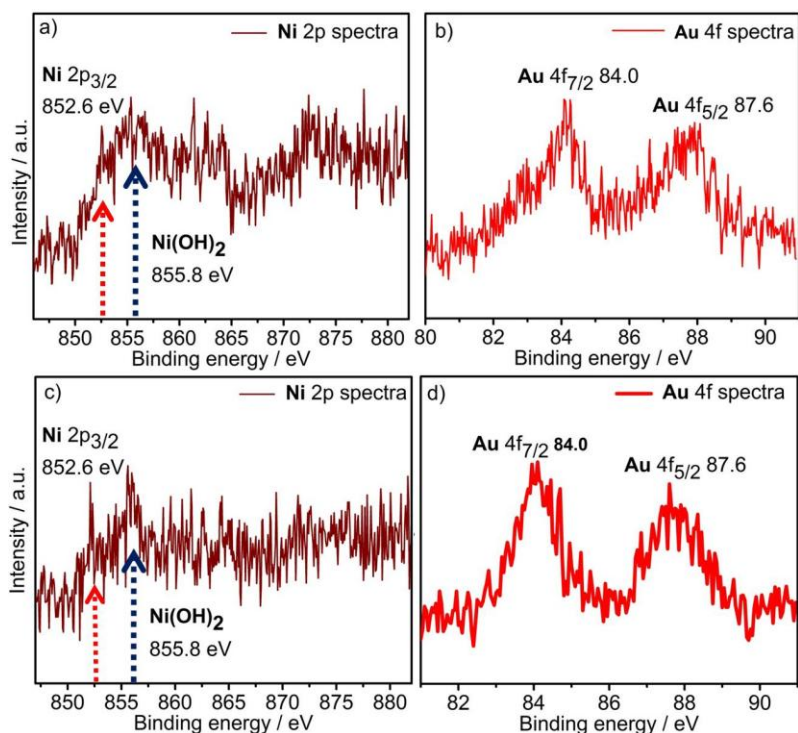


Figure 2C.5 Individual XP spectra of nickel (Ni 2p) and gold (Au 4f) recorded for core-shell (a-b) Au@Ni nanochains and (c-d) Au@Ni nanoparticles. Red dotted line indicates the nickel metallic feature whereas blue corresponds to nickel hydroxide feature.

This observation serves as a direct evidence of gold core induced electronic modification of ultra thin nickel shell which is resistant towards surface oxidation to form nickel oxide. The individual gold scan showed a binding energy value of 84 eV and 87.6 eV in both the cases (Figure 2C.5b and d) which are typical of metallic gold (0) as reported previously⁶⁶. Thus, XPS analysis proved the existence of nickel in the metallic phase with nickel hydroxide being the other often dominant feature.

2C.2.6 Catalytic Activity Results of Au@Ni Core-shell Nanostructures for Selective Hydrogenation of Phenylacetylene (P.A)

To demonstrate the efficiency and versatility of Au@Ni bimetallic nanostructures synthesised in eco-friendly soyabean oil, selective hydrogenation of phenylacetylene (P.A) was carried out. Here the substrate molecule with a triple bond offers scope for tuning the selectivity towards desired products. The hydrogenation reactions using H₂ gas were carried out in a stirred tank reactor (Parr reactor) and samples analyzed by using a gas chromatograph. Parr reactor is charged with the substrate and required amount of catalyst in

presence of solvent, and then the reactor is purged 3 times with hydrogen to remove the unwanted impurity gases inside the reactor. It was then filled with desired hydrogen pressure followed by heating the reactor to the desired temperatures. Recently Vivek et al. reported that this reaction is highly solvent specific for selectivity towards alkanes or alkenes⁶⁴. It was found that Au@Ni bimetallic core-shell nanomaterials irrespective of the morphology, showed very good conversion rate at a lower pressures (50 psi) of hydrogen and at near ambient temperatures (40 and 50 degree C). In Figure 2C.6, the red and yellow bars indicate the conversion rate of phenylacetylene in solvents MeOH and DCM with a run time of 4 and 10 hours respectively as the reaction time for these solvents. The reaction proceeded much faster in MeOH even with less amount of catalyst (5 mg) as compared to DCM (10 mg). The blue and green bars are correlated to the red and yellow conversion bars respectively, and they denote the selectivity towards ethylbenzene and styrene respectively. In case of MeOH solvent, both the bimetallic nanoparticles exhibited complete conversion of phenylacetylene (P.A) to ethylbenzene (E.B.) with 100 % selectivity in 4 hours. Here gold nanoparticles showed almost no activity in comparison with all other catalysts irrespective of the solvent (less than 5 %). The conversion of phenylacetylene to ethylbenzene in methanol solvent takes place via the intermediate styrene formation. And it was difficult to control the selectivity towards styrene in MeOH solvent. At the same time these observations revealed the superior ability of Au@Ni nanostructures for the hydrogenation of unsaturated bonds all the way to single bond. For bare nickel nanoparticles, the conversion of P.A in methanol solvent was sluggish and achieved only 60 % conversion after 4 hours of reaction. The selectivity towards E.B was 65 % with rest being styrene. In the case of DCM as solvent, the core-shell Au@Ni nanoparticles and nanochains showed complete conversion and very good selectivity for styrene which is competitive with nickel nanoparticles in a reaction period of 10 hours and at 40 °C. The reaction rate was slower in DCM as compared to MeOH solvent and the core-shell catalysts took 10 hours to complete the reaction with 78 % selectivity for styrene with rest being ethylbenzene. In the case of bare Ni nanoparticles, with DCM as solvent, the conversions achieved were only 50 % with a styrene selectivity of 75 %. The nano size regime and core-shell morphology of these surface tailored bimetallic systems offers high surface to volume ratio with maximum degree of co-ordinately unsaturated sites and easily accessible active centres. Since Au@Ni nanoparticles and nanochains exhibited almost similar kind of reactivity, there is a distinctive advantage of choosing Au@Ni nanochains. The process of synthesis is much greener as long chain organic capping agent CTAB is avoided in

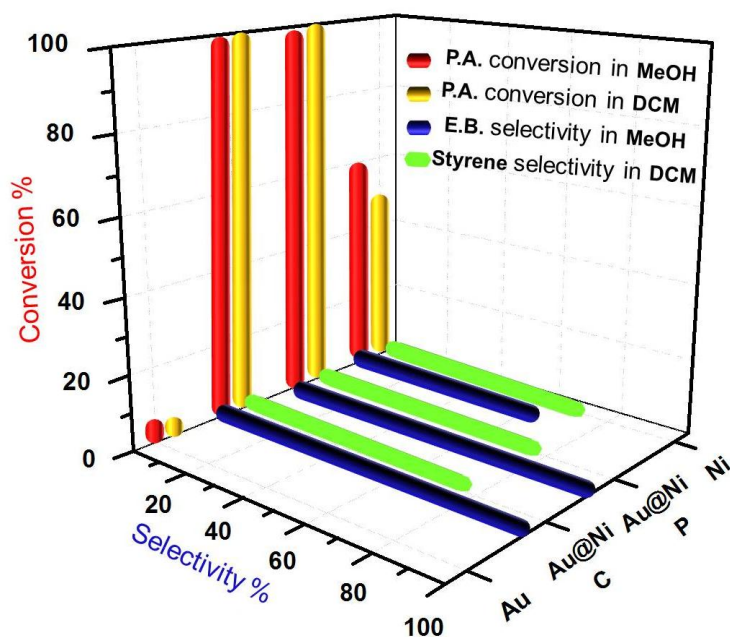


Figure 2C.6 Conversion (red and yellow bars) and selectivity (blue and green bars) results obtained for gold nanoparticles (Au), Au@Ni nanochains (Au@Ni C), Au@Ni nanoparticles (Au@Ni P) and nickel nanoparticles (Ni) for the phenylacetylene hydrogenation (P.A) in MeOH (Reaction conditions: 4 hours at 50 °C and 50 psi H₂ pressure) and DCM (Reaction conditions: 10 hours at 40 °C and 50 psi H₂ pressure) solvents.

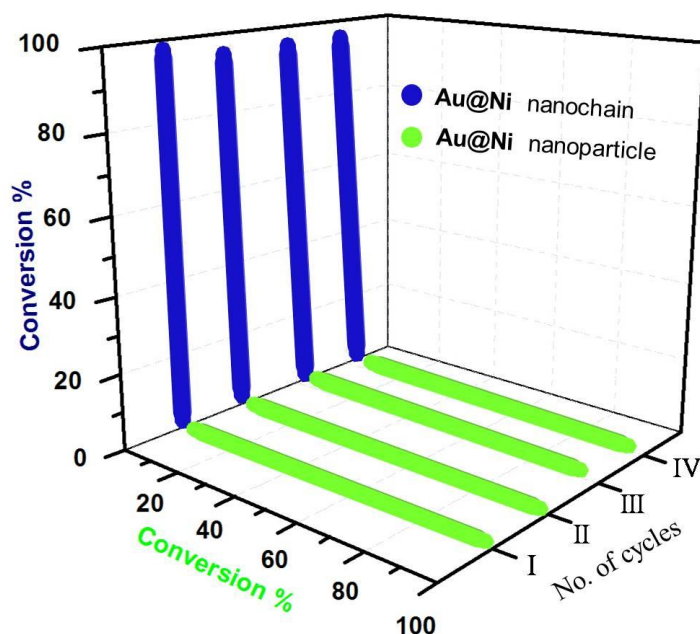


Figure 2C.7 Conversion of P.A to ethylbenzene (E.B) in MeOH by using Au@Ni nanochains (blue bar) and Au@Ni nanoparticles (green bar) during different catalytic cycles.

the synthesis. It is also demonstrated previously that nanochains offer better stability in longer run, especially in high temperature catalytic applications⁷⁰. Such an effect is not well pronounced in the reaction studied here since the reaction conditions used for both the reduction reactions were close to ambient temperatures and pressure. The core-shell bimetallic systems showed complete conversion without any loss in catalytic activity even after four catalytic cycles of P.A hydrogenation (Figure 2C.7). Both the triple bond and double bond hydrogenation to desired products have their own importance in the organic transformations and petrochemical industries and these successful results show that the catalyst can be used in case of various substrates for hydrogenating double bonds, triple bonds and nitro groups with selectivity towards desired products. Also in comparison with the previous reports in the chapter 2B, the bimetallic nanostructures synthesized through the greener path showed similar catalytic activity to those prepared by using conventional solvents.

2.2 Conclusions

The chapter demonstrated the successful one-pot synthesis of highly lattice mismatched Au@Ni core-shell nanoparticles/nanostructures by using various solvents under different reduction conditions. Magnetic and non-magnetic Au@Ni (Au@Ni_{FCC} and Au@Ni_{HCP}) bimetallic core-shell nanoparticles are generated and the nickel shell thickness can be controlled effectively by tuning the metal precursor ratios. Apart from this, a cost effective synthesis strategy with an eco friendly solvent like soyabean oil successfully employed to generate Au@Ni core-shell bimetallic nanostructures without using any expensive and hazardous surfactants. In all the cases, the nickel surface of the as synthesized bimetallic nanostructures shows synergistic effects as evidenced by various characterization tools. The XRD experiments proved the core-shell nanoparticles are extremely stable to bulk oxidation even up to 250 °C. The surface characterization using XPS clearly showed that due to synergistic effects an extremely thin nickel shell of approximately 2 nm has almost 50 % of the nickel retained in metallic form which is considered as the major reason for synergism. The versatility of the surface-engineered bimetallic nanostructures was proved for their excellent catalytic activity for nitro group reduction reaction even for the nanoparticles heated until 150 °C. This is probably the first report on the synthesis of sub 10 nm Au@Ni core-shell nanoparticles, which are truly diverse in magnetic and catalytic properties. The synergistic

effects are found to play major role in the catalytic activity of Au@Ni_{1.0.5} bimetallic combination with an optimum shell thickness of 2 nm. The thinnest nickel shell over the gold core recorded high activity than monometallic gold and nickel nanoparticles for nitro group reductions and selective hydrogenation of phenyl acetylene with sustainable activity. Au@Ni nanostructures showed enhanced catalytic activity and selectivity for hydrogenation reactions even under mild conditions of temperature and pressure. Extending the nickel shell thickness beyond 2 nm over the gold core gave bimetallic nanoparticles behaving more like bulk nickel even though they retained core-shell morphology. This work demonstrates that in the case of Au@Ni bimetallic system the synergism operates up to around 2 nm (10 atomic layers) and this aspect should be borne in mind while designing such bimetallic nanostructures for futuristic catalytic applications.

2.3 References

1. Gilroy, K. D.; Ruditskiy, A.; Peng, H.-C.; Qin, D.; Xia, Y., Bimetallic Nanocrystals: Syntheses, Properties, and Applications. *Chem. Rev.* **2016**.
2. Wang, D.; Li, Y., Bimetallic Nanocrystals: Liquid-Phase Synthesis and Catalytic Applications. *Adv. Mater.* **2011**, *23* (9), 1044-1060.
3. Lee, Y. W.; Kim, M.; Kim, Z. H.; Han, S. W., One-Step Synthesis of Au@Pd Core-Shell Nanooctahedron. *J. Am. Chem. Soc.* **2009**, *131* (47), 17036-17037.
4. Yan, J.-M.; Zhang, X.-B.; Akita, T.; Haruta, M.; Xu, Q., One-Step Seeding Growth of Magnetically Recyclable Au@Co Core-Shell Nanoparticles: Highly Efficient Catalyst for Hydrolytic Dehydrogenation of Ammonia Borane. *J. Am. Chem. Soc.* **2010**, *132* (15), 5326-5327.
5. Lakshminarayana, P.; Qing-Hua, X., A simple method for large scale synthesis of highly monodisperse gold nanoparticles at room temperature and their electron relaxation properties. *Nanotechnology* **2009**, *20* (18), 185606.
6. Hiramatsu, H.; Osterloh, F. E., A Simple Large-Scale Synthesis of Nearly Monodisperse Gold and Silver Nanoparticles with Adjustable Sizes and with Exchangeable Surfactants. *Chem. Mater.* **2004**, *16* (13), 2509-2511.
7. Mourdikoudis, S.; Simeonidis, K.; Vilalta-Clemente, A.; Tuna, F.; Tsiaoussis, I.; Angelakeris, M.; Dendrinou-Samara, C.; Kalogirou, O., Controlling the crystal structure of Ni nanoparticles by the use of alkylamines. *J. Magn. Magn. Mater.* **2009**, *321* (18), 2723-2728.
8. Shen, C.; Hui, C.; Yang, T.; Xiao, C.; Tian, J.; Bao, L.; Chen, S.; Ding, H.; Gao, H., Monodisperse Noble-Metal Nanoparticles and Their Surface Enhanced Raman Scattering Properties. *Chem. Mater.* **2008**, *20* (22), 6939-6944.
9. Chen, Y.; Peng, D.-L.; Lin, D.; Luo, X., Preparation and magnetic properties of nickel nanoparticles via the thermal decomposition of nickel organometallic precursor in alkylamines. *Nanotechnology* **2007**, *18* (50), 505703.
10. Sun, S.; Zeng, H., Size-Controlled Synthesis of Magnetite Nanoparticles. *J. Am. Chem. Soc.* **2002**, *124* (28), 8204-8205.

11. Jana, N. R.; Chen, Y.; Peng, X., Size- and Shape-Controlled Magnetic (Cr, Mn, Fe, Co, Ni) Oxide Nanocrystals via a Simple and General Approach. *Chem. Mater.* **2004**, *16* (20), 3931-3935.
12. Kovalenko, M. V.; Bodnarchuk, M. I.; Lechner, R. T.; Hesser, G.; Schäffler, F.; Heiss, W., Fatty Acid Salts as Stabilizers in Size- and Shape-Controlled Nanocrystal Synthesis: The Case of Inverse Spinel Iron Oxide. *J. Am. Chem. Soc.* **2007**, *129* (20), 6352-6353.
13. Mourdikoudis, S.; Liz-Marzán, L. M., Oleylamine in Nanoparticle Synthesis. *Chem. Mater.* **2013**, *25* (9), 1465-1476.
14. Xu, Z.; Shen, C.; Hou, Y.; Gao, H.; Sun, S., Oleylamine as Both Reducing Agent and Stabilizer in a Facile Synthesis of Magnetite Nanoparticles. *Chem. Mater.* **2009**, *21* (9), 1778-1780.
15. She, H.; Chen, Y.; Chen, X.; Zhang, K.; Wang, Z.; Peng, D.-L., Structure, optical and magnetic properties of Ni@Au and Au@Ni nanoparticles synthesized via non-aqueous approaches. *J. Mater. Chem.* **2012**, *22* (6), 2757-2765.
16. Zhang, H.; Ding, J.; Chow, G.; Ran, M.; Yi, J., Engineering Magnetic Properties of Ni Nanoparticles by Non-Magnetic Cores. *Chem. Mater.* **2009**, *21* (21), 5222-5228.
17. Kulkarni, G. U.; Vinod, C. P., Diverse reactivity patterns observed in the interaction of oxygen with nickel deposited on gold and tungsten surfaces. *Appl. Surf. Sci.* **1997**, *115* (4), 336-341.
18. Henning, A. M.; Watt, J.; Miedziak, P. J.; Cheong, S.; Santonastaso, M.; Song, M.; Takeda, Y.; Kirkland, A. I.; Taylor, S. H.; Tilley, R. D., Gold-Palladium Core-Shell Nanocrystals with Size and Shape Control Optimized for Catalytic Performance. *Angew. Chem. Int. Ed.* **2013**, *52* (5), 1477-1480.
19. Carenco, S.; Boissière, C.; Nicole, L.; Sanchez, C.; Le Floch, P.; Mézailles, N., Controlled Design of Size-Tunable Monodisperse Nickel Nanoparticles. *Chem. Mater.* **2010**, *22* (4), 1340-1349.
20. Corma, A.; Serna, P., Chemoselective Hydrogenation of Nitro Compounds with Supported Gold Catalysts. *Science* **2006**, *313* (5785), 332-334.
21. Rode, C. V.; Vaidya, M. J.; Jaganathan, R.; Chaudhari, R. V., Hydrogenation of nitrobenzene to p-aminophenol in a four-phase reactor: reaction kinetics and mass transfer effects. *Chem. Eng. Sci.* **2001**, *56* (4), 1299-1304.
22. Vaidya, M. J.; Kulkarni, S. M.; Chaudhari, R. V., Synthesis of p-Aminophenol by Catalytic Hydrogenation of p-Nitrophenol. *Org. Process Res. Dev.* **2003**, *7* (2), 202-208.
23. Aditya, T.; Pal, A.; Pal, T., Nitroarene reduction: a trusted model reaction to test nanoparticle catalysts. *Chem. Commun.* **2015**, *51* (46), 9410-9431.
24. Zhang, Q.; Wang, H., Facet-Dependent Catalytic Activities of Au Nanoparticles Enclosed by High-Index Facets. *ACS Catal.* **2014**, *4* (11), 4027-4033.
25. Downing, R. S.; Kunkeler, P. J.; van Bekkum, H., Catalytic syntheses of aromatic amines. *Catal. Today* **1997**, *37* (2), 121-136.
26. Cai, S.; Duan, H.; Rong, H.; Wang, D.; Li, L.; He, W.; Li, Y., Highly Active and Selective Catalysis of Bimetallic Rh₃Ni₁ Nanoparticles in the Hydrogenation of Nitroarenes. *ACS Catal.* **2013**, *3* (4), 608-612.
27. Feng, Z. V.; Lyon, J. L.; Croley, J. S.; Crooks, R. M.; Vanden Bout, D. A.; Stevenson, K. J., Synthesis and Catalytic Evaluation of Dendrimer-Encapsulated Cu Nanoparticles. An Undergraduate Experiment Exploring Catalytic Nanomaterials. *J. Chem. Educ.* **2009**, *86* (3), 368.
28. Jiang, Z. F.; Xie, J. M.; Jiang, D. L.; Jing, J. J.; Qin, H. R., Facile route fabrication of nano-Ni core mesoporous-silica shell particles with high catalytic activity towards 4-nitrophenol reduction. *CrystEngComm* **2012**, *14* (14), 4601-4611.

29. Sehested, J., Four challenges for nickel steam-reforming catalysts. *Catal. Today* **2006**, *111* (1–2), 103-110.
30. Cui, Q.; Shen, G.; Yan, X.; Li, L.; Möhwald, H.; Bargheer, M., Fabrication of Au@Pt Multibranching Nanoparticles and Their Application to In-situ SERS Monitoring. *ACS Appl. Mater. Interfaces* **2014**, *6* (19), 17075-17081.
31. Bai, L.; Yuan, F.; Tang, Q., Synthesis of nickel nanoparticles with uniform size via a modified hydrazine reduction route. *Mater. Lett.* **2008**, *62* (15), 2267-2270.
32. Chen, D.-H.; Hsieh, C.-H., Synthesis of nickel nanoparticles in aqueous cationic surfactant solutions. *J. Mater. Chem.* **2002**, *12* (8), 2412-2415.
33. Wu, S.-H.; Chen, D.-H., Synthesis and characterization of nickel nanoparticles by hydrazine reduction in ethylene glycol. *J. Colloid Interface Sci.* **2003**, *259* (2), 282-286.
34. Priddy, D. B.; Roe, J. M., Hydrogenation of phenylacetylene prior to styrene polymerization. US Pat. No. 4,389,517: 1983.
35. Zhang, L.; He, R.; Gu, H.-C., Oleic acid coating on the monodisperse magnetite nanoparticles. *Appl. Surf. Sci.* **2006**, *253* (5), 2611-2617.
36. Wang, D.; Li, Y., One-Pot Protocol for Au-Based Hybrid Magnetic Nanostructures via a Noble-Metal-Induced Reduction Process. *J. Am. Chem. Soc.* **2010**, *132* (18), 6280-6281.
37. Duan, H.; Wang, D.; Li, Y., Green chemistry for nanoparticle synthesis. *Chem. Soc. Rev.* **2015**, *44* (16), 5778-5792.
38. Eustis, S.; El-Sayed, M. A., Why gold nanoparticles are more precious than pretty gold: Noble metal surface plasmon resonance and its enhancement of the radiative and nonradiative properties of nanocrystals of different shapes. *Chem. Soc. Rev.* **2006**, *35* (3), 209-217.
39. LaGrow, A. P.; Ingham, B.; Cheong, S.; Williams, G. V. M.; Dotzler, C.; Toney, M. F.; Jefferson, D. A.; Corbos, E. C.; Bishop, P. T.; Cookson, J.; Tilley, R. D., Synthesis, Alignment, and Magnetic Properties of Monodisperse Nickel Nanocubes. *J. Am. Chem. Soc.* **2011**, *134* (2), 855-858.
40. Tsuji, M.; Yamaguchi, D.; Matsunaga, M.; Ikeda, K., Epitaxial Growth of Au@Ni Core-Shell Nanocrystals Prepared Using a Two-Step Reduction Method. *Cryst. Growth Des.* **2011**, *11* (5), 1995-2005.
41. Huang, L.; Shan, A.; Li, Z.; Chen, C.; Wang, R., Phase formation, magnetic and optical properties of epitaxially grown icosahedral Au@Ni nanoparticles with ultrathin shells. *CrystEngComm* **2013**, *15* (13), 2527-2531.
42. Jeon, Y. T.; Moon, J. Y.; Lee, G. H.; Park, J.; Chang, Y., Comparison of the Magnetic Properties of Metastable Hexagonal Close-Packed Ni Nanoparticles with Those of the Stable Face-Centered Cubic Ni Nanoparticles. *J. Phys. Chem. B* **2005**, *110* (3), 1187-1191.
43. Tzitzios, V.; Basina, G.; Gjoka, M.; Alexandrakos, V.; Georgakilas, V.; Niarchos, D.; Boukos, N.; Petridis, D., Chemical synthesis and characterization of hcp Ni nanoparticles. *Nanotechnology* **2006**, *17* (15), 3750.
44. Nikolaev, S. A.; Smirnov, V. V.; Vasil'kov, A. Y.; Podshibikhin, V. L., Synergism of the catalytic effect of nanosized gold-nickel catalysts in the reaction of selective acetylene hydrogenation to ethylene. *Kinet. Catal.* **2010**, *51* (3), 375-379.
45. Yuan, G.; Louis, C.; Delannoy, L.; Keane, M. A., Silica- and titania-supported Ni-Au: Application in catalytic hydrodechlorination. *J. Catal.* **2007**, *247* (2), 256-268.
46. Molenbroek, A. M.; Nørskov, J. K.; Clausen, B. S., Structure and Reactivity of Ni-Au Nanoparticle Catalysts. *J. Phys. Chem. B* **2001**, *105* (23), 5450-5458.
47. Yuan, G.; Lopez, J. L.; Louis, C.; Delannoy, L.; Keane, M. A., Remarkable hydrodechlorination activity over silica supported nickel/gold catalysts. *Catal. Commun.* **2005**, *6* (8), 555-562.

48. Jiang, H.-L.; Umegaki, T.; Akita, T.; Zhang, X.-B.; Haruta, M.; Xu, Q., Bimetallic Au–Ni Nanoparticles Embedded in SiO₂ Nanospheres: Synergetic Catalysis in Hydrolytic Dehydrogenation of Ammonia Borane. *Chem. - Eur. J.* **2010**, *16* (10), 3132-3137.
49. Ghosh, M.; Biswas, K.; Sundaresan, A.; Rao, C. N. R., MnO and NiO nanoparticles: synthesis and magnetic properties. *J. Mater. Chem.* **2006**, *16* (1), 106-111.
50. Goto, Y.; Taniguchi, K.; Omata, T.; Otsuka-Yao-Matsuo, S.; Ohashi, N.; Ueda, S.; Yoshikawa, H.; Yamashita, Y.; Oohashi, H.; Kobayashi, K., Formation of Ni₃C Nanocrystals by Thermolysis of Nickel Acetylacetonate in Oleylamine: Characterization Using Hard X-ray Photoelectron Spectroscopy. *Chem. Mater.* **2008**, *20* (12), 4156-4160.
51. Zhou, W.; Zheng, K.; He, L.; Wang, R.; Guo, L.; Chen, C.; Han, X.; Zhang, Z., Ni/Ni₃C Core–Shell Nanochains and Its Magnetic Properties: One-Step Synthesis at Low Temperature. *Nano Lett.* **2008**, *8* (4), 1147-1152.
52. Grosvenor, A. P.; Biesinger, M. C.; Smart, R. S.; McIntyre, N. S., New interpretations of XPS spectra of nickel metal and oxides. *Surf. Sci.* **2006**, *600* (9), 1771-1779.
53. Prieto, P.; Nistor, V.; Nouneh, K.; Oyama, M.; Abd-Lefdil, M.; Díaz, R., XPS study of silver, nickel and bimetallic silver–nickel nanoparticles prepared by seed-mediated growth. *Appl. Surf. Sci.* **2012**, *258* (22), 8807-8813.
54. Park, J.; Kang, E.; Son, S. U.; Park, H. M.; Lee, M. K.; Kim, J.; Kim, K. W.; Noh, H. J.; Park, J. H.; Bae, C. J.; Park, J. G.; Hyeon, T., Monodisperse Nanoparticles of Ni and NiO: Synthesis, Characterization, Self-Assembled Superlattices, and Catalytic Applications in the Suzuki Coupling Reaction. *Adv. Mater.* **2005**, *17* (4), 429-434.
55. Wang, C.-M.; Baer, D. R.; Bruemmer, S. M.; Engelhard, M. H.; Bowden, M. E.; Sundararajan, J. A.; Qiang, Y., Microstructure of the Native Oxide Layer on Ni and Cr-Doped Ni Nanoparticles. *J. Nanosci. Nanotechnol.* **2011**, *11* (10), 8488-8497.
56. Leon, C. C.; Lee, J.-G.; Ceyer, S. T., Oxygen Adsorption on Au–Ni(111) Surface Alloys. *J. Phys. Chem. C* **2014**, *118* (50), 29043-29057.
57. Singh, A. K.; Xu, Q., Synergistic Catalysis over Bimetallic Alloy Nanoparticles. *ChemCatChem* **2013**, *5* (3), 652-676.
58. Jiang, H.-L.; Akita, T.; Ishida, T.; Haruta, M.; Xu, Q., Synergistic Catalysis of Au@Ag Core–Shell Nanoparticles Stabilized on Metal–Organic Framework. *J. Am. Chem. Soc.* **2011**, *133* (5), 1304-1306.
59. Holmblad, P. M.; Larsen, J. H.; Chorkendorff, I.; Nielsen, L. P.; Besenbacher, F.; Stensgaard, I.; Lægsgaard, E.; Kratzer, P.; Hammer, B.; Nørskov, J. K., Designing surface alloys with specific active sites. *Catal. Lett.* **1996**, *40* (3-4), 131-135.
60. Sarkar, S.; Sinha, A. K.; Pradhan, M.; Basu, M.; Negishi, Y.; Pal, T., Redox Transmetalation of Prickly Nickel Nanowires for Morphology Controlled Hierarchical Synthesis of Nickel/Gold Nanostructures for Enhanced Catalytic Activity and SERS Responsive Functional Material. *J. Phys. Chem. C* **2010**, *115* (5), 1659-1673.
61. Nemanashi, M.; Meijboom, R., Synthesis and characterization of Cu, Ag and Au dendrimer-encapsulated nanoparticles and their application in the reduction of 4-nitrophenol to 4-aminophenol. *J. Colloid Interface Sci.* **2013**, *389* (1), 260-267.
62. Rostrup-Nielsen, J. R.; Alstrup, I., Innovation and science in the process industry: Steam reforming and hydrogenolysis. *Catal. Today* **1999**, *53* (3), 311-316.
63. Chin, Y.-H.; King, D. L.; Roh, H.-S.; Wang, Y.; Heald, S. M., Structure and reactivity investigations on supported bimetallic AuNi catalysts used for hydrocarbon steam reforming. *J. Catal.* **2006**, *244* (2), 153-162.
64. Polshettiwar, V.; Baruwati, B.; Varma, R. S., Nanoparticle-supported and magnetically recoverable nickel catalyst: a robust and economic hydrogenation and transfer hydrogenation protocol. *Green Chem.* **2009**, *11* (1), 127-131.

65. Grzelczak, M.; Rodríguez-González, B.; Pérez-Juste, J.; Liz-Marzán, L. M., Quasi-Epitaxial Growth of Ni Nanoshells on Au Nanorods. *Adv. Mater.* **2007**, *19* (17), 2262-2266.
66. Boyen, H.-G.; Kästle, G.; Weigl, F.; Koslowski, B.; Dietrich, C.; Ziemann, P.; Spatz, J. P.; Riethmüller, S.; Hartmann, C.; Möller, M.; Schmid, G.; Garnier, M. G.; Oelhafen, P., Oxidation-Resistant Gold-55 Clusters. *Science* **2002**, *297* (5586), 1533-1536.
67. Shao, L.; Huang, X.; Teschner, D.; Zhang, W., Gold Supported on Graphene Oxide: An Active and Selective Catalyst for Phenylacetylene Hydrogenations at Low Temperatures. *ACS Catal.* **2014**, *4* (7), 2369-2373.
68. Chen, X.; Zhao, A.; Shao, Z.; Li, C.; Williams, C. T.; Liang, C., Synthesis and Catalytic Properties for Phenylacetylene Hydrogenation of Silicide Modified Nickel Catalysts. *J. Phys. Chem. C* **2010**, *114* (39), 16525-16533.
69. Li, C.; Chen, Y.; Zhang, S.; Zhou, J.; Wang, F.; He, S.; Wei, M.; Evans, D. G.; Duan, X., Nickel–Gallium Intermetallic Nanocrystal Catalysts in the Semihydrogenation of Phenylacetylene. *ChemCatChem* **2014**, *6* (3), 824-831.
70. Sreedhala, S.; Vinod, C. P., Surfactant assisted formation of ruthenium nanochains under mild conditions and their catalytic CO oxidation activity. *Chem. Commun.* **2015**, *51* (50), 10178-10181.
71. Zhang, J.; Li, C. M., Nanoporous metals: fabrication strategies and advanced electrochemical applications in catalysis, sensing and energy systems. *Chem. Soc. Rev.* **2012**, *41* (21), 7016-7031.
72. Masel, R. I., *Principles of adsorption and reaction on solid surfaces*. John Wiley & Sons: 1996; Vol. 3.

Chapter 3

Synthesis of Au@Ni Core-shell Nanoparticle in Aqueous Medium: NAPXPS Studies on Oxidation Resistance and its Application in Selective Hydrogenation

➤ Outline of the chapter

- ✓ Aqueous phase synthesis of magnetic Au@Ni core-shell nanoparticles
- ✓ Low temperature synthesis strategy
- ✓ Tuning of nickel shell thickness (2-8 nm)
- ✓ Optimization of nickel shell thickness to produce synergistic effect
- ✓ In-situ analysis of surface states in Au@Ni systems under O₂ atm. using NAPXPS
- ✓ Effect of nickel shell thickness on dynamic surface changes
- ✓ Synergism is restricted to atomic layers
- ✓ Shell thickness dependent catalytic activity & selectivity for P.A hydrogenation

This chapter is adapted from the following publication to be submitted:

1. Synthesis of Au@Ni core-shell nanoparticle in aqueous medium: NAPXPS studies on oxidation resistance and its application in selective hydrogenation. Vysakh A. B., Ruchi Jain, C.S. Gopinath, C. P. Vinod.

Chapter 3: Synthesis of Au@Ni Core-shell Nanoparticle in Aqueous Medium: NAPXPS Studies on Oxidation Resistance and its Application in Selective Hydrogenation

3.1 Introduction

In the recent past there has been a profound interest in studying physiochemical properties and applications of bimetallic nanomaterials¹⁻⁴. Particularly interesting is the catalysis by bimetallic nanoparticles which demonstrates fascinating reactivity trends atypical of monometallic counterparts⁵⁻⁶. The altered reactivity patterns observed in bimetallic nanostructures are mainly due to the fundamental effects such as electronic and geometric effects operating in between dissimilar metal lattices⁷⁻⁸. The geometric effect arise when dissimilar metal atoms transform to particular ensembles on the surface, as reported for gold atoms in a dissimilar nickel matrix for steam reforming reaction⁹. Electronic effects are caused by the atomic interaction of two distinctively different metal atoms and the electronic interactions can cause perturbations in the electronic structure of metals which guides the reactivity trends¹⁰. Finally, geometric and electronic effects plays crucial role in deciding the properties of the resulting bimetallic nanostructures and it depends on various parameters like lattice matching, surface strain, valence band electron density, electronegativity differences, d-band structure, etc¹¹⁻¹². Au-Ni bimetallic system with 16 % lattice mismatch¹³⁻¹⁴ offers an interesting prototype where both ligand and geometric effects¹⁵⁻¹⁶ are expected to play a role. Out of various bimetallic nanoparticle systems¹⁷ core-shell nanoparticles serves as an ideal system as they provide a homogeneous surface comprised of only one type of metal atoms which is uniformly surface modified by a different type of core metal atoms¹⁸. Probing the extend of synergism in core-shell nanoparticles is always a hurdle and the question remains how far the geometric and electronic perturbations operate in a core-shell system? What is the optimum shell thickness up to which synergistic effects can be seen in catalysis?¹⁹⁻²⁰ There is a high demand for a thorough understanding of above facts which is necessary for careful design of new catalyst materials with improved performance. The synthesis of Au-Ni bimetallic structures were largely motivated by earlier surface science reports which showed interesting and diverse reactivity trends^{9, 21}. Nickel is prone to ambient oxidation which is found to be detrimental in its catalytic activity²². The surface science studies on nickel overlayers on polycrystalline Au foil showed that sub monolayer coverage of Ni on Au can

resist oxidation due to electronic effects²¹. The previous reports demonstrated the synthesis of Au@Ni core-shell nanoparticles with controlled size by diverse methods in various organic solvents^{19, 23-24}. The XRD heating experiments in air on Au@Ni proved that the material was resistant to oxidation even up to 200 °C¹⁹. There is growing interest in making surfactant free synthesis of nanomaterials or greener routes for potentially eliminating toxic reagents used in the synthesis²⁵⁻²⁶. Such synthesis also yields cleaner surface for catalytic applications which reduces the labor of removing the surfactants before desired applications²⁷. Even though the organic phase synthesis strategies provide uniformity in size and shape of the nanoparticles²⁸, it is difficult to recover the catalyst materials from the synthesis medium with high purity. Here in the present work, synthesis of Au@Ni core-shell nanoparticles in aqueous medium is reported for the first time through a low temperature sequential reduction strategy by avoiding costly and harmful organic solvents. The synthesized materials are characterized by HR-TEM and other associated techniques. The surface modifications of Ni due to Au core were further probed by NAPXPS to demonstrate the oxidation resistance of Ni atomic layers toward oxygen. The XPS (or PES – X-ray photoelectron spectroscopy) results from this study demonstrate that the surface is resistant to oxidation with an optimum Ni shell thickness of ~ 2 nm. And this surface has a different decomposition pattern of the oxide ad layers compared to those with larger Ni shell. The tailor made Au@Ni core-shell nanoparticles further demonstrated for the hydrogenation of phenyl acetylene with higher activity for optimum Ni shell thickness whereby reaction proceeds under mild reaction conditions. Due to synergistic effects Au@Ni bimetallic nanoparticles outweighed their monometallic counterparts in catalytic activity for phenyl acetylene hydrogenation in various solvents.

3.2 Experimental Section

Metal precursors hydrogentetrachloroaurate(III)trihydrate [HAuCl₄.3H₂O], and nickelacetylacetonate [Ni(acac)₂], along with the other reagents sodiumborohydride [NaBH₄], hydrazinehydrate 80 % [NH₂-NH₂.H₂O], and cetyltrimethylammoniumbromide [CTAB] were purchased from Sigma Aldrich [Germany] and used as received. Sodiumhydroxide [NaOH], isopropanol [IPA] and acetone were obtained from Merck, India. The reagents phenylacetylene [P.A], methanol [MeOH] and dichloromethane [DCM] for catalytic activity tests were also purchased from Merck, India. All the synthesis procedure was carried out in ultra pure Millipore water.

Synthesis of Au@Ni core-shell nanoparticles with varying Ni shell thickness

An aqueous solution of 2.5×10^{-4} M $\text{HAuCl}_4 \cdot 3\text{H}_2\text{O}$ was made in 50 ml of millipore water. The gold precursor solution was stirred gently, and after a while 650 microliter (μL) of 0.1M freshly prepared ice cold NaBH_4 solution in millipore water was added and stirring continued for another 15 minutes. The reduction of gold ions to colloidal gold nanoparticles was observed with an abrupt colour change from pale yellow gold precursor solution to wine red colour upon the addition of reducing agent NaBH_4 . In the later stage, the colloidal gold solution was heated to 70°C with a ramping rate of $3^\circ\text{C}/\text{min.}$, simultaneously nickel acetylacetonate (Nickel precursor) was added to the solution with desired ratio to the gold metal (for obtaining various shell thickness) and stirred well. After the nickel precursor addition, the capping agent cetyltrimethylammoniumbromide (CTAB) was added to the solution and dispersed thoroughly. When the temperature reached to 70°C , a mixture of 750 microliter (μL) hydrazine hydrate and NaOH (prepared by dissolving 80 mg NaOH dissolved in 2ml 80 % hydrazine hydrate) was added to the solution drop wise for reducing nickel ions. The solution turns to a black colloidal suspension after a while indicating the formation of Au@Ni core-shell nanoparticles. The mole ratio of gold to nickel was adjusted by changing the nickel precursor amount to tune the shell thickness. To get a 2 nm shell thickness 0.01 mmol nickelacetylacetonate is added (to increase the shell thickness to 4 nm and 8 nm, the nickel precursor ratio should be increased to 0.02 mmol and 0.04 mmol respectively, by keeping the ratio of reducing agent to the nickel precursor same). The final black colloidal core-shell nanoparticles were separated from the synthesis medium by using an external magnet as the particles were magnetic in nature. The supernatant solution was decanted and the nanoparticles were washed thoroughly with millipore water followed by a mixture of acetone and isopropanol in order to remove the excess capping agents and residual reducing agents from the nanoparticles. The core-shell nanoparticles were redispersed in isopropanol for further characterizations and dispersed in respective solvents [MeOH and DCM] prior to catalytic activity tests.

NAPXPS measurements of Au@Ni core-shell nanoparticles (in-situ experiments)

The Lab-APXPS at CSIR-NCL is built and supplied by Prevac, Poland. By using Lab-APXPS, XPS/UPS measurements can be carried out up to 1 mbar pressure and up to 873 K by conventional heating methods and at least up to 1273 K by a laser heating method on the solid surfaces. All the XPS investigations were carried out in this spectrometer (Lab-APPES) at

CSIR-NCL, Pune. The Lab-APXPS unit is equipped with VG Scienta's R3000HP electron energy analyzer (EEA). The instrument also carries X-ray monochromator MX650 from VG Scienta and it is sealed from the analysis chamber by using a thin aluminum window (5 μm). Apart from the monochromator X-ray source, dual anode X-ray source (Al K α and Mg K α) is also available for generating X-rays and both can work with an acceleration voltage of a maximum of 15 kV. Lab-APXPS carries an exchangeable cone with different apertures (0.3-5 mm) at the tip of the ELR. Currently, the high-pressure XP spectra collected here are obtained with a 1.2 mm aperture cone and by using the monochromator X-ray source (Al K α - 1486.6 eV) at 15 kV voltages unless otherwise stated. All the spectra recorded in this work are with pass energy of 50 eV at a slit width of 0.2 mm (analyzer entrance) and at a distance of 1 mm between the sample surface and analyzer cone. The analysis of different core-shell samples (prepared by drop casting the core-shell samples dispersed in isopropanol on to the conductive carbon and dried in vacuum) were carried out over a wide range of pressure ranging from UHV to 0.1 mbar under oxygen atmosphere with temperature window from room temperature (RT) to 100 $^{\circ}\text{C}$. All the spectra at various conditions were recorded after reaching stabilized conditions of temperature and pressure. The O $_2$ gas (Inox Air Products Ltd., 99.999 %) was used without any further purification for creating oxygen atmosphere. All the investigations except UHV measurements were carried out under oxygen atmosphere created by oxygen dosing on the sample surface through a leak valve inside the analysis chamber. The characteristic core-levels of nickel and gold Ni 2p and Au 4f are recorded under a set of pressure and temperature conditions. The conditions were (1) UHV-RT (2) 10^{-3} mbar, RT (3) 0.1 (10^{-1}) mbar, RT (4) 10^{-3} mbar, 100 $^{\circ}\text{C}$ and (5) 0.1 (10^{-1}) mbar, 100 $^{\circ}\text{C}$. Beyond 0.1 mbar O $_2$ at 100 $^{\circ}\text{C}$, the spectral quality was poor because of the large inelastic scattering of the photoelectrons in the oxygen atmosphere. The oxygen pressure at the sample surface was precisely measured by using the CTR gauge and controlled dosing has been done by using the leak valve to maintain the requisite pressure ranges. After recording the XP spectra for all the samples, curve fitting was performed by using CasaXPS software, with asymmetric Lorentzian-Gaussian sum-type line shapes, with Shirley background subtraction.

Catalytic activity tests- Liquid phase selective hydrogenation of Phenylacetylene (PA)

Catalytic selective hydrogenation reactions were carried out by using hydrogen as reducing agent in a conventional Parr stirred tank reactor [volume 100ml] set up with the desired temperature and pressure conditions. Hydrogenations of phenylacetylene were done

under different reaction parameters in various solvents [MeOH and DCM] with continuous stirring. The samples were collected at specific time intervals and analyzed with the help of a Gas chromatograph [G.C] equipped with a flame ionization detector [F.I.D] having a HP-1 capillary column. In a typical hydrogenation reaction the stirred tank was charged with 5 mg of the Au@Ni core-shell catalysts dispersed in 50 ml solvent. After that required amount of substrate P.A [5 mmol in case of MeOH and 1 mmol in the case of DCM] was added to the reaction vessel and the reactor tank with loaded catalyst and substrates were flushed with hydrogen 3 times to remove the air and other impurities from the reaction vessel. Then it was pressurized followed by the heating to the desired reaction conditions. After the completion of the reaction [In MeOH- 3 Hrs and in DCM- 10 Hrs] the reactor was allowed to come back to the ambient conditions and the catalyst was recovered from the reaction medium with the help of an external magnet. All the compounds were identified and calibrated with the standard samples in the gas chromatograph analysis.

3.3 Results and Discussion

3.3.1 UV-Vis Spectroscopy Analysis (UV-Vis)

The schematic showing various stages involved in the successful generation of magnetic Au@Ni bimetallic core-shell nanoparticles are depicted in Figure 3.1. The synthesis of core-shell nanoparticles starts with the generation of small gold nanoparticle seeds from an aqueous HAuCl₄ solution by the reduction using sodiumborohydride (NaBH₄) at room temperature.

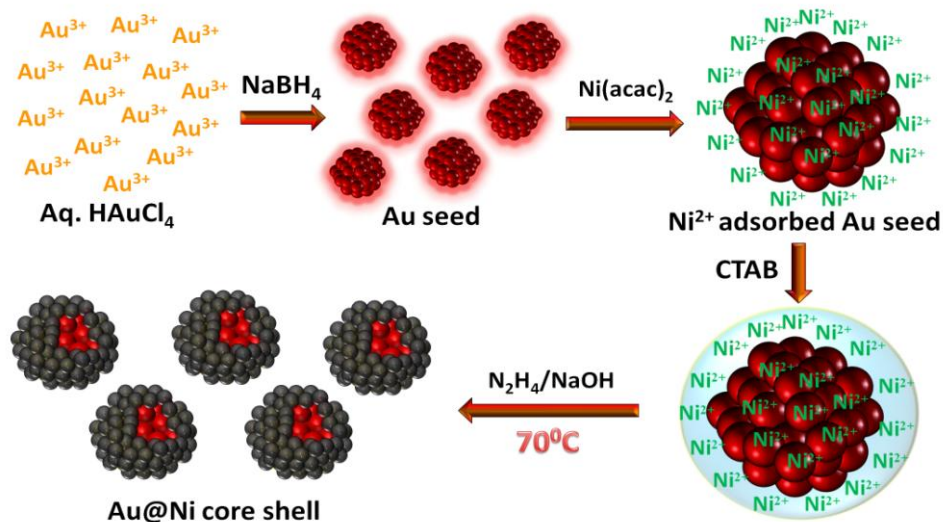


Figure 3.1 Scheme showing various steps involved in the formation of Au@Ni core-shell nanoparticles.

In each stage of the synthesis, the colloidal solution was analyzed using UV-Vis spectroscopy which gave initial evidence for the formation of core-shell morphology. An immediate colour change of the pale yellow gold precursor solution (absorbance at 220nm, Figure 3.2) to wine red color on addition of sodium borohydride which is a characteristic feature of gold nanoparticle SPR (Surface plasmon resonance)²⁹. The colloidal gold seed solution gave an absorbance at 515nm (Figure 3.2) in the UV-Vis spectra indicating the formation of nanogold. The in-situ generation of gold seeds in a one pot without any capping agent holds the key for the strong adsorption of nickel ions on to the naked gold nanoparticle surface and it also helps to control the overall size of core-shell nanoparticles. The sudden colour change of gold SPR to violet upon the addition of nickel precursor followed by capping agent cetyltrimethylammoniumbromide (CTAB) is a direct observation of the strong adsorption of nickel ions on the gold surface. It was further confirmed from the UV-Vis spectrum which shows a damping in the gold SPR feature with the appearance of a new peak around 295 nm which is due to the charge transfer of nickel ions in solution (Figure 3.2). The resultant solution was heated to 70 °C with subsequent addition of hydrazine-NaOH mixture in order to reduce the nickel ions to form a uniform shell. At this stage, a visible colour change was again observed from violet to brownish black which was the final stage of Au@Ni core-shell formation. The final colloidal solution showed no characteristic absorption in UV-Vis region (Figure 3.2) indicating the successful formation of nickel layer over the gold core. The damping of plasmonic features upon growth of a dissimilar metal has been attributed to the core-shell type growth in literature³⁰.

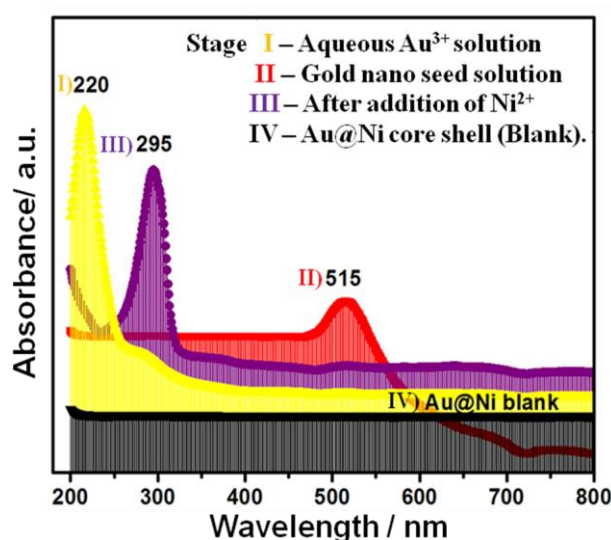


Figure 3.2 UV-Vis spectra recorded at each stage of synthesis of Au@Ni core-shell nanoparticles.

By changing the nickel metal precursor amount, Au@Ni core-shell nanoparticles with varying shell thickness ranging from 2 nm to 8 nm, keeping the same gold core was synthesized. Based on the gold to nickel metal ratio, the core-shell series of nanoparticles were designated as Au₈₀@Ni₂₀, Au₆₅@Ni₃₅ and Au₅₀@Ni₅₀ with increase in nickel shell thickness.

3.3.2 Transmission Electron Microscopy Studies (TEM)

The large area TEM and HR-TEM (High resolution TEM) images of the as synthesized Au@Ni core-shell nanoparticles are shown in Figure 3.3(a-f). All the TEM images were obtained by drop casting the samples on a Cu grid by dispersing the samples in isopropanol. The large area TEM images in Figure 3.3(a-c) show that the core-shell nanoparticles have average size around 15-20 nm for Au₈₀@Ni₂₀ with size increasing with increasing shell thickness for Au₆₅@Ni₃₅ and Au₅₀@Ni₅₀. Thus the average size of Au₆₅@Ni₃₅ and Au₅₀@Ni₅₀ were 20-22 nm and 26-28 nm respectively. With heavier atomic mass of gold compared to nickel, it is expected for Au core to appear darker in contrast with a lighter Ni shell. In the case of Au₈₀@Ni₂₀, as the shell thickness is very thin, the contrast difference is not prominent in the large area images but in other samples especially with a very high shell thickness (Au₅₀@Ni₅₀) the partition between the core and shell was clearly distinct.

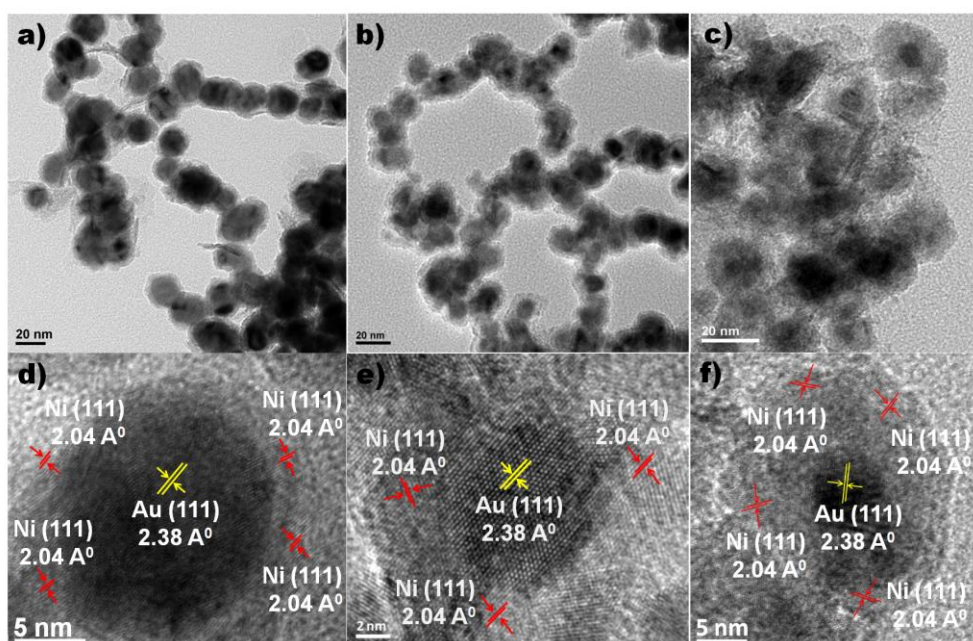


Figure 3.3 TEM images of Au@Ni core-shell nanoparticles. (a-c) corresponds to the large area TEM images and (d-f) HR-TEM images of single Au@Ni nanoparticles. Images are in the order (a and d) Au₈₀@Ni₂₀, (b and e) Au₆₅@Ni₃₅ and (c and f) Au₅₀@Ni₅₀.

Furthermore, the HR-TEM images shows that even with different nickel metal ratios the core-shell system is intact and proved the stability and growth of nickel overlayers over the gold core even with a large lattice mismatch. High resolution TEM images shown in Figure 3.3(d-f) gave d-spacing of 2.38 \AA corresponds to Au (111) planes and for Ni (111) the value is marked as 2.04 \AA ³¹. The formation of core and shell can be observed from the HR-TEM images where Ni lattice were observed around Au core.

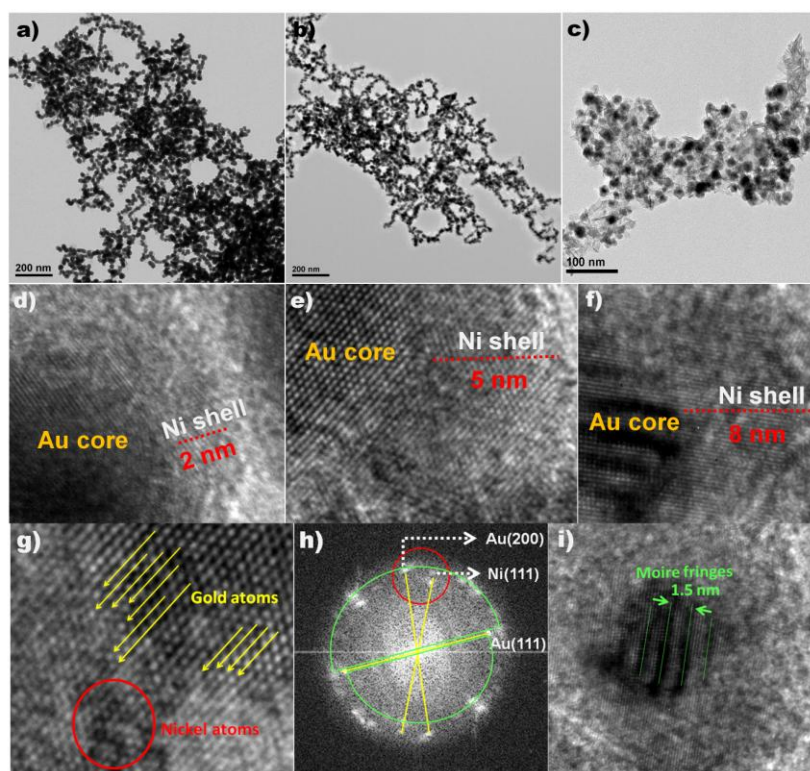


Figure 3.4 TEM images of Au@Ni core-shell nanoparticles. (a-c) corresponds to the large area TEM images and (d-f) HR-TEM images showing the nickel shell thicknesses of (a,d) Au₈₀@Ni₂₀, (b,e) Au₆₅@Ni₃₅ and (c,f) Au₅₀@Ni₅₀ core-shell nanoparticles. (g) shows an atomic resolution image of the interface of Au and Ni in Au@Ni core-shell system. (h) is the FFT (fast-Fourier-transform) pattern obtained from a single core-shell nanoparticle indicating the d-spacing values of Au, Ni and (i) demonstrates the moire fringes in Au@Ni core-shell system.

More detailed analysis of the TEM and HR-TEM images are given in the Figure 3.4(a-f). The HR-TEM images gave conclusive evidence that by increasing nickel precursor ratio the shell thickness of Au@Ni could be tuned. In the case of Au₈₀@Ni₂₀, HR-TEM analysis

showed the nickel shell thickness is approx. 2 nm and it increases to 4-5 nm and further 8-9 nm (Figure 3.4 d-f) with increasing nickel concentration for Au₆₅@Ni₃₅ and Au₅₀@Ni₅₀ respectively. The FFT pattern observed from an individual Au@Ni nanoparticle also showed the co-existence of gold and nickel planes (Figure 3.4 h). The appearance of moiré pattern with 1.5 nm (Figure 3.4 i) in the core-shell system also confirmed the growth of Ni over Au lattice³¹⁻³².

The XP spectra collected in UHV conditions from Au@Ni material gave further evidence for the core-shell architecture. With increasing Ni shell thickness over the gold core, the dampening of Au 4f signal was observed (Figure 3.5)²⁰. Thus with a nickel shell of 8-10 nm, the X-rays could barely penetrate the shell and probe the Au core. The C 1s XPS spectrum (Figure 3.5) obtained from the as synthesized Au@Ni core-shell materials showed the surface to be largely clean and devoid of carbonaceous surfactants which would be otherwise dominating the surface on a catalyst synthesized by employing organic surfactants.

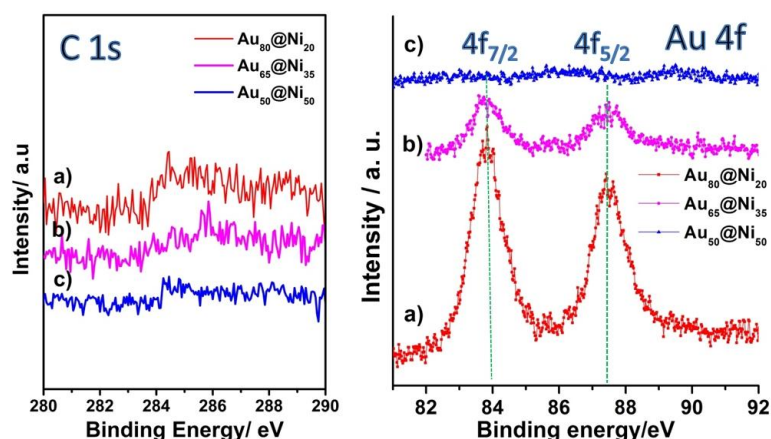


Figure 3.5 C 1s and Au 4f spectra of the as synthesized (a) Au₈₀@Ni₂₀ (b) Au₆₅@Ni₃₅ and (c) Au₅₀@Ni₅₀ core-shell nanoparticles at UHV-RT conditions.

3.3.3 Magnetic Measurements (VSM)

The magnetic properties of the Au@Ni bimetallic core-shell nanoparticles were explored by using superconducting quantum interference device (SQUID) measurements. Figure 3.6 demonstrates the hysteresis loop measured at room temperature for each of the core-shell samples using SQUID. All the three bimetallic samples showed a ferromagnetic behaviour^{31, 33} with typical saturation magnetization behaviour at room temperature

irrespective of the nickel concentration. Hence these materials play a bifunctional role of catalytic activity and their magnetic recovery by using an external magnet after the reaction. Au@Ni core-shell nanoparticles having various shell thickness showed typical hysteric behaviour with a sudden increase in magnetization initially in an external field. The samples recorded saturation magnetization values 2, 3.5 and 5 emu/gm for (a) Au₈₀@Ni₂₀, (b) Au₆₅@Ni₃₅ and (c) Au₅₀@Ni₅₀ respectively at an applied field of 5 kOe (Figure 3.6). The hysteresis width near to the zero field is also shown in the Figure 3.6 (inset-bottom) for the three core-shell compositions and they showed very low coercivity values less than 50 Oe. The relatively low saturation magnetization and coercivity values obtained for Au@Ni core-shell systems in comparison with monometallic nickel nanoparticles³⁴ can be due to the existence of nickel as a shell with thickness ranging from 2 nm to 8 nm³².

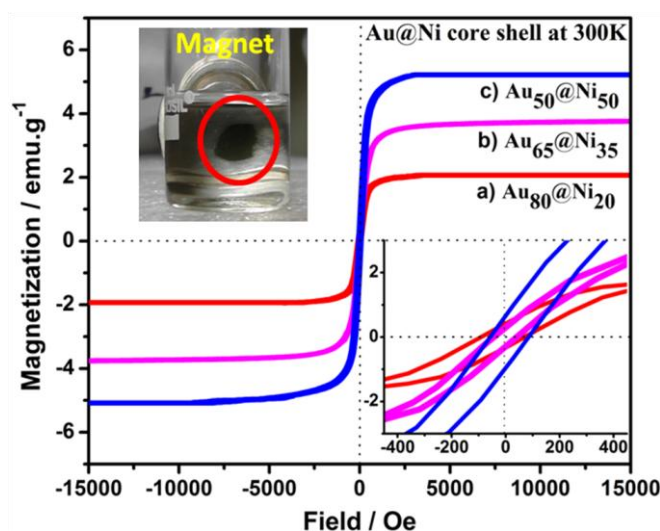


Figure 3.6 Hysteresis loops of (a) Au₈₀@Ni₂₀ (b) Au₆₅@Ni₃₅ and (c) Au₅₀@Ni₅₀ nanoparticles obtained at room temperature. Inset (down) shows the hysteresis width near to the zero magnetic field. Digital photograph shows the ferromagnetic character of Au@Ni core-shell nanoparticles.

3.3.4 X-Ray Diffraction Studies (XRD)

The powder XRD patterns obtained for the as synthesized core-shell nanoparticles (a) Au₈₀@Ni₂₀, (b) Au₆₅@Ni₃₅ and (c) Au₅₀@Ni₅₀ with different shell thickness are shown in the Figure 3.7. The standard reflections of the gold core in the FCC lattice is confirmed by the peaks at 2θ values 38.2, 44.3, 64.6 and 77.8 and it correspond to different planes of gold Au (111), Au (200), Au (220) and Au (311) respectively³³. In all the series of catalysts the gold core showed similar FWHM for Au (111) indicating the same gold seeds for the growth of

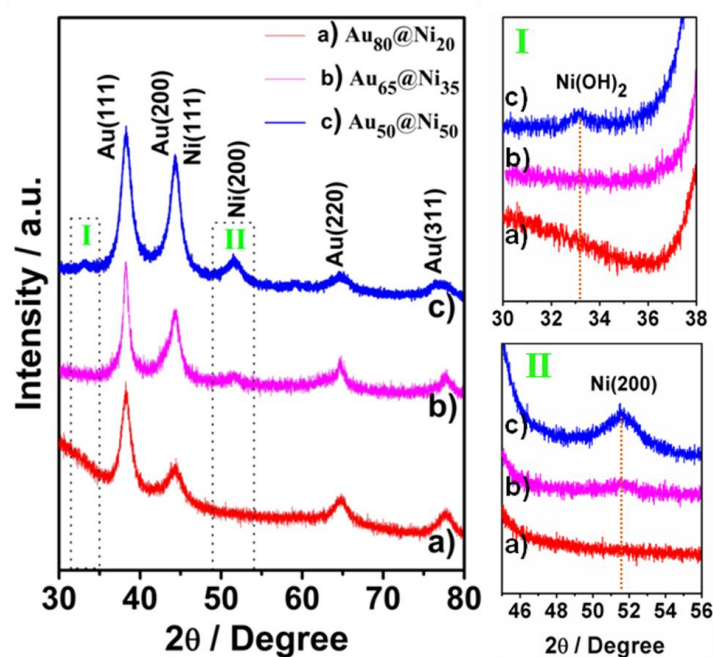


Figure 3.7 XRD patterns of core-shell (a) $\text{Au}_{80}\text{@Ni}_{20}$, (b) $\text{Au}_{65}\text{@Ni}_{35}$ and (c) $\text{Au}_{50}\text{@Ni}_{50}$ nanoparticles. (I & II) are the zoomed images of the area marked in the dotted boxes and the dotted lines corresponds to $\text{Ni}(\text{OH})_2$ and metallic Ni features respectively.

nickel overlayers. The fairly large FWHM (full width at half maximum) values of the reflections from the core-shell nanoparticles indicate the smaller size of Au@Ni structures in all the cases. The metallic nickel features appears at 44.5 and 51.8 corresponding to Ni (111) and Ni (200) planes from nickel in the FCC lattice³⁴. Since the Ni (111) reflection merges with the Au (200) it is difficult to identify the presence of nickel and it is convenient to follow the Ni (200) peak at 2θ value 51.8. From the XRD pattern it is evident that as the nickel shell thickness increases (from a - c in the Figure 3.7) the intensity of the Ni (200) peak also increases (Figure 3.7II). In the case of $\text{Au}_{80}\text{@Ni}_{20}$ nanoparticles with very thin Ni shell thickness of approx. 2 nm, XRD technique failed to probe the Ni shell. Whereas in $\text{Au}_{50}\text{@Ni}_{50}$ with 8nm nickel shell thickness, the Ni (111) and Ni (200) features were clearly visible with a peak intensity ratio at 44.5 approximately equal to the Au (111) peak. Apart from the features of Ni (200) it is also worth mentioning the intensity ratio comparison of the peak at 44.5 with respect to the Au (111) reflection at 38.2. Despite of the peak merging of Ni (111) along with Au (200), a gradual increase in the peak intensity was noted at 44.5 with the increase in the nickel ratio. The above observations validate the growth of metallic nickel lattice over the gold core in FCC lattice structure. For $\text{Au}_{50}\text{@Ni}_{50}$, the appearance of a new peak at 33.2 corresponding to (100) plane of $\text{Ni}(\text{OH})_2$ was noticeable (Figure 3.7I)³⁵. The presence of

Ni(OH)₂ feature gives a strong indication of the nature of a nickel surface that is prone to ambient oxidation which is expected for a monometallic nickel nanoparticle.

3.3.5 UHV and In-situ NAP-XPS Analysis of Au@Ni Core-shell Nanoparticles [Au₈₀@Ni₂₀, Au₆₅@Ni₃₅ and Au₅₀@Ni₅₀] under Various Temperature and Pressure Conditions

The previous ambient heating XRD study showed that Ni surface in Au@Ni bimetallic combination prepared by organic surfactant route can resist oxidation and demonstrated synergistic effects in catalysis with an extremely thin nickel shell¹⁹. Since XRD is a bulk technique, it is important to probe the bimetallic nanoparticles through XPS under reactive gas environment (oxygen in this case) to unravel the dynamics of Ni surface with an Au core. The samples were prepared by drop casting the concentrated colloidal solution on to a graphite substrate followed by vacuum drying in a desiccator. The dried samples were then immediately introduced inside the load lock chamber of the XPS spectrometer without much exposing to the atmosphere.

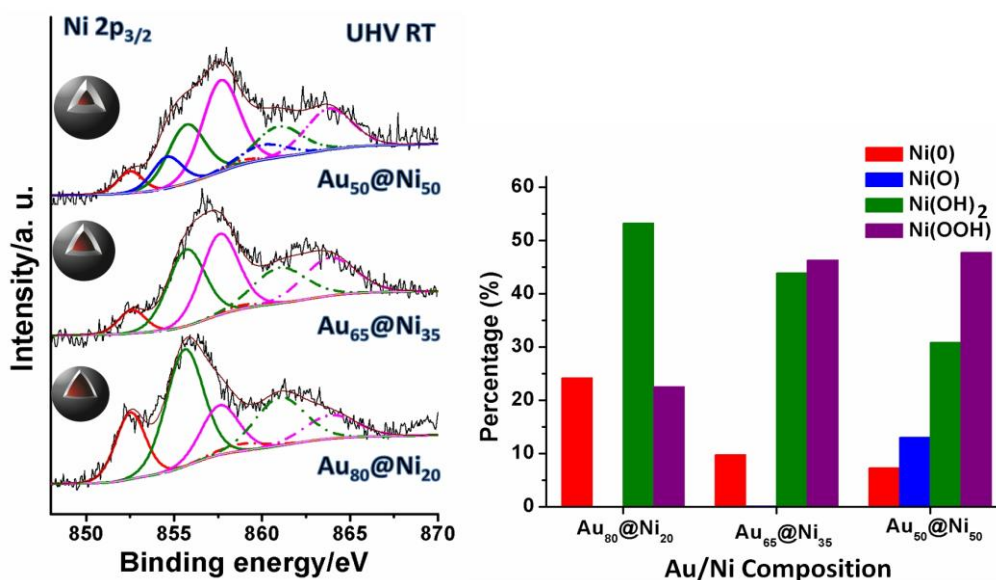


Figure 3.8 Ni 2p_{3/2} spectra and its deconvolution obtained for Au₈₀@Ni₂₀, Au₆₅@Ni₃₅ and Au₅₀@Ni₅₀ core-shell nanoparticles under UHV-RT conditions. Corresponding percentage composition of various nickel species present in Au₈₀@Ni₂₀, Au₆₅@Ni₃₅ and Au₅₀@Ni₅₀ nanoparticles under UHV-RT conditions [Red-metallic Ni, green-Ni(OH)₂, magenta-Ni(OOH) and blue-NiO. Solid lines indicate the deconvolution from the major species and dotted lines indicate the corresponding satellite features].

The XP spectra of the core-shell nanoparticles were recorded initially at UHV-RT (ultra high vacuum- room temperature) atmosphere followed by gradual increase in oxygen pressure and then temperature. Since the preliminary aim was to identify the synergistic effect of Au-Ni and the oxidation landscape of nickel which is obvious for monometallic nickel, a systematic temperature dependent XPS study is reported. Ni $2p_{3/2}$ core-level spectrum collected at UHV conditions and at room temperature is shown in Figure 3.8. Peak fittings were done for the whole Ni $2p_{3/2}$ region for the goodness of the fit. The stacked plots is the deconvoluted nickel spectra recorded at RT and UHV condition for Au@Ni core-shell nanoparticles with increasing shell thickness arranged from bottom to top of the graph. Au@Ni nanoparticles prepared in aqueous medium through a colloidal phase reduction method are dominated by nickel in different oxidation states. Au₈₀@Ni₂₀ with an extremely thin nickel shell thickness (~ 2 nm) was dominated by the peaks metallic nickel [Ni (0) - B.E. 852.6 eV], nickel hydroxide [Ni(OH)₂ - B.E. 855.8 eV] and nickel oxy hydroxide [Ni(OOH) - B.E. 857.6 eV]. On increasing the shell thickness, the oxidic Ni features increased with diminishing metallic Ni (0) component. With thickest shell (Au₅₀@Ni₅₀), the emergence of fourth peak was evident at B.E 854.6 eV which is ascribed to NiO. The assignments of binding energy (B.E) values for different Ni species were metallic nickel [Ni (0) - B.E. 852.6 eV], nickel hydroxide [Ni(OH)₂ - B.E. 855.8 eV], nickel oxide [NiO - B.E. 854.6 eV] and nickel oxy hydroxide [Ni(OOH) - B.E. 857.6 eV] based on the literature³⁶⁻³⁷. A detailed surface science study on the oxidation behaviour of monometallic nickel surface especially in presence of water vapour was reported by Payne et al³⁸. Their study demonstrated the ease of oxidation if the nickel is present in metallic form; the oxidation process is very quick under oxygen atmosphere as compared to water vapour. Generally, the nickel nanoparticles synthesized by colloidal route will be composed of mainly oxidic species which can be either hydroxide or oxide or sometimes both and the stabilization of metallic nickel is nearly impossible. From the peak intensities, it was possible to identify the major contribution from the hydroxide feature followed by oxy hydroxide and metallic. The metallic peak was well distinguishable from the other features and proves the existence of Ni (0) unambiguously. The quantification results of the deconvoluted peaks calculated from the peak area of the individual peaks for all the three series of core-shell nanoparticles are shown in the Figure 3.8. Au₈₀@Ni₂₀ core-shell nanoparticle consisted of almost 25 % of metallic nickel along with 50 % Ni(OH)₂ and the rest being oxy hydroxide. In the case of Au₆₅@Ni₃₅ and Au₅₀@Ni₅₀ samples the metallic feature was almost half of the amount that obtained for Au₈₀@Ni₂₀ core-

shell system. Au₆₅@Ni₃₅ core-shell nanoparticles were dominated by the oxidic species which was composed of almost equal amounts of hydroxide and oxy hydroxide. Also a sharp increase can be observed in the amount of oxy hydroxide as we move to Au₆₅@Ni₃₅ core-shell system (~ 45 %) which was around 20 % in the case of Au₈₀@Ni₂₀. Finally in Au₅₀@Ni₅₀, the emergence of NiO contributing more than that of metallic nickel is clearly evident with hydroxide and oxyhydroxide contributing to 30 and 40 % respectively to the surface species. Here XPS results necessitate the importance of surface analysis of the catalyst materials as XRD technique failed to probe the existence of oxide. From the above results it is clear that the as synthesised Au@Ni core-shell nanoparticles with a thin nickel shell shows the existence of an electronically/geometrically modified nickel surface. As the shell thickness increases, a transition to more oxidic nature was observed which can be a decoupling effect from the gold core beyond a certain limit of nickel overlayers.

After carrying out the UHV-RT measurements, the core-shell nanoparticles were exposed to different oxygen pressures at room temperature and at 100 °C. The individual deconvoluted spectral analysis is summarized in Figure 3.9. The stacked plots in each series of the samples (a) Au₈₀@Ni₂₀ (b) Au₆₅@Ni₃₅ and (c) Au₅₀@Ni₅₀ in the Figure 3.9 correspond to the spectra obtained under in-situ oxygen atmosphere conditions along with UHV-RT for comparison.

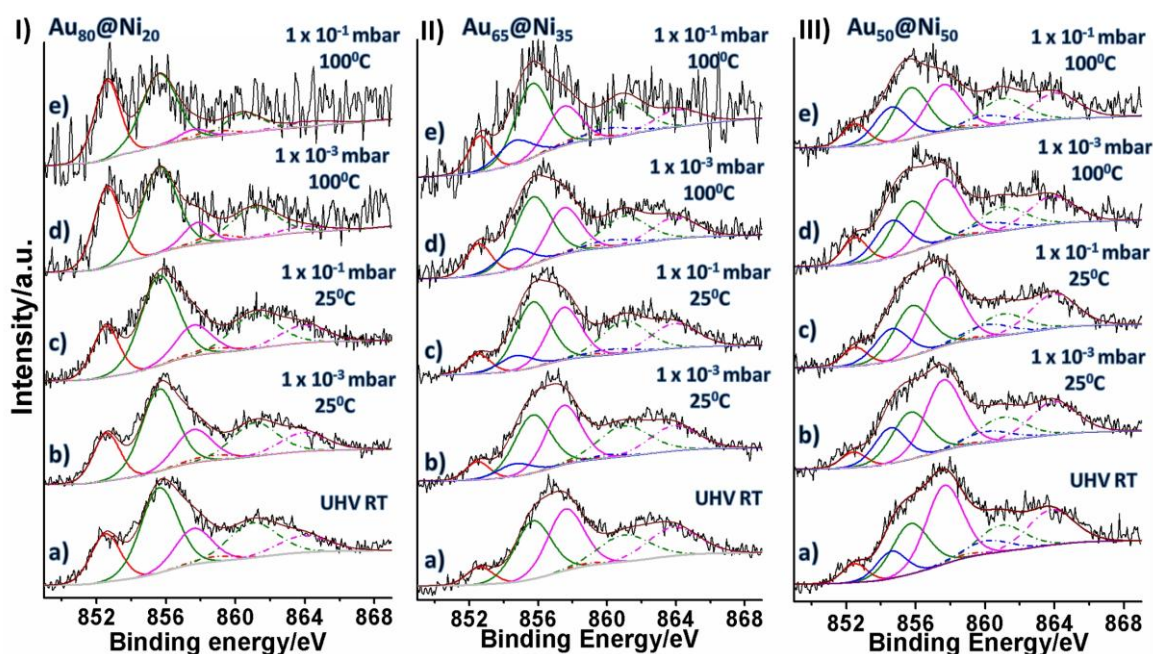


Figure 3.9 Ni 2p_{3/2} spectra and its deconvolution obtained for Au₈₀@Ni₂₀, Au₆₅@Ni₃₅ and Au₅₀@Ni₅₀ under oxygen atmosphere at various oxygen pressures & temperature conditions

[Red-metallic Ni, green-Ni(OH)₂, magenta-Ni(OOH) and blue-NiO. Solid lines indicate the deconvolution from the major species and dotted lines indicate the corresponding satellite features].

The Ni 2p spectra obtained at room temperature and at different O₂ pressures did not show much change in the electronic nature of nickel for the three samples. While Au₈₀@Ni₂₀ did not show any change for RT recorded spectra, Au₆₅@Ni₃₅ showed emergence of oxide (NiO) feature at B.E value of 854.6 eV at 10⁻³ mbar O₂. In the case of Au₅₀@Ni₅₀ the stable NiO feature was already present at UHV-RT condition spectra showing that the surface was more like bare Ni (monometallic) nanoparticle. The spectra collected at 100 °C and at O₂ atmosphere threw more insights into the oxidation behaviour of Ni with different shell thickness with Au core. The high pressure and temperature conditions caused a drop in the photoelectron intensity from the core-shell materials, but still a reasonably good XP spectrum was obtained at 100 °C and at 0.1 mbar O₂. In all the three compositions studied, the metastable Ni(OOH) with a B.E of 857.6 eV decomposes at 100 °C and at 0.1 mbar O₂. On the three compositions studied, nickel hydroxide contributes to the major surface species with varying proportions depending on the shell thickness. This observation is perfectly in agreement with nickel nanoparticles synthesized by wet chemical reduction route where the surface was mainly composed of various types of oxides and Ni(OH)₂ is considered as one of the stable surface species in the as synthesised form³⁹.

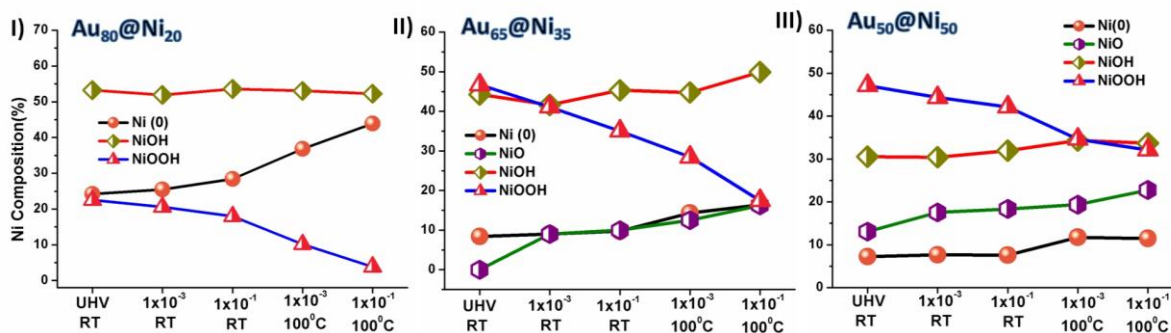


Figure 3.10 Changes in percentage composition of various nickel species present in Au₈₀@Ni₂₀, Au₆₅@Ni₃₅ and Au₅₀@Ni₅₀ at various pressures and temperature conditions.

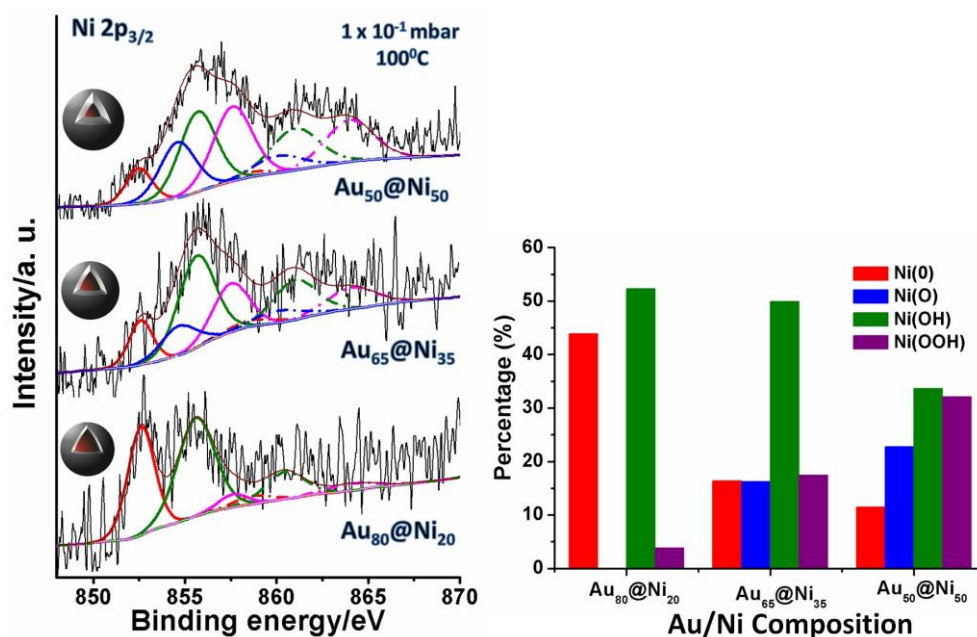


Figure 3.11 Ni $2p_{3/2}$ spectra and its deconvolution obtained for Au₈₀@Ni₂₀, Au₆₅@Ni₃₅ and Au₅₀@Ni₅₀ core-shell nanoparticles at 0.1mbar oxygen pressure and 100 °C. Figure b) Corresponding percentage composition of various nickel species present in Au₈₀@Ni₂₀, Au₆₅@Ni₃₅ and Au₅₀@Ni₅₀ nanoparticles at 0.1mbar oxygen pressure and 100 °C.

Another observation is that the NiO is absent on both Au₈₀@Ni₂₀ and Au₆₅@Ni₃₅ bimetallic core-shell nanoparticles under UHV conditions whereas 10-12 % NiO was already present in Au₅₀@Ni₅₀ to begin with. While nickel hydroxide is the major component in the first case, Ni(OOH) is found to be dominant on Au₆₅@Ni₃₅ and Au₅₀@Ni₅₀ surface along with Ni(OH)₂. Ni(OOH) species is considered as the metastable oxide phase which decomposes to other stable hydroxide and oxide phases⁴⁰. The various changes in the surface states of nickel at each stage of in-situ experimental conditions (from UHV-RT to 0.1 mbar, 100 °C) are shown in the Figure 3.10. On increasing the oxygen pressure, a decrease in the Ni(OOH) component was observed which undergoes a drastic reduction in XPS intensity at 100 °C. Interestingly, Au₈₀@Ni₂₀ core-shell nanoparticles with a very thin shell thickness of ~ 2 nm; the entire metastable oxide phase was converted to metallic Ni (0), whereas in Au₆₅@Ni₃₅ a larger proportion was converted to stable oxides at 100 °C and 0.1 mbar O₂ (Figure 3.11 for spectra and quantification details at 0.1 mbar and 100 °C). While this is the case, for Au₅₀@Ni₅₀ a considerable amount of NiO was there to begin with which either stabilises or inhibits the decomposition of Ni(OOH) to a large extent. The decomposition products of Ni(OOH) at 0.1 mbar and 100 °C as compared with initial state (UHV-RT) is shown in Figure 3.12 [Pie chart

is prepared by considering the total amount of Ni(OOH) at UHV-RT as 100 % in each of the respective cases and taking into consideration the changes in various surface species at 0.1 mbar and 100 °C are on the expense of decomposition of Ni(OOH)]. The decomposition analysis gave a clear indication that an extremely thin nickel shell (Au₈₀@Ni₂₀) of ~ 2 nm produces metallic Ni species on the surface whereas the other compositions having 4 nm and 8 nm Ni shell thickness produced predominantly other oxidic species. This demonstrates the diverse reactivity trends of Ni with Au core towards O₂ atmosphere.

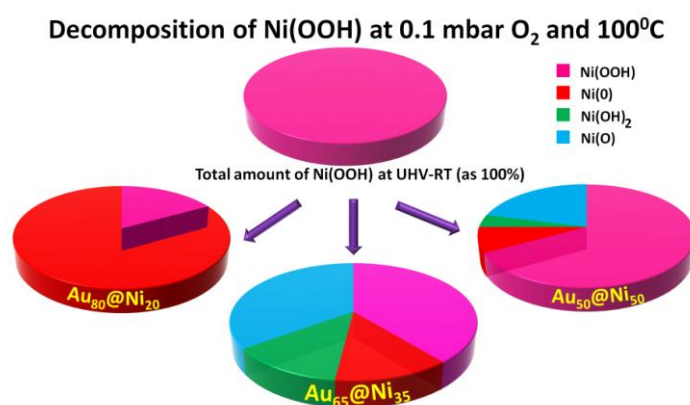


Figure 3.12 Pie chart demonstrating the percentage composition of various surface species of nickel formed from the decomposition of Ni(OOH) at 0.1 mbar O₂ and 100 °C as compared with the initial amount of Ni(OOH) at UHV-RT.

What is interesting to note here was the proportion of metallic Ni species on Au₆₅@Ni₃₅ and Au₅₀@Ni₅₀ species on Ni(OOH) decomposition. This would mean that Ni(OOH) species formed on Au₈₀@Ni₂₀ is highly metastable and decomposes to metallic Ni. The metallic Ni thus formed is highly resistant to further oxidation at 0.1 mbar O₂ and at 100 °C. With higher shell thickness the decomposition of Ni(OOH) at higher temperature led to the formation of other oxidic species also with a small increment in the amount of metallic Ni. This suggests that the Au₆₅@Ni₃₅ and Au₅₀@Ni₅₀ core-shell nanoparticles were highly prone to oxidation and readily converted to NiO since there was a major increase in NiO feature on these core-shell particles similar to Pt-Ni nanoparticles under oxygen atmosphere reported recently⁴¹. On Au₅₀@Ni₅₀ also the Ni(OOH) was found to be stabilized by other oxidic features which inhibits the decomposition to a large extent. From the above observations it is clear that when the nickel overlayers are very thin and in the close proximity of the gold core; the metallic form retained its stability and exhibited high resistance to oxidation at 0.1 mbar O₂ and 100

⁰C. Whereas in the other two cases with higher nickel shell thickness, the increase in stable oxide features (NiO and Ni(OH)₂) is predominant thereby undergoing the usual pathway of decomposition and oxidation which is typical of monometallic nickel⁴⁰. Also, the rate of decomposition of Ni(OOH) is found to be less in the case of thicker Ni shells; it attributes the findings by Payne et al, which demonstrated that stable oxide species (like NiO and Ni(OH)₂) stabilizes metastable Ni(OOH) once the surface layers gets covered with stable oxidic species³⁸.

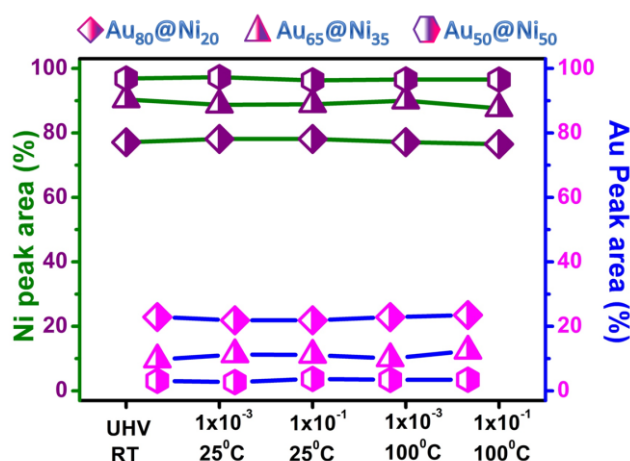


Figure 3.13 Total percentage composition of Au and Ni at the surface in Au₈₀@Ni₂₀, Au₆₅@Ni₃₅ and Au₅₀@Ni₅₀ core-shell nanoparticles under various in-situ conditions.

The core-shell nanoparticle like Rh-Pd and Pt-Pd reported in literature, showed dynamic surface reconstruction under reactive gases⁴². To probe this, the total percentage composition of Ni 2p and Au 4f at different conditions (Figure 3.13) was calculated. The plot illustrates the total peak area obtained for gold and nickel and their percentage comparison under the given experimental conditions. In the case of Au₈₀@Ni₂₀ and Au₆₅@Ni₃₅ samples, the Au 4f peaks showed only metallic species Au (0) [B.E of Au 4f_{7/2}- 84.0 eV and Au 4f_{5/2}- 87.6 eV] under all the experimental (UHV-RT and in-situ) conditions (Figure 3.14 I-II). The nature of gold proved that gold does not undergo any changes in its oxidation state while carrying out the NAPXPS investigations and preserve its noble character which was present in the as synthesised form of core-shell systems. [In the case of Au₅₀@Ni₅₀ with a thicker nickel shell, the limitations of the escape depth of the photoelectrons generated by soft X-rays resulted in extremely weak Au 4f signal and considered as negligible (close to zero) - Figure 3.14 III]. The results shown in the Figure 3.13 prove that all the three core-shell systems were stable under the reactions conditions of 0.1 mbar O₂ and up to 100 °C. The steady nickel

composition shows that the structural transformations like decomposition of metastable phases is limited only to the nickel shell and does not have any geometrical effect with the gold core such as diffusion or segregation. In any such case of segregation, there should be a variation in the percentage composition of gold and nickel in the XP spectra as reported in the previous literature of highly lattice mismatched Pt-Ni system⁴¹.

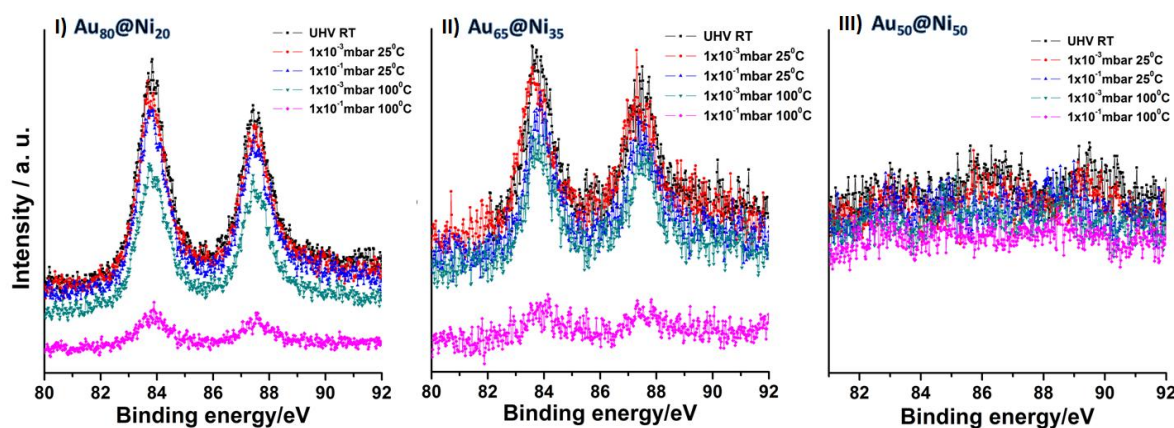


Figure 3.14 Au 4f spectra obtained for (I) Au₈₀@Ni₂₀, (II) Au₆₅@Ni₃₅ and (III) Au₅₀@Ni₅₀ under oxygen atmosphere at various pressure and temperature conditions.

3.3.6 Catalytic Activity Results of Au@Ni Core-shell Nanoparticles [Au₈₀@Ni₂₀, Au₆₅@Ni₃₅ and Au₅₀@Ni₅₀] for Selective Hydrogenation of Phenylacetylene (P.A)

One of the most important driving force to synthesis a surface engineered tailor made Au@Ni core-shell nanostructures is to realize how lattice mismatched nickel-gold surface could influence the reactivity trends in catalysis. The literature reports already showed the synergistic behaviour of gold-nickel surfaces towards various catalytic conversions not necessarily a core-shell system^{22, 43}. To explore this, colloidal phase hydrogenation of phenyl acetylene was carried out and the activity results of these core-shell nanoparticles where the role of metallic nickel surface is beneficial²³. Normally the monometallic nickel surfaces are prone to ambient oxidation and it is found that such surfaces pass through an induction period in order to retain their metallic feature followed by the catalytic conversion on the surface²². All the catalysts were tested for phenylacetylene hydrogenation reactions by using gaseous hydrogen in various solvents (MeOH and DCM) under milder conditions of pressure and temperature than reported for other modified hybrid nickel nanoparticles⁴⁴⁻⁴⁵. The results proved that the core-shell catalysts can efficiently hydrogenate alkynes to corresponding

alkenes and alkanes depending on the solvent medium as reported previously⁴⁶. The catalytic activity and selectivity results observed for phenylacetylene hydrogenation (alkyne) are shown in the Figure 3.15 and 3.16.

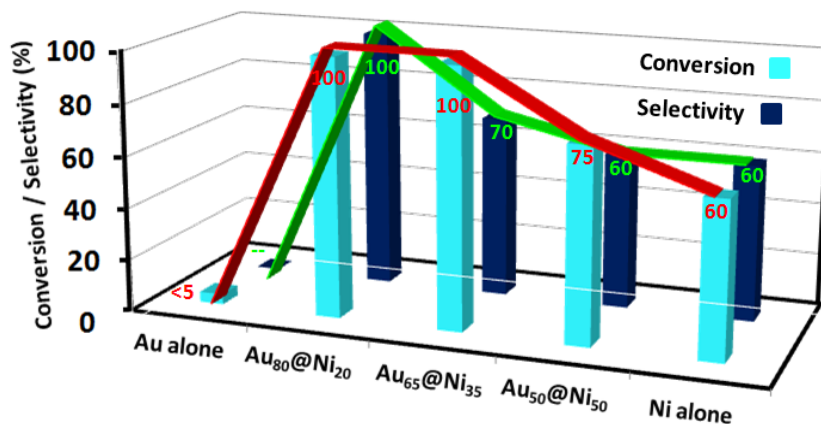


Figure 3.15 P.A hydrogenation in MeOH by using Au@Ni core-shell nanoparticles with various shell thickness along with their monometallic analogues Au and Ni nanoparticles in MeOH (Time - 3 hrs, Red line connectivity- Conversion and green line connectivity-selectivity).

Figure 3.15 demonstrates the comparison of catalytic activity of various core-shell catalysts with that of monometallic gold and nickel nanoparticles⁴⁶. The core-shell catalyst with a composition of Au₈₀@Ni₂₀ gave full conversion and complete selectivity towards ethylbenzene demonstrating superior conversion and selectivity. The one with next higher shell thickness Au₆₅@Ni₃₅ showed 100 % conversion where as selectivity towards E.B was 70 % with rest being styrene. The conversion and selectivity dropped to 75 % and 60 % for Au₅₀@Ni₅₀ and the performance was similar to monometallic nickel nanoparticles. From the selectivity graphs, it should be noted that in MeOH solvent the hydrogenation is so rapid that it could completely hydrogenate P.A all the way to corresponding alkanes. Styrene is commercially more valuable product than EB, but Au₈₀@Ni₂₀ shows that it can completely saturate the triple bond in P.A with high efficiency. The reports proved the excellent activity and selectivity of Au₈₀@Ni₂₀ for ethylbenzene production and outweigh the monometallic counterparts. The gold nanoparticles alone showed a weak activation of phenylacetylene.

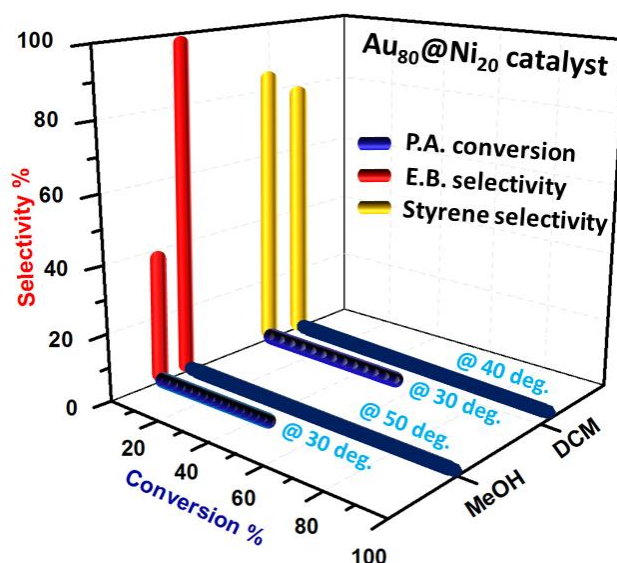


Figure 3.16 Catalytic activity results obtained for P.A. hydrogenation by using Au₈₀@Ni₂₀ nanoparticles in MeOH and DCM (50 ml) by using a Parr reactor at different temperatures & pressures [in MeOH and DCM, the substrate (P.A) is 5 & 1 mmol, respectively. Time- 3 hrs in MeOH and 10 hrs in DCM].

It has been reported previously that the styrene selectivity towards P.A. hydrogenation on nickel nanoparticles can be tuned by choosing a suitable solvent. The core-shell bimetallic catalyst reported here also showed similar solvent effects. By changing the solvent from methanol (MeOH) to dichloromethane (DCM) there is a selectivity change from ethylbenzene (E.B) to an industrially important styrene production (Figure 3.16). Here, Au₈₀@Ni₂₀ catalysts in DCM gave 100 % conversion of phenylacetylene and 80 % selectivity for styrene under very low hydrogen pressures and near ambient temperatures (40 °C). The Au₈₀@Ni₂₀ catalyst was found active even at room temperature but with lesser activity (in both the solvents- Figure 3.16) and in the case of DCM solvent it showed slightly higher selectivity for styrene at room temperature at the expense of conversion. Thus, the catalytic activity demonstrated on core-shell Au@Ni bimetallic nanoparticles unambiguously demonstrate the importance of surface engineering nanomaterials for desired catalytic applications.

3.4 Conclusions

Bimetallic Au@Ni core-shell nanoparticles have been synthesized in aqueous medium and at milder conditions not reported so far. The size of the Ni shell could be tuned from 2 nm up to 8 nm by changing the nickel precursor concentration. The landscapes of metastable Ni(OOH) decomposition and the oxidation behavior of Au@Ni has been probed by NAPXPS. The NAPXPS studies shows that the decomposition pathways of metastable Ni(OOH) species is vastly different on Au₈₀@Ni₂₀ with extremely thin Ni shell (~ 2 nm) which mainly converts to metallic nickel and it is found to be stable in oxygen atmosphere even at 100 °C. On the other surfaces, Ni(OOH) surface species predominantly gets converted to more stable oxidic (Ni²⁺) species which is typical for monometallic nickel surfaces. The NAPXPS surface studies corroborates well with a model catalytic reaction study of selective hydrogenation of P.A which is found to be extremely facile on Au₈₀@Ni₂₀ bimetallic particle as compared with monometallic counterparts and core-shell systems with higher nickel shell thickness.

3.5 References

1. Duan, S.; Wang, R., Bimetallic nanostructures with magnetic and noble metals and their physicochemical applications. *Prog. Nat. Sci.: Mater. Int.* **2013**, *23* (2), 113-126.
2. Gilroy, K. D.; Ruditskiy, A.; Peng, H.-C.; Qin, D.; Xia, Y., Bimetallic Nanocrystals: Syntheses, Properties, and Applications. *Chem. Rev.* **2016**.
3. Major, K.; De, C.; Obare, S., Recent Advances in the Synthesis of Plasmonic Bimetallic Nanoparticles. *Plasmonics* **2009**, *4* (1), 61-78.
4. Toshima, N.; Yonezawa, T., Bimetallic nanoparticles-novel materials for chemical and physical applications. *New J. Chem.* **1998**, *22* (11), 1179-1201.
5. Alayoglu, S.; Eichhorn, B., Rh–Pt Bimetallic Catalysts: Synthesis, Characterization, and Catalysis of Core–Shell, Alloy, and Monometallic Nanoparticles. *J. Am. Chem. Soc.* **2008**, *130* (51), 17479-17486.
6. Yan, J.-M.; Zhang, X.-B.; Akita, T.; Haruta, M.; Xu, Q., One-Step Seeding Growth of Magnetically Recyclable Au@Co Core–Shell Nanoparticles: Highly Efficient Catalyst for Hydrolytic Dehydrogenation of Ammonia Borane. *J. Am. Chem. Soc.* **2010**, *132* (15), 5326-5327.
7. Maroun, F.; Ozanam, F.; Magnussen, O. M.; Behm, R. J., The Role of Atomic Ensembles in the Reactivity of Bimetallic Electrocatalysts. *Science* **2001**, *293* (5536), 1811-1814.
8. Chen, M.; Kumar, D.; Yi, C.-W.; Goodman, D. W., The Promotional Effect of Gold in Catalysis by Palladium-Gold. *Science* **2005**, *310* (5746), 291-293.
9. Besenbacher, F.; Chorkendorff, I.; Clausen, B. S.; Hammer, B.; Molenbroek, A. M.; Nørskov, J. K.; Stensgaard, I., Design of a Surface Alloy Catalyst for Steam Reforming. *Science* **1998**, *279* (5358), 1913-1915.
10. Rodriguez, J. A.; Goodman, D. W., The Nature of the Metal-Metal Bond in Bimetallic Surfaces. *Science* **1992**, *257* (5072), 897-903.

11. Mavrikakis, M.; Hammer, B.; Nørskov, J. K., Effect of Strain on the Reactivity of Metal Surfaces. *Phys. Rev. Lett.* **1998**, *81* (13), 2819-2822.
12. Ruban, A.; Hammer, B.; Stoltze, P.; Skriver, H. L.; Nørskov, J. K., Surface electronic structure and reactivity of transition and noble metals. *J. Mol. Catal. A: Chem.* **1997**, *115* (3), 421-429.
13. Luedtke, W. D.; Landman, U., Stability and Collapse of Metallic Structures on Surfaces. *Phys. Rev. Lett.* **1994**, *73* (4), 569-572.
14. Zhou, X. W.; Wadley, H. N. G., Misfit dislocations in gold/Permalloy multilayers. *Philos. Mag.* **2004**, *84* (2), 193-212.
15. Holgado, J. P.; Ternero, F.; Gonzalez-de-laCruz, V. M.; Caballero, A., Promotional Effect of the Base Metal on Bimetallic Au–Ni/CeO₂ Catalysts Prepared from Core–Shell Nanoparticles. *ACS Catal.* **2013**, *3* (9), 2169-2180.
16. Chandler, B. D.; Long, C. G.; Gilbertson, J. D.; Pursell, C. J.; Vijayaraghavan, G.; Stevenson, K. J., Enhanced Oxygen Activation over Supported Bimetallic Au–Ni Catalysts. *J. Phys. Chem. C* **2010**, *114* (26), 11498-11508.
17. Wang, D.; Li, Y., Bimetallic Nanocrystals: Liquid-Phase Synthesis and Catalytic Applications. *Adv. Mater.* **2011**, *23* (9), 1044-1060.
18. Alayoglu, S.; Zavalij, P.; Eichhorn, B.; Wang, Q.; Frenkel, A. I.; Chupas, P., Structural and Architectural Evaluation of Bimetallic Nanoparticles: A Case Study of Pt–Ru Core–Shell and Alloy Nanoparticles. *ACS Nano* **2009**, *3* (10), 3127-3137.
19. Chapter 2A of this Thesis
20. Chapter 2A of this Thesis
21. Kulkarni, G. U.; Vinod, C. P., Diverse reactivity patterns observed in the interaction of oxygen with nickel deposited on gold and tungsten surfaces. *Appl. Surf. Sci.* **1997**, *115* (4), 336-341.
22. Sarkar, S.; Sinha, A. K.; Pradhan, M.; Basu, M.; Negishi, Y.; Pal, T., Redox Transmetalation of Prickly Nickel Nanowires for Morphology Controlled Hierarchical Synthesis of Nickel/Gold Nanostructures for Enhanced Catalytic Activity and SERS Responsive Functional Material. *J. Phys. Chem. C* **2010**, *115* (5), 1659-1673.
23. Chapter 2B of this Thesis
24. Chapter 2C of this Thesis
25. Li, P.-Z.; Aijaz, A.; Xu, Q., Highly Dispersed Surfactant-Free Nickel Nanoparticles and Their Remarkable Catalytic Activity in the Hydrolysis of Ammonia Borane for Hydrogen Generation. *Angew. Chem. Int. Ed.* **2012**, *51* (27), 6753-6756.
26. Duan, H.; Wang, D.; Li, Y., Green chemistry for nanoparticle synthesis. *Chem. Soc. Rev.* **2015**, *44* (16), 5778-5792.
27. Lopez-Sanchez, J. A.; Dimitratos, N.; Hammond, C.; Brett, G. L.; Kesavan, L.; White, S.; Miedziak, P.; Tiruvalam, R.; Jenkins, R. L.; Carley, A. F.; Knight, D.; Kiely, C. J.; Hutchings, G. J., Facile removal of stabilizer-ligands from supported gold nanoparticles. *Nat. Chem.* **2011**, *3* (7), 551-556.
28. Mourdikoudis, S.; Liz-Marzán, L. M., Oleylamine in Nanoparticle Synthesis. *Chem. Mater.* **2013**, *25* (9), 1465-1476.
29. Eustis, S.; El-Sayed, M. A., Why gold nanoparticles are more precious than pretty gold: Noble metal surface plasmon resonance and its enhancement of the radiative and nonradiative properties of nanocrystals of different shapes. *Chem. Soc. Rev.* **2006**, *35* (3), 209-217.
30. Henning, A. M.; Watt, J.; Miedziak, P. J.; Cheong, S.; Santonastaso, M.; Song, M.; Takeda, Y.; Kirkland, A. I.; Taylor, S. H.; Tilley, R. D., Gold–Palladium Core–Shell Nanocrystals with Size and Shape Control Optimized for Catalytic Performance. *Angew.*

Chem. Int. Ed. **2013**, 52 (5), 1477-1480.

31. She, H.; Chen, Y.; Chen, X.; Zhang, K.; Wang, Z.; Peng, D.-L., Structure, optical and magnetic properties of Ni@Au and Au@Ni nanoparticles synthesized via non-aqueous approaches. *J. Mater. Chem.* **2012**, 22 (6), 2757-2765.
32. Huang, L.; Shan, A.; Li, Z.; Chen, C.; Wang, R., Phase formation, magnetic and optical properties of epitaxially grown icosahedral Au@Ni nanoparticles with ultrathin shells. *Crystengcomm* **2013**, 15 (13), 2527-2531.
33. Zhang, H.; Ding, J.; Chow, G.; Ran, M.; Yi, J., Engineering Magnetic Properties of Ni Nanoparticles by Non-Magnetic Cores. *Chem. Mater.* **2009**, 21 (21), 5222-5228.
34. Chen, Y.; Peng, D.-L.; Lin, D.; Luo, X., Preparation and magnetic properties of nickel nanoparticles via the thermal decomposition of nickel organometallic precursor in alkylamines. *Nanotechnology* **2007**, 18 (50), 505703.
35. Xu, L.; Ding, Y.-S.; Chen, C.-H.; Zhao, L.; Rimkus, C.; Joesten, R.; Suib, S. L., 3D Flowerlike α -Nickel Hydroxide with Enhanced Electrochemical Activity Synthesized by Microwave-Assisted Hydrothermal Method. *Chem. Mater.* **2008**, 20 (1), 308-316.
36. Biesinger, M. C.; Payne, B. P.; Grosvenor, A. P.; Lau, L. W. M.; Gerson, A. R.; Smart, R. S. C., Resolving surface chemical states in XPS analysis of first row transition metals, oxides and hydroxides: Cr, Mn, Fe, Co and Ni. *Appl. Surf. Sci.* **2011**, 257 (7), 2717-2730.
37. Grosvenor, A. P.; Biesinger, M. C.; Smart, R. S.; McIntyre, N. S., New interpretations of XPS spectra of nickel metal and oxides. *Surf. Sci.* **2006**, 600 (9), 1771-1779.
38. Payne, B. P.; Biesinger, M. C.; McIntyre, N. S., The study of polycrystalline nickel metal oxidation by water vapour. *J. Electron. Spectrosc. Relat. Phenom.* **2009**, 175 (1-3), 55-65.
39. Prieto, P.; Nistor, V.; Nouneh, K.; Oyama, M.; Abd-Lefdil, M.; Díaz, R., XPS study of silver, nickel and bimetallic silver–nickel nanoparticles prepared by seed-mediated growth. *Appl. Surf. Sci.* **2012**, 258 (22), 8807-8813.
40. Moroney, L. M.; Smart, R. S. C.; Roberts, M. W., Studies of the thermal decomposition of β NiO(OH) and nickel peroxide by X-ray photoelectron spectroscopy. *J. Chem. Soc., Faraday Trans. 1* **1983**, 79 (8), 1769-1778.
41. Ahmadi, M.; Behafarid, F.; Cui, C.; Strasser, P.; Cuenya, B. R., Long-Range Segregation Phenomena in Shape-Selected Bimetallic Nanoparticles: Chemical State Effects. *ACS Nano* **2013**, 7 (10), 9195-9204.
42. Tao, F.; Grass, M. E.; Zhang, Y.; Butcher, D. R.; Renzas, J. R.; Liu, Z.; Chung, J. Y.; Mun, B. S.; Salmeron, M.; Somorjai, G. A., Reaction-Driven Restructuring of Rh-Pd and Pt-Pd Core-Shell Nanoparticles. *Science* **2008**, 322 (5903), 932-934.
43. Nikolaev, S. A.; Smirnov, V. V.; Vasil'kov, A. Y.; Podshibikhin, V. L., Synergism of the catalytic effect of nanosized gold-nickel catalysts in the reaction of selective acetylene hydrogenation to ethylene. *Kinet. Catal.* **2010**, 51 (3), 375-379.
44. Chen, X.; Zhao, A.; Shao, Z.; Li, C.; Williams, C. T.; Liang, C., Synthesis and Catalytic Properties for Phenylacetylene Hydrogenation of Silicide Modified Nickel Catalysts. *J. Phys. Chem. C* **2010**, 114 (39), 16525-16533.
45. Chen, X.; Li, M.; Guan, J.; Wang, X.; Williams, C. T.; Liang, C., Nickel–Silicon Intermetallics with Enhanced Selectivity in Hydrogenation Reactions of Cinnamaldehyde and Phenylacetylene. *Ind. Eng. Chem. Res.* **2012**, 51 (9), 3604-3611.
46. Polshettiwar, V.; Baruwati, B.; Varma, R. S., Nanoparticle-supported and magnetically recoverable nickel catalyst: a robust and economic hydrogenation and transfer hydrogenation protocol. *Green Chem.* **2009**, 11 (1), 127-131.

Chapter 4

Surfactant free Synthesis of Au@Ni Core-shell Nanochains in Aqueous Medium as Efficient Transfer Hydrogenation Catalysts

➤ Outline of the chapter

- ✓ Surfactant free aqueous phase synthesis of magnetic Au@Ni nanostructures
- ✓ Chain-like Au@Ni core-shell nanostructures with thermal stability
- ✓ In-situ NAPXPS and ex-situ XRD analysis at higher Temp. (in O₂ atm) to analyze oxidation resistance of bare Au@Ni surfaces.
- ✓ Highly active bimetallic catalysts for transfer hydrogenation of acetophenone

This chapter is adapted from the following publication to be submitted:

1. Surfactant free Synthesis of Au@Ni Core-shell Nanochains in Aqueous Medium as Efficient Transfer Hydrogenation Catalysts. Vysakh A. B., K. J. Shebin, Ruchi Jain, C.S. Gopinath, C. P. Vinod.

Chapter 4: Surfactant free Synthesis of Au@Ni Core-shell Nanochains in Aqueous Medium as Efficient Transfer Hydrogenation Catalysts

4.1 Introduction

In heterogeneous catalysis, hybrid metal nanostructures¹⁻³ plays pivotal role in deciding the activity and selectivity⁴⁻⁶. The size and shape controlled synthesis of many hybrid systems are now possible by wet chemical reduction routes and it promises to design thermodynamically challenging nanostructures⁷⁻¹². In real time practices, the strict control over the synthesis protocols has been achieved only with the aid of capping agents or ligands which are generally long chain organic moieties such as surfactants or polymers¹³⁻¹⁶. During nanoparticle formation, especially in the growth stage, ligands are utilized for inhibiting the unwanted growth by adsorbing to the unstable nanoparticle surfaces. They simultaneously stabilize the nanoparticles either by compensating excess surface free energy of the nanoparticles or by transforming in to micelle formation around the nanoparticles. In either way they protect the nanoparticles from coalescence in the colloidal phase by inhibiting the inter particle interactions leading to particle growth. Hence the interfering acts of capping agents in the nanostructure synthesis are exemplary and the selection of suitable capping agents depends on the final application of the materials. However, in heterogeneous catalysis the presence of surfactants on the nanoparticle surface produces effects in most cases are detrimental on the catalytic behaviour of the materials¹⁷⁻¹⁹. Thus, the surfactant coated nanostructures are never an excellent option for catalysis since they reduces the chance of adsorption of substrates on to the catalytically active sites¹⁹⁻²⁰. Surface exposure of a catalyst or in other means the accessibility of active site of catalysts also demands equal importance in catalysis as that of size and shape control.

While, the role of capping agent in nanoparticle synthesis is well understood for nanoparticle stability, making the nanoparticle surface free from impurities for better catalytic activity is essential and less explored. In traditional catalysis the capping agents are removed by depositing the colloidal nanoparticles (impregnation) on to suitable supports and removing the capping agents by applying various methods like thermal treatments (Eg: high temperature calcination) and oxidative methods²¹⁻²². But in most of the cases the above methods lead to altered particle size and morphology from that of respective colloidal state²¹⁻²³. Recently

Hutchings and group reported a facile removal of capping ligands from supported gold nanoparticle catalysts without affecting the size and morphology and they showed their abnormally high catalytic activity for CO conversion as compared to untreated catalysts¹⁹. The report also illustrates the negative impact or poisoning effect of capping agents on the catalytic activity of the materials and necessitates the need of capping agent removal from the catalyst for better performances. In colloidal phase catalysis, the poisoning effect of such capping agents are more pronounced as the complete removal of excess capping agents are quite difficult and will result in sintering of nanoparticles²⁴. The bimetallic combinations are not an exception from the above discussions and the effect of capping agent on catalytic activity of bimetallic systems are reported by Wu and co-workers²⁵. Their results showed the poisoning effect of surfactant PVP and its facile removal through a NaBH₄ treatment to expose the real activity of the Pt-Pd bimetallic nanomaterials for hydrogen production. Meanwhile other reports also demonstrated the role of capping agent in deciding the activity and selectivity of the nanoparticle catalysts including bimetallic systems²⁶⁻²⁹. In any case the role of surface adsorbents/impurities in catalysis is important and demands thorough investigations. Previous works demonstrated that Au-Ni bimetallic system shows synergistic properties for catalytic applications and the synthesis of such challenging nanostructures can be achieved through various solution phase reduction routes³⁰⁻³². Apart from the synthesis challenge, the gold nickel core-shell systems (Au@Ni) can be applied for designing stable and sustainable catalysts which can show oxidation resistance, coke resistance, and enhanced catalytic activity³³⁻³⁵. It is really worth to synthesise such bimetallic synergistic materials having a large lattice mismatch (16 %) ³⁶⁻³⁷ without the aid of any capping agents and by keeping the size regime with optimized core and shell requirements of gold and nickel. Decoupling the unwanted effects from these structures will provide more insights into the synergistic behaviour and it will help to isolate the properties as only because of these metallic combinations. The synthesis of ligand free core-shell materials is reported here in aqueous medium with an extended network form. The materials are characterized by NAPXPS along with other routine characterization tools followed by the demonstration of its excellent catalytic activity. The eco-friendly aqueous phase synthesis strategy adopted here offers a green synthesis route for bimetallic core-shell nanostructures³⁸. There are less number of reports on the effective removal of capping agents after synthesis stage particularly for catalytic applications in the colloidal phase³⁹ which also brings special focus of this chapter.

4.2 Experimental Section

Hydrogentetrachloroaurate(III)trihydrate [HAuCl₄.3H₂O], Nickel acetylacetonate [Ni(acac)₂], Sodiumborohydride [NaBH₄], and Hydrazinehydrate 80 % [NH₂-NH₂.H₂O] were purchased from Sigma Aldrich [Germany] and used as received. Sodiumhydroxide [NaOH] and Isopropanol [IPA] were obtained from Merck, India. The substrate Acetophenone along with Potassium hydroxide [KOH] for catalytic activity tests were also purchased from Merck, India. All the synthesis procedure was carried out in ultra pure Millipore water.

Synthesis of Au@Ni core-shell nanochains

An aqueous gold precursor solution of 2.5×10^{-4} M HAuCl₄.3H₂O was made in 50 ml of millipore water and stirred gently. And after a while 650 microliter (μL) of 0.1M freshly prepared ice cold NaBH₄ solution prepared in millipore water was added quickly and stirring continued for another 15 minutes. In the second stage of the reduction, the colloidal solution was heated to 70 °C, followed by the addition of nickel acetylacetonate (0.01 mmol) to the solution and stirred well for uniform dispersion. Then a mixture of 750 microliter (μL) hydrazine hydrate and NaOH (prepared by dissolving 80 mg NaOH dissolved in 2ml 80 % hydrazine hydrate) was added to the hot solution drop wise for reducing nickel ions on the surface of gold nanoparticles. The solution turns to a black colloidal suspension initially, after a while the core-shell nanostructure turns to a leafy like structure by attracting each other and floats in the medium leaving behind a clear solvent. The floating core-shell nanochains were separated from the synthesis medium by using an external magnet as the nanostructures were magnetic in nature. The supernatant solution was decanted and the nanoparticles were washed with millipore water to remove any residual reducing agents present in the system. The core-shell nanochains were redispersed in isopropanol for further characterizations and catalytic activity tests.

NAPXPS measurements of core-shell nanoparticles (in-situ experiments)

All the XPS investigations were carried out in a custom built laboratory ambient pressure photoelectron spectrometer (Lab-APPES) at CSIR-NCL, Pune which is built and supplied by Prevac, Poland. It can be used for XPS/UPS measurements up to 1 mbar pressure and up to 873 K temperature by conventional heating methods on the solid surfaces. The XPS unit is equipped with VG Scienta's R3000HP electron energy analyzer (EEA) and X-ray monochromator MX650 from VG Scienta and it is sealed from the analysis chamber by using

a thin aluminum window (5 μm). Apart from the monochromator X-ray source, dual anode X-ray source (Al $K\alpha$ and Mg $K\alpha$) is also available for generating X-rays and both can work with an acceleration voltage of a maximum of 15 kV. Lab-APPES carries an exchangeable cone with different apertures (0.3-5 mm) at the tip of the ELR. Currently, the high-pressure XP spectra collected here are obtained with a 1.2 mm aperture cone and by using the dual anode X-ray source (Al $K\alpha$ - 1486.6 eV) at 15 kV voltages. All the spectra were recorded with pass energy of 50 eV at a slit width of 0.2 mm (analyzer entrance) and at a distance of 1 mm between the sample surface and the analyzer cone. The analysis of core-shell samples (prepared by drop casting the core-shell samples dispersed in isopropanol on to the conductive carbon and dried in vacuum) were carried out under UHV and 0.1 mbar oxygen atmosphere with temperature window from room temperature (R.T) to 200 $^{\circ}\text{C}$. All the spectra at various conditions were recorded after reaching stabilized conditions of temperature and pressure. The O_2 gas used for creating oxygen atmosphere is purchased from Inox Air Products Ltd., 99.999 % and used without any further purification. The oxygen pressure at the sample surface was accurately measured by using a CTR gauge and controlled dosing has been done with the help of a leak valve to maintain the requisite pressure on the sample surface. After recording the XP spectra, curve fitting has been done by using CasaXPS software, with asymmetric Lorentzian-Gaussian sum-type line shapes, preceded by the Shirley background subtraction.

Catalytic activity tests- Transfer hydrogenation reactions of acetophenone using IPA

Transfer hydrogenation reactions of acetophenone using isopropanol as the hydrogen donor and solvent under different reaction parameters like temperature, catalyst and base amounts were carried out in a 5 ml volume sealed glass tube. In a typical hydrogenation reaction 1 mmol of the substrate was mixed with 3 ml isopropanol and specified amounts of base KOH with Au@Ni core-shell catalysts. Then the reaction cell sealed tight, sonicated for 5 minutes and kept at predesigned temperatures (80 $^{\circ}\text{C}$ and 120 $^{\circ}\text{C}$) for the required time intervals. After the completion of the reaction samples were collected from the sealed tube and catalyst was separated with the help of an external magnet. The reactant mixture collected and analyzed with the help of a Gas Chromatograph (G.C) equipped with a flame ionization detector (F.I.D) having a HP-1 capillary column. All the compounds were calibrated with standard sample retention times in the G.C.

4.3 Results and Discussion

4.3.1 UV-Vis Spectroscopy Analysis (UV-Vis)

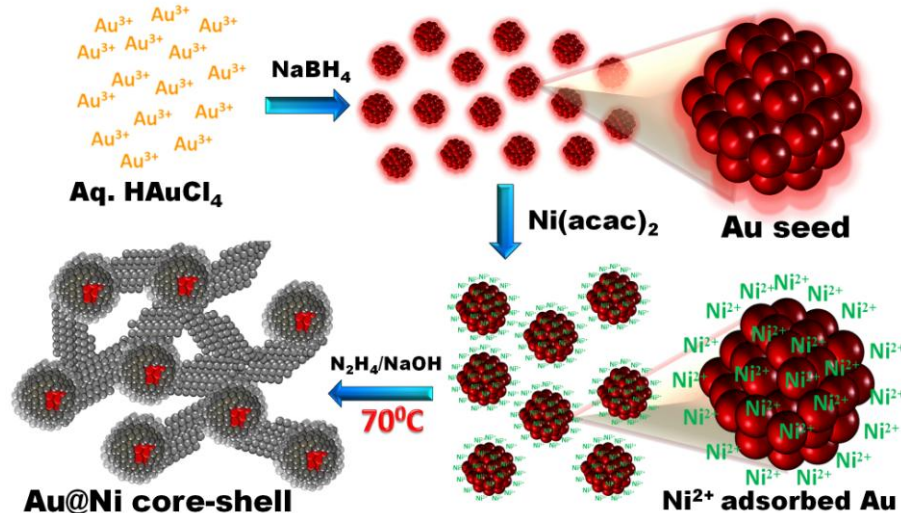


Figure 4.1 Scheme showing various stages of generating surfactant free Au@Ni core-shell nanochains in aqueous medium.

The growth of Au@Ni nanochains were monitored at various stages of formation by using UV-Vis spectroscopy. Figure 4.1 represents the scheme of formation Au@Ni core-shell morphology based on the UV-Vis spectra observations obtained at different stages of the synthesis process and Figure 4.2 shows the UV-Vis spectra obtained for the colloidal solutions. The gold precursor solution in aqueous medium with characteristic yellow colour gave a peak at 220 nm in UV-Vis analysis. The colour change to wine red colloidal solution due to SPR⁴⁰ absorbance at 515 nm indicated the formation of gold nanoparticles⁴¹. These bare gold nanoparticles served as the nucleation sites for the adsorption of the nickel ions in the later stage. It was found that the absence of capping agents in the reaction medium facilitated the ease of nickel ion adsorption on the gold seeds which was evident by the rapid colour change of the wine red colour colloidal solution with the addition of nickel precursor. The violet colour of the solution (peak at 295 nm) gave a clear indication of strong binding of nickel ions on the SPR active gold nanoparticles. The same colour was absent in the case of bare nickel ions dispersed in water which resulted in a greenish appearance. The subsequent reduction of nickel ions attached to gold nanoparticle surface was done by heating to a pre-designed temperature in the presence of hydrazine and resulted in the formation of bimetallic core-shell nanochains. The complete damping of the gold plasmon band after the reduction and deposition of nickel on the gold surface showed the successful formation of

nickel shell on the gold core⁴². After the nickel reduction generating Au@Ni core-shell, the magnetic nature the core-shell nanoparticles and surfactant free conditions were resulted in lattice penetrated core-shell nanochains. The Au@Ni core-shell nanochains found structurally stable and the chain like networks were found to extend several hundreds of nanometers to microns (evidenced from TEM and SEM analysis- discussed later).

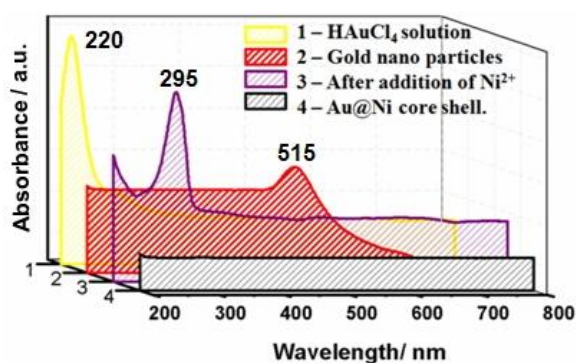


Figure 4.2 UV-Vis spectra recorded at various stages of synthesis of Au@Ni core-shell nanochains.

4.3.2 Transmission Electron Microscopy Studies (TEM)

As synthesised Au@Ni core-shell nanochains were dispersed in isopropanol by sonication and drop casted on the Cu grid for carrying out transmission electron microscopy (TEM) analysis. Large area images and HR-TEM (high resolution transmission electron microscopy) images were collected from various spots on the TEM grid and analyzed for the macroscopic morphology. Unlike to the previously demonstrated Au@Ni core-shell nanoparticles in this thesis which are well separated from each other by definite boundaries (Chapter 3 of this thesis), the surfactant free synthesis yielded a long extending network like nanostructures which is evident from the large area TEM images given in Figure 4.3. They roughly gave the appearance of long chain networks with single stranded or multi stranded branching without breaking the continuity of the extended network. The size (or width) of this nanochain structures measured from an isolated single stranded area (Figure 4.3b) corresponded to a maximum of 20 nm and with an average of 15 nm firmly ascertained the belief that the nanochain organization started after the individual core-shell nanoparticle formation. It is believed that the absence of stabilizing agents of the nanoparticles by the way of capping agents in the synthesis medium allowed them to interact each other forming extended long chain structures. The inherent ferromagnetic domains of nickel shell directed the nanoparticles to assemble in a chain like manner. The contrast difference between heavier

noble metal (Au) and lighter (Ni) non noble metal were observed in the TEM images particularly in HR-TEM analysis. The HR-TEM image obtained from a single stranded isolated nanochain demonstrated in Figure 4.3b showed a clear contrast difference in the inner and outer area indicating the formation of core-shell morphology in the nanochains. The lattice fringe analysis (Figure 4.3b) carried out at the core and the shell gave values of 2.38 Å and 2.04 Å respectively which corresponds to the Au (111) and Ni (111) d-spacing values⁴³. To get a detailed information about the core-shell structure; a single core-shell moiety connected to the neighbouring particle with a ligament was spotted (Figure 4.4). A careful analysis was done on this area to extract the minute details of the bimetallic structure (Figure 4.4). It can be seen that the dense core area is composed of gold atoms with characteristic lattice fringe values of gold and the outer most layers were consistent with the nickel d-spacing values which covered the gold core completely. Apart from that the ligaments between each core-shell nanoparticle which connect them each other mainly consist of nickel atoms and the lattice fringe measurements proved the presence of only nickel in this area (Figure 4.4). SEM was employed to explore the three dimensional morphology of the bimetallic nanostructure. The SEM images obtained for the as synthesised bimetallic materials recorded after drop casting to a clean silicon wafer are shown in Figure 4.3e-f. The images cover an area of more than tens of micrometers in Figure 4.3e and its higher resolution image shown in Figure 4.3f. Both the image shows that the nanostructure consists of lumps of the interconnected core-shell nanochains. The extensive interconnection and multi stranded nature of the system was confirmed from the SEM image and these behaviour gave a porous nature for the bimetallic nanochains in a large area imaging. The SEM images showed good agreement with large area images obtained in TEM analysis (Figure 4.3c). As a whole, from the microscopic investigations it was found that the size of the core-shell moiety is around 15-20 nm with an interconnected chain morphology which extends throughout the material. The Ni shell thickness was kept under 2nm, because of the results on Au@Ni core-shell systems from previous chapters (Chapter 2 and 3) proved the necessity of controlling the shell thickness for effective catalysis and maximum synergistic activity. Thus a green synthesis strategy developed in aqueous medium without any surfactants consisting of a one pot reduction method demonstrated an efficient route for novel Au@Ni core-shell architectures. Apart from the optimized size range, the porous network like morphology can enhance the catalytic behaviour of the materials and also improves the stability by preventing agglomeration⁴⁴.

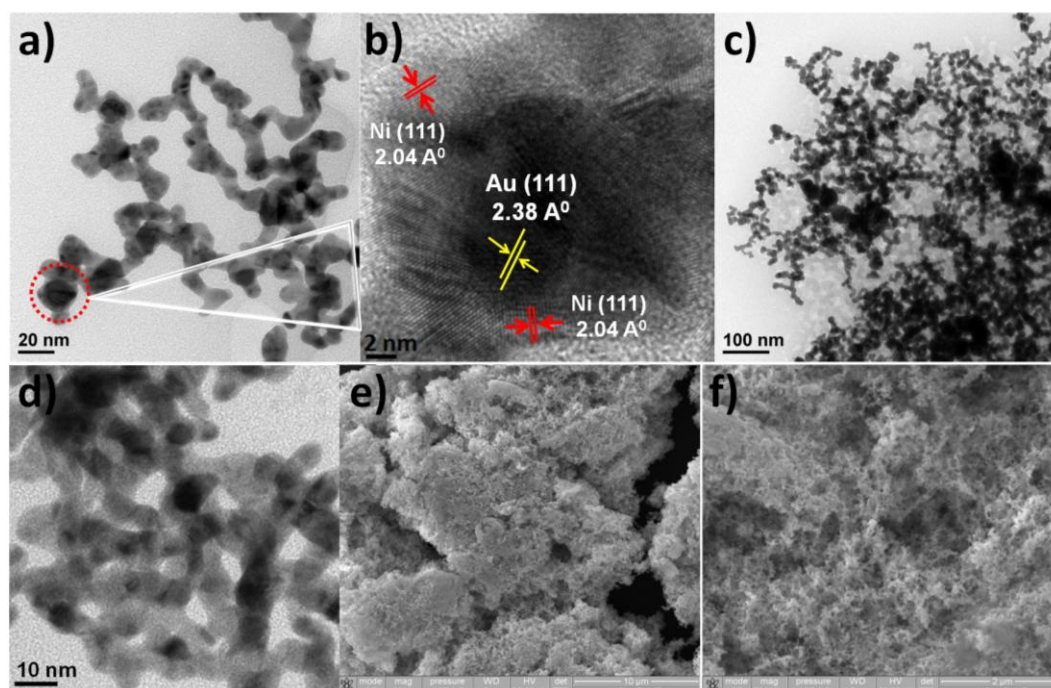


Figure 4.3 (a-d) TEM, HR-TEM images and (e-f) SEM images of Au@Ni core-shell nanochains. (a and d) corresponds to single stranded and multi stranded areas of Au@Ni nanochains. (b) HR-TEM image of Au@Ni along with lattice fringe analysis at the core and shell area and (c) representing large area TEM view. SEM images show the porous like morphology for the network structure of Au@Ni nanochains.

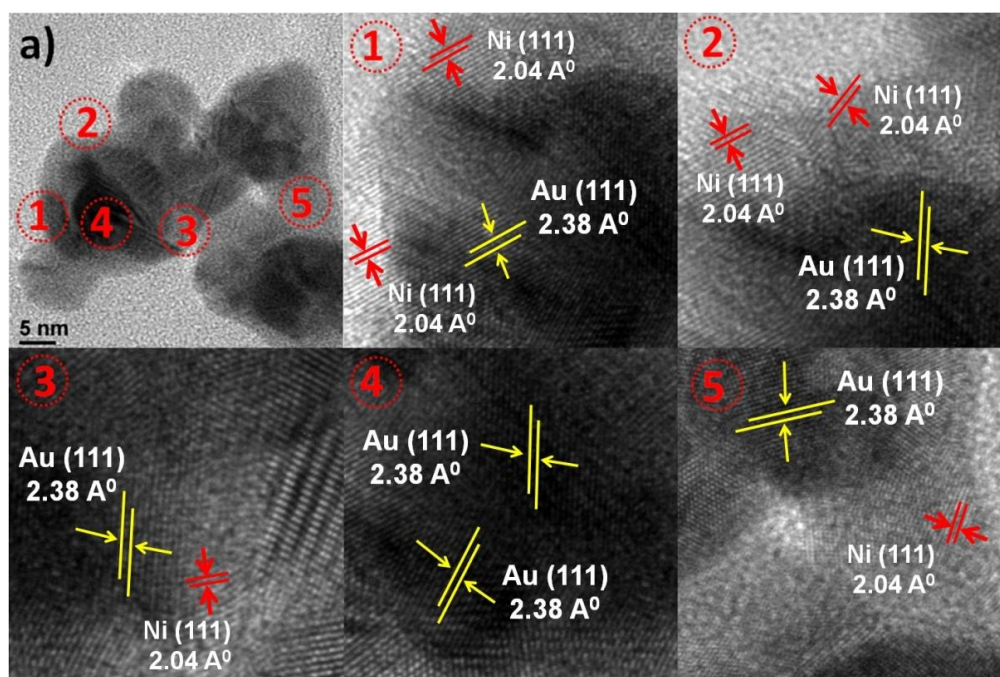


Figure 4.4 HR-TEM images and lattice fringe analysis from different spots of Au@Ni core-shell nanochains.

4.3.3 X-Ray Diffraction Studies (XRD)

XRD pattern obtained for Au@Ni core-shell bimetallic nanostructures are depicted in Figure 4.5. The X-ray diffractions gave valuable information about the crystalline phase and size of the core-shell nanostructures. Since XRD is an averaging technique from a large area of the material it gives more reliable data about the material as a bulk. In the case of core-shell nanostructures, gold reflections at 2θ values 38.2, 44.3 and 64.6 corresponding to Au (111), Au (200) and Au (220) respectively⁴⁵ showed the standard peak positions without any alloying effects. Also XRD failed to probe the characteristic feature of nickel in the core-shell nanostructures (Figure 4.5 I red dotted box). The absence of nickel feature shows the lack of extended lattice ordering of nickel shell confirming the presence of very thin nickel shell even after the formation of nanostructures. Meanwhile the broad reflections from the gold core with fairly large FWHM (full width at half maximum) values is a proof for the size controlled formation of nanostructures and effective stabilisation of the gold nanoparticle core by complete nickel coating. The particle size calculation by using Scherrer equation corroborated with the TEM analysis and confirmed the size of gold core to be around 15 nm. The most intense peak for the identification of nickel is Ni (111) at 44.5 which overlap with Au (200) reflection and hence it was required to check the other secondary reflections of nickel [Ni (200)-51.8 highlighted in the red dotted box in Figure 4.5 II]⁴⁶. Unfortunately, characteristic feature of nickel reflection was not observed and the thin nickel lattice over the gold core was also not expected to show any appreciable diffraction.

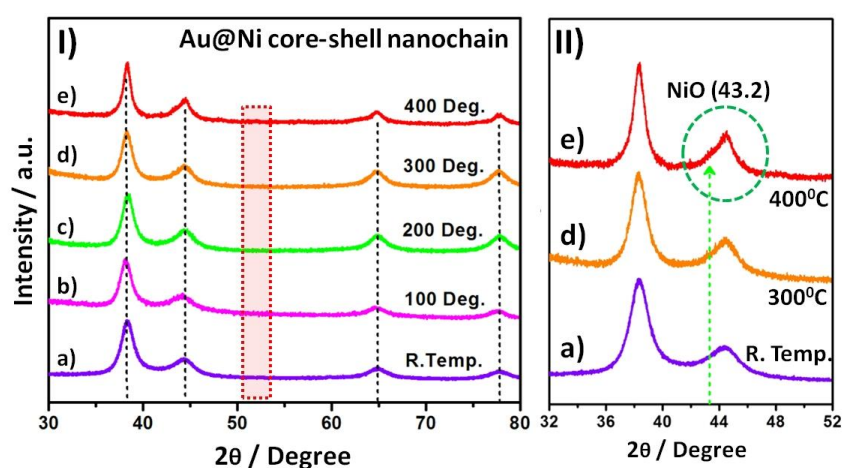


Figure 4.5 Temperature-dependent XRD of Au@Ni core-shell nanochains. Dotted lines indicate the standard Au reflections. Red dotted box indicates the absence of nickel diffraction at 51.8. Image (II) is the enlarged area of (I) and the green circled area shows the broadening & appearance of a new peak at 43.2 corresponding to nickel oxide after heated to 400 °C.

Because of the structural diversity of the core-shell nanostructures synthesised through a surfactant free strategy, it was essential to check for the structural stability of the materials and synergistic behaviour especially towards oxidation. Hence a temperature dependent XRD analysis was done by heating at various temperatures up to 400 °C. Such analysis can provide a wealth of information about the structural stability and oxidation behaviour of material under air. Figure 4.5 represent the diffraction patterns obtained after heating at various temperatures. Figure 4.5 II is the enlarged image of Figure 4.5 I and in all the figures the metallic nickel feature was absent (highlighted in the red dotted box) confirming the absence of extended nickel lattices which can happen only by agglomeration of the particles. The enlarged XRD image confirms the structural stability of the nanochains, since from room temperature to 300 °C there was no difference in the broad Au (111) reflection retaining a similar FWHM value. At 400 °C there was an observable sharpening of the peak with lowering of FWHM values reflecting an increase in particle size due to high temperature heating. Furthermore at 400 °C a new shoulder peak appeared at 43.2 corresponding to NiO reflection³⁰. The NiO feature started emerging at 300 °C as evident by the broadening of Au (200) reflection at 44.3. The XRD observations from the as synthesised and high temperature heated samples proved that the material is structurally stable and bulk oxidation resistant up to 200 °C. The XRD analysis indirectly proves the existence of very thin nickel lattice which does not undergo agglomeration even in the absence of capping agents and protects the gold core apart from the oxidation resistance nature.

4.3.4 Magnetic Measurements (VSM)

The magnetic properties of the Au@Ni bimetallic core-shell nanochain were explored by using VSM measurements. It was indispensable to carry out VSM analysis to prove the existence of nickel since XRD could not probe the characteristic features of nickel. Also it was helpful to know the crystalline phase of nickel apart from the magnetic properties. From the earlier reports, the ferromagnetic nature of core-shell Au@Ni was established from the FCC nickel lattice^{30, 47}. Figure 4.6 demonstrates the hysteresis loop obtained at room temperature (300 K) for the core-shell nanochains and it resemble a ferromagnetic behaviour with a typical saturation magnetization close to 2 emu/gm. The very low coercivity values observed as a result of narrow width of the hysteresis loop near to the zero fields can be due to the existence of very thin nickel shell⁴⁸. The ferromagnetic behaviour of Au@Ni can be utilized for the catalyst recovery by using an external magnet.

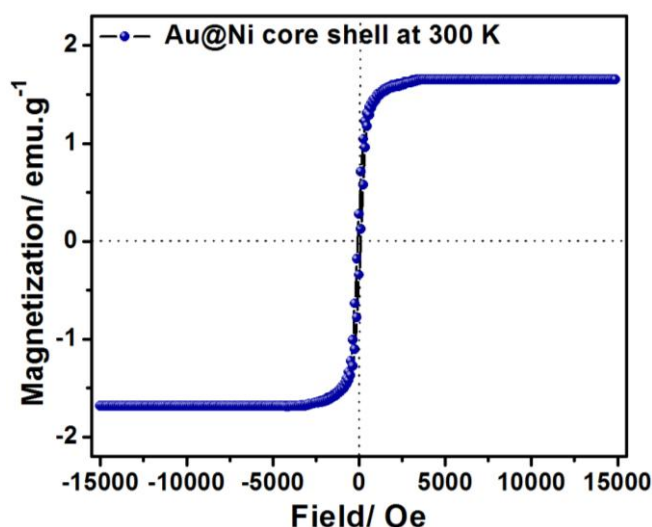


Figure 4.6 Hysteresis loop measured at room temperature for Au@Ni magnetic core-shell nanochains.

4.3.5 NAP-XPS Analysis of Au@Ni Core-shell Nanochains under Various Temperature and Pressure Conditions

The XRD heating experiments of the Au@Ni core-shell nanochains proved the bulk oxidation resistance and structural stability up to 200 °C. The data obtained from the XRD analysis demonstrated synergistic effects in the bimetallic combinations which is unusual for monometallic nickel and demands more investigation about the electronic nature of the core-shell nanochains. Since adsorption is purely a surface phenomenon, it was interesting to know about the surface properties of these core-shell nanochains especially the exposed nickel surface. Hence the core-shell nanochains synthesised in a ligand free medium are characterized by using XPS. All the conditions employed in the modified aqueous phase synthesis strategy were not favourable for retaining the metallic feature of nickel particularly at the exposed surfaces. The absence of capping agent was expected to provide facile interaction of oxygen molecules with the surface. Also, the high pH medium (because of NaOH and hydrazine) will facilitate the hydroxide formation and lack of inert atmosphere and temperature (70 °C) expected to favour the oxidation more readily. Therefore, it was expected that the nickel surface will be composed of mainly different oxidic species such as hydroxide, oxy hydroxides, defective oxides and pure oxides as it is likely to observe in case of monometallic nickel nanoparticles.

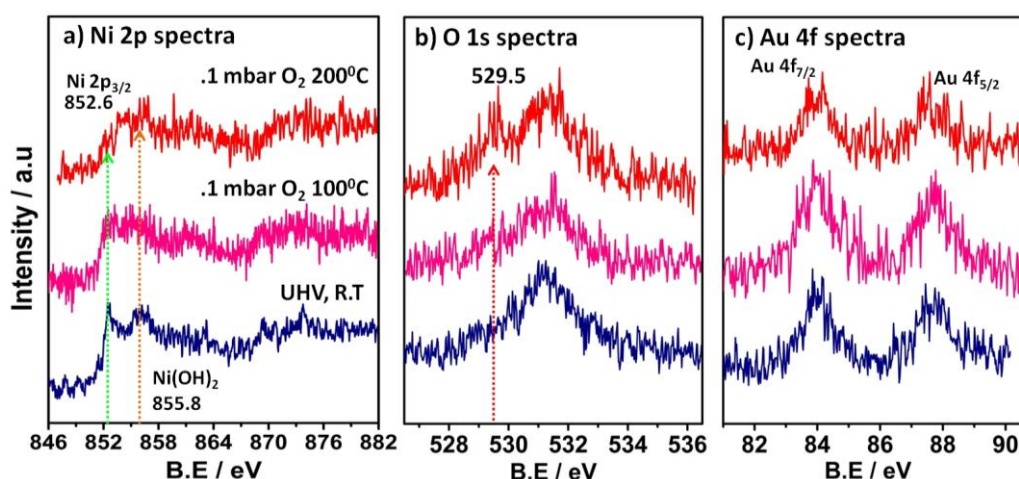


Figure 4.7 In-situ NAPXPS data recorded individually for Ni, O and Au at various O₂ pressure and temperature conditions. The green and red dotted lines in the Ni spectra indicate the metallic and hydroxide species of Ni respectively. The lower binding energy in the O spectra denoted by the dotted lines indicates the oxide species and Au shows standard B.E values for metallic species.

The previous NAPXPS investigation of Au@Ni core-shell nanoparticles synthesized in aqueous medium with thin shell thickness showed the synergistic properties as compared to other series of core-shell materials (Chapter 3 of this thesis), the surfactant free bimetallic nanostructures with same composition was designed to reproduce similar synergy. Since, the synthesis was carried out under surfactant free conditions; it is easy to decouple all the other external parameters that can influence the electronic modification like capping agents etc²⁵. The initial XPS studies of the core-shell nanochains were carried out at room temperature under UHV conditions by using an Al K α dual anode X-ray source. The results are shown in Figure 4.7 and it consists of individual scans for nickel, oxygen and gold respectively. In a guest-host concept of bimetallic overlayers in surface science, core-shell structure gold contributes the host metal and nickel overlayers corresponds to the guest element and the effect of surface modification mainly to the nickel surface⁴⁹. Figure 4.7 shows the gold 4f spectra along with nickel 2p in the bimetallic system. It was highly useful to record the O 1s spectra, since it carries a lot of information about the presence of various oxidic species. Also any changes in the nickel features will reflect in the oxygen spectra as both can give complementary informations.

The UHV-RT spectra recorded for Ni, O and Au are shown in blue colour (Figure 4.7) and it was unexpected to perceive a remarkably high percentage of metallic nickel species

dominating over hydroxide feature. The hydroxide feature present at 855.8 eV was obvious in many instances of colloidal nickel nanoparticle synthesis. The metallic feature present at 852.6 eV (Ni 2p_{3/2}) contributing to almost 50 % of nickel without any ligand protection at the surface was remarkable. The observations were in total contrast to bare nickel nanoparticle which generally shows 854 eV. Complementary results were obtained from the corresponding oxygen spectra recorded under similar conditions and same time. The oxygen 1s spectrum was dominated mainly by the hydroxide peak centered around 532 eV. The presence of only hydroxide feature in the O 1s spectra also confirmed the absence of nickel oxide in the core-shell nanochains as evident from the nickel spectra. The Au 4f peaks gave a usual doublet with a separation of 3.6 eV for the spin orbit coupled energy levels (4f_{5/2} and 4f_{7/2}) at 84 and 87.6 eV representing the typical metallic nature of gold. The UHV measurements thus revealed the synergistic effect of gold-nickel bimetallic system, by retaining the naked nickel surface in its metallic form influenced by the gold core, imparting inertness to the oxidation behaviour. To investigate whether the stability of the electronic structure of nickel is only at UHV-RT conditions? What will be the behaviour of this metallic nickel surface under reactive environments particularly in presence of oxygen? These questions were addressed by *in-situ* NAPXPS studies of the core-shell nanochains subjecting them to oxygen atmosphere and at elevated temperatures. From the previous results of core-shell nanoparticles, it was found that synergism can operate more than 100 °C even under oxygen atmosphere. The spectra recorded at higher temperatures (100 °C and 200 °C) with a constant oxygen pressure of 0.1 mbar at the sample surface is given in the Figure 4.7 (pink and red). The remarkable stability of metallic nickel surface against oxidation was proved whereby the major Ni metallic peak at 852.6 eV was retained even at 100 °C in presence of oxygen atmosphere. The temperature was further raised to 200 °C under 0.1 mbar of oxygen and the transition of metallic nickel into oxidic phase was clearly observed. In the nickel spectra, the metallic peak at 852.6 eV came down drastically and merged with hydroxide species by the emergence of a new peak centered at 854 eV corresponding to nickel oxide (NiO). Meanwhile in the oxygen spectra, the generation of a new peak emerged at 529.5 eV which is assigned to oxygen species present in nickel oxide. This confirmed the transformation of metallic nickel to nickel oxide at the surface. Apart from these informations about the oxidation behaviour of electronically/geometrically modified nickel surfaces in gold-nickel core-shell structures, NAPXPS studies was also useful to elucidate structural stability of such system under the same conditions. The NAPXPS results showed that gold can impart its inert behaviour to the nickel overlayers by altering its

electronic structure. The implications in the altered electronic properties of the nickel surfaces have crucial influence on the catalytic behaviour of such core-shell bimetallic nanostructures and have been probed by carrying out transfer hydrogenation reaction. This reaction has been reported on bimetallic variations of nickel recently⁵⁰. So it was worthwhile to have a direct comparison with the Au@Ni nanostructures prepared in this report.

Hence a combined thermal analysis by XPS and XRD under oxygen and oxygen containing atmospheres (air) respectively confirmed the synergistic properties of Au@Ni core-shell nanochains. The collective investigations confirmed the surface and bulk oxidation resistance of the material and also the thermal stability without any alloying or segregation.

4.3.6 Catalytic Activity Results of Au@Ni Core-shell Nanochains for Transfer Hydrogenation of Acetophenone by Using IPA as Hydrogen Donor

To check the catalytic performance of the clean Au@Ni core-shell surface, transfer hydrogenation reaction was carried out to convert carbonyl groups in to the corresponding alcohols. Transfer hydrogenation provides an alternative source of hydrogen which can be abstracted from the reaction medium itself for reducing various functional groups⁵¹. Transfer hydrogenation contribute greatly to the catalysis in many aspects like avoiding commonly available hazardous and unsafe reducing agents, use of safe and eco-friendly alternatives like isopropanol as hydrogen donor, easier methods which does not require pressurized conditions, etc. Usually the transfer hydrogenation reactions are carried out by using isopropyl alcohol (IPA) as the hydrogen source in presence of a base. The advantage of using isopropyl alcohol is that it plays the dual role of solvent and hydrogen donor for the reaction. The effective transfer of hydrogen species from isopropyl alcohol to the substrate leads to the oxidation of IPA to form ketone (acetone) and the rate kinetics is highly modified by the presence of a catalyst. First row transition metals like Ni, Fe, and Co along with precious metals (Ru, Rh, Pt, Ir, etc) are found to be good candidates for transfer hydrogenation effectively at moderate temperatures but still require modifications in the catalytic activity and sustainability⁵¹. The major challenge in their reaction is the abstraction and insertion of hydrogen in between two different molecules. The extremely higher mole ratios of the catalyst materials required for the reaction and relatively lower conversion rates as compared to conventional hydrogenation methods made this process less popular. But in recent time the search for safe and environmentally benign methods for catalytic conversions insisted the researchers to revisit

the transfer hydrogenation protocol⁵². Tailored bimetallic catalysts have shown good promise in transfer hydrogenation reactions^{50, 52}. The challenge in the area is to use low temperature for activation of the molecules with lesser quantities of base (KOH) and catalyst materials. Acetophenone hydrogenation to 1-phenylethanol stands as a bench mark in transfer hydrogenation reactions where various functional groups mainly aldehydes and ketones have been reported⁵². Also it allows the optimization of the catalytic activity of Au@Ni core-shell nanochains under milder reaction parameters to prove the synergistic activity of the Au-Ni bimetallic combination.

| Serial No. | Catalyst | Amount (mg) | Substrate (mmol) | Base [KOH] (mmol) | Time (Hrs) | Temp. (deg C) | Conversion (%) |
|------------|----------|-------------|------------------|-------------------|------------|---------------|----------------|
| 1 | --- | --- | 1 | 0.1 | 6 | 80 | N.R |
| 2 | --- | --- | 1 | 0.25 | 6 | 80 | N.R |
| 3 | Au@Ni | 5 mg | 1 | 0.1 | 12 | 80 | 12% |
| 5 | Au@Ni | 5 mg | 1 | 0.25 | 6 | 80 | 52% |
| 6 | Au@Ni | 10 mg | 1 | 0.1 | 12 | 80 | 30% |
| 7 | Au@Ni | 10 mg | 1 | 0.25 | 6 | 80 | 75% |
| 8 | Au@Ni | 10 mg | 1 | 0.25 | 12 | 80 | 92% |
| 9 | Au@Ni | 5 mg | 1 | 0.1 | 12 | 120 | 88% |
| 10 | Au@Ni | 5 mg | 1 | 0.25 | 3 | 120 | 92% |
| 11* | Ag@Ni | 50 mg | 1 | 1.5 | 2 | 80 | 94% |
| 12* | Fe-Ni | 50 mg | 1 | 0.1 | 45 | 100 (M.W) | 98% |

Table 4.1 Optimized reaction conditions for acetophenone transfer hydrogenation to 1-phenylethanol with Au@Ni catalysts using IPA (3 ml) as hydrogen donor at different temperatures, catalyst and base amounts. Entry 11 & 12 represents the literature reports.

Transfer hydrogenation of acetophenone was carried out in a 5 ml sealed tube under different temperature and base conditions using varying amounts of Au@Ni core-shell catalysts. All the reactions were carried with isopropanol as solvent and hydrogen donor for the hydrogenation of carbonyl group present in acetophenone. Progress of the reaction was monitored with the help of a gas chromatograph (GC) and the reactants and products were calibrated with the retention time obtained for the standard samples. After each catalytic

activity tests the catalyst was recovered from the reaction medium with the help of an external magnet by utilizing the magnetic properties of nickel shell. Hence the recycling of the catalyst was done easily which is an important aspect in heterogeneous catalysis. The catalyst activity was done at optimized conditions and the results are shown in the Table 4.1. In the absence of catalyst (blank) and under various amounts of base, the reaction hardly progressed, showing that the reaction under consideration is catalytic. As compared to the previous literature reports (Table 4.1), Au@Ni core-shell catalyst were found to be more efficient than other reported bimetallic nickel catalysts even with lesser amount of base and catalyst quantity. One of the major challenges in transfer hydrogenation catalysis is the need of very high mol % of the catalyst with respect to the substrate typically 10 or 20 times more than a normal catalytic amount. The activity results showed that even with a lesser amount of the catalyst the transformation progressed smoothly with optimized time duration, operating temperatures and base amounts. The metallic feature of the nickel surface is believed to play a key role in activating the substrate molecules while carrying out the hydrogenation reactions. The oxide layer formation on the surface will lead to an induction period for the catalyst to initiate the conversion by reaching to its active phase. Metals that are prone to ambient oxidation are always found to proceed with an induction period for initiating the catalytic cycle particularly for hydrogenation reactions. The prime importance of Au@Ni core-shell catalysts with a nickel shell which can resist the aerial oxidation behavior and to show excellent catalytic properties due to the electronically/geometrically modified properties of nickel from the gold core is demonstrated in this case.

The reaction results from Table 4.1 reveal that there is interplay between the reaction parameters of transfer hydrogenation such as temperature, amount of base and catalyst to get maximum activity results in a specified time. The initial reactions were carried out at a lesser temperature 80 °C, with 5 and 10 mg amount of the catalyst at varying base amounts of 0.1 and 0.25 mmol. All the parameters employed in this stage of the reactivity analysis were found to be lesser than the currently reported literature values especially in the case of catalyst and base amounts. The literature reports showed the need of almost 10 times more amount of catalyst or base to facilitate the reaction⁵⁰. From the reaction results it is clear that even with these milder optimization conditions Au@Ni core-shell nanochains initiated the catalytic conversion. The reaction gave 92 % conversion to 1-phenylethanol at 80°C with 0.25 mmol of base and 10 mg of the catalyst, which is remarkable with 12 hrs reaction time. Whereas in the

other two cases where the reactions were done at higher temperature 120°C with only 5 mg core-shell catalyst and varying base conditions gave almost 90 % conversion with different reaction time (3 and 12 hrs respectively). In all the cases the reactions lead to the formation of 1-phenylethanol as the major product which is confirmed from G.C analysis. Transfer hydrogenation results showed the possibility of tuning Au@Ni catalyst for optimum conversions under different conditions, especially with a much lower amount of catalyst and base. A time dependent conversion analysis was done at different time intervals of the reaction carried out at 80°C to understand the reaction rate progress at various stages with 10 mg of the catalyst. Results obtained from the time dependant analysis showed a linear trend in the conversion starting from the initial state of the reaction (Figure 4.8a). A similar observation is obtained for the time dependent analysis carried out at 120°C with lesser amount of catalyst, 5 mg (Figure 4.8b). These observations confirmed the absence of any induction period for core-shell catalysts which could lag the conversion in the early stages of hydrogenation. The data showed good agreement with the XPS results of nickel surface which existed mainly in the metallic feature.

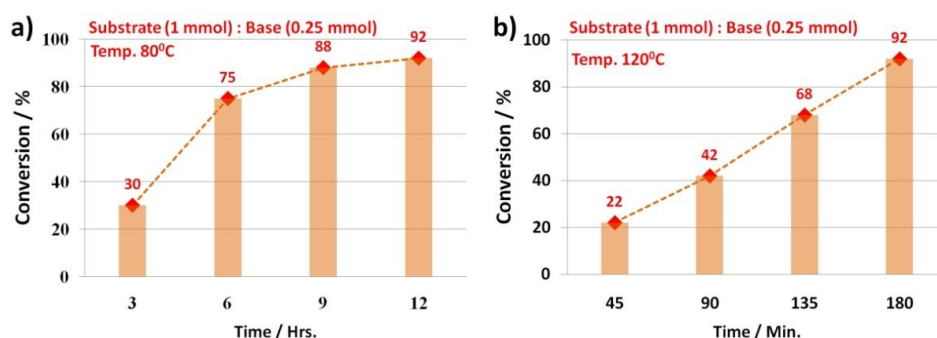


Figure 4.8 Graph represents the conversion of acetophenone at various time intervals using Au@Ni catalysts at 80°C and 120°C .

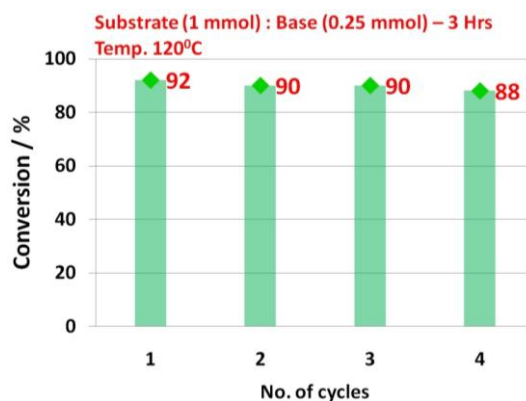


Figure 4.9 Recyclability tests done for Au@Ni catalysts for acetophenone transfer hydrogenation using IPA.

Finally the magnetic property of the core-shell catalysts was used for recovering the catalysts from the reaction medium and its recyclability tests were carried out (Figure 4.9). The catalyst showed sustainable activity results even after four catalytic cycles without any appreciable drop in activity. These results undoubtedly proved that even with a surfactant free synthesis strategy the core-shell nanochains retained their synergistic properties while demonstrating catalysis. Thus the spectroscopic observations corroborated with the catalytic activity results which confirmed the importance of such bimetallic core-shell morphology for the synergistic activity.

4.4 Conclusions

A surfactant free aqueous phase synthesis method is reported for the generation of Au@Ni core-shell nanochains without using any expensive and hazardous organic ligands. Au@Ni nanochains showed high thermal stability and bulk oxidation resistance up to 300 °C. *In situ* NAPXPS showed the bare Au@Ni nanochain surfaces under oxygen atmosphere and different temperatures to be oxidations resistant up to 200 °C. Ligand free Au@Ni nanochain surfaces are found to be highly active for transfer hydrogenation of acetophenone under various temperature and base conditions. The catalytic activity of Au@Ni nanochains showed the synergistic effects of these bimetallic combinations which catalyses transfer hydrogenation under mild conditions as compared to other bimetallic combinations reported in the literature.

4.5 References

1. Alayoglu, S.; Zavalij, P.; Eichhorn, B.; Wang, Q.; Frenkel, A. I.; Chupas, P., Structural and Architectural Evaluation of Bimetallic Nanoparticles: A Case Study of Pt–Ru Core–Shell and Alloy Nanoparticles. *ACS Nano* **2009**, *3* (10), 3127-3137.
2. Jiang, H.-L.; Xu, Q., Recent progress in synergistic catalysis over heterometallic nanoparticles. *J. Mater. Chem.* **2011**, *21* (36), 13705-13725.
3. Zhang, S.; Nguyen, L.; Liang, J.-X.; Shan, J.; Liu, J.; Frenkel, A. I.; Patlolla, A.; Huang, W.; Li, J.; Tao, F., Catalysis on singly dispersed bimetallic sites. *Nat. Commun.* **2015**, *6*, 7938.
4. Cai, S.; Duan, H.; Rong, H.; Wang, D.; Li, L.; He, W.; Li, Y., Highly Active and Selective Catalysis of Bimetallic Rh₃Ni₁ Nanoparticles in the Hydrogenation of Nitroarenes. *ACS Catal.* **2013**, *3* (4), 608-612.
5. Hughes, M. D.; Xu, Y.-J.; Jenkins, P.; McMorn, P.; Landon, P.; Enache, D. I.; Carley,

- A. F.; Attard, G. A.; Hutchings, G. J.; King, F.; Stitt, E. H.; Johnston, P.; Griffin, K.; Kiely, C. J., Tunable gold catalysts for selective hydrocarbon oxidation under mild conditions. *Nature* **2005**, *437* (7062), 1132-1135.
6. Corma, A.; Serna, P., Chemoselective Hydrogenation of Nitro Compounds with Supported Gold Catalysts. *Science* **2006**, *313* (5785), 332-334.
 7. Sneed, B. T.; Young, A. P.; Tsung, C.-K., Building up strain in colloidal metal nanoparticle catalysts. *Nanoscale* **2015**, *7* (29), 12248-12265.
 8. Sun, Y.; Xia, Y., Shape-Controlled Synthesis of Gold and Silver Nanoparticles. *Science* **2002**, *298* (5601), 2176-2179.
 9. Jana, N. R.; Gearheart, L.; Murphy, C. J., Seed-Mediated Growth Approach for Shape-Controlled Synthesis of Spheroidal and Rod-like Gold Nanoparticles Using a Surfactant Template. *Adv. Mater.* **2001**, *13* (18), 1389-1393.
 10. Xia, Y.; Xiong, Y.; Lim, B.; Skrabalak, S. E., Shape-Controlled Synthesis of Metal Nanocrystals: Simple Chemistry Meets Complex Physics? *Angew. Chem. Int. Ed.* **2009**, *48* (1), 60-103.
 11. Sekhar, A. C. S.; Meera, C. J.; Ziyad, K. V.; Gopinath, C. S.; Vinod, C. P., Synthesis and catalytic activity of monodisperse gold-mesoporous silica core-shell nanocatalysts. *Catal. Sci. Technol.* **2013**, *3* (5), 1190-1193.
 12. Sunil Sekhar, A. C.; Ziyad, K.; Soni, Y.; Vinod, C. P., Activity Enhancement upon the Incorporation of Titanium: Au@Ti-SiO₂ Core-Shell Nanocatalysts for the CO Oxidation Reaction. *ChemCatChem* **2015**, *7* (7), 1222-1230.
 13. Wang, W.; Banerjee, S.; Jia, S.; Steigerwald, M. L.; Herman, I. P., Ligand Control of Growth, Morphology, and Capping Structure of Colloidal CdSe Nanorods. *Chem. Mater.* **2007**, *19* (10), 2573-2580.
 14. Aslam, M.; Fu, L.; Su, M.; Vijayamohanan, K.; Dravid, V. P., Novel one-step synthesis of amine-stabilized aqueous colloidal gold nanoparticles. *J. Mater. Chem.* **2004**, *14* (12), 1795-1797.
 15. Ristig, S.; Prymak, O.; Loza, K.; Gocyla, M.; Meyer-Zaika, W.; Heggen, M.; Raabe, D.; Epple, M., Nanostructure of wet-chemically prepared, polymer-stabilized silver-gold nanoalloys (6 nm) over the entire composition range. *J. Mater. Chem. B* **2015**, *3* (23), 4654-4662.
 16. Mourdikoudis, S.; Liz-Marzán, L. M., Oleylamine in Nanoparticle Synthesis. *Chem. Mater.* **2013**, *25* (9), 1465-1476.
 17. Narayanan, R.; El-Sayed, M. A., Effect of Colloidal Catalysis on the Nanoparticle Size Distribution: Dendrimer-Pd vs PVP-Pd Nanoparticles Catalyzing the Suzuki Coupling Reaction. *J. Phys. Chem. B* **2004**, *108* (25), 8572-8580.
 18. Peng, X.; Pan, Q.; Rempel, G. L., Bimetallic dendrimer-encapsulated nanoparticles as catalysts: a review of the research advances. *Chem. Soc. Rev.* **2008**, *37* (8), 1619-1628.
 19. Lopez-Sanchez, J. A.; Dimitratos, N.; Hammond, C.; Brett, G. L.; Kesavan, L.; White, S.; Miedziak, P.; Tiruvalam, R.; Jenkins, R. L.; Carley, A. F.; Knight, D.; Kiely, C. J.; Hutchings, G. J., Facile removal of stabilizer-ligands from supported gold nanoparticles. *Nat. Chem.* **2011**, *3* (7), 551-556.
 20. Li, P.-Z.; Aijaz, A.; Xu, Q., Highly Dispersed Surfactant-Free Nickel Nanoparticles and Their Remarkable Catalytic Activity in the Hydrolysis of Ammonia Borane for Hydrogen Generation. *Angew. Chem. Int. Ed.* **2012**, *51* (27), 6753-6756.
 21. Tsubota, S.; Nakamura, T.; Tanaka, K.; Haruta, M., Effect of calcination temperature on the catalytic activity of Au colloids mechanically mixed with TiO₂ powder for CO oxidation. *Catal. Lett.* **1998**, *56* (2), 131-135.
 22. Menard, L. D.; Xu, F.; Nuzzo, R. G.; Yang, J. C., Preparation of TiO₂-supported Au

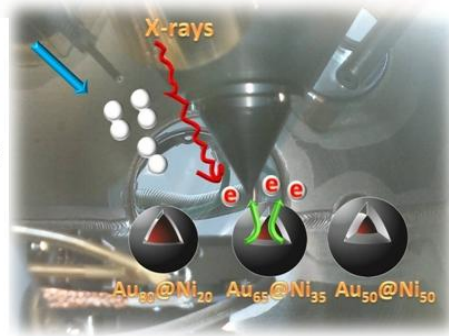
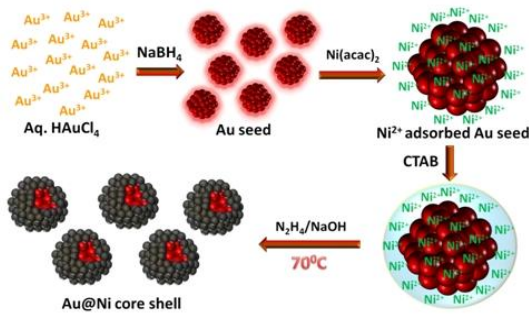
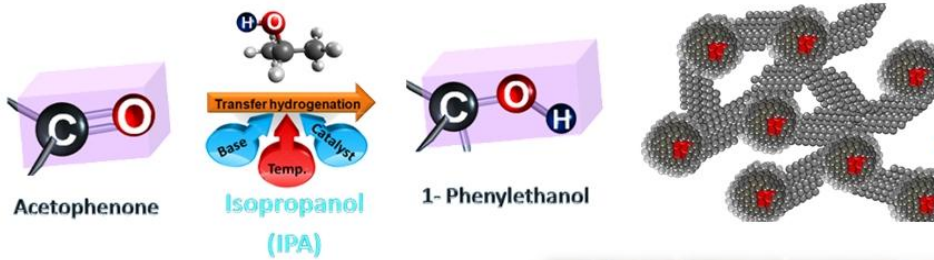
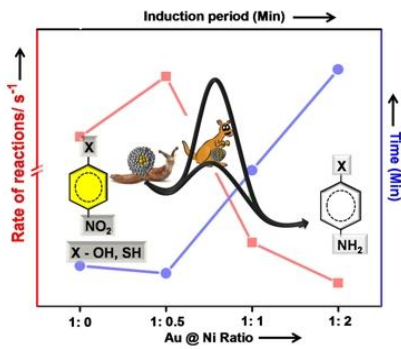
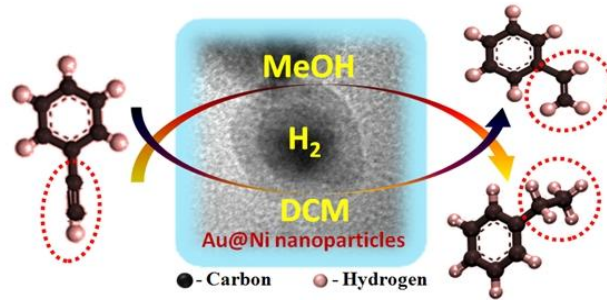
- nanoparticle catalysts from a Au₁₃ cluster precursor: Ligand removal using ozone exposure versus a rapid thermal treatment. *J. Catal.* **2006**, *243* (1), 64-73.
23. Wang, Z. L.; Petroski, J. M.; Green, T. C.; El-Sayed, M. A., Shape Transformation and Surface Melting of Cubic and Tetrahedral Platinum Nanocrystals. *J. Phys. Chem. B* **1998**, *102* (32), 6145-6151.
 24. Cao, A.; Lu, R.; Vesper, G., Stabilizing metal nanoparticles for heterogeneous catalysis. *Phys. Chem. Chem. Phys.* **2010**, *12* (41), 13499-13510.
 25. Luo, M.; Hong, Y.; Yao, W.; Huang, C.; Xu, Q.; Wu, Q., Facile removal of polyvinylpyrrolidone (PVP) adsorbates from Pt alloy nanoparticles. *J. Mater. Chem. A* **2015**, *3* (6), 2770-2775.
 26. Zhong, R.-Y.; Sun, K.-Q.; Hong, Y.-C.; Xu, B.-Q., Impacts of Organic Stabilizers on Catalysis of Au Nanoparticles from Colloidal Preparation. *ACS Catal.* **2014**, *4* (11), 3982-3993.
 27. Li, D.; Wang, C.; Tripkovic, D.; Sun, S.; Markovic, N. M.; Stamenkovic, V. R., Surfactant Removal for Colloidal Nanoparticles from Solution Synthesis: The Effect on Catalytic Performance. *ACS Catal.* **2012**, *2* (7), 1358-1362.
 28. Chen, T.; Rodionov, V. O., Controllable Catalysis with Nanoparticles: Bimetallic Alloy Systems and Surface Adsorbates. *ACS Catal.* **2016**, *6* (6), 4025-4033.
 29. Kwon, S. G.; Krylova, G.; Sumer, A.; Schwartz, M. M.; Bunel, E. E.; Marshall, C. L.; Chattopadhyay, S.; Lee, B.; Jellinek, J.; Shevchenko, E. V., Capping Ligands as Selectivity Switchers in Hydrogenation Reactions. *Nano Lett.* **2012**, *12* (10), 5382-5388.
 30. Chapter 2A of this thesis
 31. Chapter 2B of this thesis
 32. Chapter 2C of this thesis
 33. Leon, C. C.; Lee, J.-G.; Ceyer, S. T., Oxygen Adsorption on Au–Ni(111) Surface Alloys. *J. Phys. Chem. C* **2014**.
 34. Rostrup-Nielsen, J. R.; Sehested, J.; Nørskov, J. K., Hydrogen and synthesis gas by steam- and CO₂ reforming. In *Advances in Catalysis*, Academic Press: 2002; Vol. Volume 47, pp 65-139.
 35. Holgado, J. P.; Ternero, F.; Gonzalez-delaCruz, V. M.; Caballero, A., Promotional Effect of the Base Metal on Bimetallic Au–Ni/CeO₂ Catalysts Prepared from Core–Shell Nanoparticles. *ACS Catal.* **2013**, *3* (9), 2169-2180.
 36. Luedtke, W. D.; Landman, U., Stability and Collapse of Metallic Structures on Surfaces. *Phys. Rev. Lett.* **1994**, *73* (4), 569-572.
 37. Zhou, X. W.; Wadley, H. N. G., Misfit dislocations in gold/Permalloy multilayers. *Philos. Mag.* **2004**, *84* (2), 193-212.
 38. Duan, H.; Wang, D.; Li, Y., Green chemistry for nanoparticle synthesis. *Chem. Soc. Rev.* **2015**, *44* (16), 5778-5792.
 39. Niu, Z.; Li, Y., Removal and Utilization of Capping Agents in Nanocatalysis. *Chem. Mater.* **2014**, *26* (1), 72-83.
 40. Eustis, S.; El-Sayed, M. A., Why gold nanoparticles are more precious than pretty gold: Noble metal surface plasmon resonance and its enhancement of the radiative and nonradiative properties of nanocrystals of different shapes. *Chem. Soc. Rev.* **2006**, *35* (3), 209-217.
 41. Link, S.; El-Sayed, M. A., Size and Temperature Dependence of the Plasmon Absorption of Colloidal Gold Nanoparticles. *J. Phys. Chem. B* **1999**, *103* (21), 4212-4217.
 42. Henning, A. M.; Watt, J.; Miedziak, P. J.; Cheong, S.; Santonastaso, M.; Song, M.; Takeda, Y.; Kirkland, A. I.; Taylor, S. H.; Tilley, R. D., Gold–Palladium Core–Shell Nanocrystals with Size and Shape Control Optimized for Catalytic Performance. *Angew.*

Chem. Int. Ed. **2013**, *52* (5), 1477-1480.

43. She, H.; Chen, Y.; Chen, X.; Zhang, K.; Wang, Z.; Peng, D.-L., Structure, optical and magnetic properties of Ni@Au and Au@Ni nanoparticles synthesized via non-aqueous approaches. *J. Mater. Chem.* **2012**, *22* (6), 2757-2765.
44. Sreedhala, S.; Vinod, C. P., Surfactant assisted formation of ruthenium nanochains under mild conditions and their catalytic CO oxidation activity. *Chem. Commun.* **2015**, *51* (50), 10178-10181.
45. Zhang, H.; Ding, J.; Chow, G.; Ran, M.; Yi, J., Engineering Magnetic Properties of Ni Nanoparticles by Non-Magnetic Cores. *Chem. Mater.* **2009**, *21* (21), 5222-5228.
46. Chen, Y.; Peng, D.-L.; Lin, D.; Luo, X., Preparation and magnetic properties of nickel nanoparticles via the thermal decomposition of nickel organometallic precursor in alkylamines. *Nanotechnology* **2007**, *18* (50), 505703.
47. Chapter 2A of this thesis
48. Huang, L.; Shan, A.; Li, Z.; Chen, C.; Wang, R., Phase formation, magnetic and optical properties of epitaxially grown icosahedral Au@Ni nanoparticles with ultrathin shells. *CrystEngComm* **2013**, *15* (13), 2527-2531.
49. Ruban, A.; Hammer, B.; Stoltze, P.; Skriver, H. L.; Nørskov, J. K., Surface electronic structure and reactivity of transition and noble metals. *J. Mol. Catal. A: Chem.* **1997**, *115* (3), 421-429.
50. Gawande, M. B.; Guo, H.; Rathi, A. K.; Branco, P. S.; Chen, Y.; Varma, R. S.; Peng, D.-L., First application of core-shell Ag@Ni magnetic nanocatalyst for transfer hydrogenation reactions of aromatic nitro and carbonyl compounds. *RSC Adv.* **2013**, *3* (4), 1050-1054.
51. Wang, D.; Astruc, D., The Golden Age of Transfer Hydrogenation. *Chem. Rev.* **2015**, *115* (13), 6621-6686.
52. Polshettiwar, V.; Baruwati, B.; Varma, R. S., Nanoparticle-supported and magnetically recoverable nickel catalyst: a robust and economic hydrogenation and transfer hydrogenation protocol. *Green Chem.* **2009**, *11* (1), 127-131.

Chapter 5

Summary and Conclusions



Chapter 5: Summary and Conclusions

The need for stable, active and sustainable catalyst materials in heterogeneous catalysis, with tunable selectivity has resulted in the synthesis of next generation of nanocatalysts. Bimetallic nanoparticles are a hybrid class of “designed catalysts” which can enhance the efficiency of catalytic transformations by imparting chemical stability and functionality. Work presented in this thesis shows the synthesis, characterization and catalytic properties of Au@Ni core-shell bimetallic nanostructures. Furthermore, this thesis is focussed to understand the synergistic effects operating on Au@Ni core-shell bimetallic nanostructures through *insitu* NAPXPS tool. The previous works done on Au-Ni bimetallic model surfaces showed interesting reactivity pattern, where sub-monolayer Ni coverages on Au (and vice versa) was found to resist oxidation and coking. To realize the potential applications of Au-Ni bimetallic combination, Au@Ni core-shell nanoparticles were synthesized and utilized for catalysis. The work presented in the thesis also gives evidence for the importance of core-shell nanostructures and the optimum composition for obtaining best synergistic catalytic effects.

Chapter 1 of this thesis gives a general introduction and literature survey about the progress of heterogeneous catalysis in the recent time. The role of quantum confinement effects in nanoparticles in deciding the physiochemical properties of nanomaterials which in turn perturbs the chemical reactivity trends have been discussed. Nanocatalysts can be considered as promising materials in heterogeneous catalysis and their “tailor-made” structures offer a lot of prospect as futuristic catalyst materials. The chapter also discusses the early works on bimetallic systems and their development as catalyst materials. The studies on bimetallic over layer surfaces showed that synergistic effect in bimetallic combinations arises due to geometric and electronic modifications and it depends on the interacting atoms and nature of interaction. In the continuing discussion, it is explained that the real world catalysis differs from the ‘materials used for employing molecular level understanding of the catalytic mechanism’ which is traditionally done through ultra high vacuum surface science studies. The importance of “bridging the material and pressure gap” in surface science studies is also briefly reviewed. Later part of the chapter discusses the

importance of gold (Au) - nickel (Ni) bimetallic surface which forms the central working material for the thesis. The chapter also provides the information about the various bimetallic architectures and their colloidal phase synthesis protocols. Finally, the chapter describes the catalytic applications of colloidal bimetallic nanoparticles with special focus on Au-Ni bimetallic catalyst materials. The characterization tools used in this dissertation is also discussed in this chapter including one of the recent advancement in XPS called near ambient pressure photoelectron spectroscopy (NAPXPS).

Chapter 2 describes various synthesis strategies for the generation of Au@Ni core-shell nanostructures. In this chapter, the organic phase synthesis of Au@Ni core-shell system is reported. In all the cases a one-pot sequential reduction strategy is employed to generate Au@Ni core-shell morphology. Depending on the chemical reduction route and solvent used for the generation of Au@Ni nanoparticles, the chapter is sub divided in to three namely 2A, 2B and 2C. The synthesis of Au@Ni core-shell systems, their characterization using UV-Vis, HR-TEM, VSM, XRD and XPS followed by catalytic activity measurements for various hydrogenation reactions forms these chapters.

Chapter 2A discusses the synthesis of magnetic and non-magnetic Au@Ni (Au@Ni_{FCC} and Au@Ni_{HCP}) bimetallic core-shell nanoparticles via a thermal reduction route in oleyl amine solvent. The crystalline phases of nickel shell are controlled by a carefully designed synthesis method to form FCC and HCP nickel layer over sub 10 nm gold nanoparticles to generate core-shell morphology. The overall size of the core-shell nanoparticles is restricted below 10 nm using a one-pot sequential reduction strategy. By varying the thermal reduction temperature of nickel precursor, magnetic (FCC) and nonmagnetic nickel (HCP) shells over the gold core is generated. The nickel surface of Au@Ni core-shell nanoparticles in the as synthesized form shows oxidation resistance with small shell thickness as revealed by XRD analysis. Finally, the Au@Ni bimetallic catalyst is demonstrated to show synergistic catalytic activity with an optimum shell thickness of 1-2 nm for p-nitrophenol and nitrothiophenol reduction reactions.

Chapter 2B presents modified synthesis method by using oleyl amine as solvent, Au@Ni nanoparticles are synthesized at milder temperature conditions than reported

previously. The core-shell nanoparticles are formed from the same gold seeds and the nickel reduction has been carried out with hydrazine as reducing agent at milder temperatures. A good control over the nickel shell thickness to limit at 2 nm is demonstrated in this chapter. The enhanced activity and selectivity of the Au@Ni core-shell catalysts for selective hydrogenation of phenyl acetylene (P.A) is demonstrated and compared with its individual metal counterparts.

Chapter 2C provides a cost effective and economically viable green synthesis strategy to generate Au@Ni core-shell nanostructures by using environmentally benign solvent soyabean oil instead of hazardous organic solvents. This chapter demonstrate the synthesis of Au@Ni core-shell nanostructures by completely avoiding all the hazardous and harmful organic solvents and capping agents. The synthesis was accomplished in a one-pot synthesis method carried out through a low temperature reduction route. Two distinctly different morphologies are demonstrated in the presence and in the absence of capping agent CTAB. Without using the capping agent, core-shell nanochains are formed whereas the other one lead to the formation of core-shell nanoparticles. The chapter also includes a thorough characterisation of both the materials along with a detailed discussion about the catalytic activity of the bimetallic nanostructures in comparison with monometallic Au and Ni towards selective hydrogenation of phenyl acetylene (P.A).

Chapter 3 deals with the synthesis of Au@Ni core-shell nanoparticles through a low temperature sequential reduction method in aqueous medium. The method employed here at milder conditions and greener route for generating bimetallic Au-Ni system with tunable shell thickness offers an environmental friendly process. The Ni shell thickness could be tuned from 2 nm to 10 nm by changing the metal ratios as reported with oleyl amine in chapter 2A. The catalytic results obtained for the transfer hydrogenation reactions in this chapter once again confirms that the synergistic effect operates best with a thin nickel shell and it outweighs the monometallic parent metal nanoparticles. The spectroscopic understanding of the nature of electronically modified nickel surface and the reason for synergism in Au-Ni bimetallic combination is demonstrated through in-situ NAPXPS study. The landscapes of oxidation behaviour of nickel surface which rests on the noble metal gold core is explored for varying Ni shell thickness. The metastable Ni(OOH) decomposition and

the product distribution confirmed that Au@Ni core-shell systems behaves differently with the changes in shell thickness. The decomposition pathways of metastable Ni(OOH) species is vastly different on Au₈₀@Ni₂₀ with extremely thin Ni shell (~2 nm) which mainly converts to metallic nickel which is found to be stable and resistant to oxidation even under oxygen atmospheres at 100 °C. On the other surfaces, Ni(OOH) surface species predominantly gets converted to more stable oxidic (Ni²⁺) species which is typical characteristics of monometallic nickel surfaces. The NAPXPS results discussed in this chapter shows the effect of gold core in modifying the properties of nickel overlayers.

Chapter 4 discusses about the need for improved synthesis strategies for creating cleaner catalyst surfaces without using a great amount of surfactants. In this chapter, a surfactant free synthesis method to generate Au@Ni core-shell nanoparticles without compromising on the aqueous solvent medium and under low temperature pathway is reported. The size controlled core-shell Au@Ni nanochains were synthesized with an optimum Ni shell thickness of approximately 2 nm for exploring maximum catalytic efficiency. Surfactant free Au@Ni nanochains with clean surfaces are shown for transfer hydrogenation of acetophenone using isopropanol as the hydrogen donor at various temperature and base conditions with good efficiency compared to literature results.

In summary, bimetallic Au@Ni core-shell nanoparticles/nanostructures with large lattice mismatch has been synthesized using conventional methods as well as with green solvents. It is also shown in the thesis that a surfactant free route can also be employed for making Au@Ni core-shell nanochains. The Au@Ni core-shell materials are demonstrated to show superior catalytic activity compared to their monometallic counterparts. Electronic/geometric effects are responsible for the bimetallic synergism and the modifications of Au@Ni bimetallic core-shell catalysts and are explored through bulk & surface characterization tools including in-situ NAPXPS. The surface modifications operate up to a few atomic layer on the nickel shell from the gold core and is the optimum for best catalytic performance, beyond which the material resembles the monometallic counterpart.

List of Research Credentials, Awards and Patents

Publications

- Phenylacetylene hydrogenation on Au@Ni bimetallic core-shell nanoparticles synthesized under mild conditions. **Vysakh, A. B.**; Lazar, A.; Yadukiran, V.; Singh, A. P.; Vinod, C. P., Catal. Sci. Technol. 2016, 6 (3), 708-712.
- Synthesis of Au@Ni bimetallic core-shell nanoparticle and nanochains in soyabean oil and their catalytic hydrogenation reactions. **Vysakh, A. B.**; Yadukiran, V.; Lazar, A.; Singh, A. P.; Vinod, C. P., ChemistrySelect 2016, 1 (2), 140-146.
- Demonstration of synergistic catalysis in Au@Ni bimetallic core-Shell nanostructures. **Vysakh, A. B.**; Babu, C. L.; Vinod, C. P., J. Phys. Chem. C 2015, 119 (15), 8138-8146.
- Synthesis and reactivity of magnetically diverse Au@Ni core-Shell nanostructures. **Vysakh, A. B.**; Raj, G. K.; Joy, P. A.; Vinod, C. P., Part. Part. Syst. Char. 2014, 31 (2), 236-244.
- Synthesis of Au@Ni core-shell nanoparticle in aqueous medium: NAPXPS studies on oxidation resistance and its application in selective hydrogenation. **Vysakh, A. B.**, Ruchi Jain, C.S. Gopinath, C. P. Vinod (Manuscript to be submitted).
- Surfactant free Synthesis of Au@Ni Core-shell Nanochains in Aqueous Medium as Efficient Transfer Hydrogenation Catalysts. **Vysakh, A. B.**, K. J. Shebin, Ruchi Jain, C.S. Gopinath, C. P. Vinod (Manuscript to be submitted).

Awards and Patents

- Best poster presentation award in Catalysis and Inorganic Chemistry division at “National Science Day” organized by CSIR-National Chemical Laboratory, Pune from 27-28 February 2015.
- AN IMPROVED PROCESS FOR THE PREPARATION OF BIMETALLIC CORE-SHELL NANOPARTICLES, C.P.Vinod and **Vysakh, A. B.** (Applied for patent – October 2016).

About the Author

Vysakh.A.B, son of Mr. Bharathan A.K and Omana Bharathan, was born on April 17, 1986 in Thrissur district, Kerala. After completing his secondary (2001) and higher secondary education (2003) from Govt. Vocational Higher Secondary School Cherpu (G.V.H.S.S) Kerala, he started his Bachelors in Pure chemistry in Christ College Irinjalakuda, Kerala (2003-2006). He got his post graduation degree in Pure Chemistry from Karpagam Arts & Science College, Bharathiar University, Coimbatore, Tamilnadu (2006-2008). He was awarded UGC-Junior Research Fellowship in 2010 and he joined National Chemical Laboratory in August 2011 for his doctoral studies under the supervision of Dr. Vinod C. Prabhakaran, Catalysis and Inorganic Chemistry Division. His research interests include synthesis of strained bimetallic nanoparticles and its applications in nanocatalysis. His thesis work describes the investigation of gold-nickel core-shell bimetallic nanoparticles by using NAPXPS surface science technique and their applications in enhancing activity and selectivity of hydrogenation reactions of various functional groups.